FACULDADE DE ENGENHARIA DA UNIVERSIDADE DO PORTO

Enhancement of the mechanical properties of tool steels through laser shock peening for manufacture applications

Lucas Dourado Azevedo

SUBMITTED FOR THE DEGREE OF
DOCTOR OF PHILOSOPHY IN MECHANICAL ENGINEERING



Doctoral Program in Mechanical Engineering

Supervisor: Dr. Paulo José da Silva Tavares

Co-supervisor: Prof. Jorge Humberto Oliveira Seabra

March 23, 2021

© Lucas Dourado Azevedo, 2021

Enhancement of the mechanical properties of tool steels through laser shock peening for manufacture applications

Lucas Dourado Azevedo

Doctoral Program in Mechanical Engineering

March 23, 2021

Abstract

The economical viability of manufacturing processes is highly dependent on the performance of the tools used. This applies first and foremost to large scale series production for the automotive industry, where the profit margins are small, and tool failure can represent serious losses. It is well-established that material surfaces have a great contribution to their performance since it is typically where the failure occurs. Therefore, the improvement of the performance of metal tools operating under demanding conditions of impact and wear poses a challenge for the tool making industry. In this regard, there is a constant demand for new processing methods to improve material characteristics.

This thesis aims to provide advanced experimental knowledge in the field of laser-based tool steel surface processing and ultimately enhance the mechanical properties of cold work tool steel for manufacturing applications. For this purpose, beneficial compressive residual stresses were induced through a controlled approach using a laser-based surface processing technique commonly known as laser shock peening (LSP).

A comprehensive testing procedure has been conducted to evaluate the benefits, limitations and applicability of LSP, which includes residual stress measurement, roughness and hardness measurement, microstructural observation, tensile testing, fatigue, fatigue crack propagation and wear testing. The high-strain rates, typically experienced with the LSP process, caused a deep and uniform compressive residual stress field. Material modifications occurred, resulting in hardness and roughness increases along with substantial improvement of fatigue and wear resistance. LSP is a promising surface processing technique, still to be widely accepted, which overcomes several problems found in conventional peening techniques. However, a successful application of LSP requires significant knowledge and control over the process and its variables.

Keywords: Laser shock peening, Residual stresses, Tool steel, Mechanical properties, Mechanical Testing.

Resumo

A viabilidade económica dos processos de fabrico depende em grande medida do desempenho das ferramentas utilizadas. Isto aplica-se fundamentalmente à produção em grande escala para a indústria automóvel, onde as margens de lucro são reduzidas, e a falha das ferramentas pode implicar sérios prejuízos. É bem conhecido que as superfícies de materiais contribuem significativamente para o seu desempenho, uma vez que é normalmente onde a falha surge. Por conseguinte, a melhoria do desempenho das ferramentas metálicas que operam em condições exigentes de impacto e desgaste constitui um desafio para a indústria. Consequentemente, existe uma necessidade constante de novos métodos de processamento para melhorar as características do material.

Esta tese tem por objectivo fornecer conhecimentos experimentais avançados no campo do processamento a laser de superfícies de aço para ferramentas e, em última análise, melhorar as propriedades mecânicas do aço para ferramentas de trabalho a frio para aplicações de fabrico industrial. Para este efeito, foram introduzidas tensões residuais compressivas benéficas através de uma abordagem controlada utilizando uma técnica de processamento de superfície baseada a laser geralmente conhecida como laser shock peening (LSP).

Foram realizados procedimentos de teste abrangentes para avaliar os benefícios, limitações e aplicabilidade do LSP, que incluem medição de tensões residuais, medição de rugosidade e dureza, observação microestrutural, testes de tracção, testes de fadiga e propagação de fenda por fadiga, e testes desgaste. As elevadas taxas de deformação, tipicamente verificadas com o processo de LSP, originaram um campo de tensão residual compressivo profundo e uniforme. Verificaram-se modificações de material, que resultaram em aumento da dureza e rugosidade, juntamente com uma melhoria substancial da resistência à fadiga e ao desgaste. O LSP é uma técnica promissora de processamento de superfície, ainda não amplamente adoptada, que permite contornar vários inconvenientes encontrados nas técnicas convencionais de peening. No entanto, uma aplicação de LSP bem-sucedida requer profundos conhecimentos e controlo sobre o processo e as suas variáveis.

Palavras-chave: Laser shock peening, Tensões residuais, Aço ferramenta, Propriedades mecânicas, Ensaios mecânicos.

Acknowledgements

The work presented in this thesis would not have been possible without the support of several people and institutions. In this regard, I would like to express a special recognition and gratitude to the following institutions and individuals:

Supervisors:

- Dr. Paulo J.S. Tavares (supervisor)
- Prof. Jorge H.O. Seabra (co-supervisor)

Contributions at Quantal S.A.:

- Eng. Paulo Quintal
- Eng. Carlos Furtado

Contributions at HZG:

- Dr. Nikolai Kashaev (Head of the department WMF, HZG)
- Mr. Stefan Riekehr (support in experimental work)
- Mr. Sören Keller (analysis of residual stress measurement results; support in experimental work)
- Mr. Rene Dinse (support in experimental work)
- Mr. Christian Horstmann (support in material testing)
- Mr. Volker Verntzke (support in material testing)

Other contributions:

- Dr. Pedro Moreira (LOME, INEGI)
- Dr. Shayan Eslami (LOME, INEGI)
- Prof. Mário Vaz (FEUP)
- Eng. Miguel Figueiredo (LET, DEMec, FEUP)
- Eng. Emília Soares (DEMec, FEUP)
- Mr. Pedro Rómio (FEUP)
- Mr. Rui Rocha (CEMUP)

Involved Institutions:

- Faculdade de Engenharia da Universidade do Porto (FEUP), Porto, Portugal
- Quantal S.A., Vila do Conde, Portugal
- Helmholtz-Zentrum Geesthacht, Centre for Materials and Coastal Research, Geesthacht, Germany
- Instituto de Ciência e Inovação em Engenharia Mecânica e Engenharia Industrial (INEGI), Porto, Portugal

Financial support:

- Operation NORTE-08-5369-FSE-000046 co-funded by the European Social Fund (FSE) through NORTE 2020 - Programa Operacional Regional do NORTE.

I also want to express my sincere gratitude to all the people who indirectly but equally importantly, have supported me through this challenging journey.

- To all the wonderful people I have met in the course of my technical visit at HZG (Hamburg, Germany), for making these difficult time into such a wonderful and fulfilling experience, and for providing the friendly and familiar atmosphere I most needed in times of separation from my own family.
- To my lifelong friends, for their subtle yet invaluable support.
- And last but certainly not least, to my beloved family, for their full support, and for always encouraging me through this challenging journey.

To all of those mentioned above, I would like to express my deepest and sincere gratitude.

Lucas Dourado Azevedo

"Knowledge isn't power
until it is applied."

Dale Carnegie

Contents

Abstract i

Acknowledgements v

Abbreviations xxi

Symbols xxiii

1 Introduction 1
- 1.1 Scope . . . 1
- 1.2 Objectives . . . 2
- 1.3 Location and duration . . . 3
- 1.4 Structure of the thesis . . . 4

2 State of the art 5
- 2.1 Introduction . . . 5
- 2.2 Peening . . . 6
- 2.3 Laser shock peening . . . 7
- 2.4 Physical process of LSP . . . 8
  - 2.4.1 Laser systems for laser shock peening . . . 10
  - 2.4.2 Confinement medium . . . 11
  - 2.4.3 Ablative layer . . . 13
- 2.5 Laser parameters . . . 16
  - 2.5.1 Laser energy . . . 16
  - 2.5.2 Wavelength . . . 17
  - 2.5.3 Laser spot size and shape . . . 19
  - 2.5.4 Laser pulse width . . . 20
  - 2.5.5 Laser pulse density . . . 22
  - 2.5.6 Laser overlapping . . . 24
- 2.6 LSP effects . . . 26
  - 2.6.1 Residual stress . . . 26
  - 2.6.2 Surface modification . . . 34
  - 2.6.3 Microstructure . . . 36
  - 2.6.4 Hardness and tensile properties . . . 38
  - 2.6.5 Fatigue life and FCP . . . 39
  - 2.6.6 Tribological properties . . . 41
  - 2.6.7 Corrosion resistance behavior . . . 44
- 2.7 LSP process modelling and simulation . . . 47
  - 2.7.1 Analytical models for LSP . . . 47

2.7.2 Material constitutive model . . . 49
2.7.3 FEM for laser shock peening . . . 50
2.8 Future challenges for the LSP process . . . 51
2.9 Summary . . . 51

3 Materials & methods **53**
3.1 Introduction . . . 53
3.2 Material and specimen details . . . 53
3.3 LSP experiment . . . 55
3.3.1 First LSP application stage . . . 57
3.3.2 Second LSP application stage . . . 59
3.4 Testing procedures . . . 62
3.4.1 Residual stress . . . 62
3.4.2 Surface roughness parameters and topography . . . 68
3.4.3 Microstructure . . . 70
3.4.4 Micro hardness . . . 73
3.4.5 Tensile testing . . . 75
3.4.6 Fatigue testing . . . 77
3.4.7 Fatigue crack propagation . . . 79
3.4.8 Wear testing . . . 82

4 Results & discussion **85**
4.1 Introduction . . . 85
4.2 Residual stress field analysis . . . 85
4.2.1 ESPI hole drilling residual stress measurements . . . 85
4.2.2 Contour method . . . 94
4.3 Surface roughness and topography . . . 98
4.4 Micro hardness . . . 108
4.5 Microstructural modification . . . 112
4.5.1 Optical microscopy (OM) . . . 113
4.5.2 Electron backscatter diffraction (EBSD) . . . 115
4.5.3 Energy-dispersive X-ray spectroscopy (EDS) . . . 120
4.6 Tensile properties . . . 122
4.7 Fatigue behaviour . . . 124
4.7.1 Fractography observations . . . 127
4.8 Fatigue crack propagation . . . 135
4.9 Wear behavior . . . 140

5 Concluding remarks & future work **147**
5.1 Conclusions . . . 147
5.2 Future work . . . 150

A Technical drawings of the specimens **151**
A.1 Plate specimen . . . 151
A.2 Dogbone specimen . . . 155
A.3 M(T) specimen . . . 159
A.4 Disk specimen . . . 163
A.5 Notched specimen . . . 167

B Residual stresses **171**
B.1 ESPI Hole-Drilling method 171
B.2 Compressive stress area 177

C 3D wear track profile **181**

D Surface roughness parameters **185**
D.1 Surface parameters 185
D.2 Roughness profile 189

E Micro hardness **195**

F Microstructure **199**
F.1 Optical microscopy 199
F.2 EDS 201

References **207**

List of Figures

1.1 Map showing the main locations during the PhD work. 3

2.1 Peening techniques. 6
2.2 Schematic representation of LSP process. 9
2.3 LSP generation of compressive residual stresses. (a) During the laser-material interaction: stretching of impacted zone. (b) After the laser-matter interaction: reaction of the surrounding material includes a compressive stress field. 9
2.4 Laser–matter interaction principle. Free mode under direct ablation conditions, and confined ablation mode with a transparent medium. 11
2.5 Residual stress profiles generated by LSP with various confining medium. 12
2.6 Water stream as confinement medium for LSP. 13
2.7 Pulse pressure as a function of incident power density for LSP treated 316L steel under direct ablation mode and using an aluminium ablative layer. 14
2.8 Microstructure of LSP treated Ti-alloy under a) direct ablation mode and b) using ablative layer. 14
2.9 Stainless steel adhesive foil. 15
2.10 Peak plasma pressure in water confined mode as a function of power density at different laser wavelengths. 18
2.11 Laser spot size, shape and beam spatial profile 19
2.12 The influence of laser spot shape on the reverse loading. 20
2.13 Maximum pressure as a function of incident power density for different laser pulse widths. 21
2.14 Laser ablation with (a) nanosecond pulses and (b) femtosecond pulses. 21
2.15 In-depth residual stress distribution after LSP with different energy levels and one and two laser impacts. 22
2.16 Schematic illustration of micro-structural evolution induced by different numbers of LSP impacts. 23
2.17 Illustrations of LSP treated areas under overlapped circular laser shots with overlapping rates of 30%, 50%, and 70%. 24
2.18 Experimental and simulated distributions of residual stress fields along depth direction as a function of overlapping rate. 25
2.19 Different types of macro and micro residual stress generated from eigenstrains. . 27
2.20 Typical residual stress state after LSP. 28
2.21 Classification of measurement techniques. 28
2.22 Diagram of the principle of the hole drilling technique. 31
2.23 Experimental set-up for ESPI measurements of strain relaxation by incremental hole drilling. 32
2.24 Key steps of stress measurement by the contour method. 34

2.25 Macroscopic features and 3D morphology on the surface of the specimens (a) before and (b) after LSP. . . . 35
2.26 Surface micrographs of AZ31B Mg alloy. . . . 36
2.27 SEM images of fractured specimens after tensile testing. . . . 37
2.28 The effect of LSP treatment with different confining layers on ER8 steel: (a) surface hardness and (b) hardness depth profile. . . . 38
2.30 Fatigue tests for as-received and LSP treated material: (a) uniaxial tension-tension fatigue testing of ATI 718 Plus alloy and (b) three-point bending fatigue testing of Ti–6Al–4V . . . 40
2.31 Crack length on LSP treated Ti-6Al-4V specimens. . . . 41
2.32 Wear tracks observed after the scratch tests at various laser power densities. . . . 42
2.33 Size distribution of the wear particles. . . . 43
2.34 Wear rate as a function of laser pulse density and laser energy. . . . 44
2.36 Surface morphology of LSP treated AISI 304 stainless steel after electrochemical attack. . . . 46
2.37 Schematic presentation of the LSPwC effect on prevention of intergranular corrosion initiation on the AA6082-T651 alloy . . . 46

3.1 LSP experimental setup. Image courtesy of Department of Joining and Assessment in the Institute of Materials Research, Helmholtz-Zentrum Geesthacht. . . . 56
3.2 Schematic representations of the LSP application area and laser application pattern referred to as laser scanning direction and laser advancing direction. . . . 58
3.3 LSP treated areas and surface appearance. . . . 58
3.4 LSP treated areas in M(T) specimens. . . . 59
3.5 LSP treated zone in dogbone specimens. . . . 60
3.6 LSP treated zone in notched specimens. . . . 61
3.7 LSP treated zone in disk specimens. . . . 62
3.8 Prism measurement setup. Image courtesy of Department of Joining and Assessment in the Institute of Materials Research, Helmholtz-Zentrum Geesthacht. . . . 63
3.9 ESPI hole drilling measurement analysis area. . . . 64
3.10 Location of extraction of the notched specimens (S-NS). . . . 66
3.11 CMM surface measurement experimental setup. . . . 66
3.12 Raw measurement data (a, b) BM and (c, d) LSP treated specimen. . . . 67
3.13 FEM mesh used for calculating the residual stresses. . . . 68
3.14 Surface parameters measurement setup using the Hommel Werke T8000 system: (a) specimen orientation on the measuring system and (b) close-up of the measuring direction of the specimens using a Stylus Profilometer type Taster TKL 300/17. 69
3.15 Non-contact surface measurement: (a) Bruker NPFLEX 3D surface metrology system and (b) specimen plate surface topography measurement. . . . 70
3.16 (a) Resin mounted specimens and (b) optical microscope Zeiss Axiophot. . . . 71
3.17 Schematic representation of (a) calculation concept for the grain size, grain aspect ratio and grain orientation and (b) EBSD scanning specimen direction. . . . 73
3.18 (a) Vicker's micro harness measurement setup and (b) levelling of the sample during measurement . . . 74
3.19 (a) Gap between indentation centre and surface, and (b) gap between adjacent indentations. . . . 75
3.20 Dogbone specimen gauge section representation. . . . 76
3.21 BM dogbone specimens (S-DB) after tensile testing. . . . 76
3.22 LSP treated dogbone specimens (S-DB) after tensile testing. . . . 76

3.23 Fatigue testing setup. Schenk Hydropuls-testing machine. 77
3.24 BM specimens (S-DB) after fatigue testing. 78
3.25 LSP treated specimens (S-DB) after fatigue testing. 78
3.26 FCP test setup. 80
3.27 COD gauge and microscope setup. 81
3.28 M(T) specimen during FCP testing. 81
3.29 Pin-on-disk wear testing apparatus. 83
3.30 Measurement setup of the wear tracks in disk specimens (S-DS). 84

4.1 Residual stress profile of BM and LSP 1J: (a) and (b) 200 pulses/cm^2. 86
4.2 Residual stress profile of BM and LSP 2J: (a) 100 and (b) 200 pulses/cm^2. 86
4.3 Residual stress profile of BM and LSP 3J: (a) 100 and (b) 200 pulses/cm^2. 86
4.4 Residual stress profile of BM and LSP 4J: (a) 100 and (b) 200 pulses/cm^2. 87
4.5 Residual stress profile of BM and LSP 5J: (a) 100 and (b) 200 pulses/cm^2. 87
4.6 (a) Peak residual stress and (b) maximum stress depth at different laser energy and pulse density of 100 pulses/cm^2 along the transverse direction (σ_{xx}). 89
4.7 (a) Peak residual stress and (b) maximum stress depth at different laser energy and pulse density of 100 pulses/cm^2 along the longitudinal direction (σ_{yy}). 89
4.8 (a) Peak residual stress and (b) maximum stress depth at different laser energy and pulse density of 200 pulses/cm^2 along the transverse direction (σ_{xx}). 90
4.9 (a) Peak residual stress and (b) maximum stress depth at different laser energy and pulse density of 200 pulses/cm^2 along the longitudinal direction (σ_{yy}). 90
4.10 Schematic illustration of a typical LSP residual stress profile for compressive stress area calculation. 91
4.11 Compressive stress area of BM and LSP treated specimens at different laser energy and pulse density of (a, b) 100 and (c, d) 200 pulses/cm^2. 92
4.12 Calculated residual stress perpendicular to the cut surfaces in BM specimen (S-NS-3). 94
4.13 Calculated residual stress perpendicular to the cut surfaces in LSP treated specimen (a) S-NS-1 and (b) S-NS-2. 95
4.14 Schematic illustration of the residual stress profile measurement location. 95
4.15 Residual stress profile of BM (S-NS-3) along (a) thickness and (b) width. 96
4.16 Residual stress profile of LSP (S-NS-1) along (a) thickness and (b) width. 96
4.17 Residual stress profile of LSP (S-NS-2) along (a) thickness and (b) width. 96
4.18 Resulting surface after wire-cutting EDM. 97
4.19 Surface parameters of BM and LSP treated material at various laser energy levels and pulse densities. (a) Average surface roughness, (b) root-mean-square roughness, (c) maximum height profile, (d) average waviness height, (e) total waviness height and (f) profile height. 99
4.20 Schematic illustration of the non-contact surface topography measurement zone. . 102
4.21 Surface topography of 1J LSP treated material at (a, c and e) 100 pulses/cm^2 and (b, d and f) 200 pulses/cm^2. 103
4.22 Surface topography of 2J LSP treated material at (a, c and e) 100 pulses/cm^2 and (b, d and f) 200 pulses/cm^2. 104
4.23 Surface topography of 3J LSP treated material at (a, c and e) 100 pulses/cm^2 and (b, d and f) 200 pulses/cm^2. 105
4.24 Surface topography of 4J LSP treated material at (a, c and e) 100 pulses/cm^2 and (b, d and f) 200 pulses/cm^2. 106

4.25 Surface topography of 5J LSP treated material at (a, c and e) 100 pulses/cm^2 and (b, d and f) 200 pulses/cm^2. 107
4.26 Surface topography of base material. 108
4.27 Micro hardness profile of BM and LSP treated material at different pulse densities and laser energy of (a) 1J, (b) 2J, (c) 3J, (d) 4J and (e) 5J. 110
4.28 Phase equilibrium for AISI D2 tool steel base material. 112
4.29 OM images of the etched base material AISI D2 tool steel microstructure with eutectic carbides network. 113
4.30 Micrograph of LSP treated material (3J and 200 pulses/cm^2). 114
4.31 EBSD-SEM maps of the (a) BM and (b) LSP treated material (3J and 200 pulses/cm^2). EBSD maps of the (c) BM and (d) LSP treated material (3J and 200 pulses/cm^2). 116
4.32 (a) Grain size, (b) misorientation angle, (c) grains shape aspect ratio of BM and LSP treated material (3J and 200 pulses/cm^2). 118
4.33 Grain boundary map of BM rotation angle. 119
4.34 Grain boundary map of LSP treated material (3J and 200 pulses/cm^2) rotation angle. 119
4.35 SEM/EDS images of LSP treated AISI D2 steel showing the selected region analysis (a) A, B and C, and (b) D. 120
4.36 EDS spectrum analysis of BM, LSP-S and LSP-C according to the selected regions (a) A, (b) B, (c) C and (d) D. 121
4.37 Tensile properties of BM and LSP treated AISI D2 tool steel. 123
4.38 Fatigue testing results for BM and LSP treated AISI D2 specimens. 125
4.39 Schematic representation of (a) fatigue fracture location on dogbone specimens (S-DB) and (b) distinct SEM observed regions within the fracture surface. The edge regions on the left and right sides correspond to LSP application zones. . . . 127
4.40 Macro representations of the fractured surfaces at 27× magnification. (a, c and e) for the BM specimen (S-DB-17); and (b, d and f) for the LSP treated specimen (S-DB-1). 128
4.41 Overview of the fractured surfaces at 500× magnification. (a, c and e) for the BM specimen (S-DB-17); and (b, d and f) for the LSP treated specimen (S-DB-1). . . 129
4.42 Detail representations of the fractured surfaces at 5000× magnification. (a, c and e) for the BM specimen (S-DB-17); and (b, d and f) for the LSP treated specimen (S-DB-1). 130
4.43 Macro representations of the fractured surfaces at 27× magnification. (a, c and e) for the BM specimen (S-DB-22); and (b, d and f) for the LSP treated specimen (S-DB-6). 131
4.44 Overview of the fractured surfaces at 500× magnification. (a, c and e) for the BM specimen (S-DB-22); and (b, d and f) for the LSP treated specimen (S-DB-6). . . 132
4.45 Detail representations of the fractured surfaces at 5000× magnification. (a, c and e) for the BM specimen (S-DB-22); and (b, d and f) for the LSP treated specimen (S-DB-6). 133
4.46 Fatigue crack growth, a vs N for the BM and LSP treated specimens at initial crack length (a) a_0 = 2.5 mm and (b) a_0 = 9.0 mm. 137
4.47 Fatigue crack growth rate, da/dN vs ΔK for the BM and LSP treated specimens. . 139
4.48 Crack closure behaviour. 140
4.49 Microscopic images of the wear track. 141
4.50 2D wear track profile of BM and LSP treated specimen at (a) 1800, (b) 3600, (c) 34500 and (d) 69000 cycles. 142

4.51 2D wear track profile of BM and LSP treated specimen at (a) 103500, (b) 138000, (c) 172500 and (d) 207000 cycles. 143
4.52 (a) Average wear volume loss, (b) wear track depth, (c) wear rate and (d) specific wear rate of BM and LSP treated material. 144
4.53 Micro hardness profile of BM and LSP treated specimen at 207000 cycles. 145

B.1 Residual stress profile of BM. 171
B.2 Residual stress profile of LSP treated material using laser energy of 1J and laser pulse density of (a) 100 and (b) 200 pulses/cm^2. 172
B.3 Residual stress profile of LSP treated material using laser energy of 2J and laser pulse density of (a) 100 and (b) 200 pulses/cm^2. 173
B.4 Residual stress profile of LSP treated material using laser energy of 3J and laser pulse density of (a) 100 and (b) 200 pulses/cm^2. 174
B.5 Residual stress profile of LSP treated material using laser energy of 4J and laser pulse density of (a) 100 and (b) 200 pulses/cm^2. 175
B.6 Residual stress profile of LSP treated material using laser energy of 5J and laser pulse density of (a) 100 and (b) 200 pulses/cm^2. 176
B.7 Compressive stress area of BM. 177
B.8 Compressive stress area of LSP treated material using laser energy of 1J and laser pulse density of 100 and 200 pulses/cm^2. 177
B.9 Compressive stress area of LSP treated material using laser energy of 2J and laser pulse density of 100 and 200 pulses/cm^2. 178
B.10 Compressive stress area of LSP treated material using laser energy of 3J and laser pulse density of 100 and 200 pulses/cm^2. 178
B.11 Compressive stress area of LSP treated material using laser energy of 4J and laser pulse density of 100 and 200 pulses/cm^2. 179
B.12 Compressive stress area of LSP treated material using laser energy of 5J and laser pulse density of 100 and 200 pulses/cm^2. 179

C.1 3D Wear track profile after 1800 cycles for (a) BM and (b) LSP treated material. . 181
C.2 3D Wear track profile after 3600 cycles for (a) BM and (b) LSP treated material. . 182
C.3 3D Wear track profile after 34500 cycles for (a) BM and (b) LSP treated material. 182
C.4 3D Wear track profile after 69000 cycles for (a) BM and (b) LSP treated material. 182
C.5 3D Wear track profile after 103500 cycles for (a) BM and (b) LSP treated material. 183
C.6 3D Wear track profile after 138000 cycles for (a) BM and (b) LSP treated material. 183
C.7 3D Wear track profile after 172500 cycles for (a) BM and (b) LSP treated material. 183
C.8 3D Wear track profile after 207000 cycles for (a) BM and (b) LSP treated material. 184

D.1 Roughness profile of BM. 189
D.2 Roughness profile of LSP treated material using laser energy of 1J and pulse density of (a) 100 and (b) 200 pulses/cm^2. 190
D.3 Roughness profile of LSP treated material using laser energy of 2J and pulse density of (a) 100 and (b) 200 pulses/cm^2. 191
D.4 Roughness profile of LSP treated material using laser energy of 3J and pulse density of (a) 100 and (b) 200 pulses/cm^2. 192
D.5 Roughness profile of LSP treated material using laser energy of 4J and pulse density of (a) 100 and (b) 200 pulses/cm^2. 193
D.6 Roughness profile of LSP treated material using laser energy of 5J and pulse density of (a) 100 and (b) 200 pulses/cm^2. 194

E.1 Vickers micro hardness test results of BM. 195
E.2 Vickers micro hardness test results of LSP treated material using laser energy of 1J and laser pulse density of (a) 100 and (b) 200 pulses/cm^2. 196
E.3 Vickers micro hardness test results of LSP treated material using laser energy of 2J and laser pulse density of (a) 100 and (b) 200 pulses/cm^2. 196
E.4 Vickers micro hardness test results of LSP treated material using laser energy of 3J and laser pulse density of (a) 100 and (b) 200 pulses/cm^2. 197
E.5 Vickers micro hardness test results of LSP treated material using laser energy of 4J and laser pulse density of (a) 100 and (b) 200 pulses/cm^2. 197
E.6 Vickers micro hardness test results of LSP treated material using laser energy of 5J and laser pulse density of (a) 100 and (b) 200 pulses/cm^2. 198

F.1 Micrographs of LSP treated material using laser energy of 1J and laser pulse density of (a) 100 and (b) 200 pulses/cm^2. 199
F.2 Micrographs of LSP treated material using laser energy of 2J and laser pulse density of (a) 100 and (b) 200 pulses/cm^2. 200
F.3 Micrographs of LSP treated material using laser energy of 3J and laser pulse density of (a) 100 and (b) 200 pulses/cm^2. 200
F.4 Micrographs of LSP treated material using laser energy of 4J and laser pulse density of (a) 100 and (b) 200 pulses/cm^2. 201
F.5 Micrographs of LSP treated material using laser energy of 5J and laser pulse density of (a) 100 and (b) 200 pulses/cm^2. 201
F.6 (a and b) SEM figures of BM with marked regions and EDS spectra for region (c) A, (d) B, (e) C and (f) D. 202
F.7 (a and b) SEM figures of LSP-C with marked regions and EDS spectra for region (c) A, (d) B, (e) C and (f) D. 203
F.8 (a and b) SEM figures of LSP-S with marked regions and EDS spectra for region (c) A, (d) B, (e) C and (f) D. 204
F.9 (a) SEM figure and EDS maps: (b) Cr, (c) Fe, (d) Mo (e) Si and (f) V for BM specimen. 205
F.10 (a) SEM figure and EDS maps: (b) Cr, (c) Fe, (d) Mo (e) Si and (f) V for LSP treated specimen. 206

List of Tables

2.1 Advantages and drawbacks of laser shock peening over conventional shot peening. 7
2.2 LSP applications across several industries. 8
2.3 Classification of strain rate in different regimes and loading methods. 10
2.4 Comparison of residual stress assessment techniques. 29
2.5 Advantages and drawbacks of strain measurement techniques. 30

3.1 Chemical composition of AISI D2 (wt.%), Ramada Aços values. 54
3.2 AISI D2 material properties. 54
3.3 Specimen identification and summary of testing procedures. 55
3.4 LSP laser parameters. 57
3.5 Residual stress analysis info. 65
3.6 Hertzian contact stress calculation parameters. 82
3.7 Wear measurement steps according to the number of cycles. 84

4.1 Compressive residual stress layer depth [mm]. 93
4.2 Increase (in %) of the surface parameters after LSP (with varying processing conditions) as compared to BM. 100
4.3 Surface micro hardness of BM and LSP treated material. 109
4.4 EBSD analysis average results. 117
4.5 Chemical composition (wt.%). 122
4.6 Tensile properties of BM and LSP treated AISI D2 specimens. 123
4.7 List of examined fractured fatigue specimens. 127
4.8 FCP results. Final crack length and corresponding number of cycles for BM and LSP treated specimens according to initial crack length and SIF range. 138

D.1 Surface parameters of BM. 185
D.2 Surface parameters of LSP treated material using laser energy of 1J and laser pulse density of 100 pulses/cm^2. 186
D.3 Surface parameters of LSP treated material using laser energy of 2J and laser pulse density of 100 pulses/cm^2. 186
D.4 Surface parameters of LSP treated material using laser energy of 3J and laser pulse density of 100 pulses/cm^2. 186
D.5 Surface parameters of LSP treated material using laser energy of 4J and laser pulse density of 100 pulses/cm^2. 186
D.6 Surface parameters of LSP treated material using laser energy of 5J and laser pulse density of 100 pulses/cm^2. 187
D.7 Surface parameters of LSP treated material using laser energy of 1J and laser pulse density of 200 pulses/cm^2. 187

D.8 Surface parameters of LSP treated material using laser energy of 2J and laser pulse density of 200 pulses/cm^2. 187
D.9 Surface parameters of LSP treated material using laser energy of 3J and laser pulse density of 200 pulses/cm^2. 187
D.10 Surface parameters of LSP treated material using laser energy of 4J and laser pulse density of 200 pulses/cm^2. 188
D.11 Surface parameters of LSP treated material using laser energy of 5J and laser pulse density of 200 pulses/cm^2. 188

Abbreviations

2D	Two dimension
3D	Three dimension
AISI	American Iron and Steel Institute
ANSI	American National Standards Institute
ASTM	American Society for Testing and Materials
BM	Base material
CAD	Computer-Aided Design
CMM	Coordinate measuring machine
EBSD	Electron backscatter diffraction
ECLSP	Elastic Contact Laser Shock Peening
EDM	Electrical discharge machining
ESPI	Electronic speckle pattern interferometry
FCP	Fatigue crack propagation
FEM	Finite element method
FSW	Friction Stir Welding
FWHM	Full width at half maximum
HB	Brinell hardness
HCF	High-cycle fatigue
HEL	Hugoniot elastic limit
HV	Vicker's micro hardness
HZG	Helmholtz-Zentrum Geesthacht
ISO	International Organization for Standardization
JC	Johnson-Cook
LASER	Light Amplification by Stimulated Emission of Radiation
LCF	Low-cycle fatigue
LSP	Laser Shock Peening
LSPwC	Laser Shock Peening Without Coating
M(T)	Middle-crack-tension
Nd:YAG	Neodymium-doped yttrium aluminium garnet
OM	Optical microscope
R&D	Research and Development
RPM	Rotation per minute
SCC	Stress corrosion cracking
SEM	Scanning electron microscope
SIF	Stress intensity factor
SP	Shot Peening
UIT	Ultrasonic impact treatment
UTS	Ultimate tensile strength
XRD	X-Ray Diffraction

Symbols

A_L	Laser spot size
a	Crack length
a_0	Initial crack length
a_f	Final crack length
B	Plate thickness
C	Paris law coefficient
C_e	Velocity of elastic longitudinal waves
C_p	Velocity of plastic longitudinal waves
D_i	Shock velocity
d	Average grain diameter
da/dN	Fatigue crack propagation rate
E	Young's modulus
F	Force
f_l	Focal length
HV	Vicker's hardness
I_0	Incident laser power density
K_{app}	Applied stress intensity factor
K_{eff}	Effective stress intensity factor
k_i	Specific wear rate coefficient
K_{max}	Maximum stress intensity factor
K_{min}	Minimum stress intensity factor
K_{res}	Initial residual stress intensity factor
K_y	Material constants of Hall-Petch equation
L_p	Plastically affected depth
m	Paris law exponent
N	Number of cycles
P	Laser-induced shock wave pressure
P_t	Total profile height
Q_L	Laser pulse energy
R	Stress ratio
R_a	Average roughness
R_{hole}	Radius of the drilled hole
R_{in}	Inner radius
R_{out}	Outer radius
R_q	Root-mean-square roughness

R_z	Maximum roughness profile height
r	Radius
S_A	Compressive stress area
s	Sliding distance
T	Temperature
T_L	Laser pulse width
T_m	Melting temperature
t	Time
V_i	Wear volume loss
W	Plate width
W_a	Average waviness
W_t	Total waviness
Z_i	Shock impedance
ΔK	Stress intensity factor range
ΔK_{eff}	Effective stress intensity factor range
ΔL	Total elongation
ΔP	Loading range
ε	Strain
ε_p	Surface plastic strain
$\dot{\bar{\varepsilon}}^p$	Effective plastic strain rate
$\bar{\varepsilon}^p$	Effective plastic strain
λ	Wavelength
λ_c	Wavelength cut off filter
ν	Poisson's ratio
ρ_i	Density
σ	Stress
$\bar{\sigma}$	Von Mises flow stress in Johnson-Cook model
σ_0	Initial residual stress
σ_i	Material constants of Hall-Petch equation
σ^{dyn}	Dynamic yield strength of the material
σ_{max}	Maximum tensile stress
σ_{surf}	Surface residual stress
σ_{xx}	Transverse stress direction
σ_{yy}	Longitudinal stress direction
σ_Y	Yield strength
τ	FWHM of laser pulses
ω_0	Incident beam radius
ω_f	Focused beam radius

Chapter 1

Introduction

The performance improvement of components working under demanding conditions is a major engineering challenge. Such demanding operating conditions often combine high-speed impact, cyclic temperatures, high-pressures and abrasive environments. A component surface is the primary protective barrier against the challenging working environment and, inevitably, one that is most exposed to damage. Therefore, the performance of materials largely depends on surface characteristics.

Over several decades, surface modification techniques have been applied to enhance the material surface properties. These techniques enable the high-performance and safety requirements of components and structures to be achieved. Included are requirements for a component's service life under high temperature, wear and fatigue. However, with increasingly challenging economic and technological demands, the traditional surface processing techniques are not entirely fulfilling the ever-changing requirements. To address these challenges, advanced laser treatment techniques such as laser shock peening (LSP) or laser surface hardening have been developed. Currently, techniques for metal surface processing generate plastic deformation on the surface, as a result of severe impacts from high-energy laser sources. Comparing to traditional surface treatment techniques such as shot peening, LSP features a focalized laser beam which presents multiple advantages over traditional techniques. A major advantage of LSP over similar techniques is real-time computer control, enabling integration into highly automated production lines (Ding and Ye, 2006).

1.1 Scope

This PhD was developed in an industrial framework at Quantal S.A. Accordingly, a subject area was selected which would contribute towards the strategic goals of the company, both in terms of solving a problem and optimising working processes. In this regard, certain key issues have been detected in Quantal's production process. The service life of cutting tools has a significant impact

on production process, and there is a constant need to disrupt the production to perform tool replacement and repair operations. Therefore, LSP represents an important step for the improvement of material properties and performance.

Since its early introduction in the aerospace industry, LSP has demonstrated superior performance compared to conventional shot peening when it comes to extending the component service life. The high-energy laser impacts leads to severe plastic deformation, microstructural modifications and generation of compressive residual stresses. However, the high temperature gradients throughout service life can partially or entirely cause the relaxation of the LSP induced compressive residual stresses. As a result of the beneficial influence of compressive residual stresses, some industries are incorporating LSP in their manufacturing processes. The potential advantages and economic benefits of extending the life of a component can go far beyond the value of the component itself: reduction of raw materials used, production costs and efficiency improvements. When it comes to the enhanced material properties resulting from compressive residual stresses, LSP consistently outperforms shot peening. In addition, LSP has proved to be superior to shot peening in many performance-related applications such as retaining compressive residual stresses at higher temperatures, improving fatigue resistance and extending the service life of welded components, retarding or preventing fatigue crack initiation and propagation, enhancing wear and corrosion resistance.

The first chapter provides the objectives, framework, and general information regarding the development of this thesis. The structure and order of different chapters composing this manuscript are explained, highlighting the connections among the various topics.

1.2 Objectives

The economic success of many manufacturing technologies strongly depends on the performance of the used tools. Several of these processes are not economically feasible due to high tool wear and related repair costs. If a tool performs optimally, it lasts longer, which translates as an increase in productivity. In this regard, it is important to study LSP, as it potentially increases tool performance.

The investigation and review of state-of-the-art related to the subject under study has revealed a significant lack of information on the applicability, parameters and effects of the LSP in tool steels for cold working applications. This dissertation work set out to achieve a valuable contribution towards improving this lacune.

Considering the above information, the objectives of this study are (1) LSP process control and optimization by choosing a suitable set of laser parameters, (2) Generation of deep, uniform and beneficial compressive residual stresses, (3) Improve the performance and mechanical properties of cold-work tool steels, and (4) Demonstrate the applicability and feasibility of LSP as a superior metal surface enhancement technique.

LSP is particularly relevant not only to Quantal but to all companies using manufacturing processes, since high tool wear rates pose a challenge to productivity and optimization.

1.3 Location and duration

This work was developed mainly at four locations in Portugal and Germany, represented in Figure 1.1. The principal location was the Faculty of Engineering of the University of Porto (FEUP), Institute of Science and Innovation in Mechanical and Industrial Engineering (INEGI) and Quantal S.A., in Porto, Portugal. A significant amount of experiments were carried out, over the course of six months, at the Helmholtz-Zentrum Geesthacht, Centre for Materials and Coastal Research (HZG) in Hamburg, Germany.

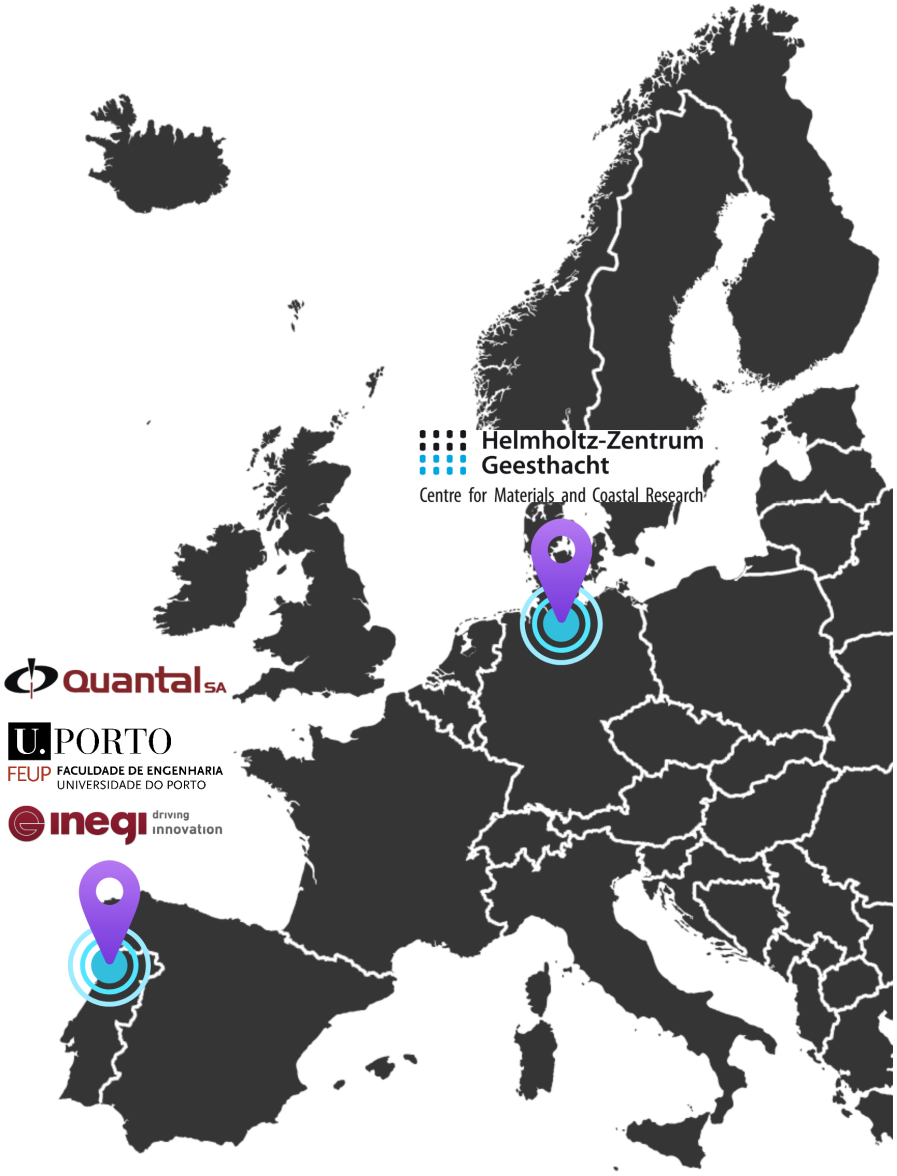


Figure 1.1: Map showing the main locations during the PhD work.

1.4 Structure of the thesis

The state of the art is reviewed in Chapter 2, which provides relevant research on LSP as well as the impact of LSP processing parameters on the ultimate characteristics and properties of metals. A comprehensive description of the materials involved is provided in Chapter 3. It is further described in this chapter the LSP procedure and testing for assessing the effectiveness of LSP on AISI D2 tool steel. Chapter 4 presents and discuss the effects of LSP on AISI D2 properties and characteristics. Findings regarding the effects of LSP on the residual stress state, tribological performance, micro-hardness, fatigue performance, fatigue crack propagation, wear resistance, tensile properties, and the microstructural modifications will be presented. Conclusions, general remarks and a future perspective of the work are provided in Chapter 5.

Chapter 2

State of the art

2.1 Introduction

For decades, surface modification techniques have been developed and applied to enhance the surface properties of a wide range of metallic materials. These techniques ensure the high performance and safety requirements of components and structures exposed to high-temperature gradients, wear, corrosion and fatigue. Typically, the surface of materials is the most demanding area due to the high concentration of stresses, and exposure to damage and environmental conditions. Therefore, the surface and sub-surface are critical failure zones.

Peening techniques are surface modification techniques especially applied to improve fatigue strength as well as wear and corrosion resistance. Mechanical methods as shot peening (SP) have been used effectively and extensively for several decades. However, the introduction of laser technology has opened up numerous possibilities regarding the processing of materials.

LASER is the acronym for "light amplification by stimulated emission of radiation", and very broadly speaking, is a device that delivers coherent light through a process of optical amplification based on the stimulated emission of electromagnetic radiation (Hecht, 1999). It was first developed in the 1960s, although laser manufacturing for industrial applications took place only a decade later when industries, particularly the automotive industry, became aware of its potential for processing materials (Ion, 2005). Lasers are widely used in manufacturing with a wide range of engineering materials, in addition to developing a wide range of applications in the most diverse industries. Over the years, lasers have always been considered synonymous with precision, quality and speed. However, lasers are not limited to industrial applications such as metal cutting, welding, engraving or surface hardening. Laser applications are so widespread that we are unaware of the number of everyday applications where lasers are applied.

Laser processing, and specifically laser-induced shock waves, has been employed to investigate the modification of material surfaces for improving fatigue and corrosion resistance since the 1970s (Anderholm, 1970; Clauer et al., 1977). Advanced laser treatment techniques have been developed and, today, high energy and high repetition pulsed lasers are used in surface modification techniques such as laser shock peening (LSP).

2.2 Peening

Peening is a mechanical process applied on the surface of components to improve material properties by intentionally causing plastic deformation. There are several techniques available such as shot peening, hammer peening, cavitation peening or water jet peening, laser shock peening, ultrasonic impact peening, and oil jet peening, as presented in Figure 2.1. The material surface layer is prevented from expanding laterally during peening due to the elastic properties of the sub-surface. As a result, compressive residual stresses develop in the surface layer, which are compensated by tensile residual stresses inside the material. The maximum compressive residual stresses can be found below the surface, specially for hard materials, or directly on the surface, for soft materials, according to the prevailing process (Scholtes and Voehringer, 2001). In addition, peening can also cause strain hardening of the surface metal.

Compressive residual stresses are often beneficial as they promote fatigue and corrosion resistance (Zhou et al., 2018; Lu et al., 2014). Very often and inaccurately, the compressive residual stresses are seen as the only significant effect of peening. Another major effect is the increased dislocation density and grain refinement due to plastic deformation. Additionally, dislocation density strongly influence fatigue behaviour (Ge and Xiang, 2016). Upon peening, there is no stress relieving but instead a stress redistribution, therefore the benefits of the compressive stresses arise at the cost of greater and deeper tensile stresses on the workpiece. Nevertheless, the fatigue properties of the part are enhanced, as surface stresses are typically considerably higher due to imperfections and surface damage. Cold-working also contributes to hardening the surface of the material. This reduces the risk of surface cracking and increases wear resistance. However, it is important to consider that when metal undergoes strain hardening, its yield strength increases, whereas the ductility of the metal decreases. Regardless of the advantages of peening, caution is necessary regarding any thin parts due to possible shrinkage. Depending on geometry it may be necessary to make trade-offs in part design or process application.

The different peening techniques meet different applications, and a particular one is not necessarily better than all the others. Peening techniques are typically cold-working, except for LSP. The most widely used technique is shot peening, which consists of blasting the metallic surface with

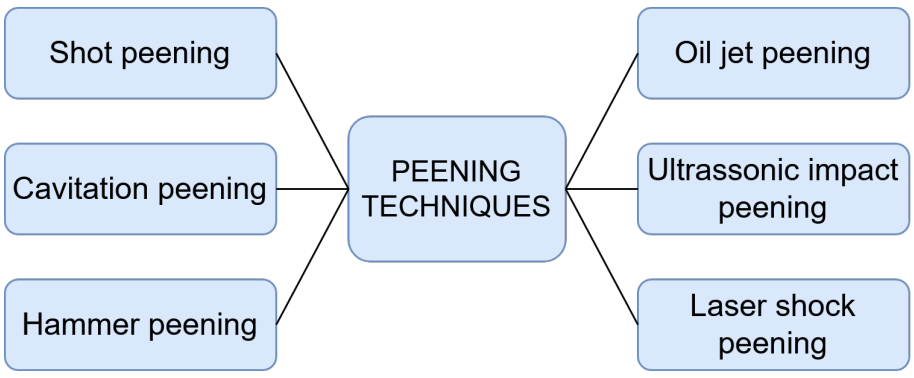


Figure 2.1: Peening techniques.

spherical-shaped beads (metal, glass, ceramics) in different sizes. These beads are fired through a high-speed air stream system towards the target surface.

Laser shock peening emerged as an alternative to overcome the shortcomings of shot peening, particularly the inability to generate sufficiently large compressive residual stresses to extend the service life of components. Besides, LSP features advantages compared to conventional techniques, including uniform plastic deformation, higher and deeper range of compressive residual stresses (Trdan et al., 2011; Luong and Hill, 2010; Montross et al., 2002; Pant et al., 2013) and minimal cold-work induced, because when compared to SP, compressive residual stresses induced by LSP can retain benefits at higher temperatures. LSP is a highly controlled process capable of processing complex components (Hammersley et al., 2000), with no need to protect sensitive adjacent areas. Additionally, LSP features minimal surface damage (Gao, 2011), low surface roughness and no waste product, resulting from shot beads debris in SP. Table 2.1 summarizes the advantages and drawbacks of LSP over the conventional shot peening.

Table 2.1: Advantages and drawbacks of laser shock peening over conventional shot peening (Antunes and Oliveira, 2015).

Processing features	**Advantages**	**Drawbacks**
Microstructural modifications	Increased dislocation density and twinning (increased hardness)	-
Compressive residual stress	Higher and deeper compressive residual stresses	Generation of high balancing tensile residual stress
Residual stress stability	-	More intense stress relaxation effects during cyclic loading
Surface morphology	Smoother surface of LSP processed parts	-
Process control	Laser power controlled easily to adapt the final residual stress profile	-

2.3 Laser shock peening

Laser shock peening is a promising laser-based surface processing technique to enhance the mechanical and physical properties of metals. Improved material properties include longer fatigue life (Pavan et al., 2019; Pant et al., 2016) and increased wear and corrosion resistance (Sánchez-Santana et al., 2006; Kumar et al., 2015; Lu et al., 2014), and are primarily attributed to the beneficial compressive residual stress and work-hardened surface layer. A high amplitude and short duration laser pulse reaches the material surface, and the shock wave propagates through the metal resulting in permanent deformation, and subsequently compressive residual stress at the

surface region develop (Ding and Ye, 2006). The plastic deformation induced by the shock wave pressure can be enlarged through the application of an ablative layer and confinement medium. The ablative layer provides thermal protection while ensuring a purely mechanical contact (Gill et al., 2015). Besides, the confinement medium acts as a transparent barrier to laser light, that effectively contains the rapid expansion of the plasma explosion, resulting in a higher laser-induced shock waves pressure (Oros, 2002; Nguyen et al., 2018). Table 2.2 presents several industries and applications where LSP can be used to improve part quality and performance, reduce wear and damage, reduce preventive maintenance and downtime, and to increase safety and reliability.

Table 2.2: LSP applications across several industries (Technologies, 2020).

LSP Applications		
Aerospace	Manufacture & Tooling	Automotive
- Turbine, fan and compressor blades; - Brakes and landing gears; - Welded components; - Wing attachments.	- Pilger dies; - Hot forging dies; - Stamping dies: - Casting dies; - Custom tooling.	- Transmission gears; - Springs; - Crankshafts; - Valves; - Rotating components.
Maritime	Energy	Heavy Equipment
- Shafts; - Propellers; - Ship hull; - Welded joints.	- Fan blades; - Steam turbine generators; - Welds in pressurized water reactors.	- Camshafts; - Crankshafts; - Valves; - Bearings; - Pumps.

2.4 Physical process of LSP

The physical principle involved in LSP is schematically illustrated in Figure 2.2 and it can be described as follows. A high-energy ultra-short laser pulse is focused on a target metal surface and plasma is generated as a result of the ablative interaction (Ding and Ye, 2006). A confinement barrier, consisting of running tap water, is applied to contain the expanding plasma explosion, thereby increasing the pressure up to several GPa. This results in the generation and propagation of a high-pressure shock wave, which can achieve high strain rates in the order of 10^6 - $10^7 s^{-1}$ to create permanent deformation (Peyre et al., 1996; Berthe et al., 1997). As a consequence, a biaxial compressive residual stress field is created in a plane parallel to the surface (see Figure 2.3), which remains on the material up to several millimetres below the surface. Optionally, a sacrificial layer can be applied to the workpiece surface before the laser impact to shield the part from thermal effects and achieve a purely mechanical loading. The different types of ablative layers and confinement mediums, and how they contribute positively to the LSP process efficiency are discussed in detail in further sections.

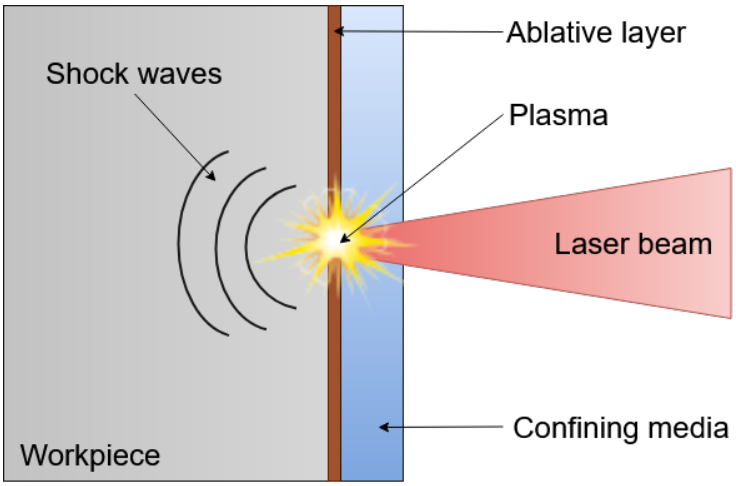
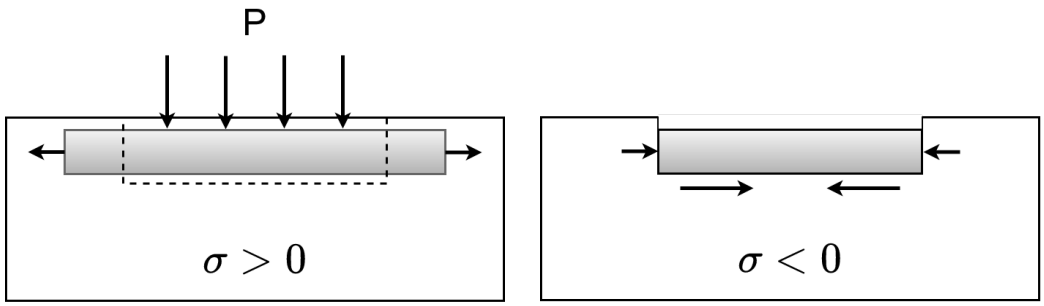


Figure 2.2: Schematic representation of LSP process. Depicted and adapted according to (Ding and Ye, 2006).



(a) (b)

Figure 2.3: LSP generation of compressive residual stresses. (a) During the laser-material interaction: stretching of impacted zone. (b) After the laser-matter interaction: reaction of the surrounding material includes a compressive stress field. Depicted and adapted from (Fabbro et al., 1998).

Most solid materials undergo plastic deformation when subjected to severe impacts. Table 2.3 presents a classification of strain rate in different regimes and different loading methods. Laser-induced shock waves have been investigated in the modification of material surfaces to improve fatigue and corrosion resistance since the 1970s (Anderholm, 1970; Clauer et al., 1977). When the shock waves propagate through the material, plastic deformation is generated to a depth where the peak stress no longer exceeds the Hugoniot Elastic Limit (HEL) (Peyre et al., 1996). For the peening effect to occur, the shock pressure generated by each impulse must exceed the HEL of the material. This threshold (HEL) is defined as the stress above which the material behaviour shifts from linear elastic to elasto-plastic, i.e., the material's yield strength under the stress state generated by LSP. HEL is expressed by the Equation 2.1:

$$\sigma_{HEL} = \frac{1-\nu}{1-2\nu}\sigma_{dyn} \tag{2.1}$$

where σ_{dyn} is the dynamic yield strength (or flow stress) of the material under uni-axial compression and ν is the Poisson's ratio. Dynamic yield strength is defined as the instantaneous stress value required to continue plastic deformation of the material and is dependent on the temperature, true strain, and strain rate.

This topic is especially important in the context of LSP since the generation and propagation of shock waves is an essential aspect of the process. Since the early 1990s, several researchers (Fabbro et al., 1990; Devaux et al., 1993; Masse and Barreau, 1995; Berthe et al., 1997; Hong et al., 1998; Berthe et al., 1999; Peyre et al., 2012) dedicated their attention to the generation of shock waves based on different ablative layers, wavelengths, confinement media, dielectric breakdown, etc. As a result, several analytical models were developed.

Table 2.3: Classification of strain rate in different regimes and loading methods (Singh et al., 2008).

Regime	**Time scale [s]**	**Strain rate [s^{-1}]**	**Types of loading**	**Dynamic considerations**	
Creep	$10^{6} - 10^{4}$	$10^{-8} - 10^{-6}$	Stress machine	Inertial forces neglected isothermal process	No wave propagation
Static	$10^{2} - 10^{1}$	$10^{-6} - 10^{-3}$	Hydraulic machine		Elastic and plastic waves propagation
Intermediate	$10^{0} - 10^{-1}$	$10^{-3} - 10^{0}$	Mechanical machine		
High	$10^{-2} - 10^{-4}$	$10^{0} - 10^{4}$	Hopkinson pressure bar	Inertial forces important adiabatic process	Shock wave propagation
Very high	$10^{-6} - 10^{-8}$	$10^{4} - 10^{8}$	Shock loading		

2.4.1 Laser systems for laser shock peening

Selecting an appropriate laser system to meet the LSP process requirements is critical. Unlike most industrial laser applications, LSP does not use continuous laser beam but instead short-pulsed laser. Hence, laser energy and pulse duration must be considered. Additionally, the high repetition rate and the wavelength of the laser are also important for effective treatment results of metallic components. Besides, it is necessary to account for specific factors such as costs, efficiencies and maintenance.

During the early development of LSP, the laser systems were large and characterized by high-energy outputs and low pulse frequencies. They were used in research facilities and thus not suitable nor cost-effective for industrial application. The first laser prototype for LSP industrial scale application became fully operational in 1986, providing 50 J output energy, 20 ns pulse width and 0.5 Hz pulse frequency (Clauer, 2019). Although this system was far more advanced

than systems used in the 1970s, it was slow and inefficient when compared to contemporary technology. Technological progress enabled the development of increasingly efficient laser systems with a smaller footprint. As a result, specially developed LSP lasers were characterized by smaller sizes and higher pulse frequencies, both desirable for industrial applications. These improvements enable scalability of LSP systems in terms of size, affordability, and ability to be customized to the specific needs of different industrial applications.

Nowadays, LSP is mostly performed using mid or low output energies. Intermediate energy lasers are generally solid-state laser systems whose active gain medium is Nd:YAG (neodymium-doped yttrium aluminum garnet; Nd:Y3Al5O12) operating in the infrared electromagnetic spectrum, with a 1064 nm wavelength (Ding and Ye, 2006). These laser systems deliver pulses of 1-10 J, a pulse width of 10 ns and a pulse frequency of 1-20 Hz. The laser spot size is generally 1-2 mm in diameter (Clauer, 2019). Therefore, the application of LSP at an industrial scale requires high-energy and high frequency pulsed laser systems, capable of generating satisfactory results and fulfilling safety, environmental and economical requirements.

2.4.2 Confinement medium

Confinement media are extensively used as a barrier to contain the rapidly expanding plasma. When a dielectric material transparent to the laser beam is used in the LSP process, the rapid expansion of the plasma explosion can be delayed as compared to the free expansion that occurs in free plasma expansion mode (see Figure 2.4). As a consequence, the plasma pressure is enlarged, which improves the process effectiveness (Fabbro et al., 1998; Oros, 2002).

Solid and liquid transparent confinement mediums (dielectric materials) are suitable for LSP applications. Solids are more effective due to their superior transmittance, which means that a

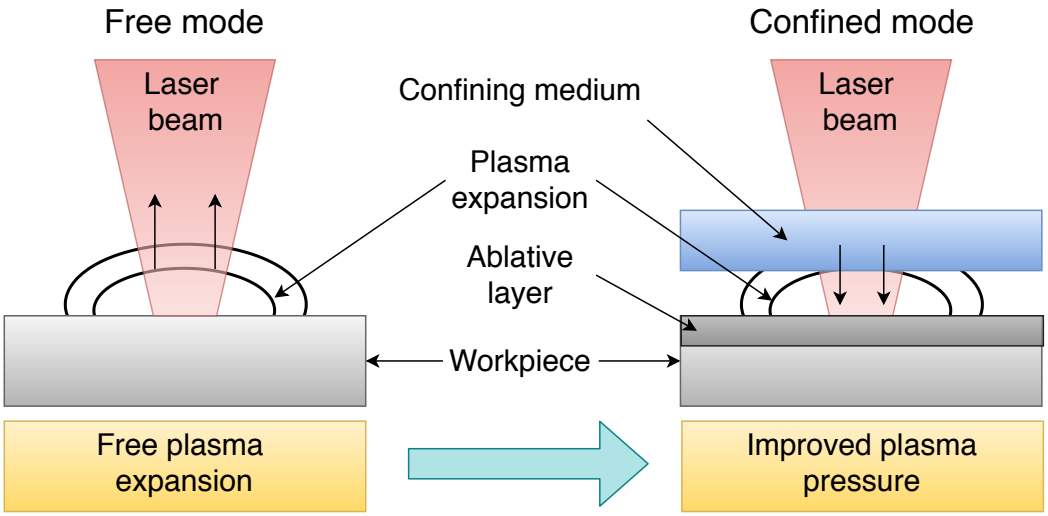


Figure 2.4: Laser–matter interaction principle. Free mode under direct ablation conditions, and confined ablation mode with a transparent dielectric material. Depicted and adapted from (Fabbro et al., 1998).

large amount of incident radiation passes unchanged through the confinement media. Figure 2.5 presents the effects of laser-induced shock waves, using both liquid and solid confinement mediums, on residual stresses of a standard steel (Masse and Barreau, 1995). Results show that solid medium requires less than half laser power density (1.7 GW/cm^2) to achieve similar residual stress levels as generated under water confined mode (4 GW/cm^2). However, the application of solid media can be challenging, especially in components with complex geometries. A commonly used solid medium in LSP applications is the BK7 borosilicate optical glass, as it provides excellent transmittance through the visible and near-infrared spectrum, and up to 350 nm in the ultraviolet spectrum. Compared to water, the BK7 optical glass can generate a shock pressure approximately 2.7 times higher (Zhang et al., 2018; Ye et al., 2011).

Recent developments regarding the use of polymer confinement regime in LSP applications, focuses on the transparency of polymer materials (acrylate and polydimethylsiloxane) in a high-intensity laser beam, and the generation of high-pressure plasma which can be very useful to treat areas which are sensitive to water (Bras et al., 2019).

Given the availability and cost-effectiveness, water is commonly used as confinement medium in LSP experiments (Lu et al., 2017d; Gomez-Rosas et al., 2010; Fang et al., 2013a). A water stream with a thickness of 1-2 mm provides plasma confinement as well as continuous removal of ablated particles by laser, ensuring a clean surface (Trdan et al., 2018; Prabhakaran et al., 2018; Liu et al., 2018b). Figure 2.6 shows the typical experimental setup/application of water as a confinement medium during the LSP process. In this way, a water nozzle with a constant flow rate is targeted slightly above the LSP application zone to achieve laminar water flow around the laser shot path.

The average plasma expansion speed in a confined water regime is approximately 70 times slower than in air, preventing the laser energy absorption across a wide area and assuring a sub-

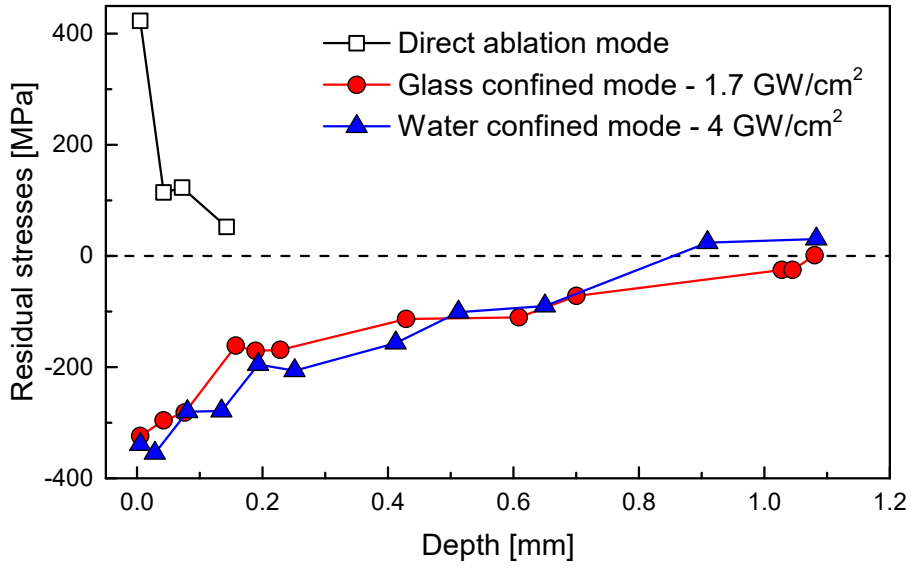


Figure 2.5: Residual stress profiles generated by LSP with various confining medium. Adapted from (Masse and Barreau, 1995).

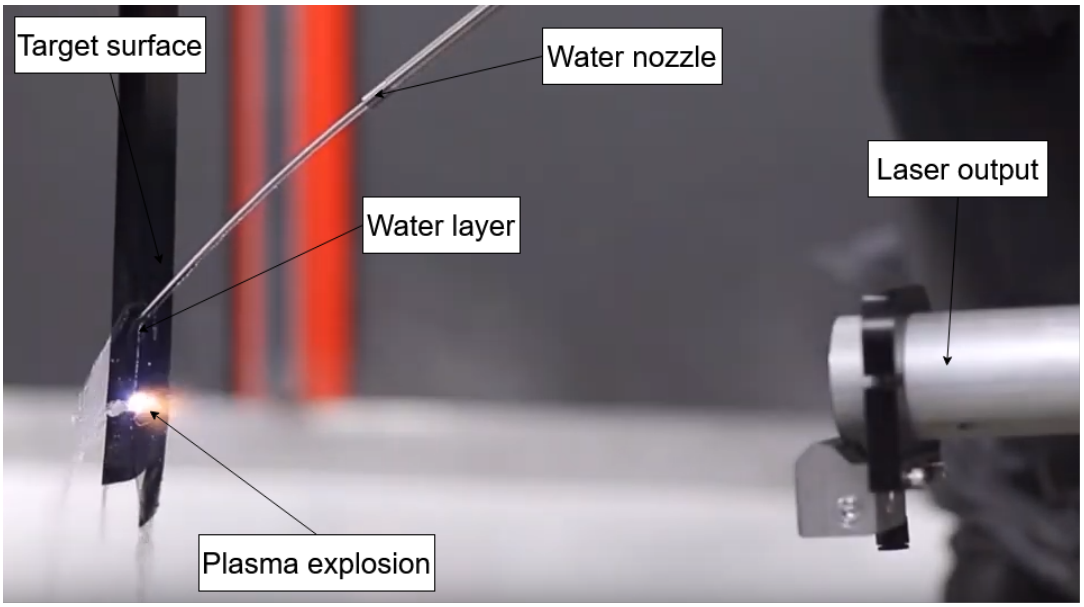


Figure 2.6: Water stream as confinement medium for LSP. Depicted and adapted from (Technologies, 2020).

stantially higher shock wave through the targeted material (Nguyen et al., 2018). However, using water as a confinement layer under service conditions can, under some circumstances, pose a challenge due to the effects of water on light absorption and scattering. Water purity control is important to prevent bubbles or suspended particles arising which can affect the LSP process by interfering with the high energy laser beam (Gomez-Rosas et al., 2005). Constant laminar water flow provides a reliable solution to avoid such disturbing elements.

2.4.3 Ablative layer

Ablative layers are frequently adopted in LSP, as they provide pure mechanical loading of the target material. Among the most commonly used are aluminium foil (Lu et al., 2017b; Zheng et al., 2017; Lu et al., 2017d; Xiong et al., 2017), black tape (Lu et al., 2017a; Shen et al., 2017; Huang et al., 2017; Hu et al., 2018), and black paint (Yang et al., 2001; Zhou et al., 2002; Wang et al., 2013). This approach requires the application of a protective layer in the interaction zone before laser shots. The ablative layer increases the absorption of laser radiation (see Figure 2.7) and additionally, prevents or reduces thermal effects caused by the relatively long exposure time between the plasma and the material (Fabbro et al., 1998; Trdan et al., 2018). The effects of different ablative layers have been experimentally studied (Yella et al., 2018; Montross et al., 2001). Recently, Petronić et al. (2020) investigated the effect of laser ablation on the microstructure and mechanical properties of Ti-alloy. An homogeneous microstructure with small size pores and no noticeable cracks was found for LSP treatment using ablative layer. Figure 2.8 presents the surface microstructure of Ti-alloy after LSP treatment with and without ablative layer.

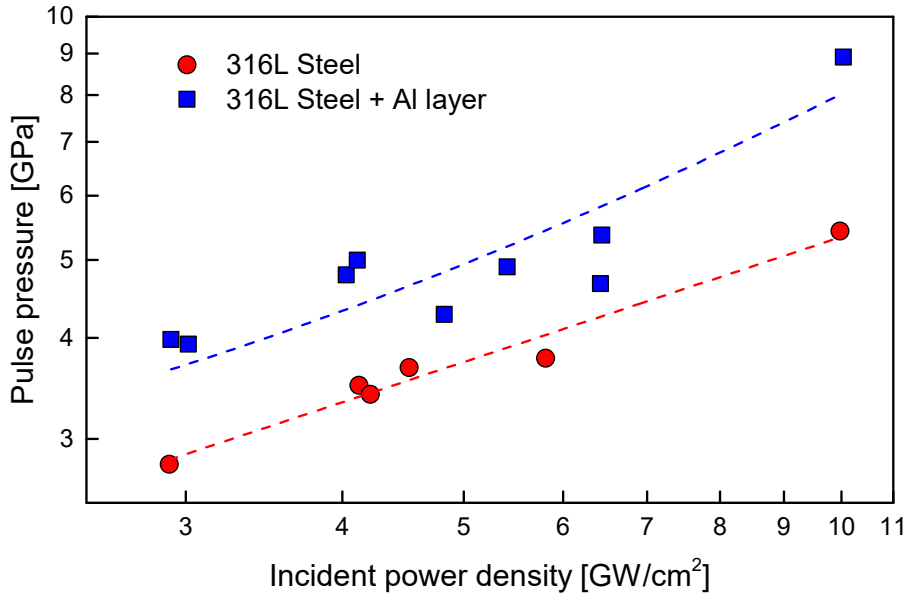
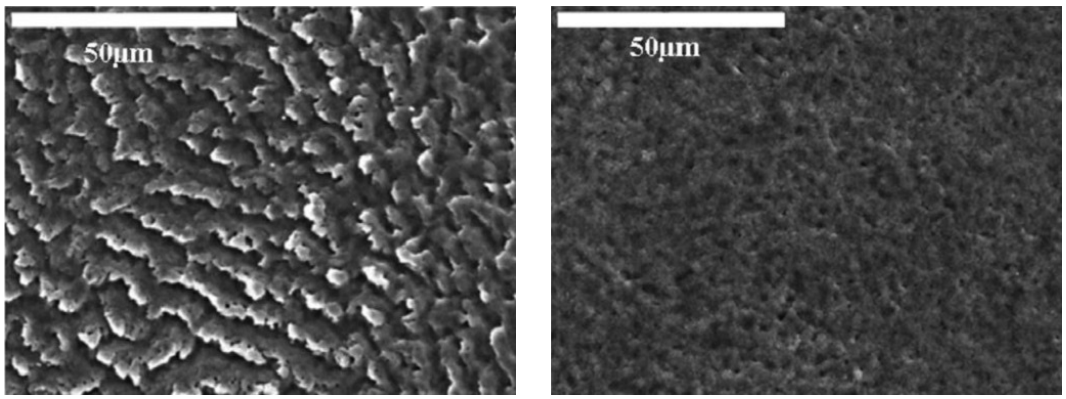


Figure 2.7: Pulse pressure as a function of incident power density for LSP treated 316L steel under direct ablation mode and using an aluminium ablative layer. Adapted from (Fabbro et al., 1998).

Nevertheless, recent investigations have shown that compressive residual stresses can be generated on materials under direct laser-material interaction (Granados-Alejo et al., 2018; Ramkumar et al., 2017; Prabhakaran et al., 2018; Umapathi and Swaroop, 2018).

In the absence of ablative layer, the laser beam interacts directly with the target surface, and minor ablation occurs. Laser shock peening without coating (LSPwC) can be cost-effective and time-saving in comparison to standard LSP (Dhakal and Swaroop, 2018). Alongside these advantages, LSPwC is well-suited to environments were applying a ablative layer can be challenging (Mukai et al., 1995; Sano et al., 1997). LSP processed surfaces retain their natural appearance, while LSPwC processed surfaces exhibit a dull and rough appearance. The resultant indentations



(a) (b)

Figure 2.8: Microstructure of LSP treated Ti-alloy under a) direct ablation mode and b) using ablative layer. Depicted and adapted from (Petronić et al., 2020).

of LSPwC are slightly deeper than the ones obtained using a ablative layer (Gill et al., 2015). The depth of indentation decreases with the thickness of the layer, which can be caused by energy dissipation as the shock wave propagates across the ablative layer (Cao et al., 2010). Special consideration should be taken regarding the type of ablative layer as well as its thickness. A thicker ablative layer will cause more energy to dissipate and, as a result, less energy is available to generate plastic deformation on the target material.

Regardless of the benefits provided by the ablative layer, when multiple laser shot sequences are applied, replacement may be needed as a result of the damage during the LSP process. Figure 2.9 shows the final appearance of the stainless steel ablative layer. The material ablation that occurs on the stainless steel adhesive foil surface is the result of one complete sequence of laser shots. Its application can be challenging, considering the material geometry and the accessibility of the target component, as well as the surrounding environment (Gill et al., 2015).

A particular concern applies when performing LSP without ablative layer on high carbon steels, as decarburization can occur as a result of the effect of the temperature generated at the surface of the part. Decarburization is the reduction of the carbon content on the surface area of metals, at temperatures above 700°C, due to the reaction of carbon in the metal with oxygen or hydrogen (Purkert, 1982; Bryson, 2009). This results in material softening, mainly at the surface, and can either be beneficial or harmful. Decarburization is detrimental to the surface properties of LSP processed steels due to the softening effect caused by the high temperature on compressive residual stresses. The weakened surface layer can reduce wear resistance and promote fatigue failure. Hence, ablative layers should be applied to minimize the effect of the high temperature and ensure a purely mechanical action.

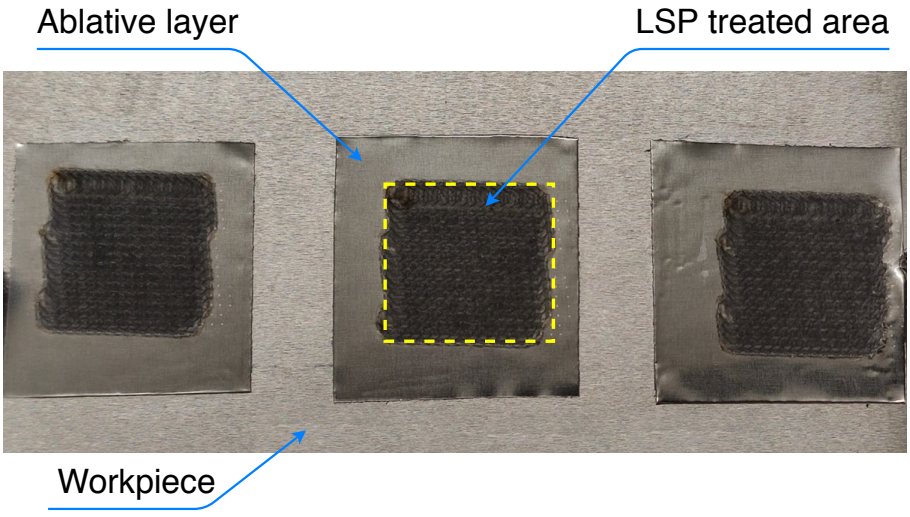


Figure 2.9: Stainless steel adhesive foil.

2.5 Laser parameters

Control over the operating parameters of the LSP is fundamental to ensure the process stability. However, LSP involves complex mechanisms, such as plasma generation and expansion, shock wave propagation, plastic deformation and mechanical effect on the material. Therefore, controlling laser parameters has a major influence on the process as it allows a uniform stress distribution on the part (Qiao et al., 2015a). Process instability results in a non-uniform distribution of residual stress, which can have a detrimental effect on component performance.

2.5.1 Laser energy

Laser energy is arguably one of the most regarded laser parameters in LSP related works. Several studies were conducted to determine its influence on LSP processed materials. The findings have consistently suggested that with increasing energy, the amplitude of the shock wave increases as well as a more uniform spatial distribution (Luo et al., 2013). As a result, there is an increase in the affected surface area, the plastically affected depth, and compressive residual stress (Leitz et al., 2011; Yella et al., 2018; Ge et al., 2018a).

However, a phenomenon known as breakdown plasma occurs above a given energy threshold. The high-intensity laser beam impinging on a target which may be solid, liquid or gas, may dissociate, excite, and/or ionize the constituent atomic species of the medium and produce a plasma, which expands and limits the medium confinement capability. Berthe et al. (1998) demonstrated that breakdown plasma occurs when laser power density exceeds 10 GW/cm^2 in LSP under water confined mode and 1064 nm wavelength. Breakdown plasma reduces laser energy absorption on the target surface, decreases the laser-induced peak pulse pressure (Berthe et al., 1999) and, consequently, the compressive residual stress magnitude decreases due to the surface release waves (Peyre et al., 1996).

When operating under the maximum energy threshold, the plastic deformation is more severe, which increases the magnitude and affected depth range of the compressive residual stress (Cao et al., 2010; Dorman et al., 2012). Many positive effects arise from increasing plastic deformation and consequently increasing compressive residual stress. The increase in laser energy on LSP processed samples show a significant impact on the improvement of tensile strength, electrochemical corrosion resistance, and stress corrosion cracking (SCC) susceptibility of AISI 304 steel (Lu et al., 2014). The surface compressive residual stress increases along with the increase in laser power density. At low laser power density, part of the laser energy is retained in the ablative layer and not completely converted into a shock wave (Luo et al., 2013). Research suggests that with increasing laser energy, the surface grain size and the average wear rate of Mg alloy decrease. Moreover, an increase of micro hardness and surface roughness was observed by increasing the laser energy (Ge et al., 2018b). The reduction of fatigue striation spacing after laser peening indicates a significant decrease in fatigue crack growth rate and the inhibition effect increases with the increase in laser energy (Huang et al., 2013a; Sheng et al., 2016; Zhang et al., 2009; Chahardehi et al., 2010; Huang et al., 2013a).

LSP with high laser energy generates a thicker surface layer of compressive residual stresses, although residual stress values near the surface tend to be lower due to the stress saturation rate. When residual stress reaches a saturation point, it will generate a permanent reverse strain, resulting in a drop in residual stress (Sun et al., 2018a).

Despite the advantages provided by the energy increase, some effects may also occur, which, if not addressed, may adversely impact the component. Geometry distortion by single-side LSP in thin structures is sensitive to laser pulse energy (Hu et al., 2018). As the laser power density increases, the average indentation depth increases, which results in a greater surface roughness (Cao et al., 2010). Surface roughness can be detrimental to fatigue performance, thus a balance is necessary to ensure that compressive residual stresses enhance fatigue performance while surface roughness does not act as a limiting factor. This phenomenon can be explained by rising peak pressure of the shock wave induced by different laser pulse energies. Generally, the high-pressure shock wave generates higher plastic deformation, which causes deeper indentations. On the other hand, this effect can be used to control geometric part deformations, when both sides are available for LSP (Yocom et al., 2018). Therefore, the degree of plastic deformation induced by LSP increases with the increment of laser pulse energy or laser power density (Ge et al., 2018a).

The power density, commonly reported in literature, refers to the ratio between the radiated power and the area covered by the emitted beam and can be expressed as follows:

$$I = \frac{Q_L}{A_L T_L} \tag{2.2}$$

where Q_L is laser pulse energy, A_L is the laser spot size, and T_L is the laser pulse width.

2.5.2 Wavelength

The influence of wavelength is barely investigated in LSP-related studies and findings are sometimes inconsistent. The wavelength influences radiation absorption and focal length. For a Gaussian beam of radius ω_0 and wavelength λ, incident upon a lens of focal length f_l, the focal spot radius ω_f can be expressed as follows:

$$\omega_f = \frac{1}{\pi}\left(\frac{f_l \lambda}{\omega_0}\right) \tag{2.3}$$

where ω_0 is the incident beam radius. According to Equation 2.3, the power density at the focal point is inversely proportional to the square of the wavelength. Thus, the shorter the wavelength of the beam, the higher the output power density, all other conditions being equal. Furthermore, the shorter the focal length of the lens, the smaller the focal beam size and therefore the higher the power density. Thus, in LSP, the use of a lens with a shorter focal length results in deeper penetration for the same beam power, especially at low power levels (Kannatey-Asibu, 2009).

Nd:YAG laser systems with wavelengths of 1064 nm, 532 nm, and 355 nm are frequently adopted because for the same energy, beam mode, beam size and optical system, they feature high power densities. Besides, these wavelengths are all harmonics of 1064 nm, therefore a single laser

is required that uses a non-linear effect to generate the second and third harmonics (Butcher and Cotter, 1990). Berthe et al. (1999) studied the plasma shock wave pressure profile generated by the laser as a function of the laser power density for wavelengths of 1064 nm, 532 nm and 355 nm. Figure 2.10 presents the peak pressures in LSP as a function of laser power density using different laser wavelength. Results show dielectric breakdown threshold reduction when decreasing the wavelength: 355 nm (4 GW/cm^2 and 3.5 GPa), 532 nm (6 GW/cm^2 and 4.5 GPa) and 1064 nm (10 GW/cm^2 and 5.5 GPa). The peak pressure measurements have shown the highest efficiency of water-laser interaction at shorter wavelengths.

Gomez-Rosas et al. (2010) studied the influence of 1064 nm and 532 nm wavelength in the LSP process using aluminium alloys. Despite the higher energy losses in water confinement medium at 1064 nm, this wavelength is capable of generating compressive residual stresses of greater magnitude. Regardless of the reported differences, both wavelengths allow obtaining satisfactory results. This results are not consistent with Montross et al. (2002), which concluded that for constant laser power densities, decreasing the wavelength from 1064 nm to 355 nm increases beam-material interaction while increasing shock wave generation. However, this can also decrease the peak pressure because the decrease in wavelength reduces the critical power density threshold for the dielectric breakdown, which, in turn, limits the peak pressure.

The effects of different wavelengths on hardening and softening mechanism and fatigue behaviour in LSP processed Titanium alloy was studied by Umapathi and Swaroop (2017). According to the authors, surface softening was observed to depths of 0.5 mm (532 nm) and 0.2 mm (1064 nm), which was attributed to the laser-material thermal interaction. Mechanical softening was considered a function of the laser wavelength, and it was concluded that the beginning of this softening started earlier for shorter wavelengths. A similar trend was observed in the residual stress and fatigue behaviour that supported the softening mechanism.

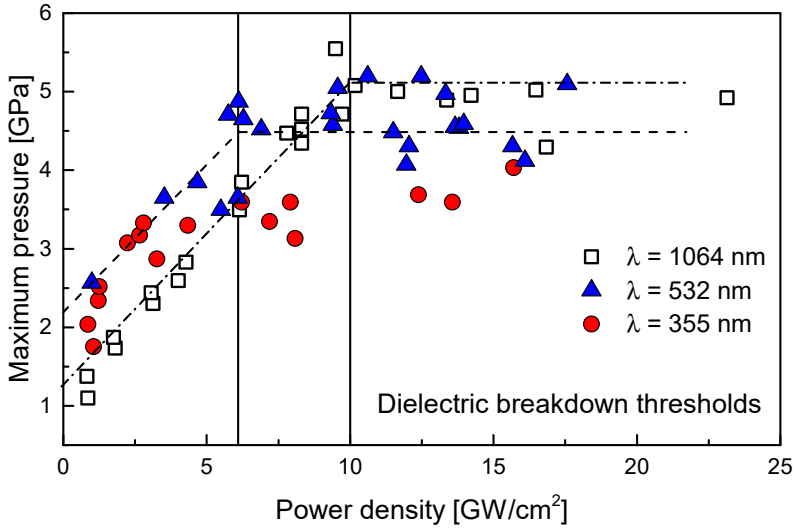


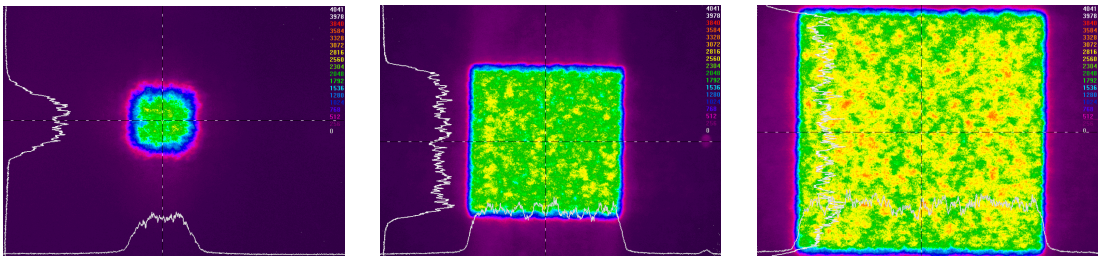
Figure 2.10: Peak plasma pressure in water confined mode as a function of power density at different laser wavelengths. Adapted from (Berthe et al., 1997, 1999).

2.5.3 Laser spot size and shape

Most research in LSP employs circular laser spots in a relatively well-defined range (0.1 - 5 mm), yet neither the influence of the spot size nor its shape has been comprehensively addressed. Varying the spot size while maintaining energy and laser pulse width constant, results in different power densities, according to the Equation 2.2. Therefore, the influence of the laser spot size can not be properly evaluated due to the variation of power density. Example of this is one study reported by Petan et al. (2016). Findings showed that keeping pulse energy constant at 2.8 J, laser power density decreased from 15.8 GW/cm^2 to 9.8 GW/cm^2 and 5.7 GW/cm^2 with spot diameter increase from 1.5 mm to 2.0 mm and 2.5 mm, respectively. Besides, the lowest surface roughness was generated by using smaller laser spots with the highest power density (15.8 GW/cm^2). Figure 2.11 presents the laser beam profile, size and shape available in the laser system used to conduct the experimental work for this thesis.

Depending on laser spot size, the plastically affected depth can be explained by the shock wave propagation as described by Fabbro et al. (1998). A smaller laser spot size leads to higher energy losses during shock wave propagation through the material, due to the scattering effects of the spherical wave-front. Furthermore, the high energy losses of the shock waves for a small spot size leads to a lower compressive residual stress affected depth. On the other hand, a larger laser spot size results in a flatter wave-front, which leads to low energy losses during shock wave propagation. Keller et al. (2018) studied the influence of the laser spot size on the LSP process using two square spot sizes (1×1 mm^2 and 3×3 mm^2) for a constant laser power density. The smaller laser spot size (1×1 mm^2) induced higher compressive residual stresses, whereas, the compressive stress affected depth was smaller compared to the stress depth resulting from the larger laser spot size (3×3 mm^2).

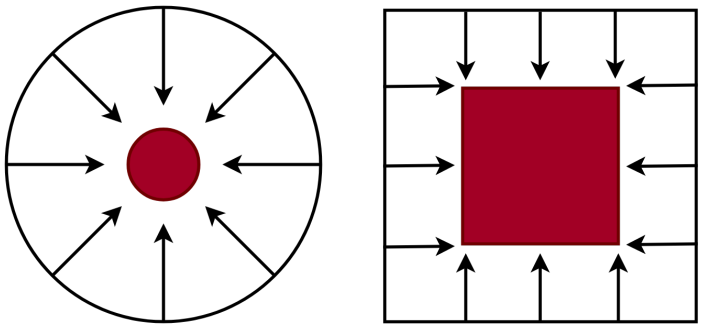
Similarly, Ling et al. (2008) and Dai et al. (2014) reported a significant increase in the plastically affected depth as a result of increasing the laser spot size. The shock wave resulting from the smaller spot size expanded as a sphere, while the larger spot size resultant shock wave behaved as planar front. The energy attenuation rate was found to be smaller for the larger spot size. Therefore, the planar shock wave propagated deeper into the material.



(a) (b) (c)

Figure 2.11: Laser spot size, shape and beam spatial profile: (a) 1×1 mm^2 spot size, (b) 3×3 mm^2 spot size, and (c) 5×5 mm^2 spot size. Image courtesy of Department of Joining and Assessment in the Institute of Materials Research, Helmholtz-Zentrum Geesthacht.

A numerical model was adopted by Hu et al. (2009) to investigate the effects of round and square laser spots on the residual stress field. The compressive residual stress induced by the round laser spot is more intense than that induced by the square laser spot. This is attributed to the radial release waves from the impact edges after the interaction and focusing simultaneously on their centre (see Figure 2.12). However, LSP processing using a circular laser spot might pose challenges to achieving a uniform residual stress field, and furthermore a large overlap ratio is required to avoid untreated areas. Applying LSP using a square spot enhances the process efficiency and provides a more uniform LSP surface, particularly when applying several laser shot sequences (Cao et al., 2012).



(a) Circular laser spot. (b) Square laser spot

Figure 2.12: The influence of laser spot shape on the reverse loading. Depicted and adapted from (Hu et al., 2009).

2.5.4 Laser pulse width

The plastically affected depth in LSP treated material is also influenced by the laser pulse width. Given that peak power is the ratio of energy to laser pulse width, decreasing the pulse width causes an increase in peak power and, consequently, an increase in plastic deformation (Fabbro et al., 1998). This increase is expressed on the magnitude of the compressive residual stresses. Figure 2.13 shows the maximum pressure as a function of incident power density for different laser pulse widths. When a short duration laser pulse is adopted, the mechanical shock wave will be consequently applied quicker, meaning a lower exposure to high temperatures developed during the plasma explosion (Sano et al., 2006a). Therefore, thermal effects are limited to a smaller surface area.

The beam-matter interaction mechanism involved in laser ablation is dependent on the laser pulse width. For laser pulses in the nanosecond range (see Figure 2.14a), the material ablation is primarily achieved by heat conduction, surface melting, evaporating and finally plasma generation. A temperature field is generated due to the heat conduction caused by laser energy absorption. Depending on the temperature reached at the surface of the material during the LSP, either melting and evaporation occurs, or material shifts to a plasma state (Leitz et al., 2011). Hence, the ablation

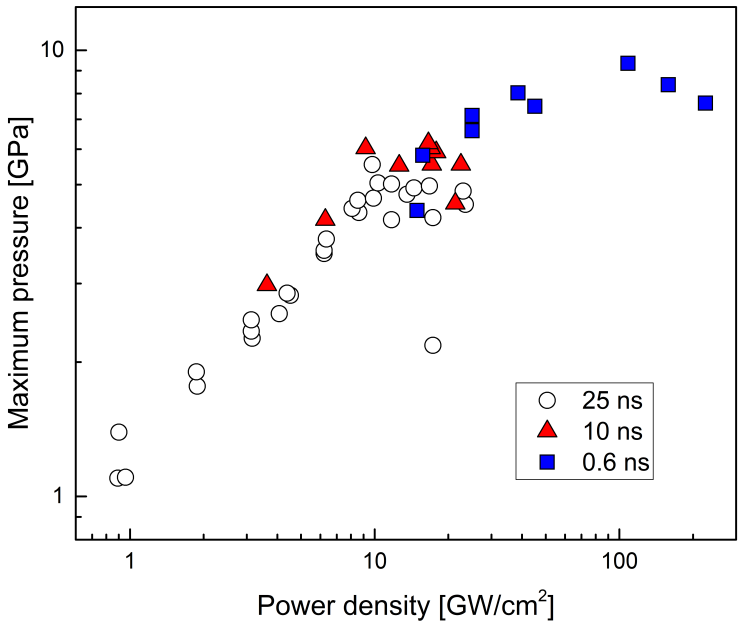


Figure 2.13: Maximum pressure as a function of incident power density for different laser pulse widths. Adapted from (Fabbro et al., 1998).

of material in the nanosecond range is dependent on the pulse duration and energy and is driven by evaporation as well as removal of the melted material.

The same mechanism can not be applied to ultra-short femtosecond laser pulses (see Figure 2.14b) as a result of the extreme peak power densities. This results in a build-up of extreme pressures and temperatures. Due to the ultra-short interaction time, the ionized material fails to

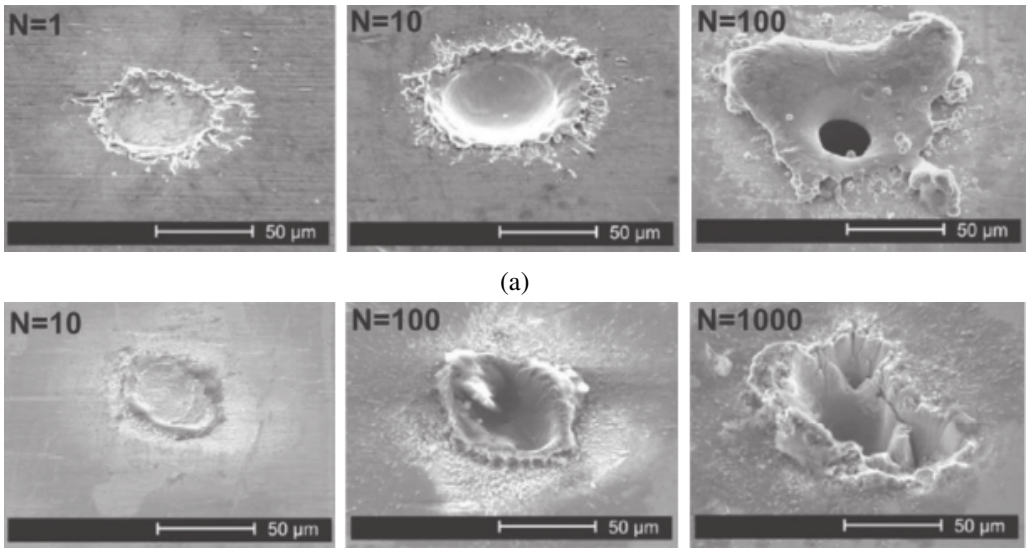


Figure 2.14: Laser ablation with (a) nanosecond pulses and (b) femtosecond pulses. N represents the number of laser pulses. Depicted and adapted from (Leitz et al., 2011).

evaporate continuously. Instead, it is transferred to a rapidly expanding overheated liquid state that melts into a high-pressure mixture of liquid droplets and vapour. Such mechanism is commonly recognized as phase explosion or explosive boiling (Miotello and Kelly, 1999; Lu et al., 2002; Mannion et al., 2004; Niso et al., 2013). Therefore, using laser systems with a pulse width in the nanosecond range allows for better ablation efficiency, as the material is barely overheated. On the other hand, the ablation efficiency using lasers with a pulse width in the femtosecond range is significantly lower.

Laser systems allow a wide range of pulse widths and most studies in this field adopt values ranging from 3 ns to 30 ns (Zhang et al., 2009; Peyre et al., 2007a; Bugayev et al., 2006; Nikitin and Altenberger, 2007; Zou et al., 2012). However, the laser peening process in the femtosecond range demonstrates potential in various applications where conventional peening methods are not suitable. It can be conducted under environmental conditions with no need for a plasma confinement medium (Sano et al., 2017).

2.5.5 Laser pulse density

Compressive residual stresses can be generated deeper beneath the surface through successive laser impacts (Montross et al., 2002) and, with an increasing number of laser impacts, greater compressive residual stress peak can be generated (Sun et al., 2017), as shown in Figure 2.15.

Saklakoglu et al. (2014) studied the near-surface modification of Al-alloy induced by single and double laser impacts. The double impacted material was subjected to a high strain rate leading

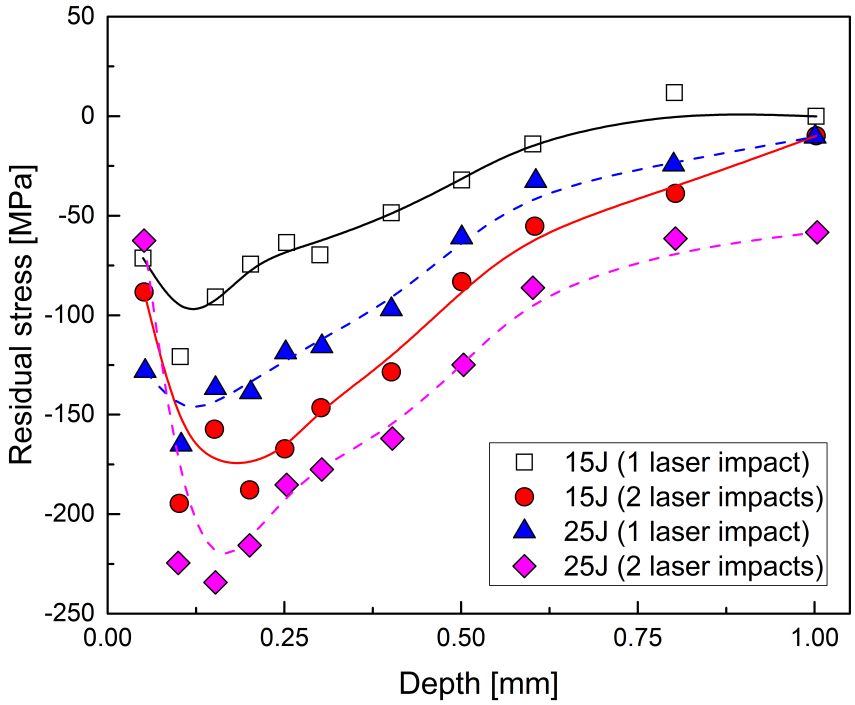


Figure 2.15: In-depth residual stress distribution after LSP with different energy levels and one and two laser impacts. Adapted from (Sun et al., 2017).

to an accumulation of plastic deformation and consequently higher compressive stress. However, as the laser impact number increased, the compressive stress affected depth did not change significantly. Similarly, Li et al. (2013) suggested the existence of a threshold value for the number of repeated laser impacts after which the plastically affected depth will not increase significantly. This can be attributed to the effect of strain hardening of the material. As plastic deformation increases, the material's strength and micro-hardness gradually increase, causing plastic deformation to be increasingly difficult, eventually resulting in a saturation point.

The effective stress intensity factor (K_{eff}) and fatigue crack propagation (FCP) rate are positively affected by an increase in compressive stress, which is a consequence of the increase in the number of laser impacts (Zhou et al., 2014). Zhang et al. (2010a) reported that single and double impact LSP led to a 22.2% and 41.7% improvement in fatigue strength compared to unprocessed Ti alloy specimens, respectively. Similarly, improvements of 27% and 74% on the fatigue cycles for single and triple laser impact, respectively were reported (Hatamleh et al., 2007).

Ramkumar et al. (2017) reported an increase in hardness and tensile strength as the number of laser impacts increased. The same trend was observed for compressive residual stress. Single laser impact may not provide the expected residual stress field, meaning that the LSP process can result in minimal improvement (Dorman et al., 2012). Improvements in strength and micro hardness of the Al alloy have been experimentally demonstrated through increasing the number of LSP impacts. For 3 LSP impacts, the tensile strength and surface micro hardness respectively increase 20.7% and 72.4% when compared to the unprocessed material. Additionally, high density dislocation was found in the surface layer exposed to 3 LSP impacts (Wang et al., 2019). Likewise, the micro hardness of Ti alloy can be enhanced through the application of multiple LSP impacts

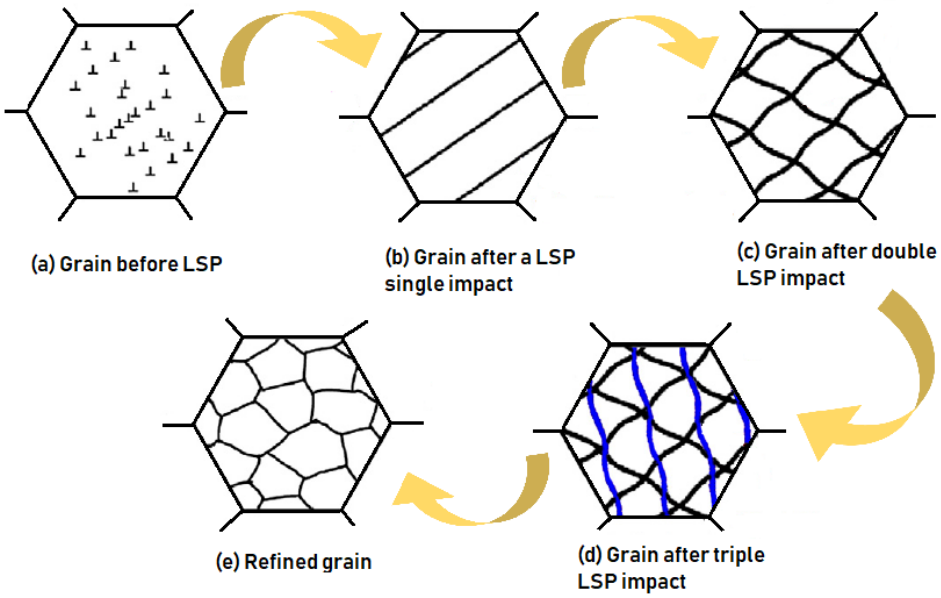


Figure 2.16: Schematic illustration of microstructural evolution induced by different numbers of LSP impacts. Depicted and adapted from (Lu et al., 2010).

(Shen et al., 2017). Additionally, it was reported an increase in surface roughness, wear resistance (44%), and refinement of the grain (67%). Similar effect was reported by Lu et al. (2010) who investigated the grain refinement mechanism of multiple laser shock processing impacts on ANSI 304 stainless steel. Figure 2.16 shows a schematic illustration the microstructural evolution induced by multiple LSP impacts.

Overall, multiple laser shocks leads to higher plastic deformation, which is reflected in higher compressive residual stress, and ultimately in the improvement of LSP processed component properties. Nevertheless, it is important to consider the existence of a threshold value for multiple laser impacts associated with strain hardening of the material.

2.5.6 Laser overlapping

According to the laser beam profile and shape, laser spot overlapping can be considered a key parameter to achieve adequate coverage of the target surface and thereby a uniform residual stress field. Overlapping is commonly defined as the percentage of superposition between successive laser pulses. Thus, it is imperative to overlap circular laser shots to achieve complete coverage of the target surface and generate a uniform compressive stress field. Figure 2.17 illustrates LSP treated areas under overlapped circular laser shots with different overlapping rates.

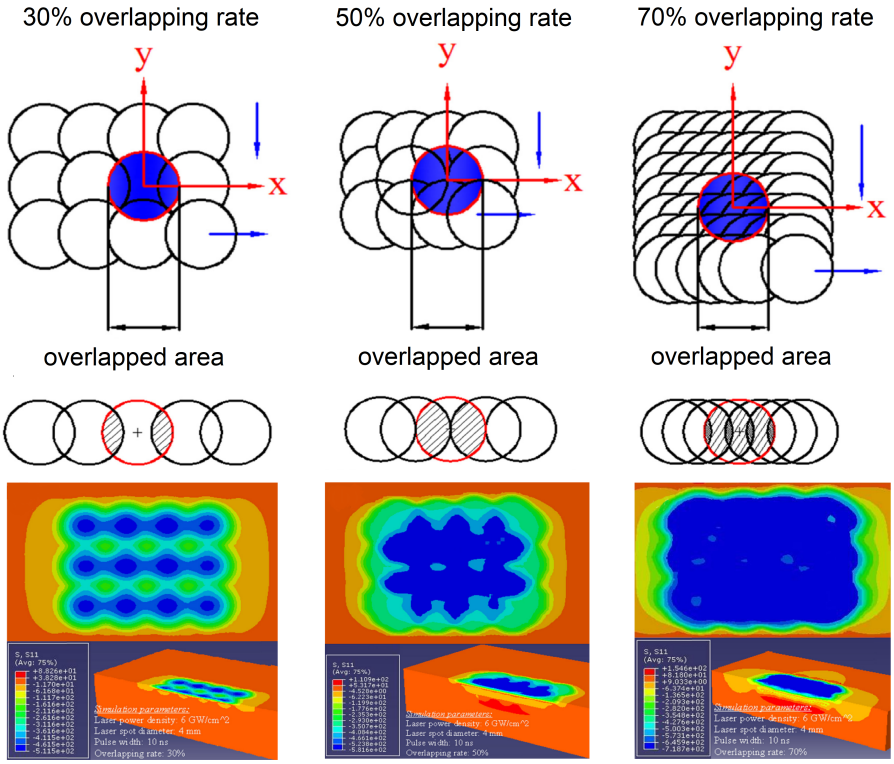


Figure 2.17: Illustrations of LSP treated areas under overlapped circular laser shots with overlapping rates of 30%, 50%, and 70% (power density of 6 GW/cm^2 and 4 mm laser spot diameter). Depicted and adapted from (Luo et al., 2013).

The hardness and surface roughness of LSP processed metals can be successfully controlled by varying the laser power and the laser pulse overlap ratio (Guo et al., 2012). Likewise, surface roughness can be induced in a controlled manner by adjusting the laser pulse overlap ratio or the pulse density (Dai et al., 2016).

The key factor with the variation of the overlap is to achieve a uniform compressive residual stress field. Overlapping rates of 50% or more have shown to provide a uniform and deeper compressive residual stress field. The degree of uniformity and depth, increase as the overlap rate increases (Luo et al., 2015). The surface roughness, micro hardness and residual compressive stresses increase with a higher LSP pulse density since a greater overlap of laser spots leads to a cumulative effect (Petan et al., 2016). Conversely, lower overlap rates may cause an oscillatory stress field, which can be harmful to the component performance. The effects of different overlapping rates on the residual stress field are shown in Figure 2.18. However, the increase in the uniformity of the compressive residual stress field may not be proportional to an increase in the overlapping rate. The overlapping rate should be set to allow the entire area coverage. Luo et al. (2013) found that a 70% overlap ratio does not significantly improve compressive residual stress homogeneity compared to a 50% overlap ratio. Despite the affected depth of residual stress increased with overlap ratio, a 50% overlap ratio during multiple LSP impact is a better option in terms of improved effects and work efficiency. High overlapping rates can result in excess power density at the surface and hence a high-temperature gradient which can result in the relaxation of compressive residual stresses.

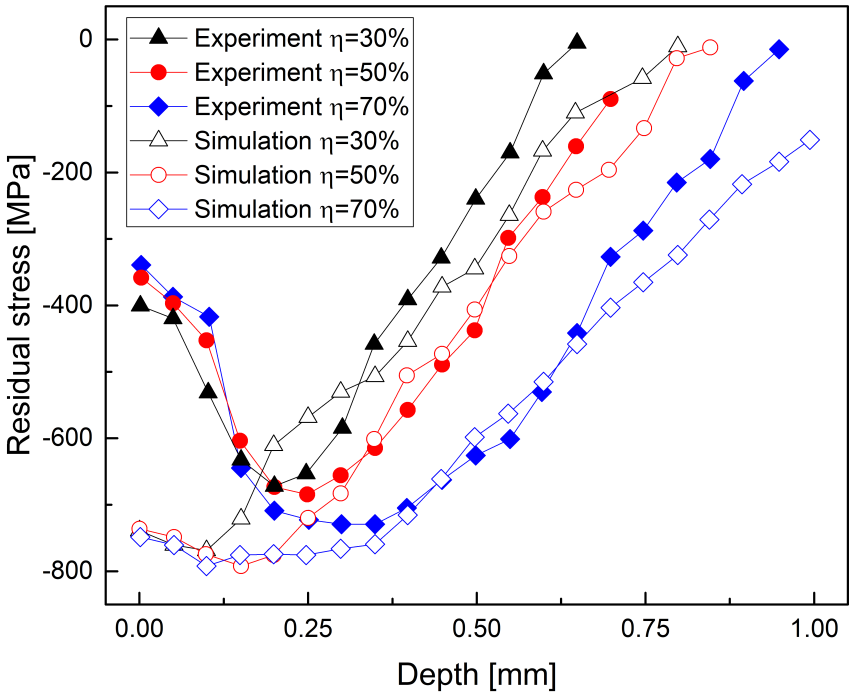


Figure 2.18: Experimental and simulated distributions of residual stress fields along depth direction (power density of 12 GW/cm^2 and a 4 mm laser spot diameter) as a function of overlapping rate. Adapted from (Luo et al., 2013).

Prabhakaran et al. (2018) reported improvements of the mechanical and surface corrosion properties of austenitic stainless steel by LSP with a variable overlap ratio. The compressive residual stress increased gradually up to 75% overlap. A decrease in residual stress values to 85% overlap was observed due to thermal stress relaxation. Surface corrosion properties can be improved by using high overlapping rates. Caralapatti and Narayanswamy (2017a) found that as the overlapping rate increased, the build-up of corrosion products has decreased, leading to uniform superficial corrosion in magnesium samples. Similar effect of overlap rate on corrosion were found by Guo et al. (2012).

2.6 LSP effects

2.6.1 Residual stress

The main purpose of LSP is to induce compressive residual stresses in the target component. Residual stresses are defined as the remaining self-equilibrating internal stresses in a free body after all loads and constrains have been removed (Mura, 1987). These stresses can be found in almost all solid components, metallic or non-metallic, and arise from the mechanical and metallurgical history of the component. During many manufacturing processes, including machining, stamping, forging, welding, heat treatment, among others, residual stresses are inevitably generated. Such stresses are a consequence of non-homogeneous dimensional changes due to plastic deformation, thermal gradients and phase transformations (Totten et al., 2002; Steinzig and Ponslet, 2003). Figure 2.19 shows examples for the generation of macro and micro residual stresses.

As shown in Figure 2.19, residual stresses arise from misfits between different regions. However, residual stresses can also develop during the service life of the component or structure. Compressive residual stresses are often coupled to a beneficial impact on the properties of materials or components, while tensile residual stresses are usually associated with a harmful effect (Withers and Bhadeshia, 2001).

The residual stress effects can strongly influence a component's behaviour, including its fatigue strength, dimensional stability, distortion, corrosion resistance, fracture resistance and crack propagation (Kudryavtsev, 2011). Hence, residual stress analysis becomes critically relevant for the design and performance of components under real service conditions. High repair and maintenance costs of structures are leading to a growing concern on how the residual stress states affect the behaviour and properties of the material. In this way, the residual stress effect is accounted for by advanced design in industries as aerospace, automotive and nuclear, where performance and safety requirements are very demanding and where structural failure can have catastrophic outcomes. Compressive residual stresses increase fatigue life compared to stress-free materials. This improvement can be attributed to superior wear resistance, resistance to crack initiation, and to some extent to crack growth if residual stresses are stabilized in the most critical zone (Totten et al., 2002). A superficial layer under a compressive stress state is an effective constraint to crack

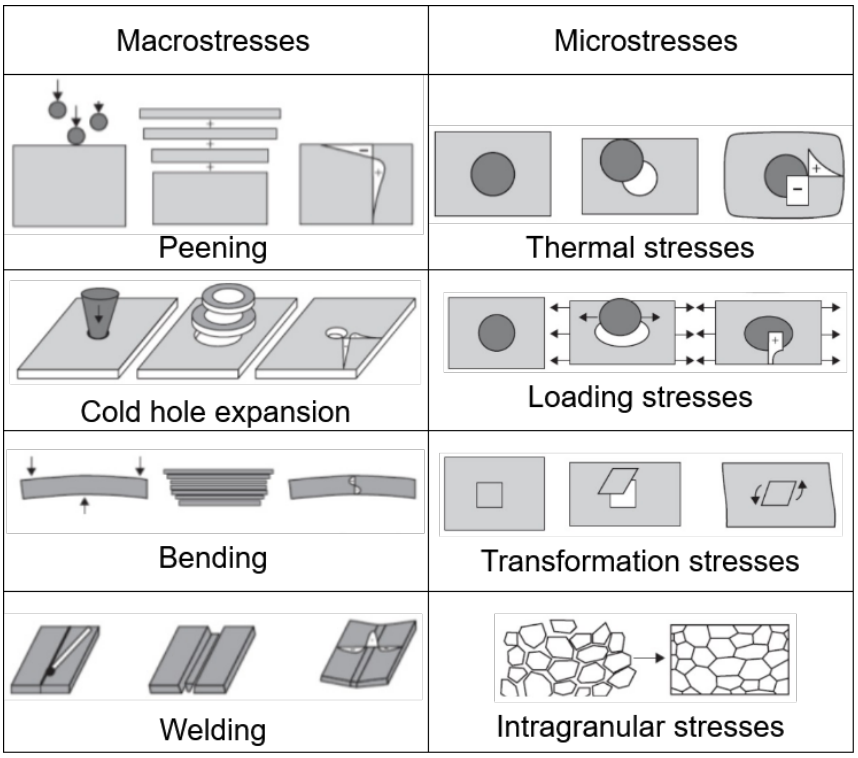


Figure 2.19: Different types of macro and micro residual stress generated from eigenstrains (Withers and Bhadeshia, 2001).

growth. Therefore, compressive residual stresses are often intentionally induced using surface treatments such as LSP.

An important consideration is that improper LSP process parameter setting can adversely affect fatigue behaviour as a result of the residual tensile stresses which are inevitably generated to counterbalance the compressive residual stresses. Consequently, a compressive residual stress field of high magnitude is not necessarily the optimal scenario to extend the service life of a component. A trade-off must be reached between compressive and tensile residual stresses within the geometrical constraints of the component. To achieve this, a residual stress field must be specifically designed to prevent the generation of large tensile residual stresses at critical sites. Figure 2.20 shows a schematic representation of the typical residual stress state after LSP treatment.

The measurement of the residual stresses is necessary to evaluate the success of the LSP treatment. For this purpose, there are several techniques available which can be selected based on the material nature and the spatial resolution amongst other factors. The residual stress measurement techniques can be divided into two categories (see Figure 2.21): 1) destructive and semi-destructive methods, which are mechanical methods based on material removal, that cause mechanical strain relaxation and enable the measurement of surface strain and 2) non-destructive methods, which are physical methods upon which the material is tested according to its physical properties. Table 2.4 presents a comparison of the techniques for evaluating residual stress.

Despite the differences between the various techniques, residual stress can only be calculated

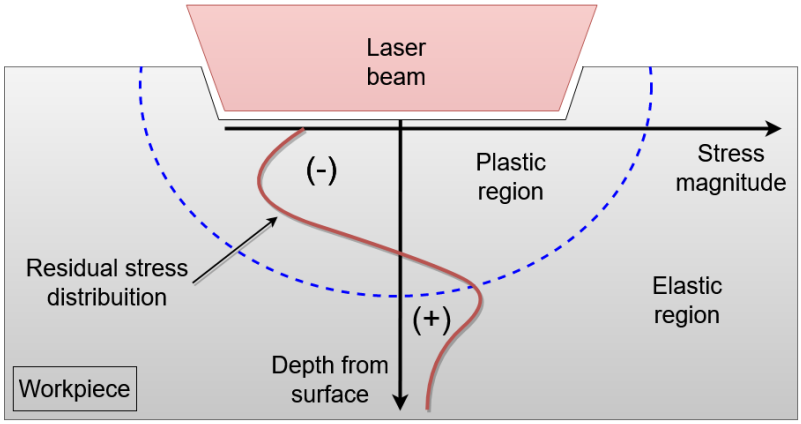


Figure 2.20: Typical residual stress state after LSP. Depicted and adapted from (Sticchi et al., 2014).

by indirectly measured quantities, such as deformation or displacement. Hence, the selection of a residual stress measuring technique is dependent on several factors, such as component geometry and material, area of interest, measurement accuracy, spatial resolution, penetration depth, surface condition, measurement speed and availability. Table 2.5 summarizes the main advantages and disadvantages of the available residual stress assessment methods.

Technological progress lead to the development and application of several different residual stress testing techniques. However, some difficulties are faced regarding the measurement of stress depth and measuring accuracy of the entire field in a two-dimensional plane. To improve accuracy, several techniques can be combined to complement or validate results. The easy access and availability of equipment and facilities along with the measurement accuracy and overall reliability were the criteria to select the measurement techniques in this work. Hence, hole-drilling and contour techniques have been used in this thesis and will be discussed in detail.

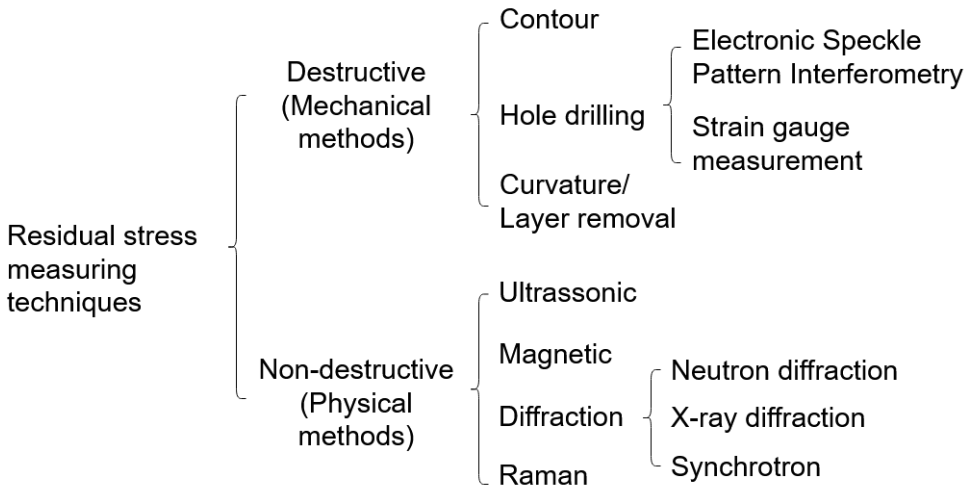


Figure 2.21: Classification of measurement techniques.

Table 2.4: Comparison of residual stress assessment techniques. Adapted from (Kandil et al., 2001; Huang et al., 2013b).

Key techniques	Physical characteristics					Practical issues			Material issues		
	Spatial resolution	Penetration	Stress type	Stress state	Reliability	Contact	Availability	Speed	Material type	Material structure	Surface prep./ condition
Hole drilling	50-100 μm depth increment	$\approx$ hole diameter	Macro	Uniaxial Biaxial	Poor/ Medium	Contact (semi-destructive)	Widespread	Fast/ Med	Metal Plastic Ceramic	Crystalline Amorphous	Critical
X-ray diffraction	20 μm depth 1 mm laterally	5 um - Ti 50 μm - Al 1 mm - layer removal	Macro Micro	Uniaxial Biaxial	Poor/ Medium	Non-contact (non-destructive)	Generally available	Fast/ Med	Metal Ceramic	Crystalline	Critical
Synchrotron	20 μm lateral to beam. 1 mm parallel	> 500 μm 100 mm - Al	Macro Micro	Uniaxial Biaxial Triaxial	High	Non-contact (non-destructive)	Specialist	Fast	Metal Ceramic	Crystalline	Not critical
Neutron diffraction	500 μm	100 mm - Al 25 mm - Fe 4 mm - Ti	Macro Micro	Uniaxial Biaxial Triaxial	Medium/ High	Non-contact (non-destructive)	Specialist	Med/ Slow	Metal Ceramic	Crystalline	Not critical
Curvature/ Layer removal	-	-	Macro	Uniaxial Biaxial	Poor/ Medium	Contact (destructive)	Generally available	Med	All	-	Not critical
Magnetic	1 mm	20 - 300 μm (Barkhausen)	Macro	Uniaxial Biaxial	Poor	Non-contact (non-destructive)	Generally available	Fast	Ferro-magnetic materials	Crystalline	Not critical
Ultrassonic	5 mm	> 100 mm along sample	Macro	Uniaxial Biaxial	Poor	Contact (non-destructive)	Generally available	Fast	Metal Ceramic	Crystalline	Not critical
Raman/ Fluorescence	< 1 μm	< 1 μm	Macro	Uniaxial Biaxial	Poor	Non-contact (non-destructive)	Generally available	Fast	Ceramic Polymers	Crystalline Amorphous	Not critical
Contour	1 mm	> 100 mm	Macro	Uniaxial Biaxial	Poor/ Medium	Contact (destructive)	Generally available	Slow	All	Crystalline Amorphous	Critical

Table 2.5: Advantages and drawbacks of strain measurement techniques. Adapted from (Withers and Bhadeshia, 2001; Kandil et al., 2001).

Key techniques	Advantages	Drawbacks
Hole drilling	- Quick and simple - Widely available - Portable systems - Wide range of materials - Affordable	- Data analysis and interpretation - Destructive - Limited strain sensitivity and resolution - Serious errors are possible due to local yielding for higher stresses (>80% of the yield strength of the bulk material)
X-ray diffraction	- Versatile and widely available - Wide range of materials - Portable systems - Macro and micro residual stresses	- Basic measurements - Laboratory-based systems - Delicate apparatus - Small components
Synchrotron	- Improved penetration and resolution of X-rays - Depth profiling - Fast measurement - Macro and micro residual stresses	- Specialist facility only - Laboratory-based systems - Delicate apparatus - Expensive
Neutron diffraction	- Excellent penetration and spatial resolution - 3D maps - Macro and micro residual stresses	- Specialist facility only - Laboratory-based systems - Delicate apparatus - Expensive
Curvature and Layer removal	- Relatively simple - Wide range of materials - Stress profile can be achieved by combination with other techniques	- Limited to simple part geometry - Destructive - Laboratory-based systems
Magnetic	- Fast - Wide variety of magnetic techniques - Portable systems	- Limited application to ferromagnetic materials - Subject to many of thelimitations and error sources of ultrasonic methods -Highly non-linear response with low sensitivity to tensile stresses
Ultrassonic	- Generally available - Fast - Affordable -Portable systems	- Limited spatial resolution - Bulk measurement over whole volume - Require relatively long gauge lengths and stress-free reference standards. - Errors caused by transducer coupling preferred orientation, cold work, temperature,and grain size. - Sensitivity varies with the material
Raman/ Fluorescence	- High spatial resolution - Portable systems	- Surface measurements only - Interpretation - Calibration - Limited range of materials
Contour	- Good for determination of residual stress distribution extending over large depths	- Restricted to simple geometries - Only suitable for measuring stress normal to the plane of interest

2.6.1.1 Hole drilling technique

The hole drilling technique, first introduced by Mathar (1934), is one of the most available and widely used residual stress testing techniques. The American Society for Materials Testing (ASTM) developed a standard residual stress hole drilling method (ASTM E837-13a, 2013). This technique generally uses strain gauges to measure strain data after drilling in the tested area, which has the advantages of simple, fast, readily available and low testing costs. Besides, this method is very versatile and can be carried out in the laboratory or the field, on different materials, and components of a wide range of geometries. This technique causes damage to the material, which is often negligible and for this reason, the method is considered as semi-destructive (Schajer and Whitehead, 2013). Under this method, a certain amount of material is removed, and the resultant measured relieved strain is used to calculate the residual stress (see Figure 2.22).

The hole drilling method is based on drilling a small blind hole through a thin and wide plate under uniform plane stress. This setup is rarely representative of the application at hand, due to differences in geometry. The purpose of the drilling method is to assess the residual stresses in a plane that can be assumed to have uniform depth. However, many real applications are not uniform, leading to measurement errors. The incremental drilling technique, which involves drilling in a series of small steps, improves the versatility of the method and allows the increase of stress depth and gradients to be measured.

Drilling a hole in a body under the influence of residual stresses causes stress relaxation at that location (TN-503, 2010). The elimination of these stresses at the surface of the hole, modifies the stress state in the surrounding region, causing the local stresses to change accordingly. Residual stresses can be calculated with the measured strains and calibration coefficients according to the calculation principles specified in ASTM E837-13a (2013). Strain gauges proved to be robust and reliable data acquisition devices. They provide accurate and stable strain measurement. Also, they are compact and highly portable, which allows effective field use (Schajer and Whitehead, 2013). This capability to perform accurate measurements across a wide range of measurement settings is a major factor for the widespread adoption of the strain gauge hole drilling method.

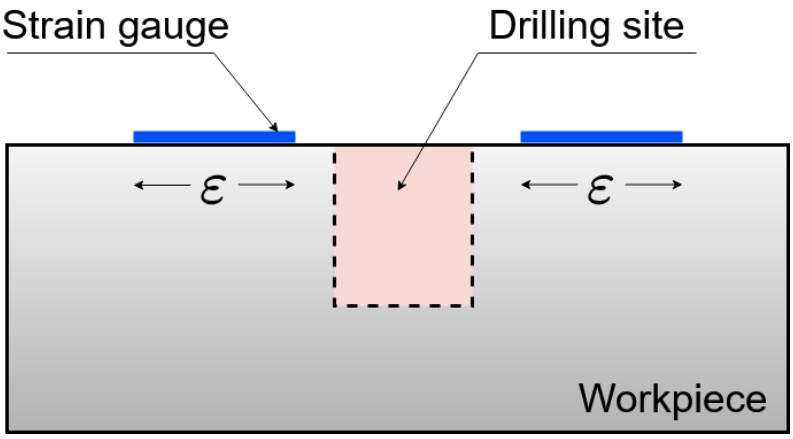


Figure 2.22: Diagram of the principle of the hole drilling technique.

Recently, the hole drilling technique has been significantly improved with the implementation of non-contact strain measurement with optical techniques for measuring strain relaxation. In fact, the data provided by a full-field method and the high sensitivity connected with the interferometric measurements can significantly reduce the problem of the effects of strain measurements errors on the residual stress evaluation (Barile et al., 2014a). This technique is based on the hole drilling technique, and uses electronic speckle pattern interferometry (ESPI) to measure the displacement field changes around the hole location, which are later converted to deformations and respective in-plane residual stresses. ESPI uses laser light to capture images of the measurement surface before and after each drilling increment so that surface displacement due to the stress relief can be quantified (Rickert, 2016). Unlike the strain gauge hole drilling technique, which provides average data from a few areas in the vicinity of the hole, the ESPI hole drilling technique allows a full-field analysis. One of the advantages of this technique is that it correlates displacements directly with stresses through a set of coefficients. In practice, the elimination of strain gauges allows performing several measurements in a sample, which is essential to verify accuracy. ESPI hole drilling technique is significantly faster than strain gauge hole drilling technique and provides detailed information about the deformations that occur as a result of the hole drilling (Steinzig and Ponslet, 2003).

Prism is the commercial designation of a residual stress measuring system developed by Stresstech (see Figure 2.23) that optically measures the surface distortion using ESPI-based technology. This system provides faster and accurate measurements requiring minimal sample preparation. Besides, it enables analysis of large surface areas surrounding the hole, rather than just averaging certain areas as is the case using strain gauges. Hence, the system captures the relax-

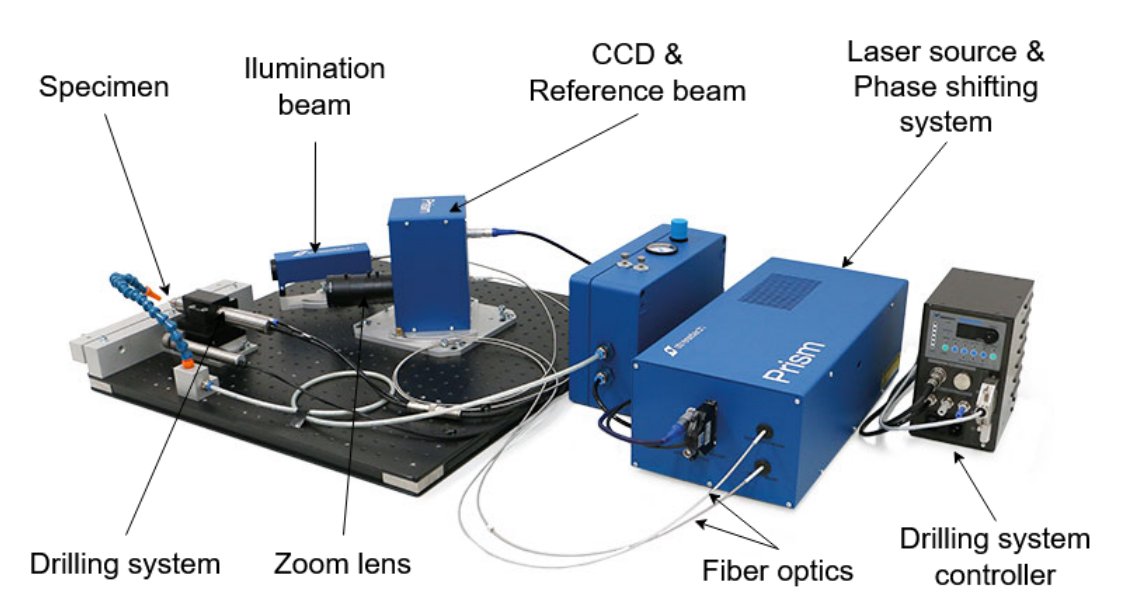


Figure 2.23: Experimental set-up for ESPI measurements of strain relaxation by incremental hole drilling. Depicted and adopted from Stresstech.

ation of the surface during incremental drilling to assess the residual stresses using the integral method. The system is based on three principles: drilling, strain measurement and residual stress calculation.

However, it should be noted that reliable measurements are only achieved by restricting the residual stresses below 80% of the yield strength (σ_Y) of the bulk material (ASTM E837-13a, 2013). Once the residual stresses approach or exceed that threshold, local plastic deformation occurs around the hole boundary as a result of the notching effect. This phenomenon leads to a substantial change in material linearity that is assumed by the integral method. This issue can be addressed by correcting the residual stress profile, as proposed by Chupakhin et al. (2017), where the effect of plasticity for LSP induced stress fields was investigated using finite element modelling and artificial neural networks. This method addresses the limitations of the hole drilling method related to effects of plasticity and enables the correction of non-uniform residual stress profiles of the typical LSP residual stress profiles.

2.6.1.2 Contour method

The contour method is categorised as a destructive (mechanical) stress measuring method (see Figure 2.21). This technique has been recently developed by Prime (2001) and allows the determination of residual stress distribution extending over large depths directly from the measured deformations. The contour technique allows the measurement of both simple and complex geometries but is only suitable for measuring normal stresses to the plane of interest, as presented in Tables 2.4 and 2.5. The experimental procedure to perform the contour technique, schematically presented in the Figure 2.24, is fairly simple and involves a sequence of steps as follows:

1. Cutting the part along the plane intended to determine residual stress.

2. Measurement of deformation in both halves cut using a coordinate measuring machine or a non-contact surface measuring machine.

3. Calculation of the average of both measured halves to remove the effect of transverse stress, as the contour method can only measure normal stresses.

4. Stress calculation using FEM to determine the stress required to deform the surface back to the original position before relaxation.

This procedure involves cutting a component, which retains residual stress, into a section of interest. By cutting the part, stress relaxation occurs and, consequently, deformation of the surfaces resulting from the cut. Further steps involve measuring the surfaces and superimposing the matrix of measured points to calculate the average displacement obtained. The average result calculated is used as a boundary condition in the FEM, where the deformed surface is brought to a perfectly flat plane, and the necessary loads are calculated which correspond to the residual stress that was present in the component before cutting.

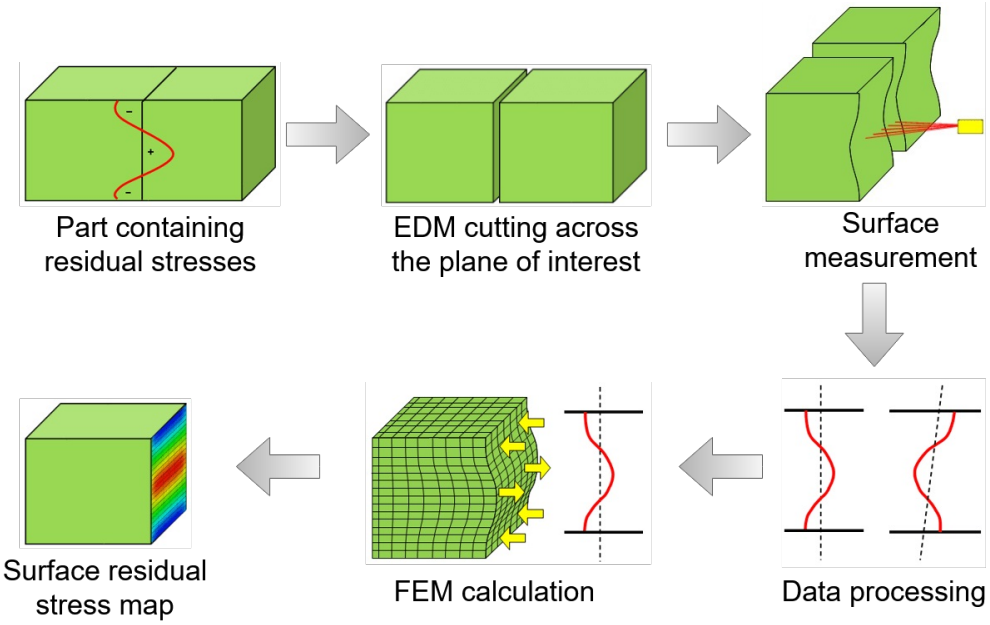


Figure 2.24: Key steps of stress measurement by the contour method. Depicted and adapted from (Oliveira, 2018).

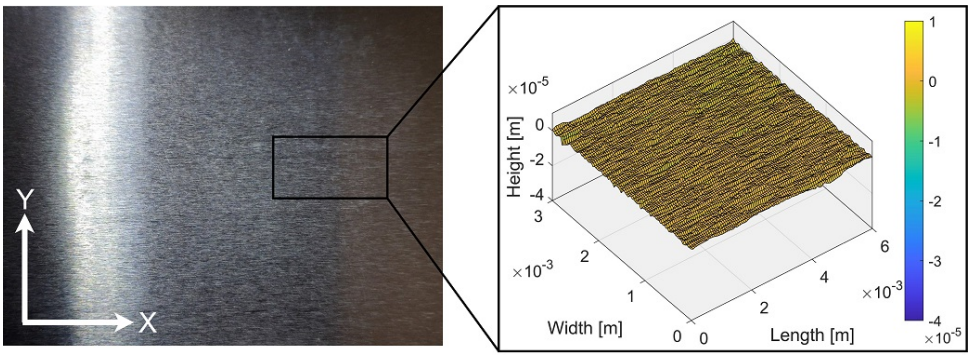
Important consideration arises concerning the cutting procedure in this technique as it assumes perfectly flat surfaces, and deviations from the planarity are only attributed to the deformation caused by the stress relaxation. Therefore, EDM cutting should not introduce any stresses affecting the deformation of the cut surface. Hence, the contour method is strongly dependent on the cutting process and the surface measurement.

2.6.2 Surface modification

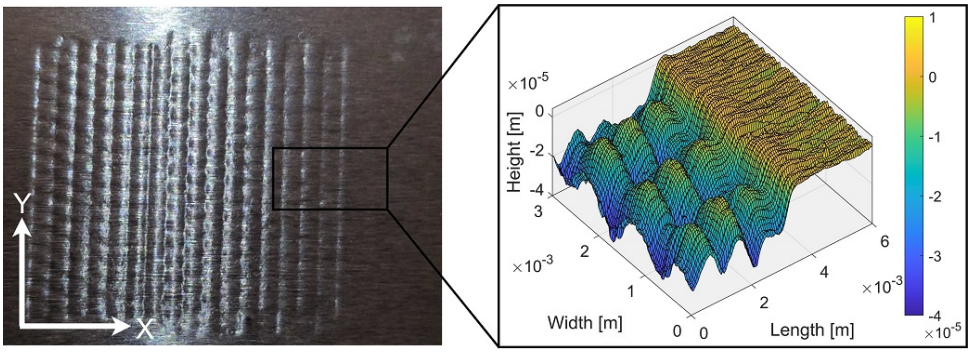
The surface topography or roughness is a fundamental indicator to describe the surface integrity of a component since surface roughness can be detrimental to the fatigue life of metal alloys (Peyre et al., 1996). In addition, the surface of components or structures is critical failure sites because they are generally regions of higher stress concentration as well as environmental exposure.

As previously discussed in Section 2.4.3, LSP involves severe plastic deformation on the surface and possibly material ablation if the target surface is not protected by an ablative layer. Therefore significant surface modification is expected to occur which, if uncontrolled may lead to excessive roughness and adversely impact the material's behaviour. Figures 2.25a and 2.25b show the surface topography of AISI D2 tool steel before and after LSP treatment, respectively.

LSP treated surfaces are a combination of surface texture elements, which are rarely found separately but are usually independently assessed. Typically, the surface analysis includes roughness and form. An important consideration regarding surface texture is the fact that no specific or well-defined threshold exists between the surface roughness and form, since these elements are dependent upon the material application. In this sense, it can be useful to evaluate these surface



(a) Base material.



(b) LSP treated material.

Figure 2.25: Macroscopic features and 3D morphology on the surface of the specimens (a) before and (b) after LSP.

changes individually. Intuitively one can state that severe plastic deformation leads to the appearance of waviness on the target surface, which resembles the laser spatial beam profile. Moreover, it is expectable that the waviness will become more pronounced as the plastic deformation increases. Similarly, surface roughness increases with increasing plastic deformation, which in turn increases with power density (Guo et al., 2019). Thus, surface roughness increases with increasing laser power density. Recent studies on the influence of laser pulse density and laser spot size on the surface integrity of maraging steel have shown that the application of small laser spots, with higher power density at a constant pulse density, promotes the generation of low surface roughness (Petan et al., 2016). The reported effect is primarily attributed to a more uniform pulse pressure distribution.

Several investigations have been conducted on the effect of LSP on the surface roughness and techniques have been proposed to minimize the roughness induced by LSP treatment. A method called rigid contact laser shock processing (RCLSP) was presented by Dai et al. (2015), which assumes rigid contact between the target surface and the ablative layer. This method demonstrated the potential to effectively reduce the surface roughness, particularly in the treatment of rough surfaces. Additionally, Dai et al. (2016) proposed a technique called elastic contact laser shock peening (ECLSP) which allows reducing the roughness developed in areas where there are laser shots overlap. This method involves the elastic contact between the target surface and the ablative

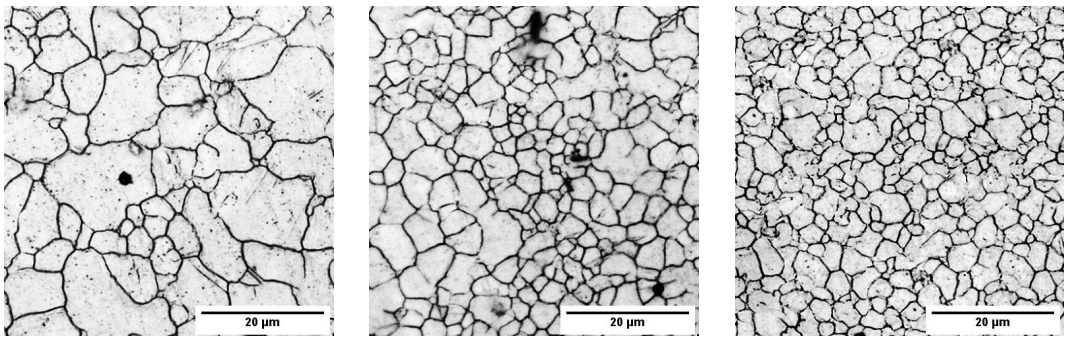
layer through the application of a metal foil. Although these techniques are slight variations of the LSP process, they constitute a valid approach to mitigate the inevitably LSP induced roughness.

Several factors can lead to an increase of roughness in LSP treated metal surfaces. These factors include the surface ablation that can occur during the LSP process and irregularities in the spatial profile of the laser beam (Dai et al., 2015). Such irregularities may arise as a result of the interaction of laser radiation with the plasma confinement medium due to the presence of water bubbles or impurities caused by the ablation of the material, which may cause non-uniformity of the pressure pulse (Trdan et al., 2012). Also, the thickness of the confinement media layer may cause the laser beam to deflect or bend, causing self-focusing (Brodeur, 1999), which may produce non-uniformity of the laser intensity, and consequently non-uniformity of the pressure pulse. This situation ultimately leads to increased surface roughness.

The ablative nature of the LSP process generated by the ionization of the vaporized material during laser irradiation, coupled with the severe plastic deformation, leads to surface modifications and increased surface roughness.

2.6.3 Microstructure

The laser-induced shock wave produces an in-depth plastic deformation, originating compressive residual stresses. Consequently, high-density dislocations and grain refinement occur in the surface and near-surface layer of the LSP processed material. Dislocations are disruptive changes in the regular arrangement of the atoms along a line in a solid crystalline arrangement. The dislocation motion occurs by sequential bond breaking and bond reforming through a process known as slip (Askeland and Wright, 2015). As the grain size decreases, the number of grain increases and thereby the amount of grain boundary area. Any dislocation moves a short distance before facing a grain limit, and strength of the metallic material increases. LSP has been successfully applied to achieve a relatively uniform fine grain microstructure for AZ31B Mg alloy (Zhang et al., 2010b). By increasing the laser pulse density, the original coarse grain structure was progressively transformed into a fine grain microstructure, as shown in Figure 2.26.



(a) (b) (c)

Figure 2.26: Surface micrographs of AZ31B Mg alloy: (a) untreated, (b) two laser impacts and (c) four laser impacts. Depicted and adapted from (Zhang et al., 2010b).

Twinning is a mechanism arising from plastic deformation, specifically shear stresses, applied to a crystalline structure. As a result, the original crystalline structure of metallic materials is rearranged. This mechanism effectively strengthens the material by forming twin boundaries within the crystalline structure, thus preventing dislocations (Askeland and Wright, 2015). With the increase of laser intensity, the depth of LSP affected zone increases as well as the depth of twinned material (Mao et al., 2018a). The stress is usually mechanical, as is the pressure applied in the LSP process. There are several factors affecting twinning deformation: grain size, strain rate, pressure and temperature. In many cases, twinning is promoted by high strain rates and low temperatures.

After LSP treatment, high-density dislocations result in high resistance and work hardening, which restrains the displacement movement to the surface. The plastic deformation at temperatures well below the melting point, also referred as cold working, causes a decrease in metals ductility (see Figure 2.27). Thus, the amount of loading cycles to initiate fatigue cracks is increased (Luo et al., 2018). The high compressive residual stresses in the near-surface layer reduce the effective stress intensity factor that controls fatigue crack propagation in LSP processed components (Hatamleh et al., 2007). As a result, the compressive residual stress can inhibit or retard the onset of cracks and reduce the propagation rate (Ge and Xiang, 2016).

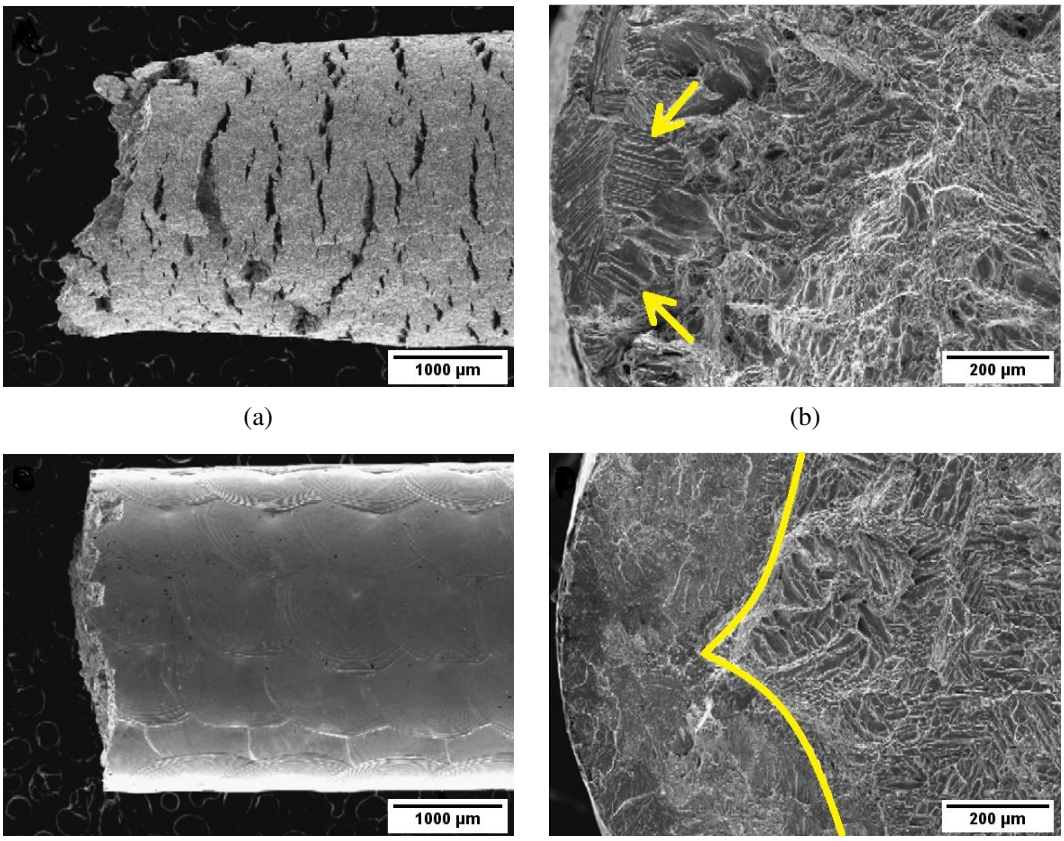


Figure 2.27: SEM images of fractured specimens after tensile testing. (a, b) untreated and (c, d) LSP treated specimen. Depicted and adapted from (Watanabe et al., 2009).

The improvement of fatigue strength in LSP processed materials can be attributed to the combined effects of the high magnitude compressive residual stresses and microstructural changes mentioned above. The strength of metal alloys can be predicted based on the grain size reduction as well as the increase in the dislocation density with plastic deformation, according to Hall-Petch equation:

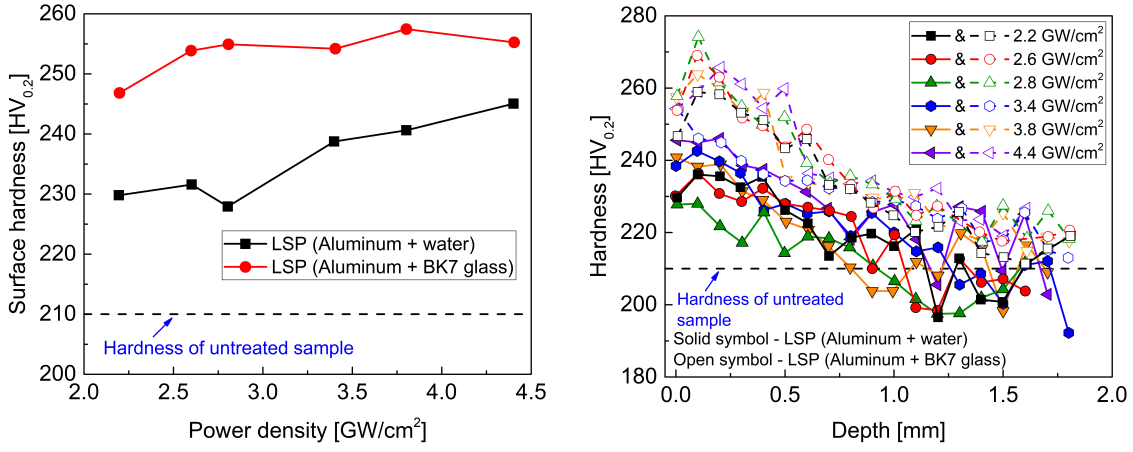
$$\sigma_Y = \sigma_i + K_y d^{-\frac{1}{2}} \tag{2.4}$$

where σ_Y is the yield strength, d is the average grain diameter, and σ_i and K_y are material constants. In a word, the finer the grain size, the higher the yield strength. The Hall-Petch relationship has been explained as the basic principle of strengthening and thoughning of steels.

2.6.4 Hardness and tensile properties

Once a material undergoes a load exceeding the yield point, and that load is then released, it ends up with a permanent deformation. If the loading is reapplied, the material will respond elastically initially until a new yield point is reached. The new yield point is higher than the initial yield point. This phenomenon is known as strain hardening. The amount of elastic strain necessary to reach the new yield point is called elastic strain recovery. The hardness, which is the resistance to plastic deformation, will increase due to permanent deformation induced by LSP.

The LSP process can improve the hardness of the metal surface throughout the treated area. The magnitude of the surface hardening depends on the LSP operating parameters, such as power density (Liu et al., 2018a; Qiao et al., 2015b), laser pulse density (Irizalp et al., 2014; Chen et al., 2018) and substrate conditions. Figures 2.28a and 2.28b show the effect of LSP with different confining media and laser power density on ER8 ferrite–pearlite steel hardness, respectively. It has been found that LSP can be effectively applied to harden the welded zones of some aluminium alloys (Liu et al., 2018b) and nickel alloys (Chen et al., 2014).

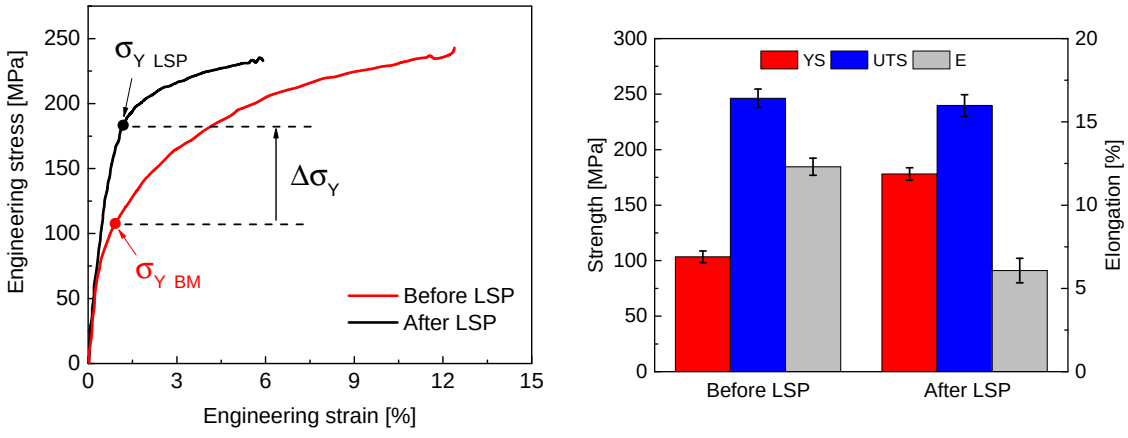


(a) (b)

Figure 2.28: The effect of LSP treatment with different confining layer on ER8 steel: (a) surface hardness and (b) hardness–depth profile. Adapted from (Zhang et al., 2019).

The hardness and Young's modulus of LSP treated AISI 304 were found higher than those of the unprocessed material (Luo et al., 2011). Similarly, the average hardness value of LSP treated AISI 304 specimens increased by 28% (Prabhakaran et al., 2018). This hardening effect can be attributed to the large plastic deformation generated during the LSP process. The micro hardness of commercial pure titanium alloy increase through the grain refinement induced by LSP (Wu et al., 2018). With increased laser energy, a significant increase in micro hardness was observed in the deformation layers after LSP treatment in brass and Mg alloys (Liu et al., 2018a; Ge et al., 2018b).

Similarly, the yield strength is also affected by the LSP. A significant enhancement of yield strength of 19% was attributed to work hardening and microstructure changes induced by LSP (Zhang et al., 2018). A recent study on tensile properties control of wire-arc additive manufactured aluminium alloy subjected to LSP, showed a remarkable increase of 72% of yield strength, while a significant decrease in elongation and no influence on ultimate tensile strength, as presented in Figure 2.29 (Sun et al., 2018b). Furthermore, a study on peening effects on the mechanical properties of FSW joint of Al2195 showed a 60% increase of yield strength after LSP when compared to SP (Hatamleh, 2008). The effects of warm LSP compared to room temperature LSP on the residual stress relaxation in Ti-6Al-4V titanium alloy were studied. Results show that the yield strength of Ti-6Al-4V, subjected to warm LSP (300°), increased 9.4% compared to room temperature LSP (Meng et al., 2017).



(a) (b)

Figure 2.29: (a) Engineering stress-strain curves of untreated and LSP treated specimens, and (b) comparison of yield strength, ultimate tensile strength and elongation before and after LSP. Adapted from (Sun et al., 2018b).

2.6.5 Fatigue life and FCP

Fatigue is a typical phenomenon observed in structures exposed to many loading cycles under regular service conditions where the maximum stresses involved are below the nominal elastic limit of the material (Lampman, 1996). It is well established that fatigue cracking frequently initiates

at the free surface of materials due to several factors: 1) stress concentration in surface defects such as indentations, 2) lower degree of restriction at the surface of cyclically loaded material, and 3) sub-surface inclusions, stress/deformation gradient field, and environmental exposure affect the distribution of local cyclic plastic deformation (Schijve, 2009; Tu and Zhang, 2016). Therefore, it is expected that compressive residual stresses in the superficial layer restrain crack initiation and propagation, positively impacting fatigue crack behaviour.

Studies conducted on titanium alloys (Zhang et al., 2010a; Nie et al., 2014), steels (Yella et al., 2019), and aluminium alloys revealed that LSP can lead to major improvements in fatigue resistance. Luong and Hill (2010) reported a significant improvement of 41% in fatigue strength of LSP treated 7050-T7451 aluminium alloy compared to base material. Figures 2.30a and 2.30b show the improvement of fatigue resistance of nickel and titanium alloys subjected to LSP, respectively.

The effect of pulse density on fatigue behaviour in titanium alloy was studied (Zhou et al., 2014). Extended fatigue lives of 29%, 40% and 108% were reported for coverage rates of 100%, 200% and 300%, respectively. Besides, LSP was successfully applied to improve the fatigue performance of nickel-based alloy GH4133B used in turbine blades (Zhou et al., 2018) and bending fatigue life of the AISI 9310 steel gear teeth (Peng et al., 2017). The effect of the laser scanning pattern on the residual stress fields and the fatigue life of stainless steel 316L specimens was studied (Correa et al., 2015a). Two *zig-zag* scanning patterns, parallel (1) and perpendicular (2) to fatigue load, were adopted. The best improvement in performance was provided by strategy 2 with a 471% increase in fatigue life, while strategy 1 provided a 166% increase at the same stress amplitude. These findings indicate a significant impact of LSP scanning pattern on the material behaviour.

Regardless of the above mentioned advantages, LSP may also decrease fatigue life due to inadequate LSP process conditions. Spadaro et al. (2017) studied the influence of LSP, without

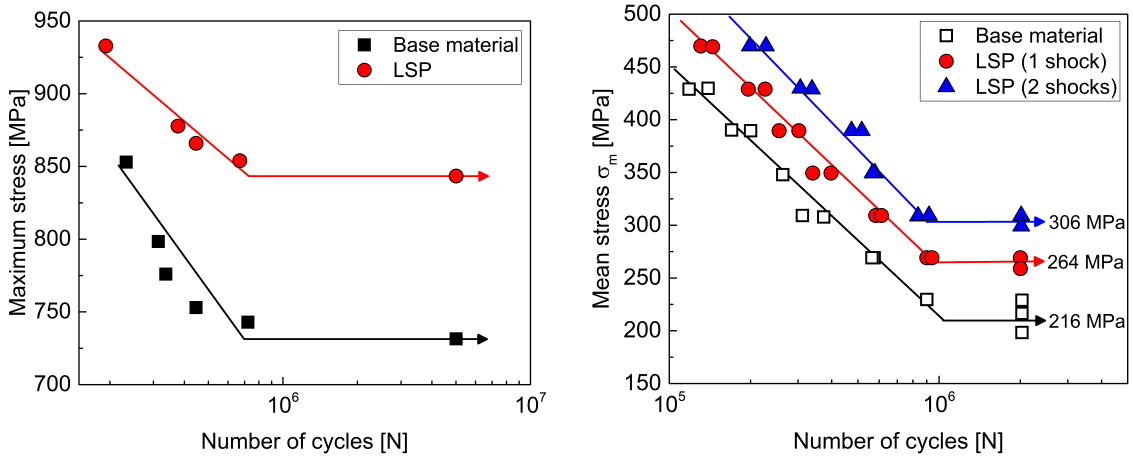


Figure 2.30: Fatigue tests for as-received and LSP treated material: (a) uniaxial tension-tension fatigue testing of ATI 718 Plus alloy and (b) three-point bending fatigue testing of Ti–6Al–4V. Adapted from (Kattoura et al., 2017) and (Zhang et al., 2010a), respectively.

protective coating and with different pulse densities, on the low cyclic fatigue behavior of a superferritic stainless steel. Results showed that LSPwC produces beneficial compressive residual stresses, however it causes intergranular corrosion that deteriorates fatigue life.

Similar to fatigue life, fatigue crack propagation is also positively affected by LSP. Crack length as function of number of cycles on Ti-6Al-4V CT samples subjected to LSP under different coverage rates is shown in Figure 2.31. Improvement in fatigue crack propagation of Ti-6Al-4V titanium alloy was reported and attributed to the combination of the positive influence of nanostructured surface layer, increased surface hardness and surface compressive residual stresses (Zhou et al., 2014). Similarly, a substantial reduction in crack propagation rate in LSP treated FSW aluminium joints was observed and may be attributed to the compression residual stresses (Hatamleh et al., 2007; Liu et al., 2018b).

Kashaev et al. (2017) investigated the effects of LSP induced residual stresses on FCP behaviour of AA2024 aluminium alloy, addressing the retardation mechanisms of LSP induced residual stresses on FCP. Significant retardation of FCP was observed for LSP treated specimens as well as crack closure effect in the region under the influence of compressive residual stresses.

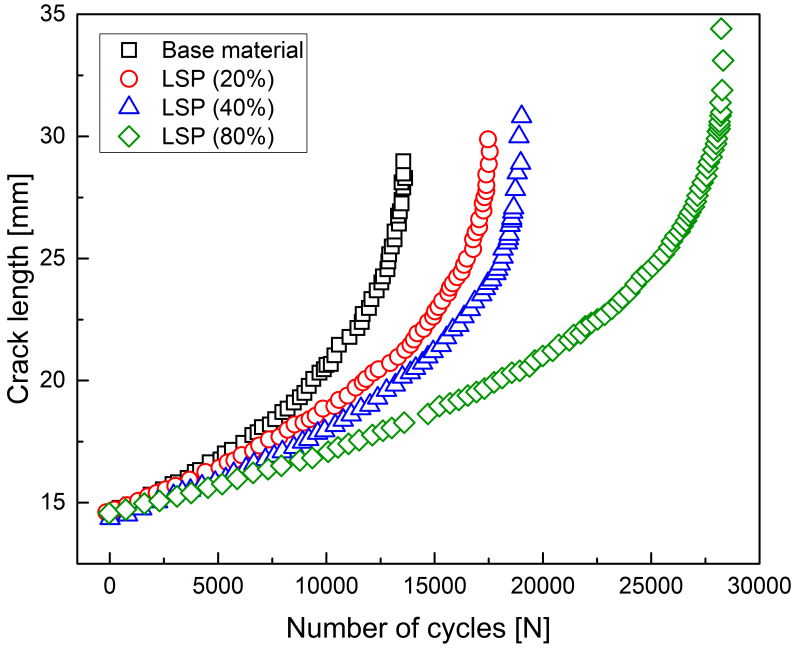


Figure 2.31: Crack length as function of number of cycles on Ti-6Al-4V CT samples subjected to LSP under different coverage rates. Adapted from (Zhou et al., 2014).

2.6.6 Tribological properties

The interaction of the high-energy laser with the target surface causes significant plastic deformation in the metal. As a result, modifications in the surface topography are observed. As previously mentioned, the free surface is a critical zone since a component failure often originates at the

surface. Therefore, the surface topography and roughness are a major indicator of the surface integrity of a component. Based on the features and advantages discussed previously, LSP is effective to inhibit the detrimental wear mechanisms on the surface of a wide variety of alloys and thereby improve wear resistance. Different investigations have been conducted concerning the friction and wear behaviour and tribological performance of LSP treated materials.

Investigations on LSP treated steels show improvements in the tribological characteristics. Siddaiah et al. (2018) characterized the effect of LSP on surface morphology and friction behaviour of 1045 steel. The influence of laser intensity on surface roughness and coefficient of friction was addressed and a surface behaviour model describing the effect of laser intensity on surface morphology has been developed. It was reported that, depending on the power density, the coefficient of friction can decrease by 17.5% – 83.25%, when compared to the untreated material. The wear tracks observed after the scratch tests at various laser power densities are shown in Figure 2.32. The proposed model represents a direct proportionality between the laser intensity and change in surface morphology due to plastic deformation of asperities.

The influence of the ablative layer on wear behaviour of LSP treated duplex stainless steel was addressed and 39% reduction on the wear volume was found from the LSP processed condition using optimized parameters (Lim et al., 2012). The impact of LSP in the tribological behaviour of 100Cr6 rolled steel was studied (Yakimets et al., 2004). Improvements in the coefficient of friction and wear rate were reported and attributed to the combined effect of hardening and compressive residual stresses. Additionally, grain refinement caused by the LSP has been found to enhance the wear resistance of AISI 8620 steel (Lu et al., 2012a).

Park et al. (2019) observed a 94% reduction in wear mass loss and a reduction in the coefficient of friction of LSP treated aluminium-silicon alloy. Also, the wear particles generated from LSP treated specimens were significantly smaller compared to untreated specimens, as shown in Figure 2.33. Trdan et al. (2018) reported that LSP treatment, without ablative layer and with a pulse density of 2500 pulses/cm2, effectively decreases the wear rate and coefficient of friction of

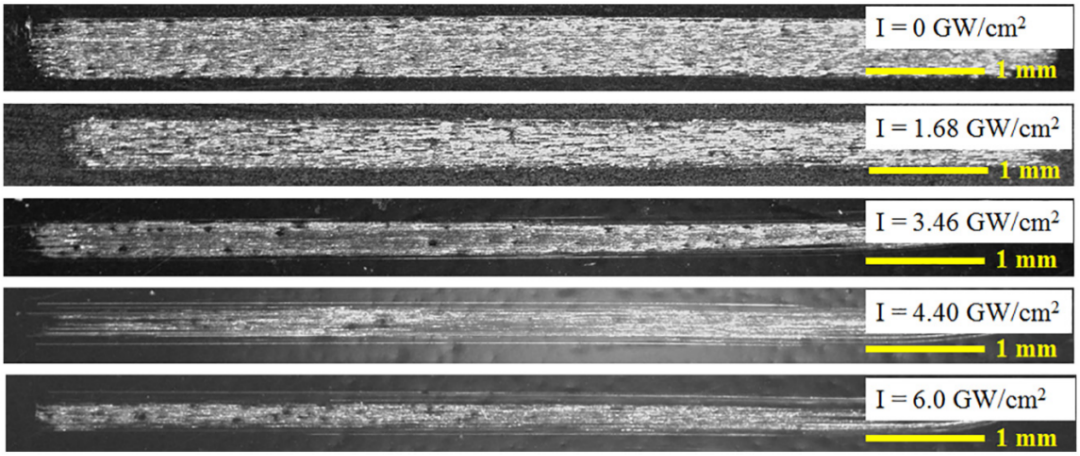


Figure 2.32: Wear tracks observed after the scratch tests at various laser power densities (Siddaiah et al., 2018).

a precipitation-hardened Al alloy by up to 29%. Similarly, Sánchez-Santana et al. (2006) studied the effect of LSP on wear, roughness and friction of 6061-T6 aluminium alloy using laser pulse densities of 900 pulses/cm^2, 2500 pulses/cm^2, and 5000 pulses/cm^2. Even though the coefficient of friction and roughness increased for LSP treated material using 5000 pulses/cm^2, these results show a 68% reduction in wear rate as compared to the base material (see Figure 2.34a). According to the authors, roughness increase due to the increment of pulse density did not imply an increment of wear rate because the compressive residual stresses dominate the wear process. Moreover, adhesion and abrasion were identified as the main wear mechanisms.

The tribological properties of LSP processed titanium and magnesium alloys were also studied. Ge et al. (2018b) investigated the impact of laser energy and laser pulse density on the wear behaviour of LSP treated material Mg-3Al-1Zn alloy. A substantial improvement on wear rate, when compared to untreated material, was found. Besides, a progressive enhancement of wear rate with the increase of laser pulse energy was observed (see Figure 2.34b). Tong et al. (2019) found that the predominant wear mechanisms of untreated TC11 alloy are delamination, adhesive and abrasive wear at elevated temperatures. However, a significant reduction of delamination and abrasive wear was observed after LSP treatment. The enhanced tribological behaviour of the LSP treated TC11 alloy can be attributed to work hardening, grain refinement, and compressive residual stress.

Low energy LSP generates a uniform strengthening layer and exhibits superior wear improvement on aluminium alloys. Conversely, high energy LSP or high pulse density LSP enhanced micro hardness and affected depth, however, more defects such as micro-cracks arise in the strengthening layer. Additionally, an increase in laser pulse density was found to increase the number of defects in the strengthening layer. These defects affect wear resistance, leading to poorer wear performance (Tan et al., 2019). Therefore, LSP parameters should be carefully selected to pre-

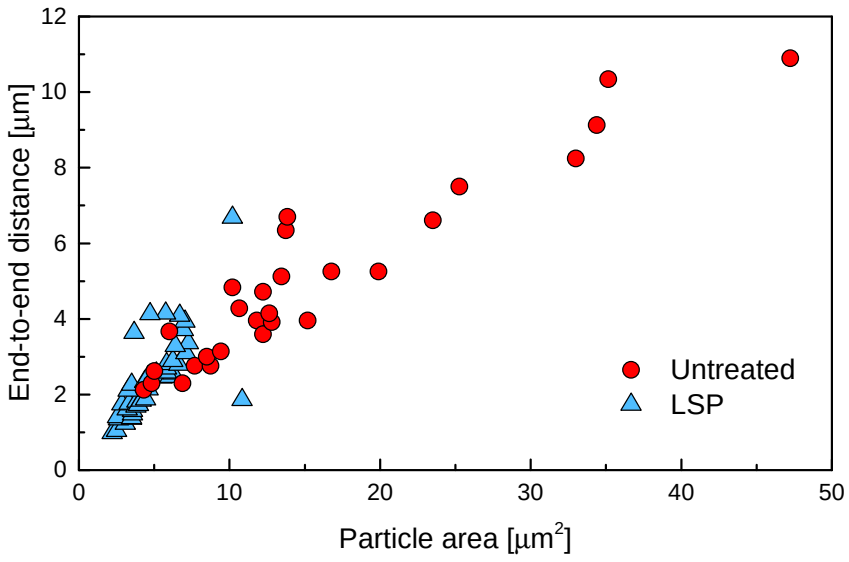
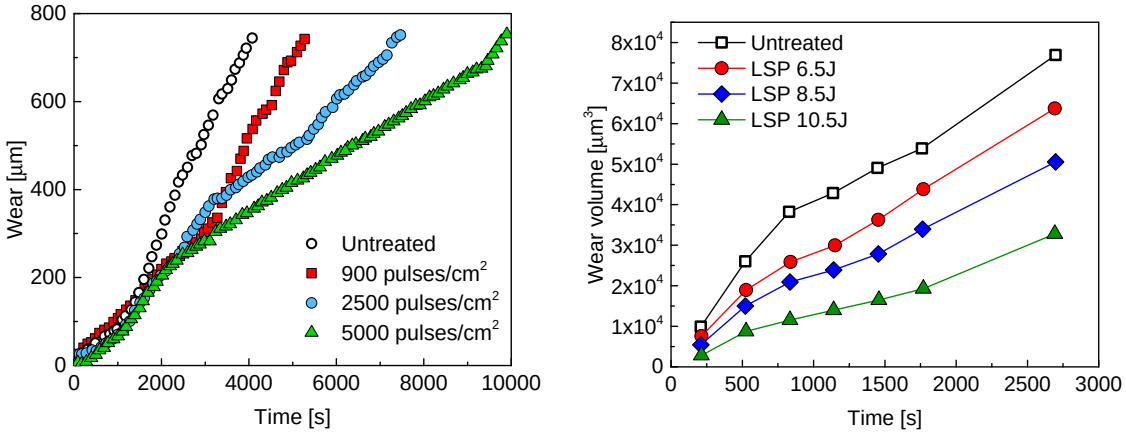


Figure 2.33: Size distribution of the wear particles. Adapted from (Park et al., 2019).



(a) (b)

Figure 2.34: Wear rate as a function of (a) laser pulse density and (b) laser energy. Adapted from (Sánchez-Santana et al., 2006) and (Ge et al., 2018b), respectively.

vent poor tribological performance. To effectively deal with this matter and establish optimal LSP conditions, Mao et al. (2018b) proposed a novel laser-based surface processing process based on laser-induced shock wave to introduce patterning and surface strengthening simultaneously, leading to enhanced wear resistance and manipulated friction values by adjusting the laser intensity.

2.6.7 Corrosion resistance behavior

The application of mechanical or thermo-mechanical laser surface treatments such as LSP can be beneficial for the mechanical strength, for the corrosion properties, and especially for pitting corrosion, often regarded as a precursor to corrosion fatigue or stress corrosion cracking (Peyre et al., 2007a). LSP parameters have a major influence on the performance of materials and several studies have been conducted concerning the corrosion behaviour and stress corrosion cracking (SCC) of LSP treated materials.

The improvement of corrosion resistance and SCC resistance can be attributed to the uniform distribution of compressive residual stress and grain refinement during LSP process. Therefore, the compressive residual stress has a positive influence on the corrosion behaviour, while tensile residual stresses can be harmful to the corrosion behaviour. A compressive layer generated by LSP appears to act as a barrier that prevents/hinders intragranular corrosion. As a result, LSP treated materials experience mainly surface corrosion, whereas untreated materials experience both surface and intragranular/pitting corrosion (Lu et al., 2012b; Caralapatti and Narayanswamy, 2017a). Experiments on LSP processed duplex stainless steel revealed a corrosion rate reduction of 74.2% while the density and size of the corrosion pits decreased by less than half compared to the untreated material, as shown in Figure 2.35a (Lim et al., 2012). Also, the overlap rate exhibits a strong impact on the corrosion rate of LSP treated Mg-alloy (Caralapatti and Narayanswamy, 2017b). As a result, the increase of the overlap rate leads to a decrease in the corrosion rate, as presented in Figure 2.35b.

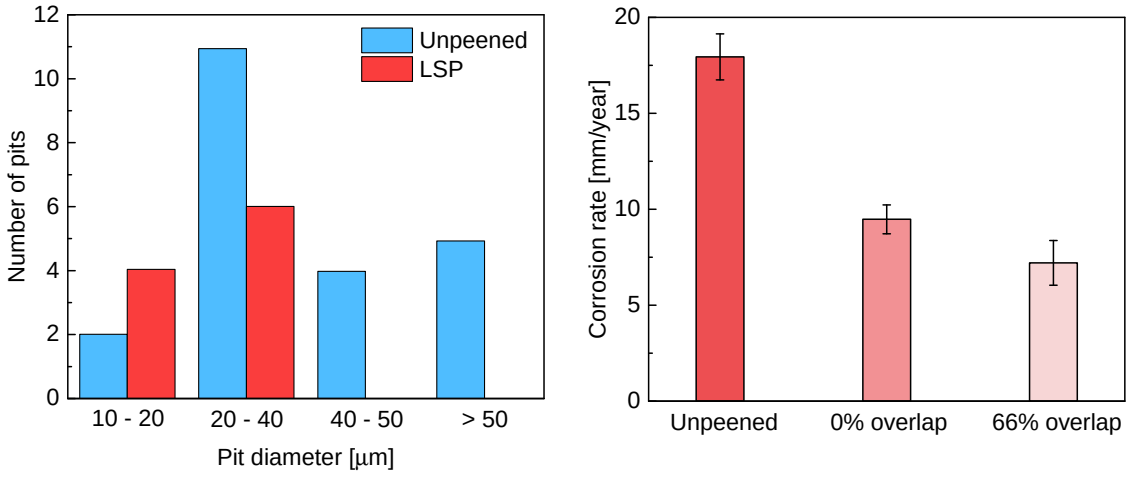
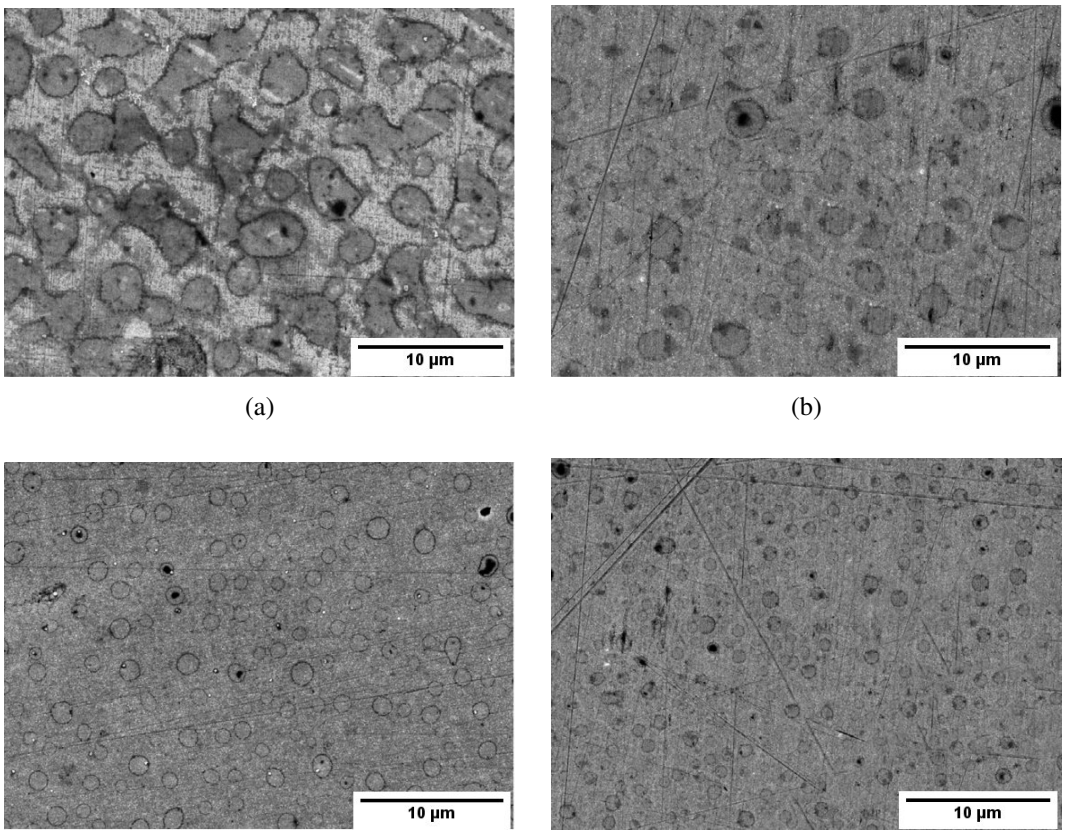


Figure 2.35: (a) Size distribution of corrosion pits and (b) corrosion rate of untreated and LSP treated specimens. Adapted from (Lim et al., 2012) and (Caralapatti and Narayanswamy, 2017b), respectively.

Laser pulse energy and pulse density play a critical role on LSP process and their influence on corrosion behaviour and SCC susceptibility of LSP treated materials have been reported (Montross et al., 2002). Lu et al. (2014) determined the influence mechanism of multiple LSP impacts with different pulse energies on corrosion behaviour of AISI 304 stainless steel. Results showed that massive LSP impacts effectively caused a significant improvement on SCC resistance and electrochemical corrosion resistance. Besides, increased pulse energy can gradually enhance its corrosion resistance behaviour, as it can be observed the reduction of eroding pits in Figure 2.36. Similarly, the corrosion resistance of AISI 304 stainless steel welds can be enhanced by LSP and by increasing the number of LSP impacts (Zhang et al., 2013; Prabhakaran et al., 2018).

The influence of massive LSP treatment on the pitting corrosion behaviour of AISI 4145 steel has been reported (Lu et al., 2017c). Results showed massive LSP treatment can effectively improve pitting corrosion resistance of AISI 4145 steel. In addition, the increased coverage layer can also gradually improve its corrosion resistance. Tong et al. (2018) observed the influence of multiple LSP impacts on corrosion behaviour of TC11 alloy. The hot corrosion resistance of the LSP treated material was improved with the increasing of LSP impacts due to the combination of the high-amplitude compressive residual stresses, crystal defects and the grain refinement induced by LSP.

The effect of LSP directly applied to the material surface without ablative layer was also studied and can effectively prevent SCC initiation and propagation of small cracks in AISI 304 steel (Sano et al., 2006b) and AA6082-T651 aluminium alloy (Trdan and Grum, 2014). The enhancement in corrosion resistance can be attributed to a more stable passive oxide film and induced compressive residual stresses in the surface layer generated during LSPwC process, as shown in Figure 2.37. On the other hand, no significant enhancement in corrosion rate was found by Kalainathan et al. (2012) when investigating the effects of LSPwC with various pulse densities



(a) (b)

(c) (d)

Figure 2.36: Surface morphology of LSP treated AISI 304 stainless steel after electrochemical attack: (a) As-received and laser energy of (b) 3J, (c) 6J and (d) 12J (Lu et al., 2014).

on the corrosion behaviour of 316L steel. In fact, the treated specimen with higher pulse density exhibited an increase in corrosion rate. However, the corrosion potential indicated the less susceptibility of LSPwC specimen to corrosion.

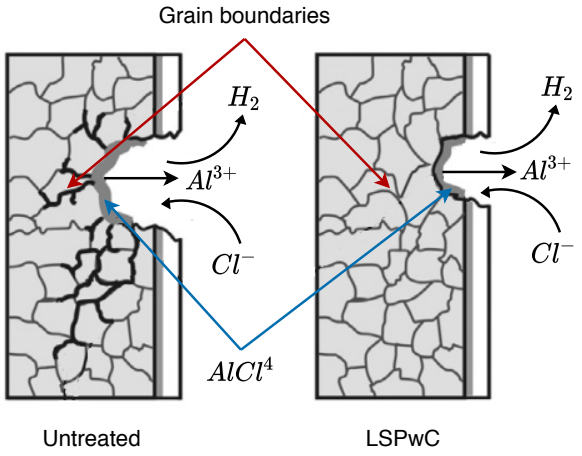


Figure 2.37: Schematic presentation of the LSPwC effect on prevention of intergranular corrosion initiation on the AA6082-T651 alloy. Depicted and adapted from (Trdan and Grum, 2014).

2.7 LSP process modelling and simulation

Given the highly complex nature of the LSP process, it is extremely challenging to experimentally investigate the dynamic response process. Moreover, analytical models are not adequate to describe such a complex process. The material behaviour at high strain rates along with plasma pressure assessment and computational effort are the biggest challenges in LSP modelling. Therefore, an in-depth knowledge regarding extreme physical phenomena such as generation and propagation of shock waves, plasma pressure and temperature is required, as the assessment of deformation and residual stress LSP effects alone do not explain the entire process. In such circumstances, a combination of the experimental and modelling approach is useful to comprehensively understand the phenomena and explore the potential and limitations of LSP.

In LSP modelling and simulation, several parameters have to be accounted for, when setting up a simulation process. a) Laser parameters such as energy, pulse duration, focus size and shape, pulse pattern and frequency. b) Process parameters such as confining layer, ablative layer and base layer. c) Material parameters such as mechanical behaviour, thermal behaviour, geometry (thickness and curvature), surface roughness and absorption.

2.7.1 Analytical models for LSP

Several researchers have addressed the characteristics of shock wave propagation, as well as modeling the typical mechanical responses of the LSP process (Fabbro et al., 1990; Ballard et al., 1991; Peyre et al., 1996). The major concern regarding these analytical models is the many simplifications and assumptions made. Hence, one must be aware that these are approximations and acknowledge all the assumptions.

"... all models are approximations. Essentially, all models are wrong, but some are useful. However, the approximate nature of the model must always be borne in mind..." (Box and Draper, 1987).

2.7.1.1 Shock wave pressure model

Fabbro et al. (1990) proposed one of the earliest and most commonly used physical models for predicting the pulse pressure as a function of the laser power density. Based on this model, the pressure of the laser-induced shock wave, P, width between the material surface and the confinement medium, L, and the velocity of the expanding plasma explosion, V, are calculated as a function of time, t, using the following Equations 2.5 and 2.6:

$$I_{(t)} = P_{(t)} \frac{dL(t)}{d_t} + \frac{3}{2\alpha} \frac{d}{d_t} [P_{(t)} L_{(t)}] \tag{2.5}$$

$$V_{(t)} = \frac{dL(t)}{d_t} = \left(\frac{1}{Z_1} + \frac{1}{Z_2} \right) P_{(t)} \tag{2.6}$$

where I is the laser pulse power density, Z_1 and Z_2 are the target material the confining layer impedance, respectively.

If certain assumptions are made, such as power density being constant and the plasma behaving like a perfect gas, the laser induced shock wave pressure can be determined using Equations 2.7 and 2.8 (Peyre et al., 1996):

$$P = 0.01\sqrt{\frac{\alpha}{2\alpha+3}}\sqrt{ZI_0} \tag{2.7}$$

$$\frac{2}{Z} = \frac{1}{Z_1} + \frac{1}{Z_2} \tag{2.8}$$

where P (GPa) is the peak pressure of the shock wave, I_0 (GW/cm^2) is the incident laser power density, Z (g/cm^{2}s) is the reduced shock impedance, Z_1 is the target material impedance and Z_2 is the confining layer impedance. Parameter α is defined as the ratio of the thermal energy to the internal energy of the plasma and, depending on the laser parameters, varies from 0.3 up to 0.5 (Fabbro et al., 1998).

If considering a water confinement mode, as it happens in most LSP experiments, the interaction between the laser radiation and the material can be further simplified as the proportional relationship between the laser power density and the surface pressure is given by (Peyre et al., 1996):

$$P = 1.02\sqrt{I_0} \tag{2.9}$$

Considering the LSP process using water confinement mode, the peak pressure can be assumed as the square root of the power density of the incident laser beam (Ding and Ye, 2006).

2.7.1.2 Modelling of LSP mechanical effects

Analytical models to predict the mechanical effects resulting from the interaction between the laser-induced shock wave and the surface of the material were developed. Ballard et al. (1991) proposed a model to predict the residual stress induced by LSP treatment. This model assumes pure uniaxial compression, uniform pulse pressure, and neglects work hardening and viscous effects. The surface plastic strain, ε_p, is assumed as function of the laser-induced pulse peak pressure, and can be expressed as (Ballard et al., 1991; Peyre et al., 1996):

$$\varepsilon_p = \frac{-2\,HEL}{3\lambda+2\mu}\left(\frac{P}{HEL}-1\right) \tag{2.10}$$

where P is the laser-induced pulse peak pressure, HEL is the Hugoniot elastic limit and μ and λ are the Lamé's constants. According to this model, the plastic strain initiates at HEL (Equation 2.1), depends linearly on the pulse pressure peak and reach a saturation point at 2 HEL. Additionally, when the peak pressure exceeds 2.5 HEL, reverse straining with surface release waves occur.

Based on this model, the optimal peak pressure should be in the range $2HEL \leq P \leq 2.5HEL$ (Ballard et al., 1991; Peyre et al., 1996).

According to Ballard et al. (1991), the plastically affected depth is function of the temporal profile of pulse pressure, L_p and can be estimated as:

$$L_p = \left(\frac{C_e C_p \tau}{C_e - C_p}\right)\left(\frac{P - HEL}{2HEL}\right) \tag{2.11}$$

where C_e and C_p are the velocity of elastic and plastic longitudinal waves in the target, respectively. The estimation of L_p assumes that plastic deformation occurs to depths where the peak stress P no longer exceeds the material HEL, and depends linearly on the pressure duration τ.

The determination of the surface residual stress induced by square laser impact in a semi-infinite body was proposed by Ballard et al. (1991) and a bi-axial and isotropic residual stress field was assumed. Assuming that the values of variables ε_p and L_p are known, the surface residual stress, σ_{surf}, using a square and round laser spot can be represented by Equations 2.12 and 2.13, respectively (Fabbro et al., 1998; Peyre et al., 1998):

$$\sigma_{surf} = \sigma_0 - [\mu\varepsilon_p(1+\nu)/(1-\nu) + \sigma_0]\left[1 - \frac{4\sqrt{2}}{\pi}(1+\nu)\frac{L_p}{a}\right] \tag{2.12}$$

$$\sigma_{surf} = \sigma_0 - [\mu\varepsilon_p(1+\nu)/(1-\nu) + \sigma_0]\left[1 - \frac{4\sqrt{2}}{\pi}(1+\nu)\frac{L_p}{r\sqrt{2}}\right] \tag{2.13}$$

where σ_0 represents the initial residual stress, a is the edge of a square laser spot, r is the radius of the circular laser spot and ν is the Poisson's ratio.

2.7.2 Material constitutive model

The Johnson-Cook (JC) model is a widely accepted material constitutive model of the dynamic response of materials. It is extensively applied to study laser impact-related applications and is available in the material model library in various commercial FEM codes. This model is effectively used to characterize the behaviour of materials subjected to high-strain rates (10^6 s^{-1}), such as high-velocity impact and explosion shock (Brockman et al., 2012). In the JC model (see Equation 2.14), the Von Mises flow stress is expressed as a function of the plastic deformation and of the strain rate as:

$$\overline{\sigma} = \left[A + B\overline{\varepsilon}^{p^n}\right] \cdot \left[1 + C\ln\left(\frac{\dot{\overline{\varepsilon}}^p}{\dot{\varepsilon}_0}\right)\right] \cdot [1 - (T)^m] \tag{2.14}$$

where $\overline{\varepsilon}^p$ is the effective plastic strain, $\dot{\overline{\varepsilon}}^p$ is the effective plastic strain rate, and $\dot{\varepsilon}_0$ is reference strain rate. A, B, C, n and m are experimentally determined constants. The variable T accounts for the thermal softening effects and is defined as:

$$T = \frac{T_c - T_0}{T_{melt} - T_0} \tag{2.15}$$

where T_c is the current temperature, T_{melt} is the melting temperature and T_0 is the reference temperature.

Thermal softening arises from heat generation during plastic deformation and leads to yield stress relief. This effect is accounted for in several LSP FEM simulations (Peyre et al., 2003, 2007b; Zhou et al., 2011). However, several studies assume LSP as a purely mechanical process (Wu et al., 2011; Correa et al., 2015a; Sticchi et al., 2015; Keller et al., 2018). As previously mentioned in Section 2.4.3, adding an ablative layer to the material surface minimizes or prevents the temperature effects and promotes a purely mechanical contact. Hence, in such condition, the influence of temperature during the LSP process can be neglected ($T = 0$).

2.7.3 FEM for laser shock peening

Adopting experimental methodologies to characterize the phenomena involved in the LSP treatment process can be expensive and challenging due to the unavailability of facilities and equipment. To understand and optimize the process, several LSP numerical studies have been published in recent years. Numerical simulation based on the finite element method (FEM) serves as a reliable and effective tool to analyze stresses in many manufacturing processes. It has been widely used to determine the ideal set of parameters for a specific application. Its key strengths are in general user friendly, well-documented, and it has a extensive libraries of implemented material models.

A comprehensive 3D model was presented by Wei and Ling (2014) to predict the development, magnitude and distribution of the LSP induced residual stress field. Based on the model, the influences of LSP parameters such as power density, spot size, number of shots and overlapping shots were analyzed. Initially, the laser beam induced pressure and other necessary parameters have been applied to produce dynamic response in the target, and explicit analysis has been performed until all plastic deformation has occurred. The dissipated energy during the dynamic response was then monitored, and the saturation acted as criteria to stop the analysis, suggesting that all plastic deformation had occurred. The second stage was static equilibrium analysis to determine the final residual stress field. Dai et al. (2014) developed a 2D model to simulate the material behavior of commercially pure aluminium by LSP. Different pressure peaks at different laser spot diameters were applied to the material surface. Arif (2003) proposed a finite difference algorithm to simulate the propagation of the stress wave in the material. This module has been explicitly coupled to each time step with a finite element module to predict strains and stresses. Hu and Yao (2008) proposed a FE model to simulate the residual stress by LSP with overlapping laser spots. The effects of different overlap rates and laser shot sequences on the residual stress distribution are analyzed to optimize the processing parameters. Fang et al. (2013b) addressed the effect of LSP with single and multiple impacts on the residual stresses of DD6 alloy engine blades.

Recently, Keller et al. (2018) proposed a comprehensive FE model with experimental calibration to predict the distribution of residual stresses in LSP process. The laser impact was simulated using a pressure load on the surface. Additionally, the same author proposed two experimentally

validated multi-step simulation strategies to predict the fatigue crack propagation rate in residual stress fields (Keller et al., 2019b) and to explain the fatigue crack retarding and accelerating mechanisms within these LSP induced residual stress fields (Keller et al., 2019a).

2.8 Future challenges for the LSP process

Over the past few years, the academic literature has been widely expanded with research papers related to LSP. The acceptance and implementation of LSP at an industrial scale are the major challenges nowadays. That is mainly due to the lack of knowledge and process control. Many of the studies rely on previously studied parameters, trial and error approaches, and oversimplified numerical modeling and simulation.

As previously mentioned in section 2.3, LSP features several advantages over conventional SP. However, the drawbacks related to the LSP technique cannot be neglected. Dimensional distortion, thermal relaxation, stability and homogeneity of the compressive residual stress distribution pose a challenge to the LSP technique. Thus, for the LSP to become widely accepted it is necessary to define an optimal set of parameters according to the characteristics of the different materials. High equipment cost and therefore the cost of each component makes the LSP highly exclusive for industries with very high standards of performance and safety.

The future of LSP involves the development of increasingly accurate and reliable numerical models capable of predicting compressive residual stresses field. However, predicting plasma pressure, material behaviour at high strain rates and the computational workload involved are the major challenges to this numerical approach. Besides, real-time LSP monitoring techniques for industrial-scale implementation are needed to detect potential problems or errors throughout the process. Recent developments have shown the feasibility to use acoustic signals generated during the LSP process for troubleshooting (Banerjee et al., 2019). The acoustic signals generated during LSP feature a distinctive signal, which contains information regarding the processed sample surface according to the material and process parameters. These acoustic signals can then be calibrated using experimental data to assess the success of the LSP.

A further challenge for the growth and acceptance of the LSP technology is the creation of facilities and service providers equipped with mid-size laser systems due to their small footprint and lower operating costs. As a result, organizations that require improved parts can either request the LSP service or purchase a complete LSP system and integrate it into the normal flow of their production lines.

2.9 Summary

LSP is a surface treatment, mostly applied to high performance components, that enhances material properties through the controlled generation of compressive residual stresses. This technology employs solid state pulsed laser systems as a high-power source. The key parameters are laser energy, pulse duration, laser spot size, overlapping and wavelength. In order to avoid the thermal

effects of the laser while promoting a purely mechanical stress, an ablative layer is often used on the surface of the material. In addition, tapping water is widely used as a confinement media, creating a barrier that effectively contains the expanding plasma explosion that occurs when the high-energy ultra-short laser pulse reaches the target material. LSP is a versatile technique as it can be applied to a wide range of metallic materials from steels, aluminium alloys, titanium alloys, nickel based alloys, cobalt-chromium alloys, and magnesium alloys. This treatment has effects on residual stresses, surface topography and microstructure. The physical and mechanical properties are also affected, including hardness, material strength, fatigue, friction, wear, and corrosion resistance behavior.

Chapter 3

Materials & methods

3.1 Introduction

This chapter addresses the experimental part of this work. The experimental campaign adopted in the present work aimed to select appropriate LSP treatment parameters for the studied material and subsequently perform a comprehensive series of material testing to evaluate the applicability and benefits resulting from the LSP treatment. This allowed to assess the LSP effects at many levels and identify the advantages and challenges of this surface processing technique.

A detailed description is provided regarding the different material specimens, along with a description of the LSP process. Additionally, all the testing procedures undertaken to confirm the LSP process success are thoroughly described.

3.2 Material and specimen details

AISI D2 tool steel was selected mainly because it is often Quantal's first choice for tool production. This is a high-carbon, high-chromium tool steel, characterized by excellent wear resistance and good hardening properties (high resistance to softening at high temperatures) as well as microstructure stability. The material composition is presented in Table 3.1. AISI D2 is typically used for manufacturing cold work tools mainly due to its high wear resistance and affordability (Bryson, 2009; Straffelini, 2015). The main applications are stamping tools, punches and dies, forming dies, shear blades and cutters. As high-quality material for cold working applications, AISI D2 offers several advantages, in particular a well-established know-how for all sorts of tool treatment and processing. Thus, this material is suitable for tooling applications that require high wear resistance and moderate toughness (shock resistance). This limited shock resistance can be a disadvantage if not carefully addressed. AISI D2 is supplied in the soft-annealed state to facilitate machining. The steel microstructure plays an essential role in the material's wear and hardness behaviour. A concern regarding the Group D steels is the large undissolved carbides in the ferritic matrix, which are generated by the carbon and carbide forming elements, particularly chromium.

Table 3.1: Chemical composition of AISI D2 (wt.%), Ramada Aços values.

Element (wt.%)	C	Si	Mn	P	S	Cr	Mo	V
Min.	1.45	0.10	0.20			11.0	0.70	0.70
Max	1.60	0.60	0.60	0.03	0.03	13.0	1.00	1.00

The strong presence of large carbides in AISI D2 cold working tool steel renders this material brittle (Roberts et al., 1998), often causing early cracking, which is primarily responsible for its low toughness and low tensile strength, thereby limiting the shock and fatigue resistance. However, the wear resistance properties benefit from the presence of large, hard carbides (Straffelini, 2015).

The AISI D2 steel used in the present study was supplied by a local dealer (Ramada Aços Special Steel Solutions Ltd., Portugal). The material was delivered in the soft annealed condition (heat through to 850ºC followed by cooling in the furnace at 10ºC /h to 650ºC, then freely in the air) in the form of blocks ($85\times85\times75$ mm^3, $105\times35\times75$ mm^3, $105\times55\times10$ 5mm^3, $285\times86\times85$ mm^3, and $285\times86\times150$ mm^3). Table 3.2 summarizes the material properties.

LSP is a surface treatment that improves the properties of metals by generating controlled compressive residual stresses. It influences the state of residual stresses, surface topography and microstructure. The physical and mechanical properties are also affected, including hardness, material strength, fatigue and wear resistance. Thereby several types of test specimens have been selected to assess the many effects of LSP on the material. Table 3.3 summarizes the different specimen geometries according to the testing application. The test specimens were manufactured at Quantal, S.A. facilities in compliance with the testing guidelines and standards for each specific testing procedure. A total of five different specimen designs were manufactured. The detailed drawings are attached in Appendix A.

Plate specimens of $100\times50\times3$ mm^3 were used to evaluate the effects of LSP processing parameters. This flat-type design was adopted to easily perform LSP as well as to perform residual stress measurements using ESPI incremental hole drilling. No standard specimen geometry specification is available for the calculation of residual stresses through the incremental hole drilling technique. There are instead standards for the hole diameter and measurement depth. The plate specimen (S-PLT) geometry is presented in Appendix A.1.

To assess the effect of LSP on fatigue resistance and tensile properties, the specimen geometry was adapted from ASTM E466-15 (2015) and ASTM E8M (2016), respectively. The specimen design is such that failure is predicted to occur in the test section (notch). The gauge cross-section was defined regarding the load capacity of the testing apparatus and a generous gauge to grip blend

Table 3.2: AISI D2 material properties.

Density [Kg/m3]	Young Modulus [GPa]	Yield strength [MPa]	Ultimate tensile strength [MPa]	Enlongation [%]	Hardness [HB]
7700	190	470	760	16	230

Table 3.3: Specimen identification and summary of testing procedures.

ID	Specimen	Standard	Tests
S-PLT	Plate specimen (Appendix A.1)	ASTM E837-13a	Surface roughness parameters, residual stress (ESPI hole-drilling), micro hardness and microstructural observation
S-DB	Dogbone specimen (Appendix A.2)	ASTM E466-15	Fatigue and tensile properties
S-MT	M(T) specimen (Appendix A.3)	ASTM E647-08	Fatigue crack propagation
S-DS	Disk specimen (Appendix A.4)	ASTM G99-17	Dry slidding wear
S-NS	Notched specimen (Appendix A.5)		Residual stress (Contour method)

radius to avoid stress concentration and prevent failure to occur outside of the gauge zone. The dogbone specimen (S-DB) geometry is presented in Appendix A.2. The geometry and dimensions of the middle-crack-tension M(T) specimen (S-MT) were prepared according to ASTM E647-08 (2008), as shown in Appendix A.3.

Disk specimens (S-DS) were prepared in compliance with ASTM G99-17 (2017) to evaluate the effect of LSP on the wear resistance. The specimen geometry is shown in the Appendix A.4. Special care was given to surface condition in order to prevent any surface or subsurface damage.

Additionally, a double side notch specimen geometry was prepared for residual stress analysis using the contour method. A $100\times30\times3$ mm^3 rectangular plate notched in the central area with a 5 mm radius notch identified as (S-NS) is shown in the Appendix A.5. No standards or specifications are available for this specimen.

3.3 LSP experiment

The LSP processing of AISI D2 tool steel specimens was performed using a high-energy Q-switched Nd: YAG Quantel laser system at Helmholtz-Zentrum Geesthacht (HZG). This solid-state laser system is based on an oscillator-amplifier that delivers maximum output energy of 5 J with available output energy ranging from 0.5 J to 5 J, operating at 10 Hz, 1064 nm wavelength, 20 ns pulse width (FWHM) and using a squared laser focus of 1 mm x 1 mm. The quantitative spatial laser beam profile is top-hat and is shown in Figure 2.11a. A convergent lens of 300 mm focal length was used to focus the laser beam on the target surface, placed ahead of the focal plane (211 mm) to avoid air breakdown. The specimens were fixed with a clamping device and mounted on a six-axis motion system KUKA KR60HA-C used to control the relative position (x, y) between the laser beam and the surface of the specimen. The LSP setup is shown in Figure 3.1. During the process of LSP no overlapping rate between the adjacent spots was defined.

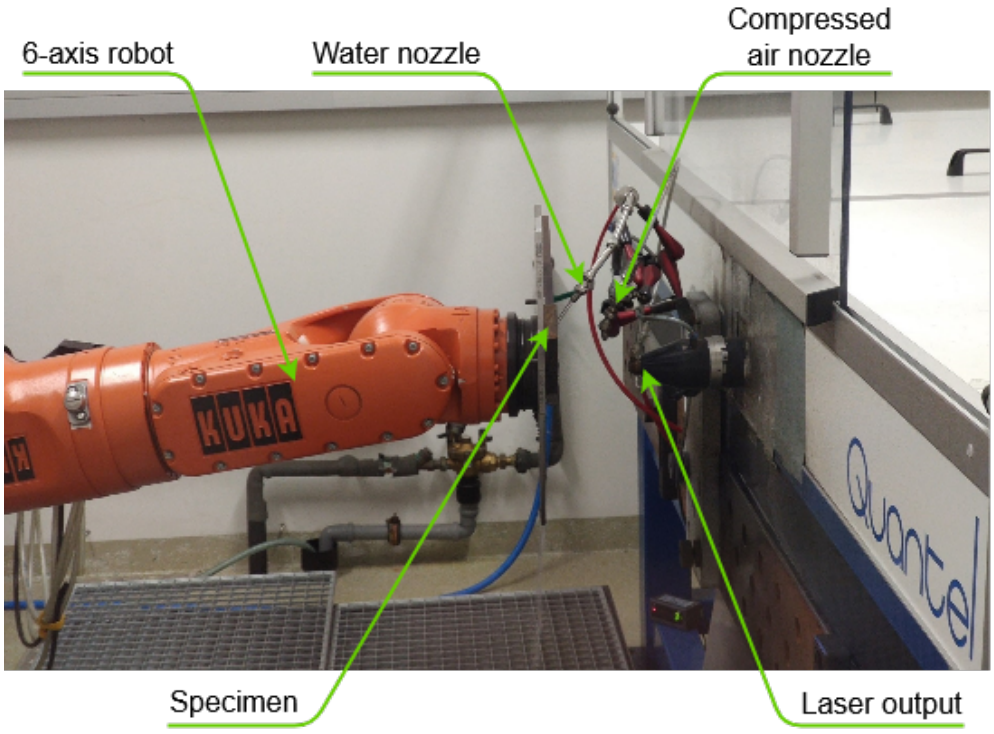


Figure 3.1: LSP experimental setup. Image courtesy of Department of Joining and Assessment in the Institute of Materials Research, Helmholtz-Zentrum Geesthacht.

Flowing water ($\approx$ 1 mm thickness) was used as a transparent confining layer to contain the expanding plasma explosion and enhance the pulse pressure effectiveness. The high energy leads to the plasma expansion causing high-pressure shock waves to propagate across the material. This results in localized surface plastic deformation leading to compressive residual stresses generation. A 0.1 mm thick TC862 stainless steel foil tape (304 Stainless Steel with acrylic adhesive), serving as an ablative layer, was applied to avoid the thermal effects and surface melting, since it may lead to the generation of undesirable tensile residual surface stress. The ablative layer was carefully applied to avoid poor contact regions and it was replaced after each laser shot sequence. In previous trials, poor adhesion zones often destroyed the ablative layer, exposing the material surface to direct interaction with the laser radiation. Also, stainless steel adhesive foil was found more effective than other ablative layers, as it can endure the interaction with the high energy levels without undergoing major damage.

Ablative layers such as aluminium foil and black adhesive tape were previously tested and proved to be ineffective for such energy levels as they were eventually destroyed. Additionally, the application of LSP in direct ablation, i.e. without a protective ablative layer, has been tested. However, the ensuing evaluation of the residual stress shown a highly non-uniform compressive residual stress field. This is explained by surface exposure to the high temperature generated during the application of LSP.

In this work, the LSP application on AISI D2 tool steel has been accomplished in two distinctive stages. The residual compressive stress state on the material provides a clear indicator

of the success of the process. Therefore, the first stage comprised the LSP treatment of the plate specimens (S-PLT) with variable parameters for assessing the compressive residual stress. The LSP laser parameters are presented in Table 3.4. As previously stated, the compressive residual stresses can benefit the material's condition, particularly in wear and fatigue resistance properties. Hence, residual stress state has been used as a criterion to establish the most effective LSP treatment condition amongst the tested parameters. During the second working stage, the rest of the specimens (see Table 3.3) were processed using only one set of parameters, as shown in Table 3.4. These parameters were selected considering the compressive residual stress results (see results on Section 4.2).

Table 3.4: LSP laser parameters.

Laser parameters	Plate specimen (S-PLT)	Other specimens (S-DB, S-MT, S-DS, S-NS)
Laser energy [J]	1, 2, 3, 4, 5	3
Power density [GW/cm^2]	5, 10, 15, 20, 25	15
Pulse density [pulses/cm^2]	100, 200	200
Pulse duration [ns]	20	20
Laser spot size [mm^2]	1	1
Repetition rate [Hz]	10	10
Wavelength [nm]	1064	1064
Laser spot shape	Square	Square

3.3.1 First LSP application stage

LSP was applied in three 15×15 mm^2 areas equally spaced on the plate specimens (S-PLT), according to the schematic representation of Figure 3.2.

Several pulse energies and pulse densities were used to investigate the effects on residual stress distribution in LSP treated material. The parameters are presented in Table 3.4. A laser pulse energy of 1, 2, 3, 4 and 5J was applied to different treatment areas. According to the laser parameters, these pulse energies deliver power densities of 5, 10, 15, 20 and 25 GW/cm^2, respectively. The laser pulse density has varied from 100 to 200 pulses/cm^2, corresponding to a single and double laser shots sequence. Additionally, the ablative layer was replaced after each laser shot sequence and only one side of the test specimen was processed. The appearance of the specimen after the LSP application is shown in Figure 3.3.

The potential effect of the interaction of residual stress fields from different processed areas has been tested. Residual stress profiles for untreated material located between adjacent treatment areas were previously evaluated and compared with residual stress profiles of untreated specimens. No appreciable variation was found, suggesting no residual stress interaction effects between the treated areas in the same specimen.

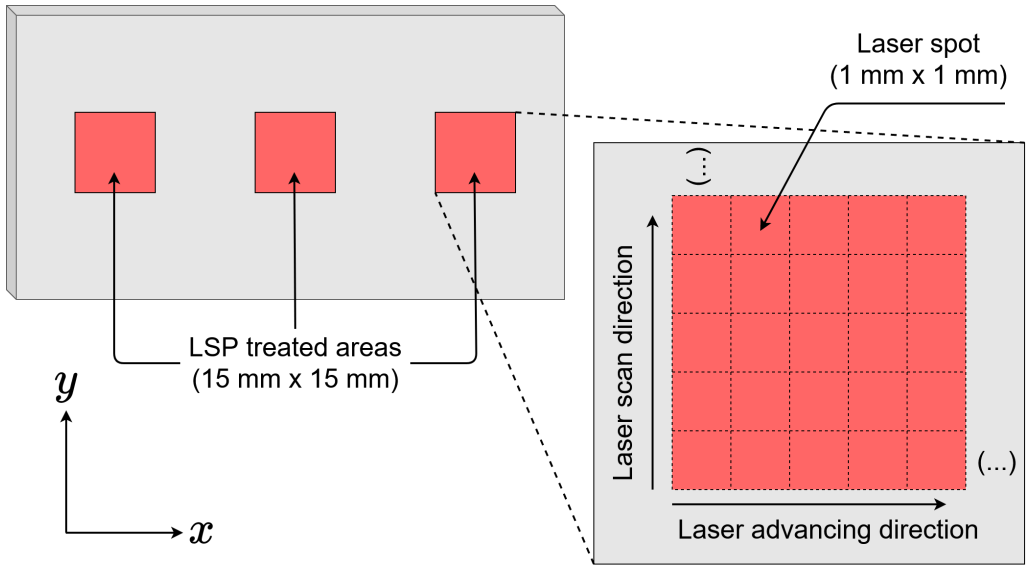


Figure 3.2: Schematic representations of the LSP application area and laser application pattern referred to as laser scanning direction and laser advancing direction.

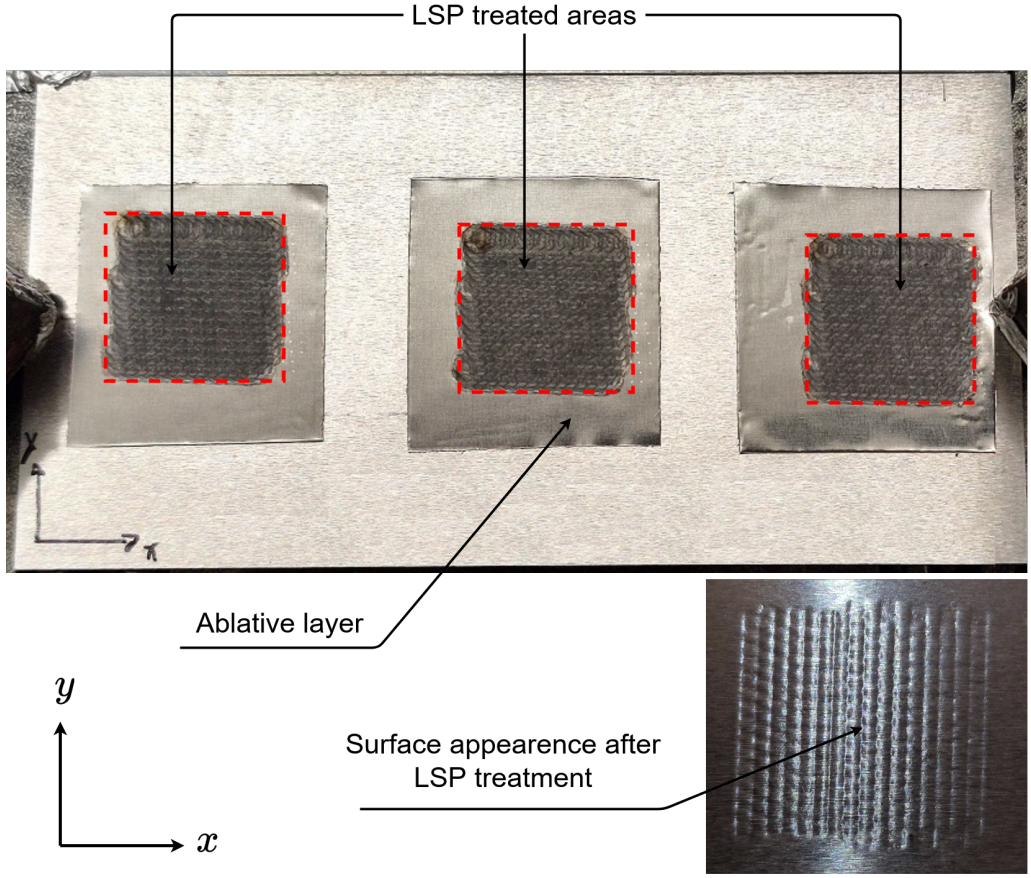


Figure 3.3: LSP treated areas and surface appearance.

3.3.2 Second LSP application stage

After assessing the impact of LSP parameters on the residual stress field of AISI D2 tool steel, a processing condition was selected to be applied to the other specimens. The selected set of parameters proved to deliver the most effective combination of maximum compressive residual stresses, affected depth and stress profile uniformity. The results are discussed in detail in Chapter 4. All specimens listed hereafter were treated using 3J laser energy and a pulse density of 200 pulses/cm^2, as shown in the Table 3.4. Particular attention was given to the application of the ablative layer to prevent low adhesion zones. Also, a new ablative layer was applied after executing each laser shot sequence.

The LSP was applied to M(T) specimens (S-MT) according to the Figure 3.4. The treatment was applied on both sides of the specimen, after opening a 2.5 mm double notch, in areas of 10×15 mm^2 located 2 mm from the edge of the notch.

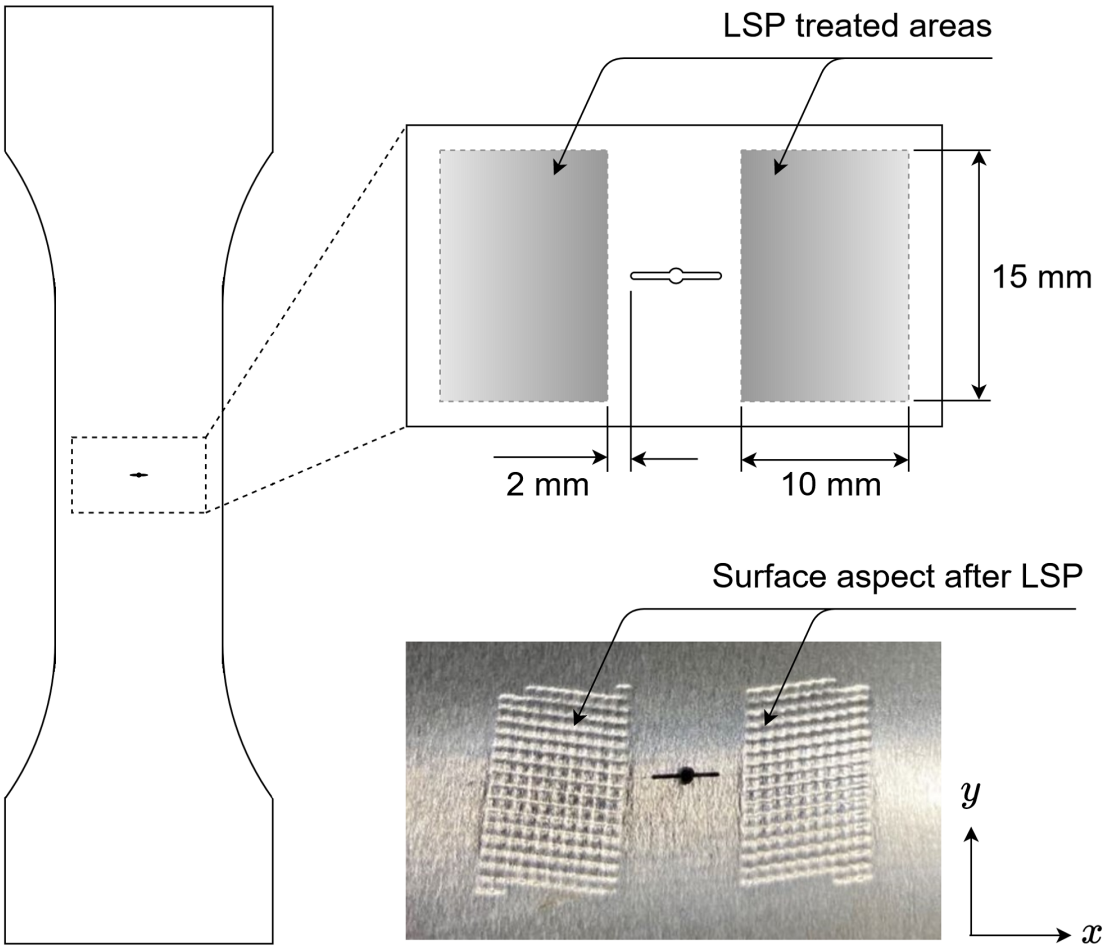


Figure 3.4: LSP treated areas in M(T) specimens.

The LSP was applied to dogbone specimens (S-DB) according to the Figure 3.5. The treatment was applied on both sides of the specimen, in areas of 10×15 mm^2 located around the center double notch.

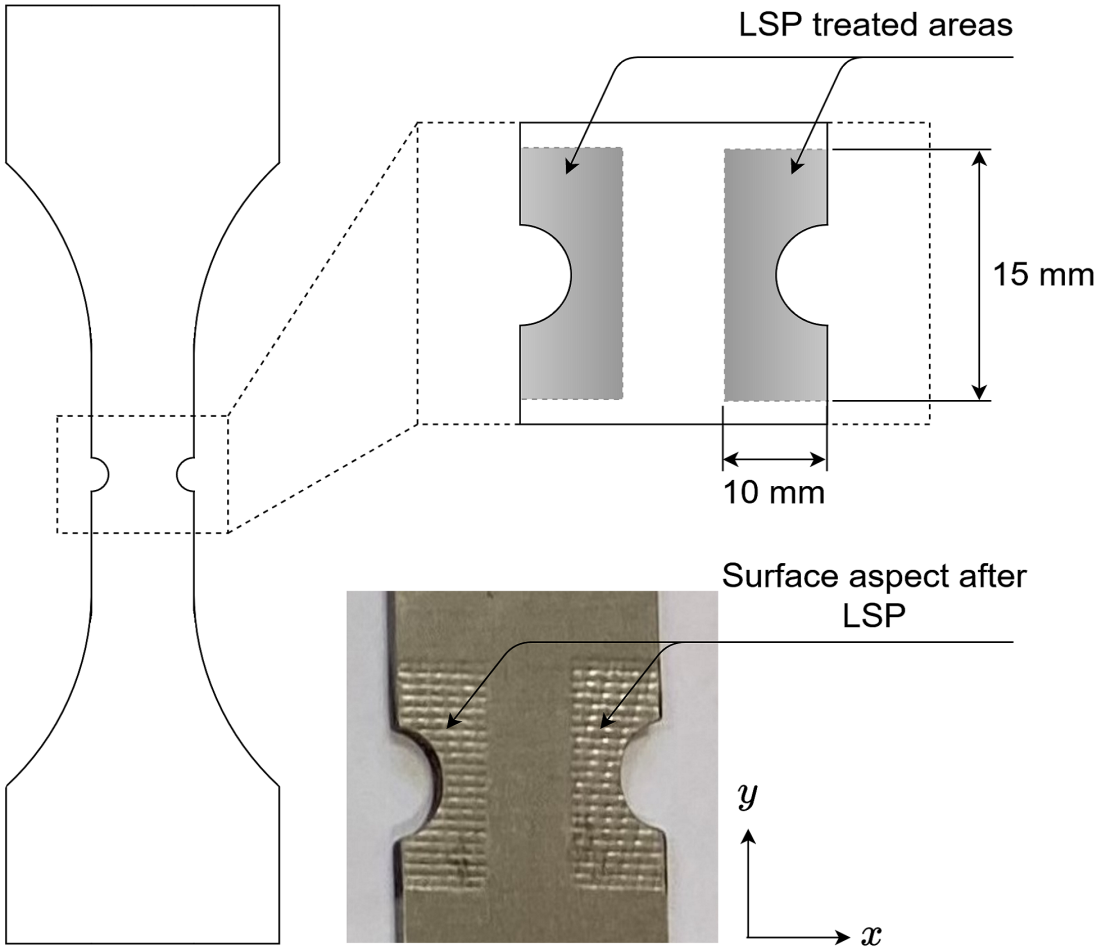


Figure 3.5: LSP treated zone in dogbone specimens.

Figure 3.6 shows the LSP treatment area in notched specimen (S-NS). LSP was applied on both sides of the specimen, in areas of 10×15 mm^2 located around the center double notch.

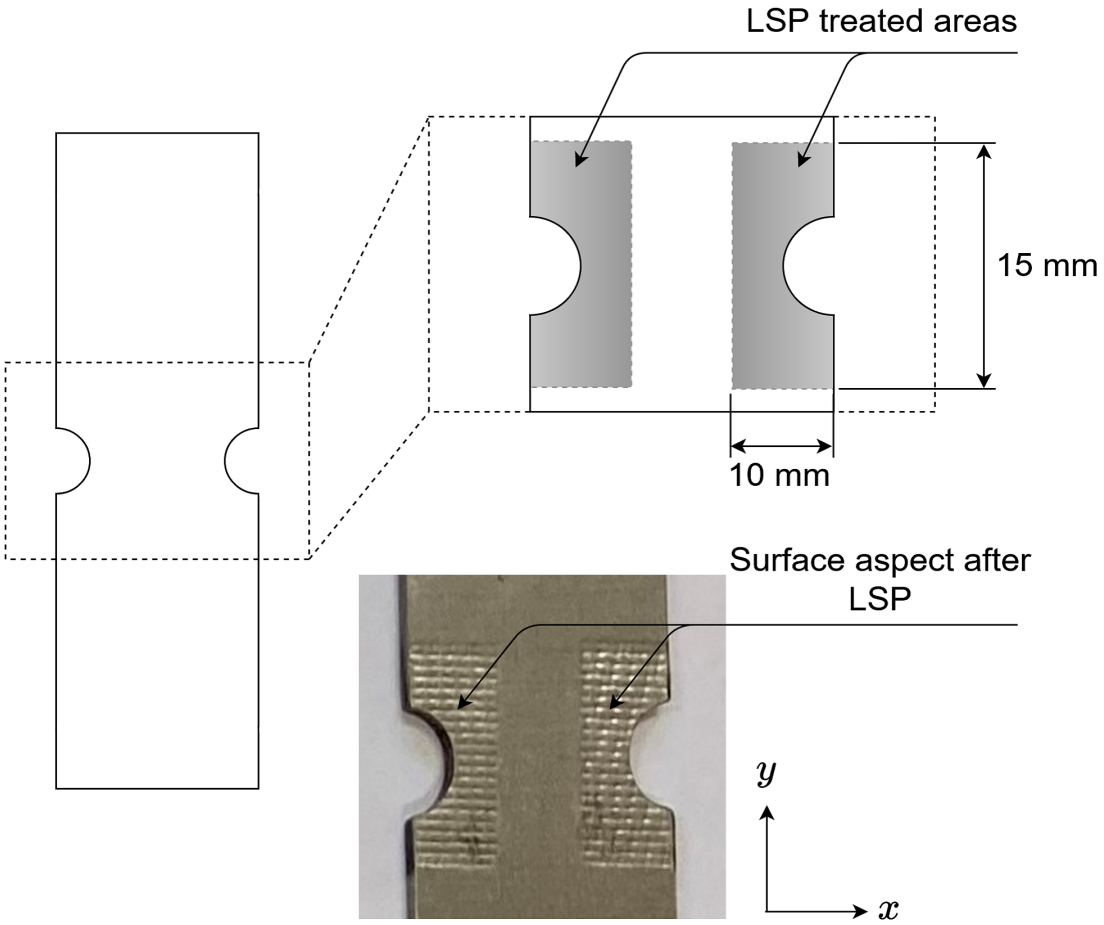


Figure 3.6: LSP treated zone in notched specimens.

Figure 3.7 shows the LSP treatment area in the disk specimen (S-DS). LSP was applied in a circular area with 25 mm radius. Only the testing side of the specimen was LSP treated.

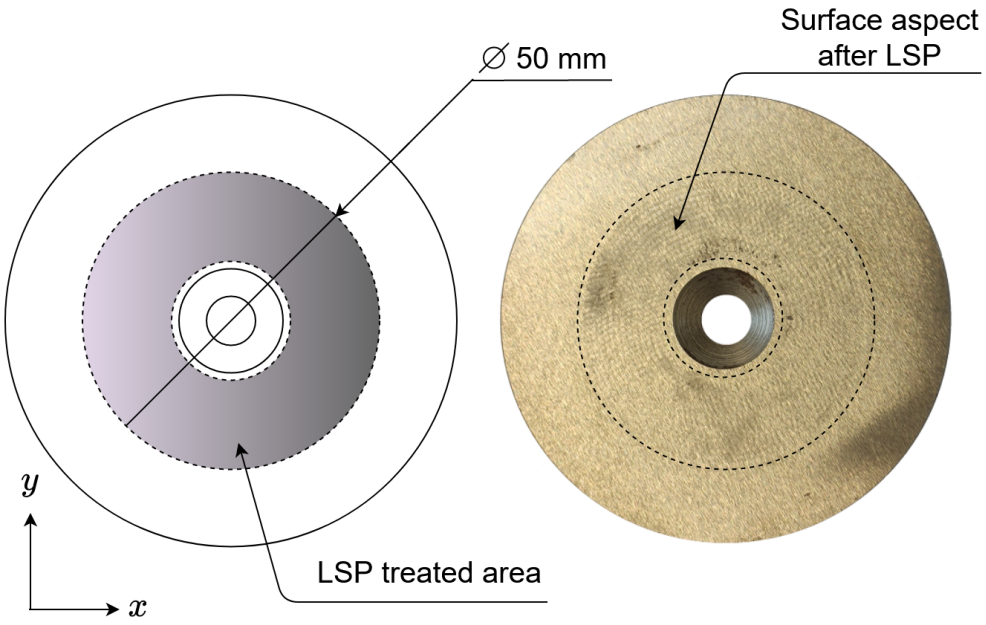


Figure 3.7: LSP treated zone in disk specimens.

3.4 Testing procedures

The following section provides a detailed description of all testing activities to verify the effectiveness of LSP treatment. Testing has been performed to assess the state of residual stress after LSP, measurement of surface roughness parameters, and microstructural observation. Further testing was conducted to assess the effects of LSP on the tensile properties, fatigue life, fatigue crack propagation, and wear resistance.

3.4.1 Residual stress

Residual stress is a key topic when discussing the application and effects of LSP. Residual stress can be defined as the stress distribution, present in a part or structure where no external load is applied (Schijve, 2009). Tensile residual stresses can adversely affect fatigue strength, whereas LSP induced compressive residual stresses may significantly improve the fatigue strength behaviour of a component. Thus, it is imperative to assess the stress state after the application of LSP. Quantifying residual stresses is a complex task because no direct measurement methods were available. However, residual stress can be calculated from strain relaxation measurements. The incremental hole-drilling strain measurement technique provides a fast and reliable technique to evaluate residual stress. Besides hole drilling, the contour method was also applied to assess the residual stress state in S-NS specimens.

3.4.1.1 ESPI hole-drilling

To estimate the effects of LSP on AISI D2 tool steel plate specimens (S-PLT), the residual stress profiles were calculated for each set of parameters and compared with the stress profiles in the untreated material. The residual stress states of the material were provided by a commercially available measurement system based on electronic speckle pattern interferometry (ESPI) and incremental hole drilling (PRISM, Stresstech), as shown in Figure 3.8.

To obtain in-depth stress profiles, it is required to establish several drilling steps as well as the distance between these steps. According to the integral method, used to calculate the residual stress (ASTM E837-13a, 2013), the calculated stress at each drilling step is dependent on the stress at each step up to that point. Consequently, the calculation of the residual stress profile is affected by the number of drilling steps. As a result, the effect of possible errors will be cumulative.

Given the above information, particular attention is required when establishing the number of drilling steps. On one hand, using many steps enhances the spatial resolution of the stress profile, but significantly affects the numerical conditioning of the residual stress calculation, leading to a greater error sensitivity. In turn, using fewer drilling steps decreases the sensitivity to calculation errors but also decreases the spatial resolution of the stress profile (Schajer, 2007). Therefore, the incremental drilling steps should be defined to reach a compromise between spatial resolution and error sensitivity.

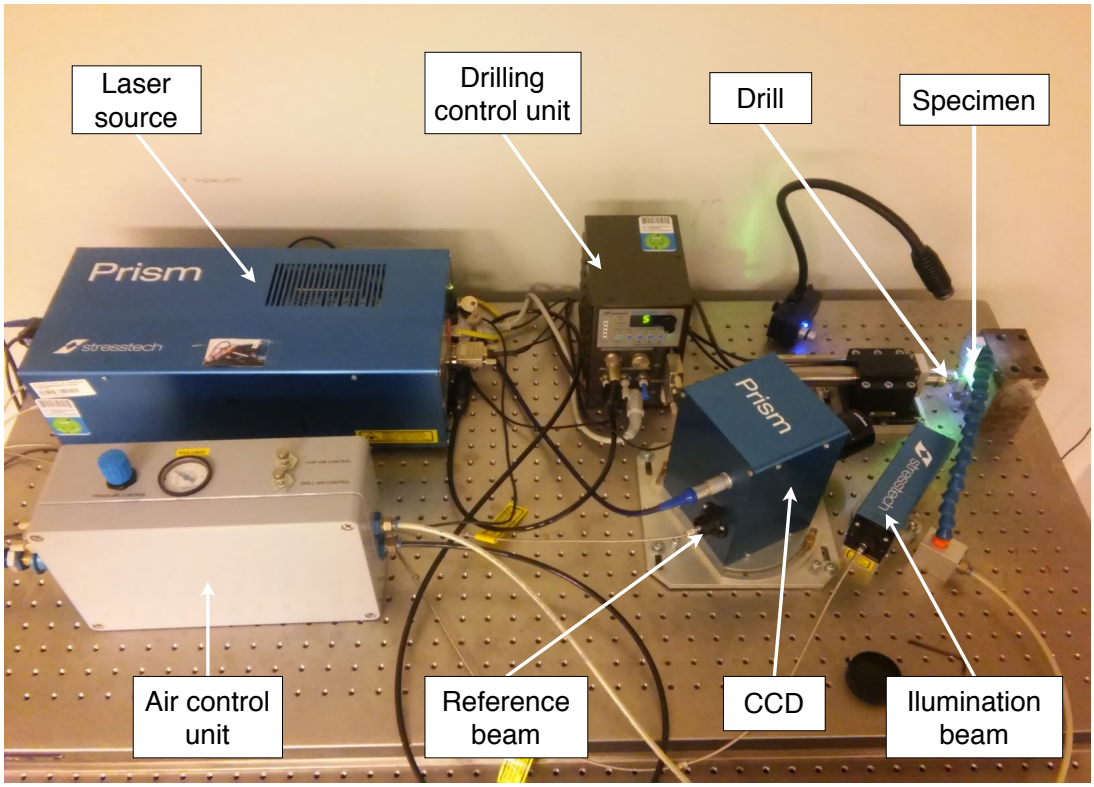


Figure 3.8: Prism measurement setup. Image courtesy of Department of Joining and Assessment in the Institute of Materials Research, Helmholtz-Zentrum Geesthacht.

Appropriate spatial resolution in the vicinity of the surface is desirable. As such, the adopted strategy for this work was to select a higher step density near the surface which decreased with increasing depth. This way, high spatial resolution is preserved in the zone of interest. ESPI measurements were carried out with a feed rate of 0.4 mm/s for a 2 mm hole diameter and total depth of 1mm. The residual stress depth profile was achieved by an iterative drilling procedure with variable depth steps. In total, 17 drilling steps were performed to calculate single in-depth stress profiles at steps of 0.025 mm down to 0.2 mm depth, 0.05 mm between 0.2 mm and 0.3 mm depth, and 0.1 mm from 0.3 mm to 1 mm depth. The measurements were repeated at least three times for each condition and the average results are presented. The residual stress components parallel (σ_{yy}) and perpendicular (σ_{xx}) to the laser scan direction were considered. Figure 3.9 shows an LSP treated specimen after the hole-drilling procedure. The base material measurement was performed on specimens that were not subjected to LSP treatment. The ASTM standard does not provide any recommendations for minimum spacing between adjacent holes. However, special care has been taken to ensure a distance between hole borders greater than three times the hole diameter to avoid/mitigate the influence of adjacent holes on the measurement results.

With more density of steps near the surface, the spatial resolution increases, enabling a better perception of the data trends as well as making errors easier to detect. For the analyzed specimens and following the procedure described in the standard test method ASTM E837-13a (2013), the computed stress is assumed to be uniform, i.e. high-stress variations between adjacent depth steps are negligible. As a result, large stress fluctuations between adjacent depth steps can be neglected, as they can represent errors, resulting in a uniform residual stress profile.

A standardized method for data smoothing with the integral method is the Tikhonov regularization, implying the implementation of a penalty function in the stress solution to minimize and

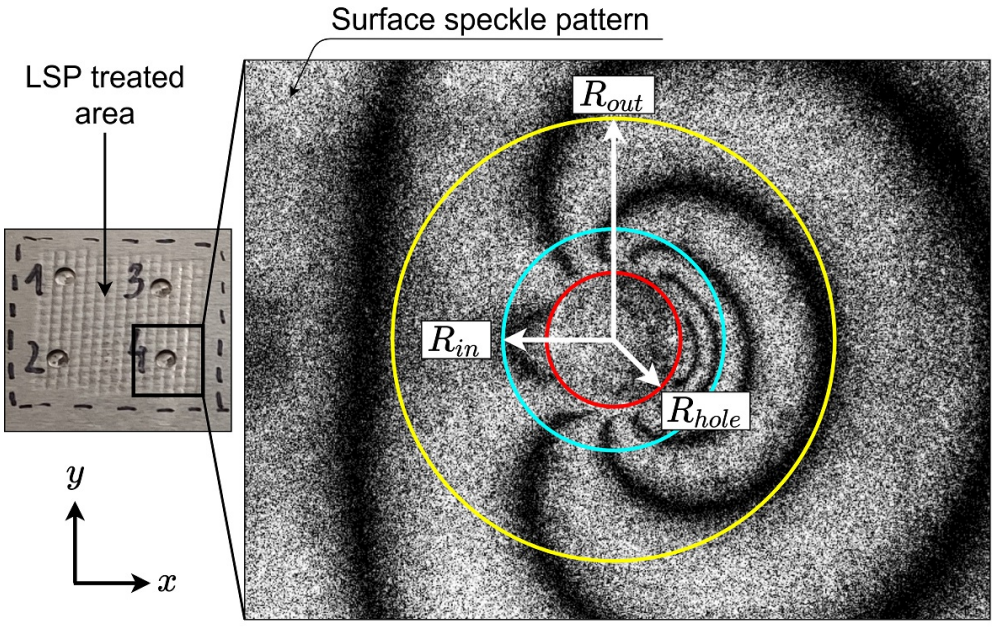


Figure 3.9: ESPI hole drilling measurement analysis area.

smooth the noise in the results (Tikhonov et al., 1995; Schajer, 2007; ASTM E837-13a, 2013). In this context, the Tikhonov regularization is a way to reduce/eliminate the multicollinearity errors of the multivariable linear regression that the PrismS software performs for the calculation of stresses with the Integral method. Good practice regarding the regularization has to minimize the distortion of the stress profile while removing most of the noise.

The strain measurements were performed within the area defined by two concentric circles around the hole. Figure 3.9 shows the area of analysis where R_{hole} is the radius of the drilled hole, R_{in} and R_{out} are the inner and outer radius of the analyzed area, respectively. Only the pixels within the area delimited by these two circles are analyzed. Particular attention is required as the size of the area of analysis can affect the results (Barile et al., 2014b). If the internal radius (R_{in}) is not large enough, the area around the hole boundary in which the plasticity effects occur as a result of the notching effect may be included in the calculation. Conversely, if the external radius (R_{out}) is too large, a region of very small deformations can be included, leading to inaccuracy in the residual stress results. Therefore, R_{in} and R_{out} were optimised using the measurement system software (PrismS), which complies with the standard ASTM E873. The material chips that are generated during the hole-drilling process can be a potential source of error when measuring strain using interferometry techniques. To prevent this issue, an compressed air nozzle was installed to allow easy extraction of the metal chips generated by the drilling process. Table 3.5 presents the residual stress analysis parameters used in PrismS software.

Table 3.5: Residual stress analysis info.

Parameters			
Material	AISI D2	Image height [pixels]	480
Poisson ratio	0.28	Hole radius [pixels]	60
Young's modulus [MPa]	190000	Hole diameter [mm]	2.0
Illumination alpha [°]	52	Inner integration radius [mm]	1.50
Camera alpha [°]	27	Outer integration radius [mm]	3.50
Image width [pixels]	640	Regularization	0.03

3.4.1.2 Contour method

The contour method was applied to calculate the residual stress state in BM and LSP treated specimens (S-NS). A full surface map of the residual stresses was obtained. The processing conditions evaluated here were 3J laser energy and pulse density of 200 pulses/cm^2. All the process steps are detailed in this section.

The specimens were cut using a FANUC $\alpha - C400iB$ EDM with a 0.25 mm diameter wire at a speed of approximately 2.5 mm/min. The specimens were tightly clamped on both sides of the cutting line. The cutting line was transversely defined in the laser scan direction (y) on both specimens, as shown in Figure 3.10. Both specimens were cut in the same way using the same cutting parameters and clamping configuration.

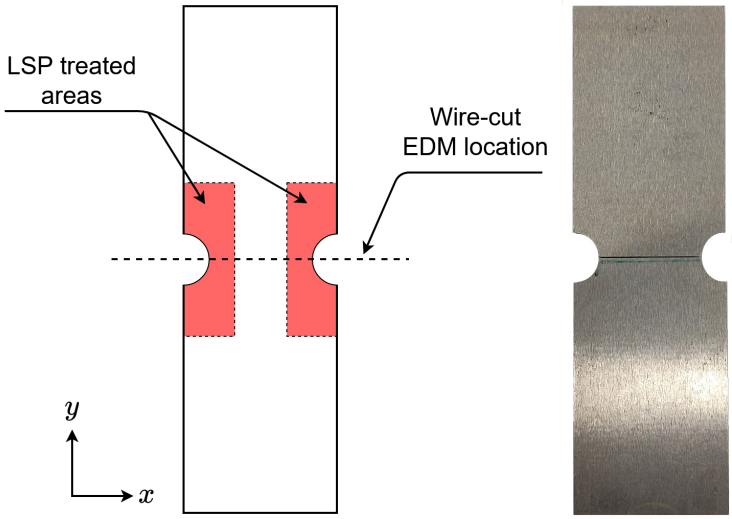


Figure 3.10: Location of extraction of the notched specimens (S-NS).

The cutting and surface measurement was performed at Quantal, S.A. A Mitutoyo CRYSTA-APEX S coordinate measuring machine (CMM) with a 1 mm diameter ruby tip was used for the measurements. Figure 3.11 shows the CMM measurement setup.

The cutting surface was measured to a distance of 0.1 mm from the side borders and 0.06 mm distance from the top and bottom borders. A total of 9898 points were acquired with high accuracy at a resolution of 1×10^{-4} mm. The distance between data points is 0.1 mm and 0.06 mm in the directions of width (x) and thickness (y), respectively. Figure 3.12a and 3.12b show the raw measured surface relaxation of the both halves of the BM notched specimen (S-NS). Figure 3.12c

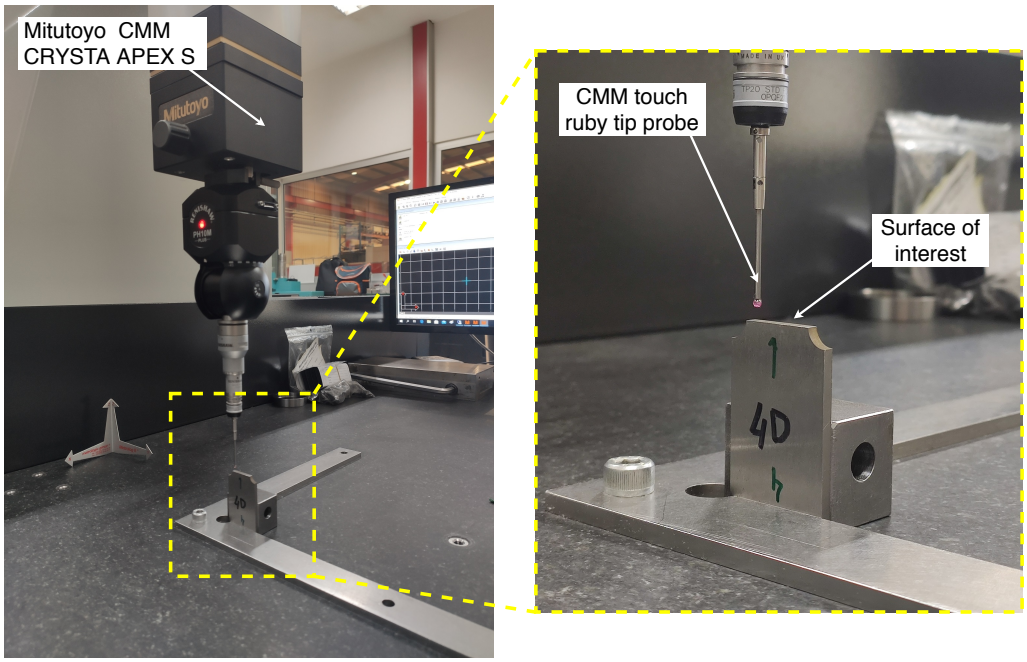


Figure 3.11: CMM surface measurement experimental setup.

and 3.12d show the raw measured surface relaxation of the both halves of the LSP treated notched specimen (S-NS).

Data conditioning was performed using MATLAB software through the following steps:

- Selecting the same origin for both specimen halves to map the measured points into the same data grid
- Aligning the most adequate plane through the centroid of all measured points into a horizontal plane through the origin
- Mapping the measured points to a rectangular grid
- Averaging of both interpolated surfaces
- Surface smoothing for noise reduction
- Writing the smoothed interpolated surface relaxation to the FEM mesh

A half linear elastic model of the S-NS specimen was modelled using FEM and the software Abaqus. Figure 3.13 shows the FEM mesh adopted. To improve simulation efficiency, the finite element mesh was refined only in the stress calculation zone. C3D6 elements (triangular prisms) were used in the test specimens in the coarse area, whereas C3D8R elements (rectangular prisms) were used in the refined area.

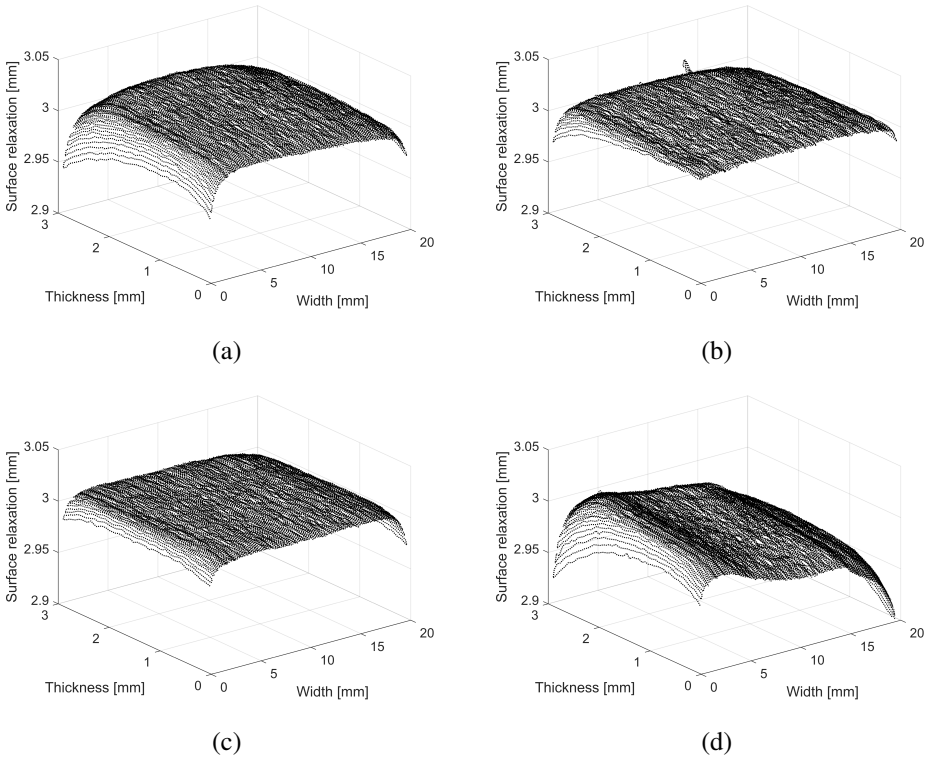


Figure 3.12: Raw measurement data (a, b) BM and (c, d) LSP treated specimen.

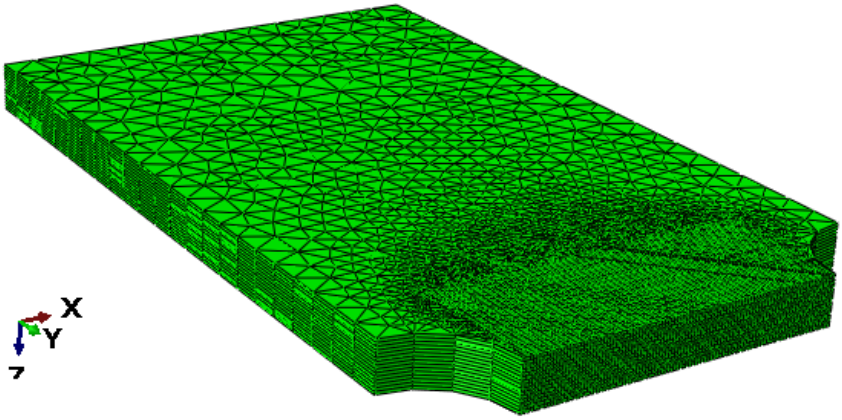


Figure 3.13: FEM mesh used for calculating the residual stresses.

3.4.2 Surface roughness parameters and topography

LSP is an advanced surface technique which involves the application and propagation of high-intensity shock waves on the target material leading to severe surface modifications. Plastic deformation leads to the wavy appearance of the target surface while material ablation resulting from the surface's interaction with high-energy laser radiation often increases the roughness.

The surface topography is quantified by different parameters according to ISO 4287 (1997) and ISO 4288 (1998). A widely used parameter in engineering applications is the average roughness, R_a, defined as:

$$R_a = \frac{1}{n}\sum_{i=1}^{n}|y_i| \tag{3.1}$$

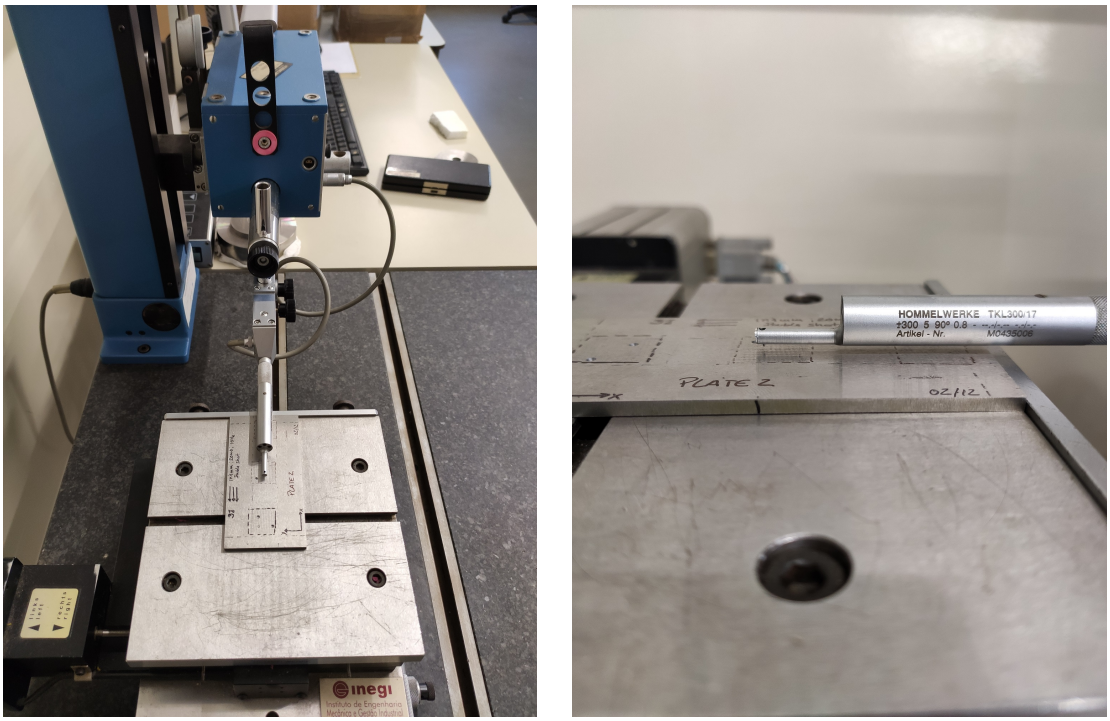
where y_i represents the distances from the mean line of n of points of the roughness profile, obtained by a surface normal section. The root-mean-square roughness, R_q, expresses the standard deviation of the surface heights distribution and is, therefore, an important engineering parameter used to characterize the surface roughness using statistical methods. This parameter is more sensitive than the average roughness, R_a, to large deviations from the mean line and, is defined as:

$$R_q = \sqrt{\frac{1}{n}\sum_{i=1}^{n}y_i^2} \tag{3.2}$$

The surface parameters of base material and LSP treated material were measured using a compact roughness measurement system Hommel Werke T8000. This system provides standard roughness parameters, surface waviness and irregularities. A Stylus Profilometer type Taster TKL 300/17 ($\pm$100 μm) was used for the measurement (see Figure 3.14).

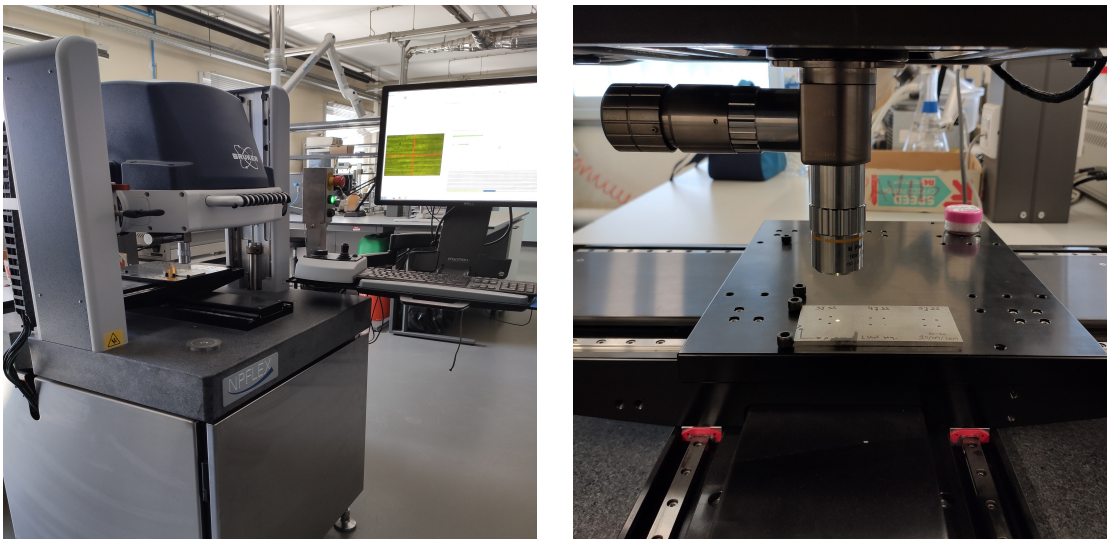
Four different positions were measured on plate specimens (S-PLT) transversely (90º) to the laser scanning direction for each set of parameters. Figures 3.14a and 3.14b show the measurement setup. The average results are presented. The arithmetic mean roughness (R_a), maximum height of the profile (R_z), root-mean-square roughness (R_q), average waviness (W_a), total waviness (W_t) and total height of profile (P_t) were measured for each condition applying a roughness filter *cut off* (λc) of 0.25 mm for a sample length of 12.5 mm in accordance with ISO 4287 (1997) and ISO 4288 (1998).

A non-contact Bruker NPFLEX 3D surface metrology system is used to measure the surface topography of the treated area. A border section between the LSP treated area and the base material was selected to highlight the effects of LSP parameters, specifically laser energy and pulse density, on the surface of the material. The measuring area is a 6 mm $\times$ 3 mm rectangle. All LSP and BM treatment conditions were measured. All results show a 95% or higher data acquisition, resulting in an excellent rendering of the surface. Three different views of each material condition are presented for easy comparison between results. Figures 3.15a and 3.15b show the non-contact 3D surface metrology system and a specimen plate surface topography measurement, respectively.



(a) (b)

Figure 3.14: Surface parameters measurement setup using the Hommel Werke T8000 system: (a) specimen orientation on the measuring system and (b) close-up of the measuring direction of the specimens using a Stylus Profilometer type Taster TKL 300/17.



(a) (b)

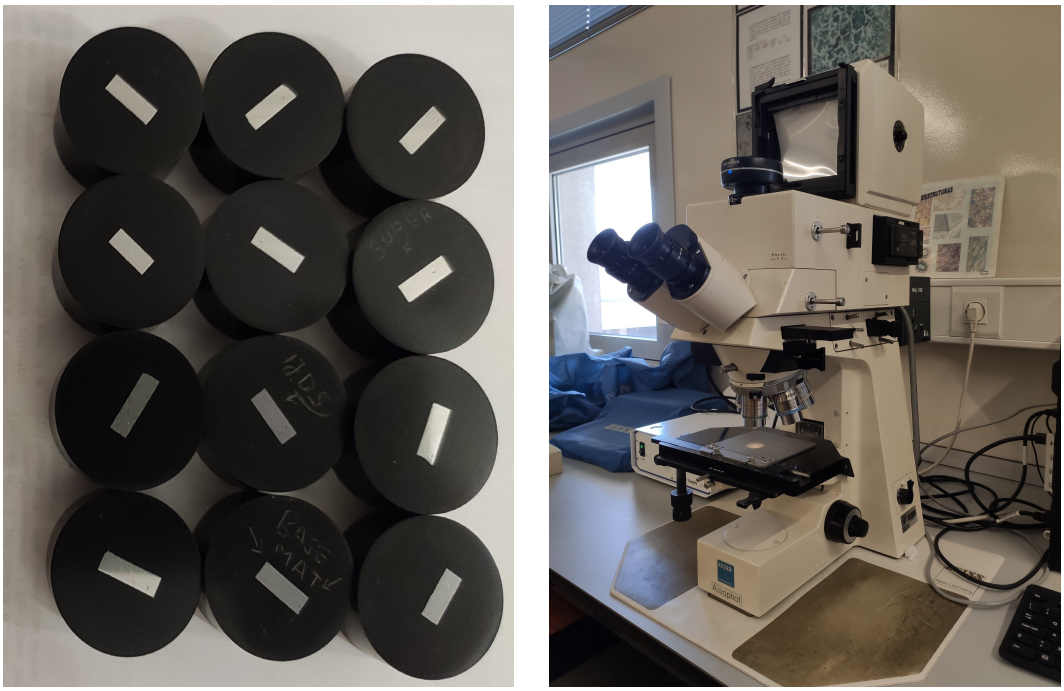
Figure 3.15: Non-contact surface measurement: (a) Bruker NPFLEX 3D surface metrology system and (b) specimen plate surface topography measurement.

3.4.3 Microstructure

Metallographic testing is essential to evaluate the microstructure of materials. As previously discussed, the high-strain rates caused by LSP can lead to microstructural modifications in a material, influencing physical properties such as strength, toughness, ductility, hardness or wear resistance. Therefore, the microstructural analysis of the AISI D2 tool steel before and after LSP treatment provide an insight into the effects of LSP in the material.

Microstructural analysis of LSP treated specimens and base material was performed by standard metallography and the microstructure was recorded by optical microscopy (OM). One BM specimen and ten LSP treated plate specimens (S-PLT) were sectioned transversely to the LSP scanning direction, mounted in a resin cylinder and subjected to several successive grinding and polishing steps. Figure 3.16a shows the specimens for microstructural observation. The most commonly used etchant for tool steels is nital (ethanol (C_2H_5OH)+nitric acid (HNO_3)). Generally, concentrations from 2 to 10% nital are suitable for most tool steels. In this work, the etching was performed by dipping the sample in the 2% Nital solution for 60 seconds at room temperature, followed by rinsing the sample with water and then drying. The microstructures of the specimens were characterized by optical microscopy using an Axiophot device from Zeiss (see Figure 3.16b). As the microscope has a vertical configuration, the sample has been levelled on a blade with clay so the polished surface remains perpendicular to the optical axis. The micro-structures of the base material specimens and LSP treated specimens were observed from the treated surface.

Further testing involved BM and LSP treated specimen characterization by electron backscatter diffraction (EBSD). EBSD data have been collected from near surface regions of BM and LSP treated specimens to provide evidence of surface induced changes in LSP. A detection area of 250



(a) (b)

Figure 3.16: (a) Resin mounted specimens and (b) optical microscope Zeiss Axiophot.

μm $\times$ 600 μm and a step size of 2 μm were selected. EBSD scans were performed at 25 kV using a FEI QUANTA 400 FEG ESEM scanning electron microscope running the EDAX PEGASUS X4M EBSD acquisition system. Figure 3.17b shows a schematic representation of EBSD scanning specimen direction. The EBSD data was analysed using the OIM Analysis^{TM} v5 software package distributed by EDAX.

It is important to clearly understand several concepts involved using the Orientation Imaging Microscopy software (OIM Analysis^{TM} v5), hereinafter designated as OIM. The material grains consist of sets of points (pixels) connected and similarly oriented through an algorithm used in OIM. For each point analyzed, the surrounding points are checked to assess whether they fall within the grain tolerance angle of the point in question. If a surrounding point lies within the tolerance angle, the neighbours of that point are checked to determine if they fall within the tolerance angle of that point. This procedure is repeated until the set of connected points (forming a grain) is delimited by points that exceed the tolerance angle concerning the surroundings.

Therefore, the user must specify the number of points required for a given set of points to qualify as a grain by setting a parameter designated "Minimum Grain Size" in pixels. Following the same principle, the tolerance angle should also be user-specified by the "Grain Tolerance Angle" parameter. Hence, the definition of grain in OIM may differ according to user-specified parameters. Based on the analysis of EBSD surface maps, the minimum grain size was set to 4 pixels and the grain angle tolerance was set to 5°. Furthermore, the grains located at the boundaries of the analyzed area were excluded to avoid misleading results. These analysis conditions were kept constant for all specimens.

For this microstructural analysis, the grain size was determined according to its diameter. The grain diameter is calculated by determining the area of grain and then assuming the grain to be circular. The grain shape aspect ratio was also considered in the present analysis. This ratio is defined as the length of the smallest axis divided by the length of the largest axis (see Figure 3.17a). The grain shape orientation is defined as the angle between the major axis of the ellipse (fitting the grain) and the horizontal direction, as shown in Figure 3.17a. The misorientation angle shows the distribution of the orientation difference of the grain boundaries.

The method applied by OIM for fitting the ellipse into the grains and for calculating grain size is presented as follows:

The distance, d_{ij}, between each endpoint of each boundary segment, x_i, y_i, is calculated:

$$d_{ij} = \sqrt{(x_i - x_j)^2 + (y_i - y_j)^2} \tag{3.3}$$

The maximum value of d_{ij} is assumed to be equal to the major axis length of the ellipse. The angle the major axis makes with respect to the horizontal direction, β, is expressed by:

$$\beta = tan^{-1}\left(\frac{y_j^{max} - y_i^{max}}{x_j^{max} - x_i^{max}}\right) \tag{3.4}$$

where x_i^{max}, y_i^{max} and x_j^{max}, y_j^{max} are the coordinates of the two boundary endpoints. The center coordinates of the ellipse are given as:

$$\bar{x} = \Sigma x_k \tag{3.5}$$

and

$$\bar{y} = \Sigma y_k \tag{3.6}$$

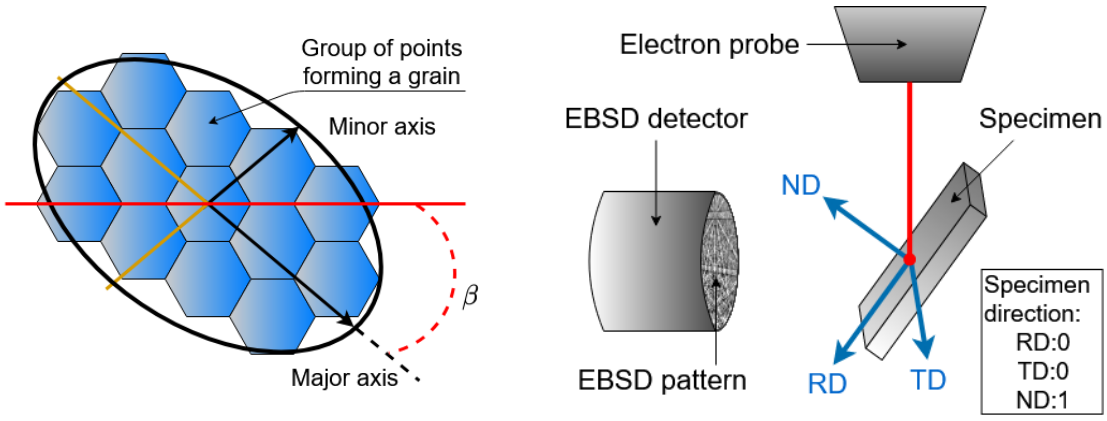
where x_k and y_k are the coordinates of all data points within the grain. In order to determine the minor axis length, it is necessary to transform the coordinates x_i, y_i into the reference frame of the ellipse as follows:

$$x_i' = (x_i - \bar{x})\cos\beta + (y_i - \bar{y})\sin\beta \tag{3.7}$$

$$y_i' = (x_i - \bar{x})\sin\beta + (y_i - \bar{y})\cos\beta \tag{3.8}$$

Finally, the minor axis length can be calculated as follows:

$$b = \frac{1}{N}\sum_{i=0}^{N}\sqrt{\frac{y_i'^2}{\left(1 - x_i'^2/a^2\right)}} \tag{3.9}$$



(a) (b)

Figure 3.17: Schematic representation of (a) calculation concept for the grain size, grain aspect ratio and grain orientation and (b) EBSD scanning specimen direction.

3.4.4 Micro hardness

Work-hardening effect is a key factor for the fatigue performance of treated material. Therefore, micro hardness of LSP treated samples are measured. Transverse cross-sections of LSP treated specimens and base material were used for micro hardness examination. Due to the relatively low hardness of the soft-annealed AISI D2 tool steel, the Vickers hardness scale is an adequate option to represent the micro hardness results.

The micro hardness measurement procedure involves the application of a load to the target surface through an indenter. After removal of the test load, the lengths of the two diagonals of the projected area of the indentation are measured, and the arithmetic mean is used to calculate the Vickers hardness number. Hence, the Vickers hardness is proportional to the test load applied to the Vickers indenter divided by the surface area of the permanent indentation, which is assumed to be a square-based pyramid with a vertical angle similar to the indenter. Such a relationship can be defined by Equation 3.10 (ASTM E92-17, 2017):

$$HV = \frac{F}{A} = \frac{2F\sin(\frac{\alpha}{2})}{d^2} \approx 0.1891\frac{F}{d_V^2} \tag{3.10}$$

where α is the face angle of the diamond indenter equal to 136°, F is the load (N) and d_V is the mean Vickers indentation diagonal length (mm).

The BM and LSP treated plate specimens (S-PTL) were sectioned using a refrigerated cutting saw (Struers Labotom-15). The samples were assembled into resin specimens and subjected to several successive steps of grinding and polishing. A total of eleven specimens were prepared, ten specimens for LSP treated material with different parameters and one BM specimen. Four micro hardness profile measurements were performed on each specimen. The micro-hardness profile was traced from the surface to a maximum depth of 1.5 mm. The Vickers micro hardness of all the tested specimens was determined by a digital micro hardness tester Matsuzawa MXT70 (see Figure 3.18a) under an applied load of 0.981N ($HV_{0.1}$) and a dwell time of 15s. The procedure

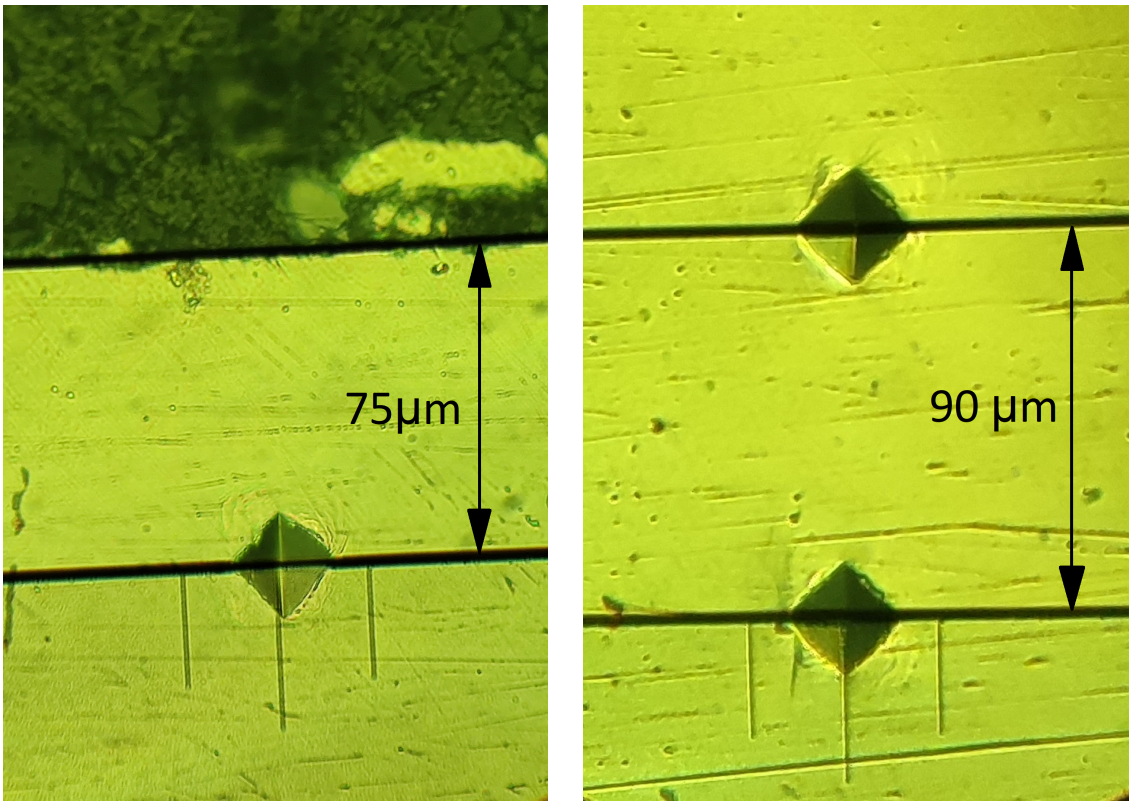
is in accordance with ASTM E92-17 (2017). Special care was devoted to ensuring the proper levelling of the samples. To achieve this, samples were evenly and firmly compressed on top of clay as can be seen in Figure 3.18b.

Several indentations are required to achieve the micro hardness profile. Hence, it is important to guarantee sufficient spacing between indentations to avoid the interference of adjacent indentations. The minimum spacing between indentations was defined as recommended in the standard ASTM E92-17 (2017). The gap between adjacent indention centres was not less than 3 times the largest of the average diagonals of these two indentations. Additionally, the distance from the centre of an indentation to the specimen edge (surface) was greater than or equal to 2.5 times the average diagonal of the indentation. Several indentations were performed to determine the average of the largest diagonal. The value used as reference was 30 μm. Hence, the distance between the center of indentation and the surface was set at 75 μm (see Figure 3.19a) and 90 μm for distance between adjacent centers (see Figure 3.19b).



(a) (b)

Figure 3.18: (a) Vicker's micro harness measurement setup and (b) levelling of the sample during measurement .



(a) (b)

Figure 3.19: (a) Gap between indentation centre and surface, and (b) gap between adjacent indentations.

3.4.5 Tensile testing

Tensile testing is one of the most widely performed tests for material characterization since it provides important information on some well-known parameters, such as yield strength and ductility of materials under uniaxial tensile stress. Such information is useful to compare the tensile properties of BM and LSP treated specimens. Furthermore, tensile testing also provides useful information regarding stress levels for conducting fatigue testing. These tests are quick, inexpensive, and readily available, making them a great option to start material characterization.

Tensile tests were performed at Helmholtz-Zentrum Geesthacht, using a digitally controlled electro-mechanical Zwick 1484 testing machine ($\pm$ 200 kN). The tests were conducted at room temperature with 10 kN applied load and displacement rate of 0.5 mm/min in compliance with ASTM E8M (2016). A video extensometer was used to measure strain in tensile tests. A 50 mm gauge length was analyzed according to Figure 3.20. A total number of six dogbone specimens (S-DB) were tested, equally divided into two groups of BM and LSP treated specimens. Figures 3.21 and 3.22 show BM and LSP treated specimens after tensile testing, respectively.

From the data obtained during the tensile test, the engineering stress and strain were calculated and plotted into a typical stress-strain plot.

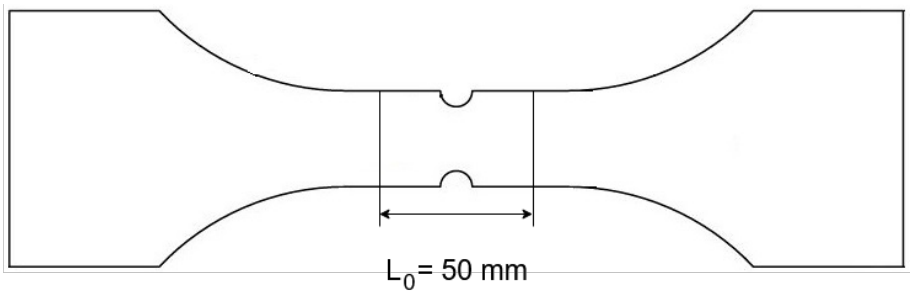


Figure 3.20: Dogbone specimen gauge section representation.



Figure 3.21: BM dogbone specimens (S-DB) after tensile testing.



Figure 3.22: LSP treated dogbone specimens (S-DB) after tensile testing.

3.4.6 Fatigue testing

Typically, metal fatigue testing provides valuable information regarding the material quality and design to extend the service life of parts and components. Fatigue testing is conducted to estimate the service life through cyclic loading simulation and the knowledge of the limits of cyclic loading that a part can withstand is helpful to prevent catastrophic failures during service. In the context of this work, fatigue testing will determine whether the application of LSP using the given parameters can extend the service life of AISI D2 tool steel components.

Fatigue tests were performed on BM and LSP treated dogbone specimens (S-DB) at room temperature under controlled load conditions. Tests were carried at Helmholtz-Zentrum Geesthacht using a servo-hydraulic Schenk Hydropuls-testing machine ($\pm$ 100 kN), according with ASTM E466-15 (2015) standards, using a sinusoidal waveform. The test setup is presented in Figure 3.23.

The applied loads were selected to cover low and high cycle fatigue regimes under controlled stress engineering mode. Fatigue tests were conducted at a 20 Hz frequency using a constant stress ratio, R = 0.1. The stress amplitude used for the fatigue tests is in the range 200 - 550 MPa, which exceeds the base material yield strength (470 MPa). Several fatigue tests have been carried out to determine the stress required to cause fatigue run-out (10^7 cycles) at low-stress amplitudes. After fatigue testing, the fractured surfaces were observed by scanning electron microscope (SEM). To provide statistically relevant data, a total of 19 specimens have been tested, divided in two sets, corresponding to nine LSP treated specimens and ten BM specimens. Figures 3.24 and 3.25 show part of the BM and LSP treated specimens after fatigue testing, respectively.

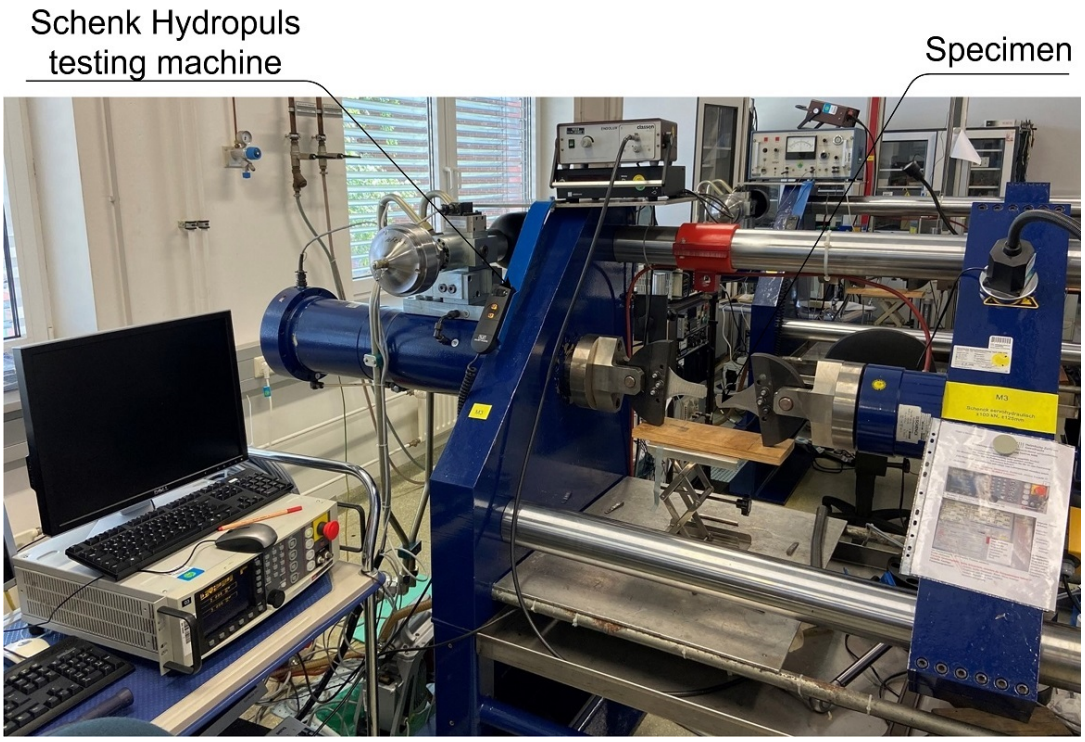


Figure 3.23: Fatigue testing setup. Schenk Hydropuls-testing machine.

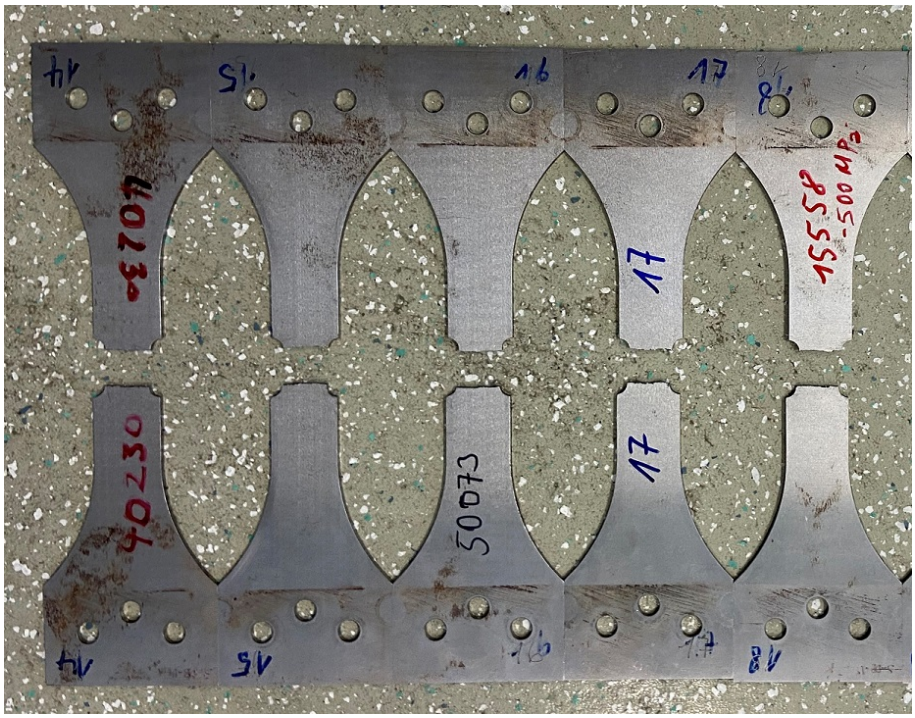


Figure 3.24: BM specimens (S-DB) after fatigue testing.

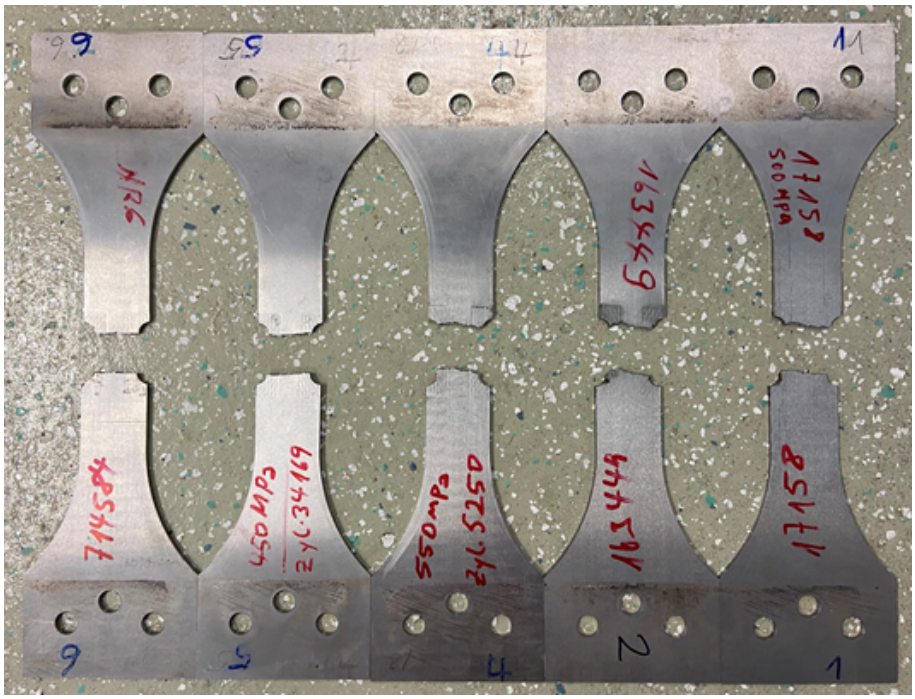


Figure 3.25: LSP treated specimens (S-DB) after fatigue testing.

3.4.7 Fatigue crack propagation

It is well established that fatigue cracking is a progressive failure resulting from cyclic loading, which is below the yield strength of the material, causing the onset of a crack that propagates in the material (Perez, 2004). The testing procedure involves cyclic loading of notched specimens that were previously cracked. The crack size (a) is determined as a function of the fatigue cycles (N) which can be analyzed to determine the crack growth rate. Crack growth rate (da/dN) is expressed as a function of the stress intensity factor (SIF) range, ΔK, which can be calculated from linear elastic stress analysis. Hence, da/dN vs ΔK characterizes the material resistance to stable crack extension under cyclic loading, and provides results regardless of geometry, thus allowing comparison of results from different specimen configurations and loading conditions (ASTM E647-08, 2008).

The relationship between the SIF range, ΔK, and the fatigue crack growth, da/dN, can be expressed through Paris law, given by Equation 3.11 (Paris and Erdogan, 1963):

$$\frac{da}{dN} = C\left[\Delta K(a)\right]^m \tag{3.11}$$

where a is the crack length, N is the number of load cycles and ΔK is the stress-intensity factor range defined by Equation 3.12. C and m are material constants and can be obtained through correlation with experimental results.

$$\Delta K = K_{max} - K_{min} \tag{3.12}$$

where K_{max} and K_{min} are the maximum and minimum stress intensity factor, respectively.

The number of loading cycles N needed to propagate the crack from the initial crack length a_0 up to the final crack length a can be provided, in the zone of uniform fatigue crack growth, by integrating Equation 3.11 (Perez, 2004):

$$\int_0^N dN = \frac{1}{C}\int_{a_0}^{a} \frac{da}{\left[\Delta K\,(a)\right]^m} \tag{3.13}$$

The SIF for a middle-crack-tension M(T) specimen, with specific crack configuration, is analytically expressed by Equation 3.14 (ASTM E647-08, 2008):

$$\Delta K = \frac{\Delta P}{B}\sqrt{\frac{\pi\cdot\alpha}{2\cdot W}\cdot sec\frac{\pi\cdot\alpha}{2}} \tag{3.14}$$

where ΔP is the difference in loading range, α is an auxiliary value (Equation 3.15), B and W are the specimen's thickness and width.

$$\alpha = \frac{2a}{W} < 0.95 \tag{3.15}$$

Fatigue crack propagation testing was performed for BM and LSP treated middle-tension M(T) specimens (S-MT) using a Schenk Hydropuls servo-hydraulic testing machine. Figure 3.28 shows the experimental setup at the Helmholtz-Zentrum Geesthacht. M(T) specimens were prepared in

compliance with the standard ASTM E647-08 (2008). A 5 mm notch ($2a_0$) was generated by EDM before the application of LSP. The specimens were LSP processed on both sides in a 10×15 mm^2 area at a distance of 2 mm from the notch tip, as shown in Figure 3.4.

Four LSP treated specimens (LSP1, LSP2, LSP3 and LSP4) and one BM specimen were tested at room temperature, at a maximum loads of 18.7kN (BM, LSP1 and LSP2), 28.5 kN (LSP4) and 37.4 kN (LSP3), and frequency of 5 Hz. The load profile is a sinusoidal waveform with a load ratio of R = 0.1. BM, LSP1 and LSP2 specimens were tested with a stress intensity factor range of ΔK = 10 MPa$\sqrt{m}$, as below this value fatigue crack growth proceeds slowly (Stage I) (Perez, 2004). However, as no crack growth was observed in the LSP treated specimens LSP1 and LSP2, ΔK had to be increased to ΔK = 30 MPa$\sqrt{m}$ (max. load of 56.1 kN) after 8.06×10^6 and 3.17×10^6 load cycles for LSP1 and LSP2, respectively. Additionally, testing of LSP treated specimens LSP4 and LSP3, with stress intensity factors range of ΔK = 15 MPa$\sqrt{m}$ and ΔK = 20 MPa$\sqrt{m}$ were carried, respectively.

All specimens were slightly polished where the crack is expected to grow in order to visualize the experiments using an optical microscope, but ensuring the polishing does not influence the material behaviour. The cycles to failure and the crack tip displacements were recorded during experiments. Crack opening displacement (COD) gauges with knife edges and a microscope were installed to determine the crack length during experiments, as shown in Figure 3.27. Figure 3.28 shows the crack development during testing. The measured data was processed and plotted to obtain crack growth test results.

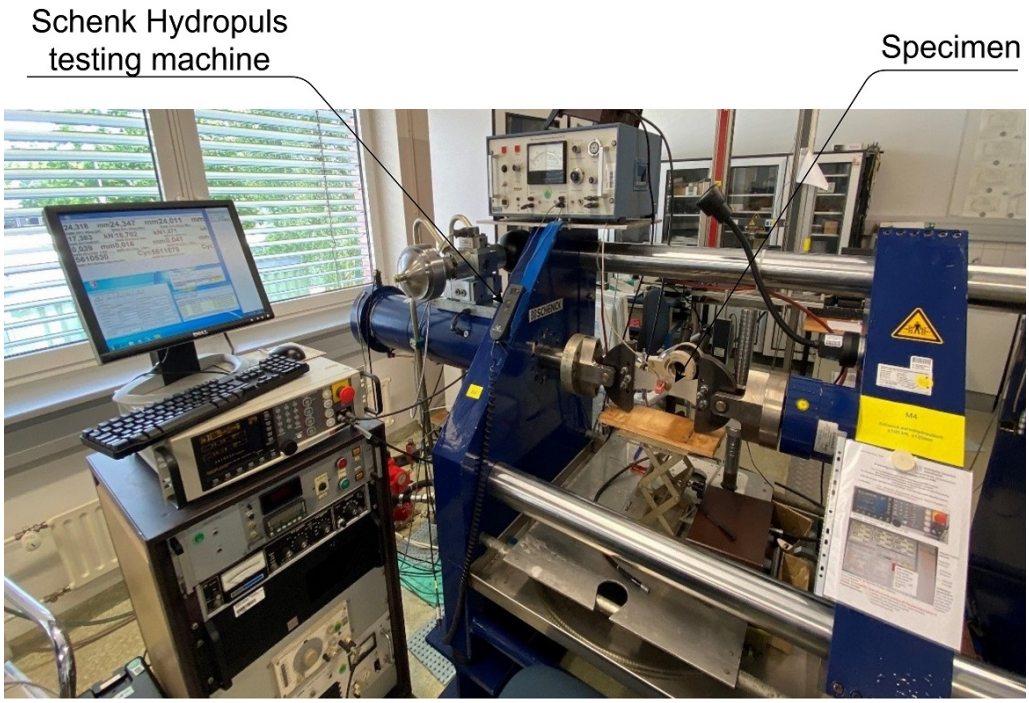


Figure 3.26: FCP test setup.

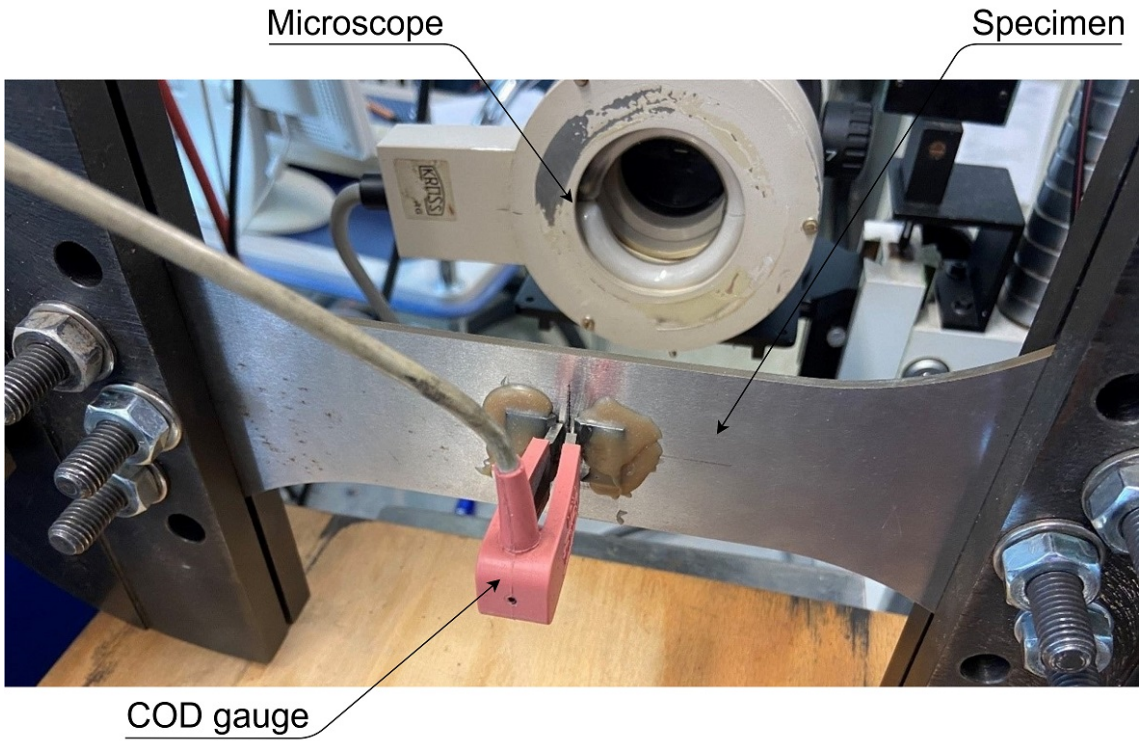


Figure 3.27: COD gauge and microscope setup.

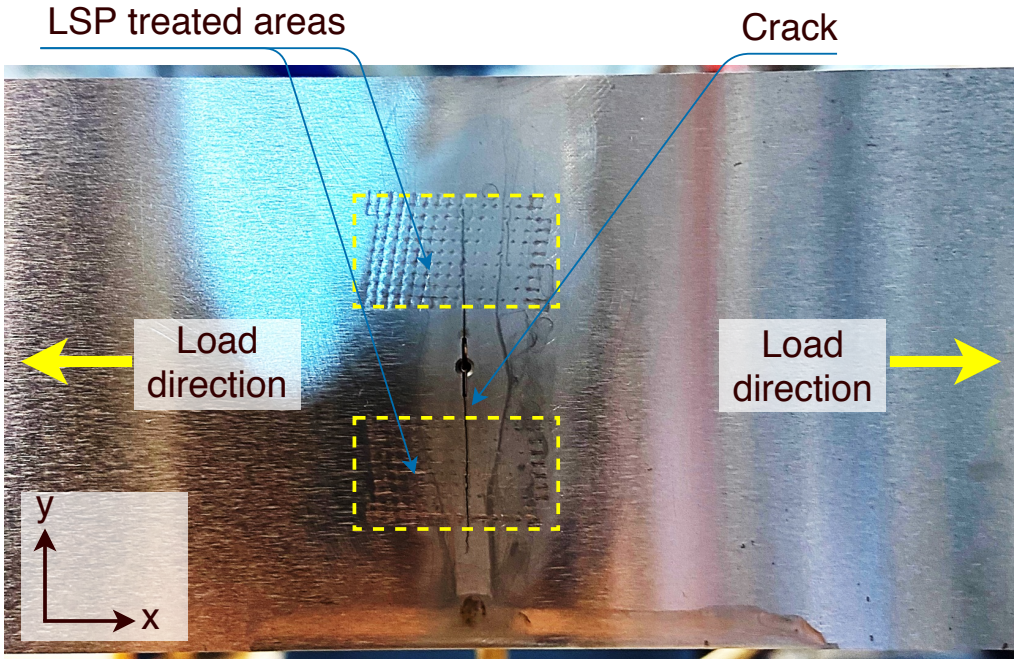


Figure 3.28: M(T) specimen during FCP testing.

3.4.8 Wear testing

As previously discussed in Chapter 2, the application of LSP can effectively improve wear resistance of metals. For this reason, wear testing was performed to evaluate the potential benefit of LSP under the given parameters in wear resistance behaviour of AISI D2 tool steel. It should be noted that no specific unit exists to describe wear resistance. However, the inverse of volume loss can be used as a relative wear resistance metric. Alternatively, the wear resistance can be quantified through the ratio of the wear volume loss of the base material over that of the LSP treated material. As part of this work, wear losses, wear rate and specific wear rate were evaluated on BM and LSP treated specimens. Wear generated on the pin was disregarded. For the present work no numerical value of wear resistance was attributed, but rather a qualitative evaluation by comparing volume losses, wear rate and specific wear rate.

The wear properties of BM and LSP treated specimens were investigated using a pin-on-disk apparatus. The procedure is in accordance with ASTM G99-17 (2017) using a Cameron Plint-TE67/7771 tribometer. For the pin-on-disk wear testing, a steel ball (AISI 52100 bearing steel) placed perpendicular to a flat circular specimen (S-DS) (Appendix A.4) is used. The testing machine rotates the disk specimen at a controlled speed of 575 RPM whereas the steel ball remains stationary. The steel ball is held against the disk specimen under a constant load of 10 N. Surface hardness tests were previously performed and hardnesses of 220.4 $\pm$ 6 HB for BM and 248.7 $\pm$ 7 HB for LSP treated material were measured. Wear testing was performed at room temperature under dry sliding conditions, and components were cleaned before testing. The sliding wear track is a circle on the surface of the disk specimen with a radius of 19 mm, resulting in a linear velocity of 1.14 m/s. The apparatus shown in Figure 3.29 enables evaluation of the wear properties of BM and LSP treated specimens under pure sliding conditions. According to the ball on a flat plane contact configuration, and the parameters used in the test (Table 3.6), an initial maximum Hertzian contact pressure of 828.6 MPa and maximum shear stress of 260.7 MPa were estimated.

Wear volume was evaluated by measuring the profile of wear track along the radial direction in three different positions (120º), using a surface profiler Stylus profilometry Hommel Werke T8000, as shown in Figures 3.30a and 3.30b.

Table 3.6: Hertzian contact stress calculation parameters.

Parameters	Steel ball (AISI 52100)	Disk specimen (AISI D2)
Poisson's ratio	0.3	0.28
Elastic modulus [GPa]	210	190
Diameter [mm]	12.7	infinite
Load [N]	10	

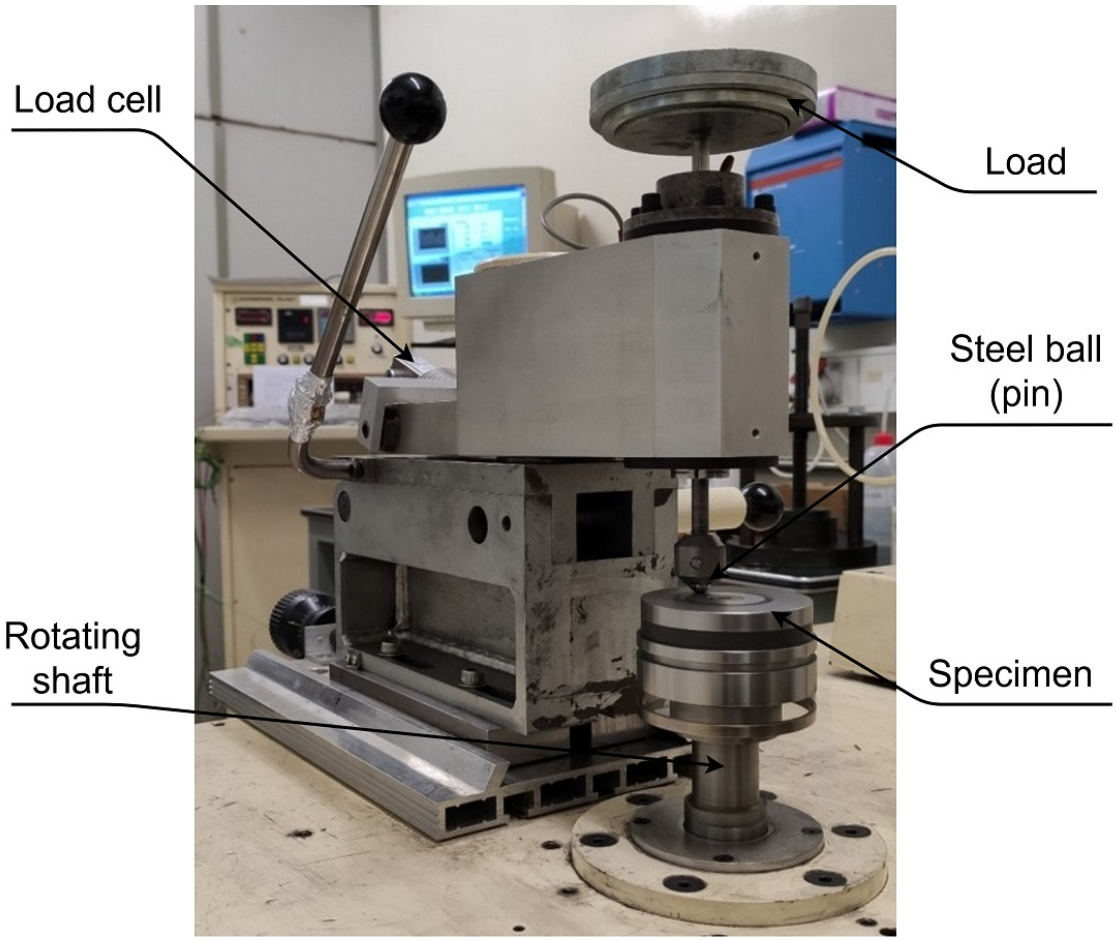


Figure 3.29: Pin-on-disk wear testing apparatus.

The average cross-sectional area of the wear track was then estimated and the wear volume loss was obtained by multiplying the cross-sectional area by the circumferential length of the wear track, as follows:

$$V_i = A_{profile} \times P_{circ} \tag{3.16}$$

where V_i is the volume loss, $A_{profile}$ the average cross-sectional area of the wear track and P_{circ} the circumferential length of the wear track. The V_i is given in mm^3.

The wear track profile measurements were performed after 1800 cycles, followed by 3600 cycles and then at intervals of 34500 cycles up to 207000 total cycles, totalling 6h of testing. The same conditions were applied for both BM and LSP treated specimens. All the measurement steps according to the number of wear cycles and sliding distance are presented in Table 3.7.

The wear generated during this test is prone to increase with sliding distance, and thereby with time. The calculated wear rate can then be defined as the material volume loss per unit sliding distance, and is expressed as follows (Hutchings et al., 2007).

$$W = \frac{V_i}{s} \tag{3.17}$$

Table 3.7: Wear measurement steps according to the number of cycles.

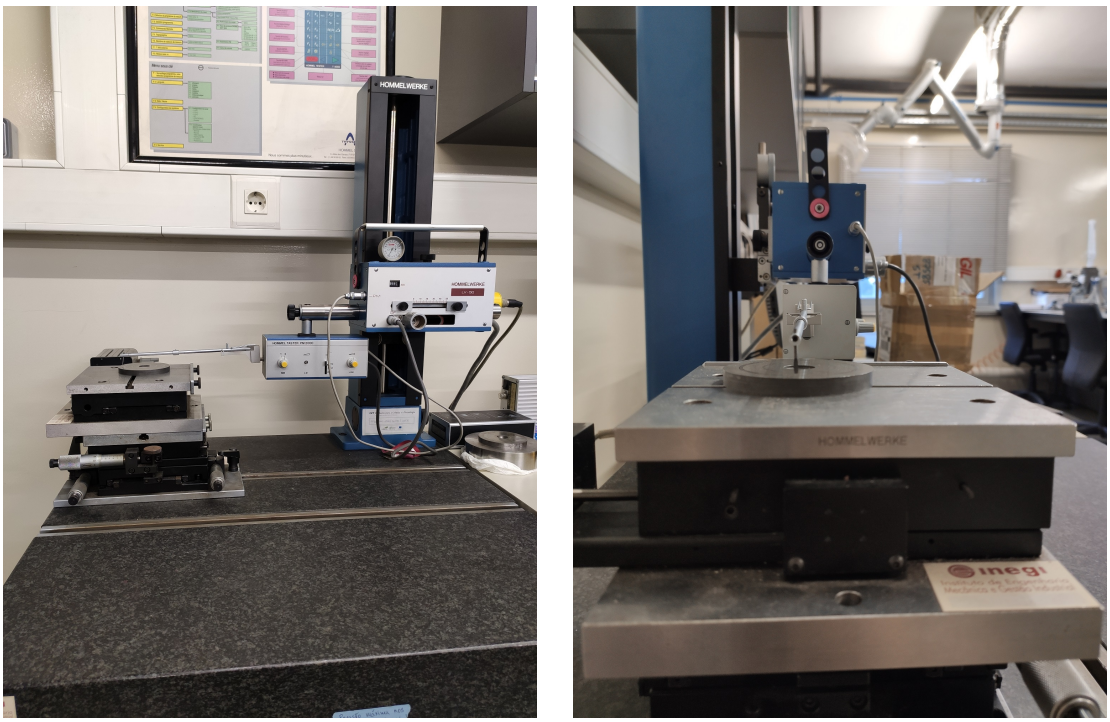
Measurement step	1	2	3	4	5	6	7	8
Wear cycles	1800	3600	34500	69000	103500	138000	172500	207000
Sliding distance [m]	214.89	429.77	4118.64	8237.29	12355.93	16474.58	20593.22	24711.87

where V_i is the volume loss, and s the the sliding distance. The W is given in mm^3/m.

A simple and useful model for comparing wear rates and material behaviour under different conditions is given by the Equation 3.18 (Archard, 1953).

$$V_i = k_i \frac{F \times s}{H} \tag{3.18}$$

where F is the normal load, s the sliding distance, H is the hardness of the softest contacting surfaces, V_i the volume loss and k_i the specific wear rate coefficient. The k-value is given in mm^3/Nm.



(a) (b)

Figure 3.30: Measurement setup of the wear tracks in disk specimens (S-DS).

Chapter 4

Results & discussion

4.1 Introduction

This chapter presents and discusses the results obtained throughout this work. The effects on the AISI D2 tool steel are characterised according to the LSP parameters adopted. The findings comprise the material residual stress state, surface and microstructure modifications, tensile properties as well as fatigue and wear behaviour.

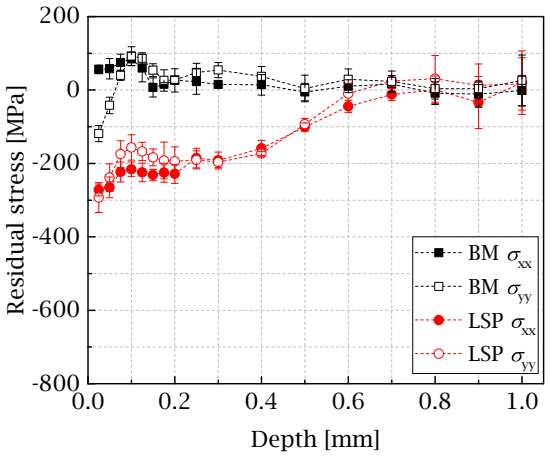
4.2 Residual stress field analysis

The residual stress profile, peak residual stress and the effects on the affected material depth were investigated. The present study provides reliable experimental data on the LSP ability to generate a uniform and compressive residual stress field at a significant depth across the workpiece. Additionally, this characterization provides an assessment of the impact of the process parameters on overall LSP performance.

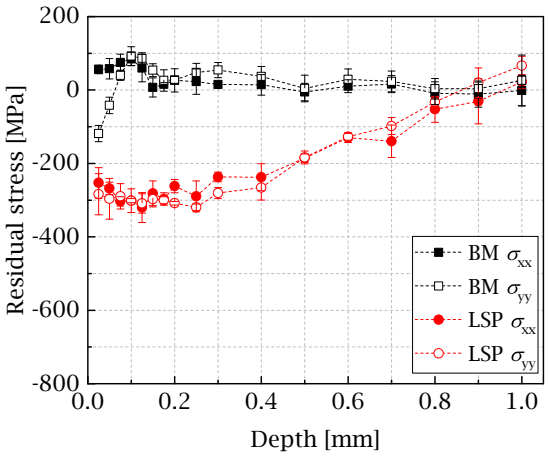
4.2.1 ESPI hole drilling residual stress measurements

In the present study, different levels of laser energy and laser pulse density were studied. Based on LSP process parameters adopted for this work, the calculation of the power density has resulted in values of 5, 10, 15, 20 and 25 GW/cm^2 for a laser energy of 1, 2, 3, 4 and 5J, respectively. The ESPI hole-drilling strain measurements were repeated a minimum of three times for each LSP treatment condition. The average residual stress values are presented in this section. All measurements reported below were performed on the plate specimens (S-PLT). The specimen geometry is shown in Appendix A.1.

Figures 4.1 to 4.5 show the in-depth residual stress profile for laser energy levels of 1, 2, 3, 4 and 5J, respectively. Each plot presents the residual stress distribution according to laser pulse density (100 and 200 pulses/cm^2), and transverse (σ_{xx}) and longitudinal (σ_{yy}) stress direction. Additionally, the BM residual stress profile is plotted with the results for each LSP treatment condition, for the purpose of facilitating the comparison of results.

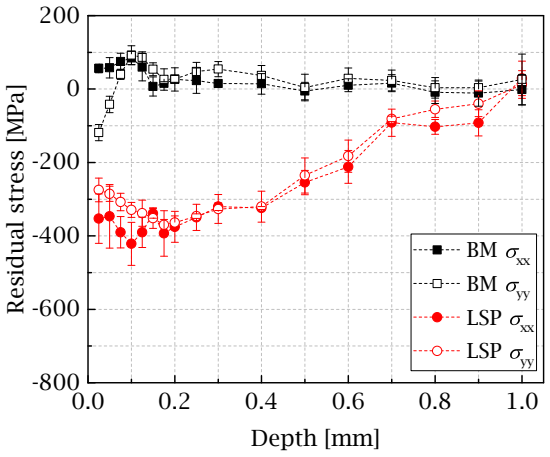


(a) 100 pulses/cm^2.

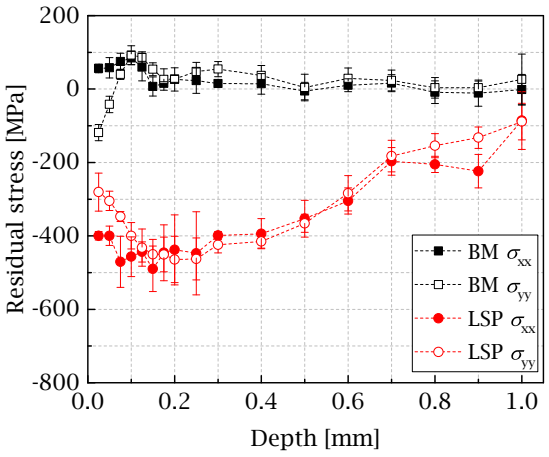


(b) 200 pulses/cm^2.

Figure 4.1: Residual stress profile of BM and LSP 1J: (a) and (b) 200 pulses/cm^2.

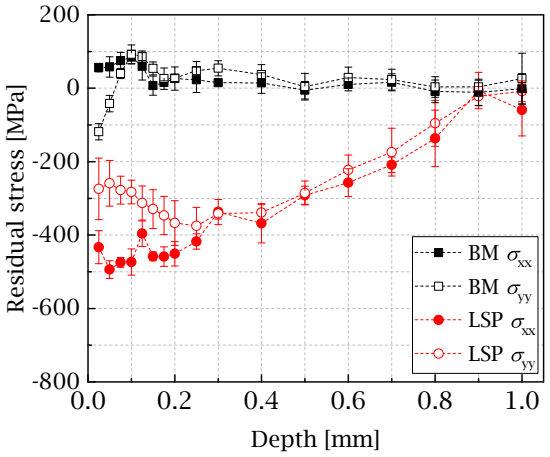


(a) 100 pulses/cm^2.

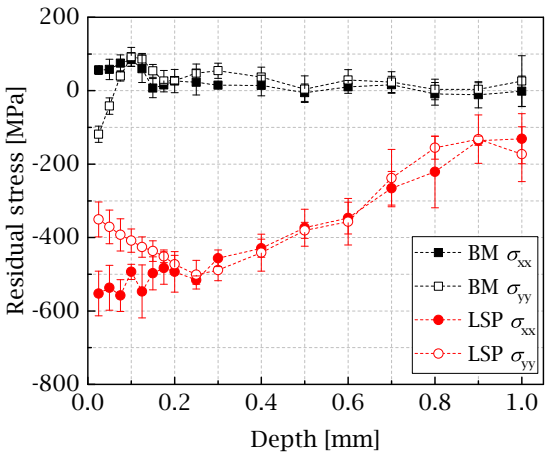


(b) 200 pulses/cm^2.

Figure 4.2: Residual stress profile of BM and LSP 2J: (a) 100 and (b) 200 pulses/cm^2.

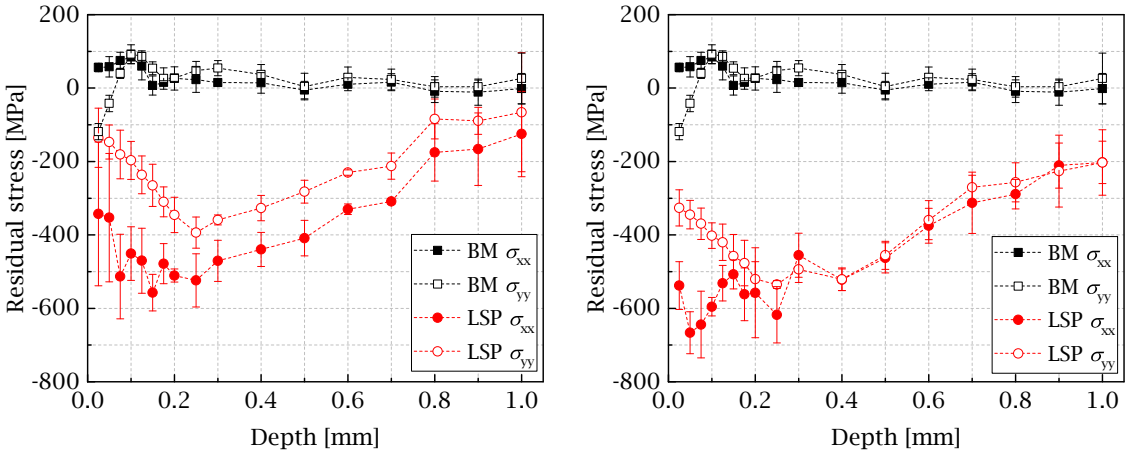


(a) 100 pulses/cm^2.



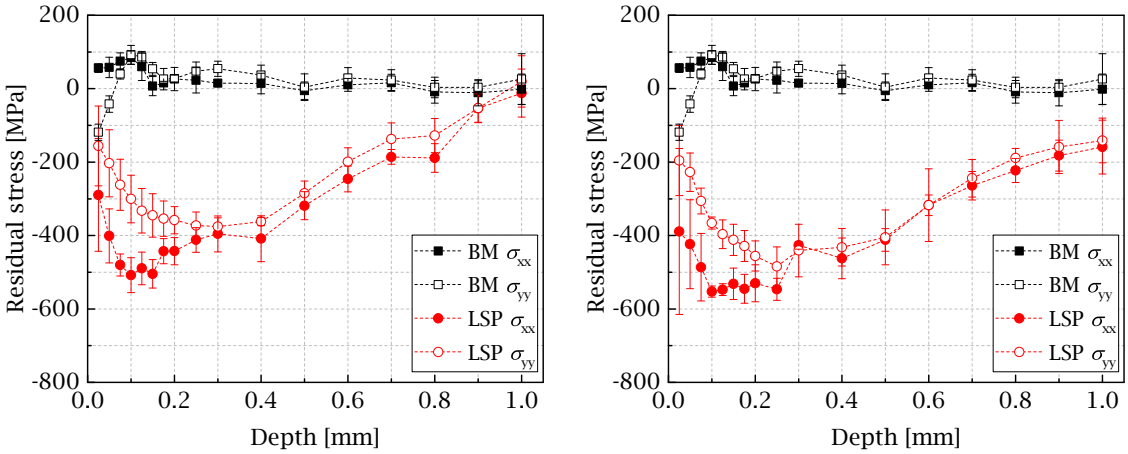
(b) 200 pulses/cm^2.

Figure 4.3: Residual stress profile of BM and LSP 3J: (a) 100 and (b) 200 pulses/cm^2.



(a) 100 pulses/cm^2. (b) 200 pulses/cm^2.

Figure 4.4: Residual stress profile of BM and LSP 4J: (a) 100 and (b) 200 pulses/cm^2.



(a) 100 pulses/cm^2. (b) 200 pulses/cm^2.

Figure 4.5: Residual stress profile of BM and LSP 5J: (a) 100 and (b) 200 pulses/cm^2.

The BM residual stress profile remains around zero, and the stresses in both directions are similar. However, compressive residual stress was found in the longitudinal direction on a very superficial layer of the material. The base material exhibited a compressive residual stress of -119 $\pm$ 22 MPa along the longitudinal direction (σ_{yy}) and a tensile stress of 56 $\pm$ 12 MPa along the transverse direction (σ_{xx}) at the surface. This difference may be explained according to the material pre-processing, in particular the rolling direction. Conversely, all LSP treated specimens indicate compressive residual stresses with higher magnitude along the transverse direction (LSP advancing direction), which is consistent with the results found by Trdan et al. (2018).

A comparison of the residual stress profiles shows a similar trend for all LSP treatment conditions. Residual stresses are compressive at the surface, reaching their maximum magnitude at depths between 0.05 and 0.2 mm, and then decreasing gradually towards the tensile regime as the depth increases. This is caused by an attenuation of the shock wave propagation through

the material. The shock wave is absorbed and becomes mainly displacement energy and plastic deformation on the surface and sub-surface.

The residual stress in the longitudinal direction (σ_{yy}) is consistently lower than the stress obtained in the transverse direction (σ_{xx}) at depths ranging from 0.025 to 0.2 mm, regardless of the LSP conditions adopted. The difference in the residual stress profile along the orthogonal directions becomes particularly obvious at higher levels of laser energy, as can be seen in Figures 4.4 and 4.5, corresponding to 4 and 5 J, respectively. However, this difference becomes less apparent from depths above 0.2 mm. Hence, a non-equibiaxial residual stress profile is observed in LSP treated AISI D2 specimens. One of the possible reasons for this difference may be the LSP scanning strategy and overlapping rate (Correa et al., 2015b; Kallien et al., 2019). Conversely, the residual stress profiles along the orthogonal directions for 1J and 2J are similar and no significant difference can be observed between both profiles (Figures 4.1 and 4.2).

According to Figures 4.4 and 4.5, it is likely that laser energy influences the residual stress profile uniformity, i. e. at higher laser energy (4 and 5 J) a pronounced variation (slope) between the stress at the surface and the peak stress is found. Such difference is less noticeable at lower laser energy (1, 2 and 3J corresponding to Figures 4.1, 4.2 and 4.3, respectively). Although an ablative protective layer was applied to the target surface, minor surface ablation may still occur. In addition, stress relaxation may have occurred due to excessive energy and high temperature. The findings indicate that the magnitude of thermal stress relaxation depends on the degree of plastic strain generated during the LSP process. The greater the initial plastic strain, the higher the stress relaxation, which is consistent with the results reported by Zhou et al. (2011).

Figures 4.6a and 4.6b show the peak stress for BM and LSP treated material (100 pulses/cm^2) along the transverse (σ_{xx}) direction and the maximum stress depth, respectively. Figures 4.7a and 4.7b show the peak stress for BM and LSP treated material (100 pulses/cm^2) along the longitudinal (σ_{yy}) direction and the maximum stress depth, respectively. Figures 4.8a and 4.8b show the peak stress for BM and LSP treated material (200 pulses/cm^2) along the transverse (σ_{xx}) direction and the maximum stress depth, respectively. Figures 4.9a and 4.9b show the peak stress for BM and LSP treated material (200 pulses/cm^2) along the longitudinal (σ_{yy}) direction and the maximum stress depth, respectively.

Interestingly, the peak residual stress is attained at different depths, which apparently is linked to the stress direction. The difference in the peak stress depths does not seem to be related to the LSP parameters, including laser energy and pulse density. As shown in Figures 4.6b and 4.8b, the residual stress profiles following the transverse (σ_{xx}) direction reach the peak at depths between 0.05 and 0.15 mm. According to the longitudinal (σ_{yy}) stress direction, however, the peak stress is attained at depths ranging from 0.175 to 0.25 mm (Figures 4.7b and 4.9b).

LSP treatment of AISI D2 tool steel using laser energy of 1J has generated a uniform compressive residual stress profile. The observed peak residual stress was -320 $\pm$ 41 MPa. With the increase of laser energy to 2J a residual stress peak of -490 $\pm$ 62 MPa was observed. Laser energy of 3J generated a peak compressive residual stress of -558 $\pm$ 43 MPa. The highest peak residual stress value across all tests and LSP processing conditions was of -667 $\pm$ 57 MPa corresponding to

4J and 200 pulses/cm^2. Despite the energy increase to 5J, there was no increase in residual stress but rather a decrease in peak stress value to -553 $\pm$ 15 MPa. Therefore, the residual stress progressively increases as the laser energy reaches 4J and then drops. This suggests that above a certain threshold, the energy increment will not translate into higher residual stress. In fact, excessive energy can adversely affect the stress state of the material due to saturation or stress relaxation because of elevated temperature as mentioned previously. LSP with higher energy generates a thick layer of compressive residual stress, although the near surface residual stress values tend to be lower due to the stress saturation rate (Farrahi et al., 1995; Ding and Ye, 2006).

Once residual stress is unsaturated, it increases as the power density increases. Conversely, when the residual stress reaches a saturation threshold, it will cause a permanent reverse deformation, leading to a drop in residual stress.

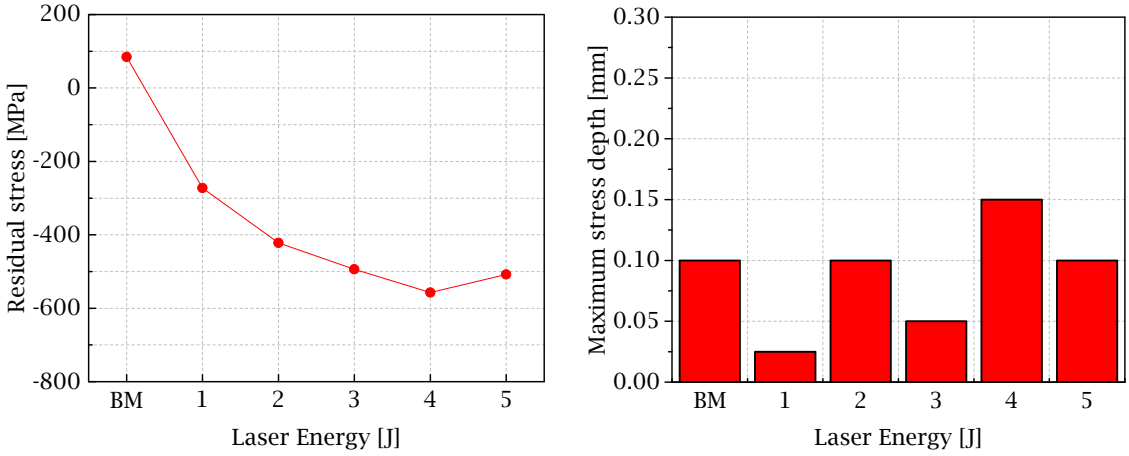


Figure 4.6: (a) Peak residual stress and (b) maximum stress depth at different laser energy and pulse density of 100 pulses/cm^2 along the transverse direction (σ_{xx}).

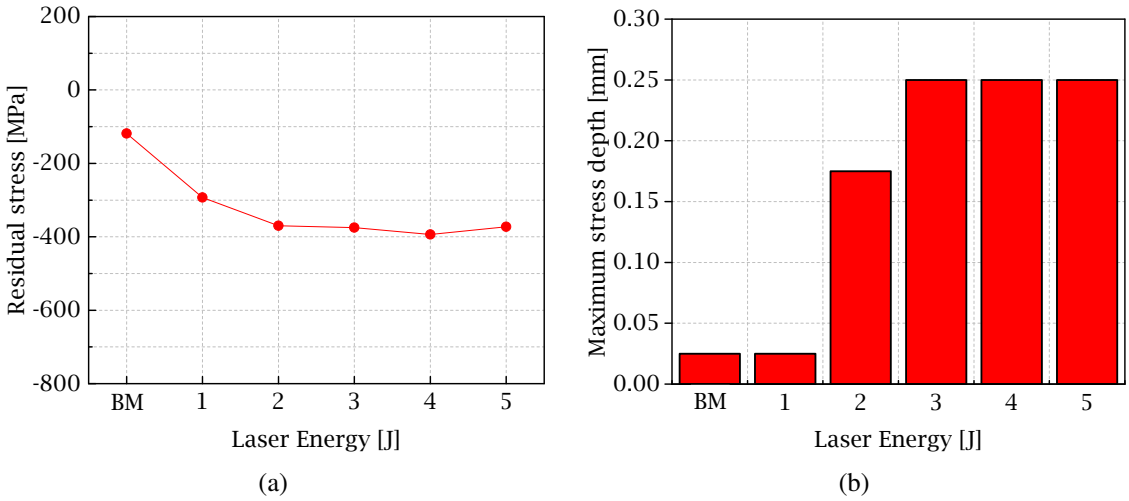


Figure 4.7: (a) Peak residual stress and (b) maximum stress depth at different laser energy and pulse density of 100 pulses/cm^2 along the longitudinal direction (σ_{yy}).

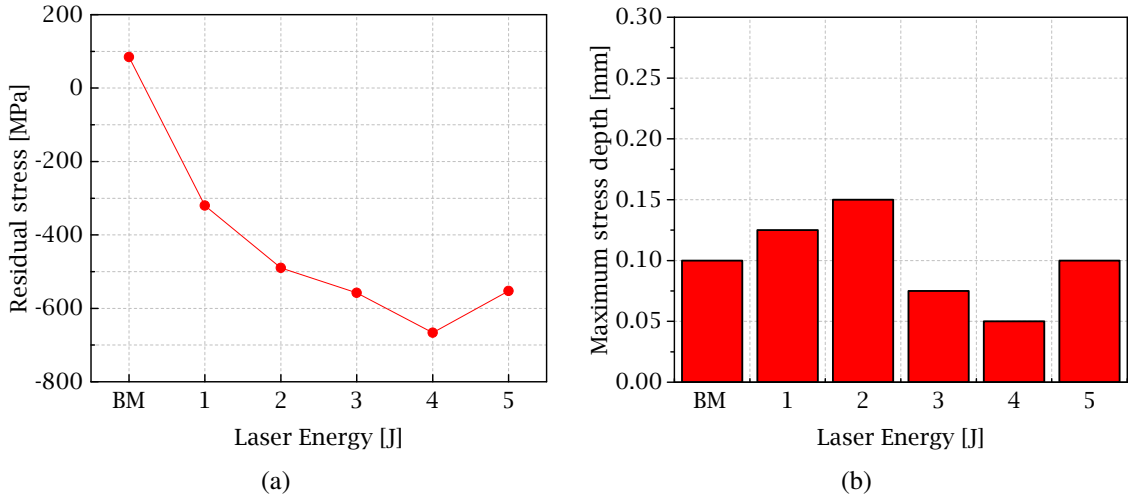


Figure 4.8: (a) Peak residual stress and (b) maximum stress depth at different laser energy and pulse density of 200 pulses/cm^2 along the transverse direction (σ_{xx}).

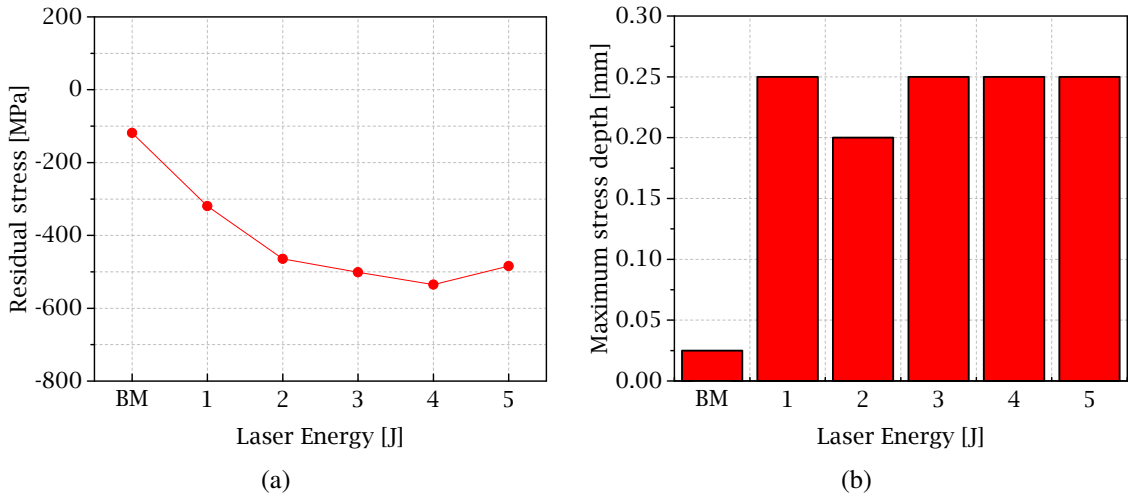


Figure 4.9: (a) Peak residual stress and (b) maximum stress depth at different laser energy and pulse density of 200 pulses/cm^2 along the longitudinal direction (σ_{yy}).

The results presented in Figures 4.8 and 4.9 might suggest an optimal power density in the range of 15 - 20 GW/cm^2, which is not consistent with Berthe et al. (1998), who found that breakdown plasma at the surface at the water is generated at power densities over 10 GW/cm^2 for a 1064 nm wavelength. The breakdown plasma leads to laser energy losses on the specimen surface, and consequently a reduction of the pulse pressure. Under optimal conditions, which is extremely difficult to achieve in experimental studies, the power density applied on the target surface should be identical to the estimated power density. However, there are power losses in optical elements and ablative layer, thus the effective power density applied in this study can be significantly lower compared to the estimated value.

A further approach to better assess the effects of LSP parameters on AISI D2 tool steel involves determining the compressive stress area of the processed material, rather than just focusing on

the peak stress or maximum penetration depth. Thereby, the compressive stress area (S_a) was determined by integrating the stress profile, $F(z)$, between minimum z, i.e. the surface, and the value of z where the stress shifts from compressive to tensile, as follows:

$$S_A = \int_{z_0}^{z_1} F(z)dz \tag{4.1}$$

The compressive stress area was calculated between the interval, [z_0, z_1], which correspond to the initial measurement point and the depth value where the stress profile changed to tensile, $f(z) \leq 0$, as depicted in Figure 4.10.

Figures 4.11a and 4.11b show the compressive stress area in BM and LSP treated material for pulse density of 100 pulses/cm^2 according to the transverse (σ_{xx}) and longitudinal (σ_{yy}) stress directions, respectively. Figures 4.11c and 4.11d show the compressive stress area in BM and LSP treated material for pulse density of 200 pulses/cm^2, according to the transverse (σ_{xx}) and longitudinal (σ_{yy}) stress directions, respectively. The base material shows a tensile stress state and, after LSP application, the stress state shifts to a compressive stress state.

The residual stress profiles become more similar along with transverse (σ_{xx}) and longitudinal (σ_{yy}) directions as pulse density increases. Therefore, according to the results presented in Figure 4.11, one can conclude that the increase in the pulse density promotes uniformity between the orthogonal directions of residual stress. An opposite effect can be observed with the increasing of laser energy, showing a more anisotropy as the energy increases. Hence, the optimum combination between laser energy and pulse density should be selected to achieve compressive residual stress of high magnitude and uniformity. The plots representing the compressive stress area for all LSP treatment conditions and BM are presented in Appendix B.2. These findings follow a similar trend as the residual stress profiles discussed above, with a progressive increase of the compressive area with the laser energy increasing up to 4J followed by a drop at 5J. Similarly, the compressive area increases with pulse density.

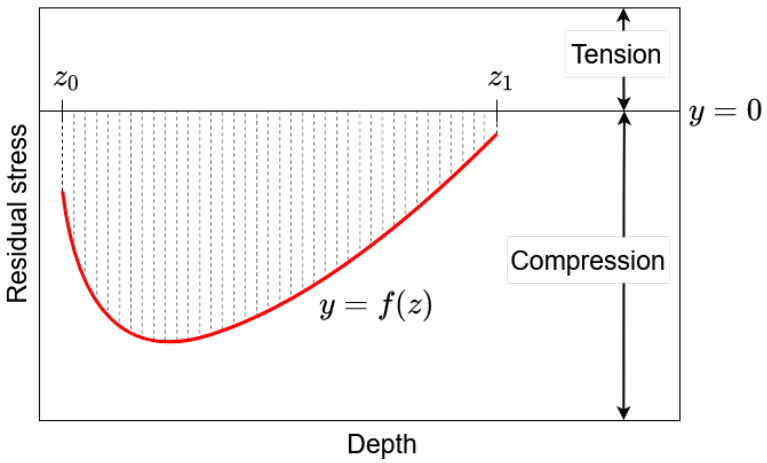
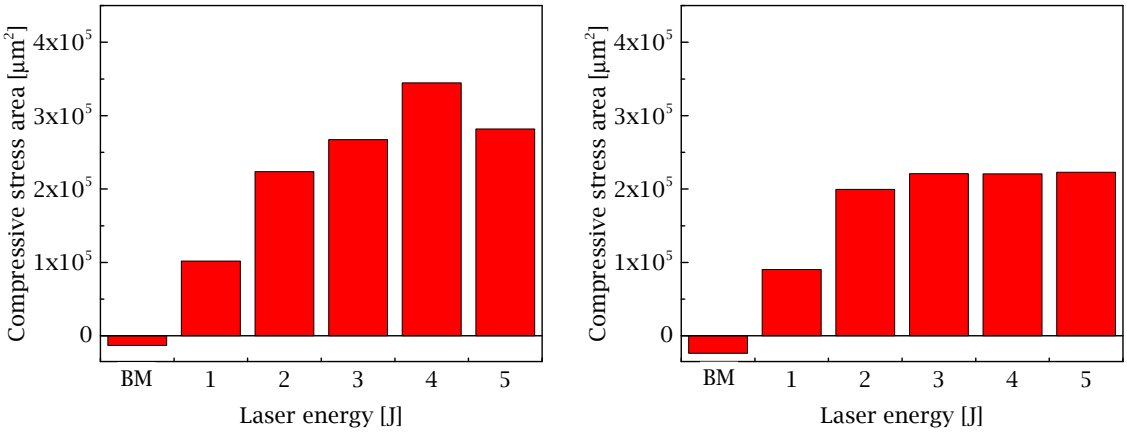
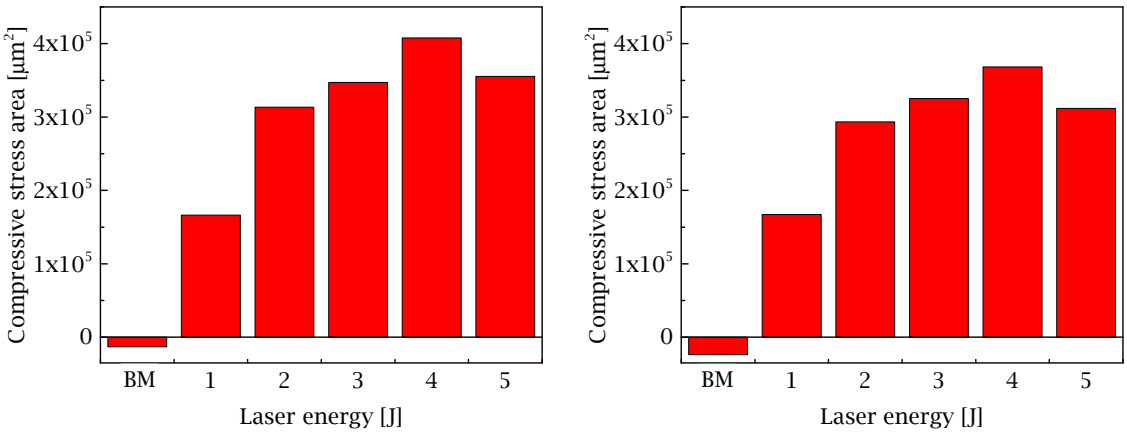


Figure 4.10: Schematic illustration of a typical LSP residual stress profile for compressive stress area calculation.



(a) 100 pulses/cm^2 (σ_{xx}). (b) 100 pulses/cm^2 (σ_{yy}).



(c) 200 pulses/cm^2 (σ_{xx}). (d) 200 pulses/cm^2 (σ_{yy}).

Figure 4.11: Compressive stress area of BM and LSP treated specimens at different laser energy and pulse density of (a, b) 100 and (c, d) 200 pulses/cm^2.

The compressive residual stress layer depth results in AISI D2 tool steel according to the laser energy and pulse density parameters is presented in Table 4.1.

A significant difference in compressive layer depth induced by LSP is observed for laser energy of 1J. This energy level shows an increase in the compressive layer depth by increasing the laser pulse density. Additionally, a significant variation of compressive stress depth is also verified depending on orthogonal stress direction. The compressive residual stress profile along the transverse direction is deeper than that along the longitudinal direction. For laser energy of 1J , the affected depth varies between 0.63 mm and 0.96 mm (see Table 4.1). For laser energy of 2J or greater, no significant variation in the plastically affected depth can be observed. The compressive layer consistently reaches depths close to 1 mm. Nevertheless, it is possible to observe that compressive stress layer depth in LSP treated AISI D2 tool steel increases along with the increase in laser energy as well as the increase in pulse density.

Table 4.1: Compressive residual stress layer depth [mm].

Pulse density [pulses/cm^2]	Stress direction	Laser energy [J]				
		1	2	3	4	5
100	σ_{xx}	0.80	0.98	1.00	1.00	1.00
	σ_{yy}	0.63	0.97	1.00	1.00	0.97
200	σ_{xx}	0.96	1.00	1.00	1.00	1.00
	σ_{yy}	0.86	1.00	1.00	1.00	1.00

It is important to mention that for some LSP processing conditions, the compressive layer depth may exceed 1 mm. Due to the specimen geometry and drill diameter (used in the ESPI hole-drilling technique), the maximum measurement depth was defined for 1 mm to ensure compliance with the specifications of the measurement technique. Despite the variations in depth, the laser energy and pulse density range adopted in this work provides residual stress profiles at satisfactory depths.

An important consideration regarding the residual stress results should be pointed out. When the peak residual stress exceeds 80% of the material's yield strength (470 MPa), the error in the determination of residual stress values can be more than 10% as indicated in studies of Chupakhin et al. (2016, 2017). These findings deserve careful analysis since it can be possible that the residual stress is being overestimated due to the assumption of purely elastic strain from the integral method used for the calculation of residual stresses (Schajer, 2010). Therefore, it is important to carefully analyze these findings. Nonetheless, the same test conditions were kept throughout the testing. Hence, a qualitative evaluation can be confidently performed.

It is noteworthy that both tensile and compressive stresses must be present to satisfy the internal force equations. Thus, the generation of compressive residual stresses is achieved at the expense of a redistribution of the overall stress state of the material, which implies the shifting of the compressive residual stress to the surface and the tensile residual stress in depth. Consequently, the higher the surface-induced residual stresses, the higher the tensile stresses in depth, which can result in sample bending. Considering all the factors discussed, namely peak compressive stress, compressive layer depth, residual stress profile uniformity and compressive area, one LSP processing condition was defined as the optimal condition for the present study. Thus, LSP using laser energy of 3J and pulse density of 200 pulses/cm^2 was considered as the optimal condition for the range of parameters covered in the present study.

LSP application generates compressive residual stresses on the surface and subsurface of AISI D2 tool steel. The effect of processing conditions is evident concerning the magnitude and distribution of the residual stress profile. The intensity levels achieved by 1064 nm wavelength laser radiation, along with the increase in laser pulse density, affected the residual stress profile and the plastically affected depth. The results show that higher laser intensities develop larger compressive residual stresses and deeper affected depths on the LSP processed AISI D2 specimens.

4.2.2 Contour method

Due to the long time required to determine the stress field using the contour method, it would be impractical to carry out the testing of every set of LSP parameters considered in this work. As such, the contour method was adopted to validate the ESPI hole drilling measurements as well as evaluate the through-thickness stress variation for the selected set of parameters (laser energy of 3J and pulse density of 200 pulses/cm^2).

Figure 4.12 shows the 2D contour map of the residual stress distribution in BM specimen. The residual stress distribution in the BM specimen is in good agreement with the results obtained by the ESPI hole drilling technique. Figures 4.13a and 4.13b show the 2D contour map of the residual stress distribution after LSP treatment.

As shown in Figures 4.13a and 4.13b, significant compressive residual stresses have been found in the lateral zones of the specimen, which is coincident with the LSP treated areas. The application of LSP on both sides of the specimen resulted in the generation of a compressive residual stress field over the whole specimen thickness. As expected, the core region of the LSP treated specimens exhibits tensile residual stresses that balance the compressive residual stresses. However, the compressive residual stress results obtained through the contour method are well above the results obtained by the ESPI hole drilling technique.

The residual stresses were obtained along several lines through the specimen, three lines along the width (x-direction) and three lines along the thickness (y-direction) as schematically presented in Figure 4.14.

Figures 4.15a and 4.15b show the residual stress profile for BM specimen along the thickness (y-direction) and width (x-direction), respectively. Figures 4.16a and 4.16b show the residual stress profile for LSP treated specimen (S-NS-1) along the thickness (y-direction) and width (x-direction), respectively. Figures 4.17a and 4.17b show the residual stress profile for LSP treated specimen (S-NS-2) along the thickness (y-direction) and width (x-direction), respectively.

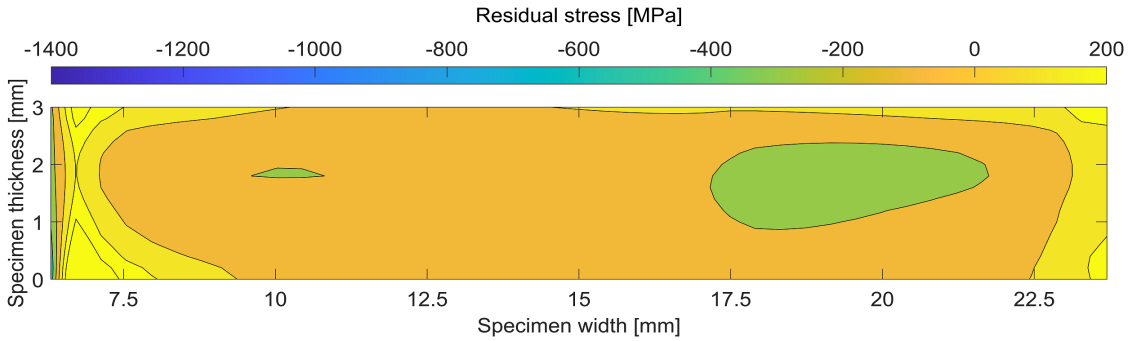
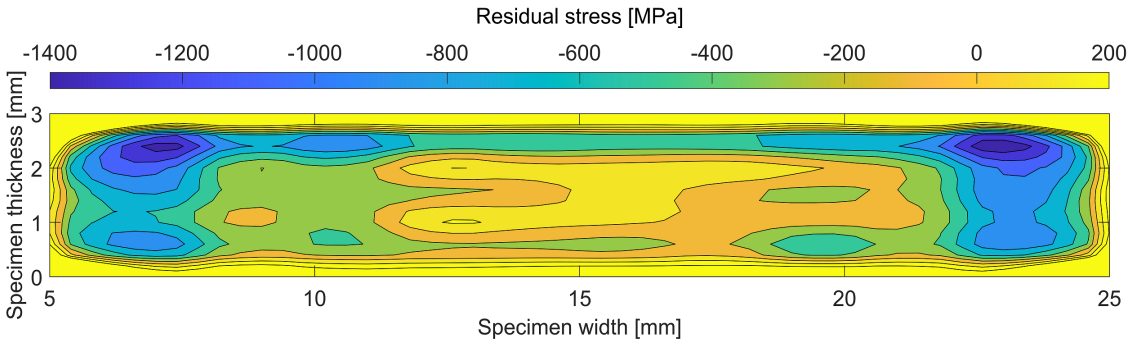
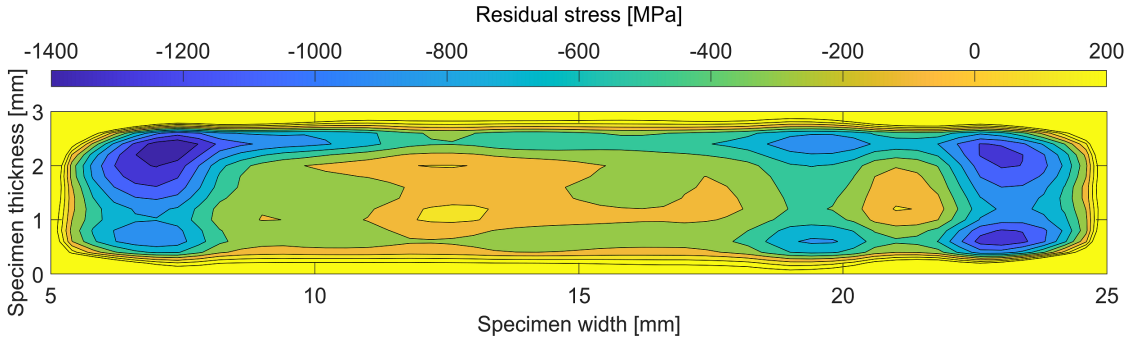


Figure 4.12: Calculated residual stress perpendicular to the cut surfaces in BM specimen (S-NS-3).



(a) 2D residual stress contour map (S-NS-1).



(b) 2D residual stress contour map (S-NS-2).

Figure 4.13: Calculated residual stress perpendicular to the cut surfaces in LSP treated specimen (a) S-NS-1 and (b) S-NS-2.

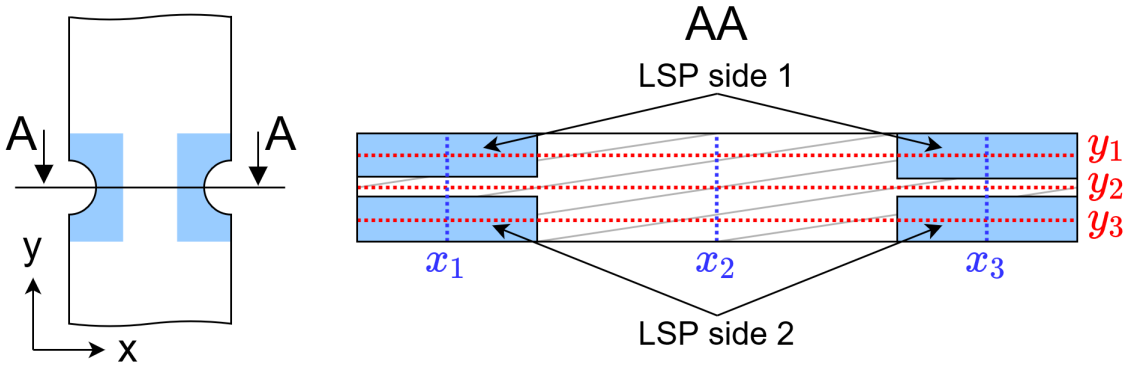


Figure 4.14: Schematic illustration of the residual stress profile measurement location.

The analysis of Figures 4.15a and 4.15b show that the residual stress profile along with the thickness (x_1 = 7.5 mm, x_2 = 15.0 mm and x_3 = 22.5 mm) and width (y_1 = 0.75 mm, y_2 = 1.50 mm and y_3 = 2.25 mm) for BM specimen (S-NS-3) exhibits values relatively close to zero with higher variation towards the edges, but still within a well-defined range of $\pm$ 200 MPa.

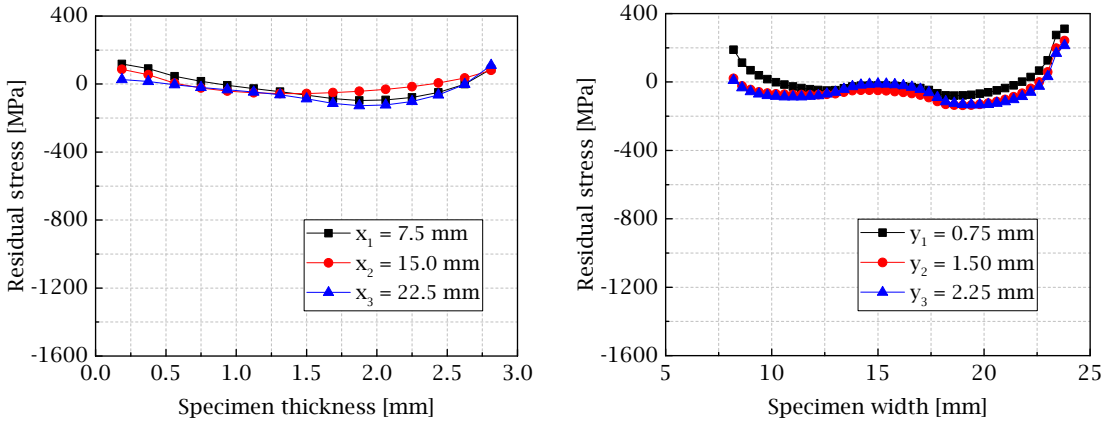


Figure 4.15: Residual stress profile of BM (S-NS-3) along (a) thickness and (b) width.

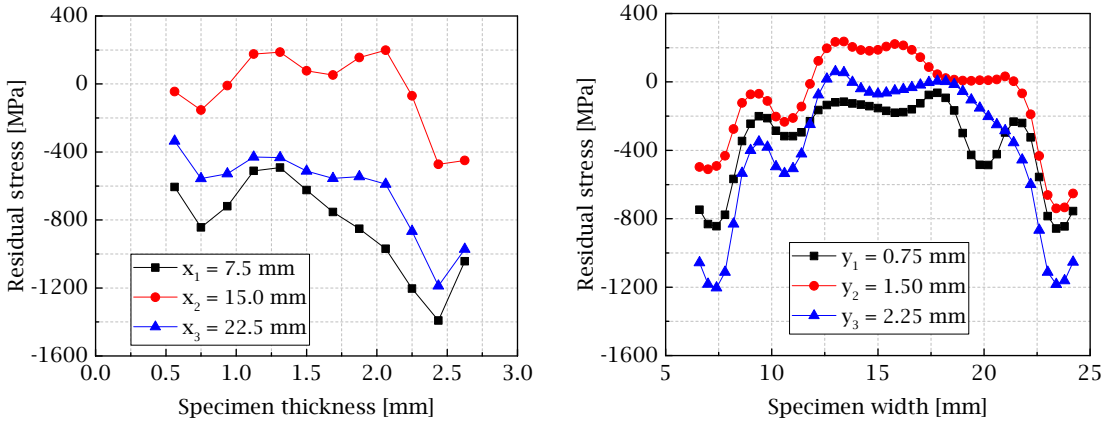


Figure 4.16: Residual stress profile of LSP (S-NS-1) along (a) thickness and (b) width.

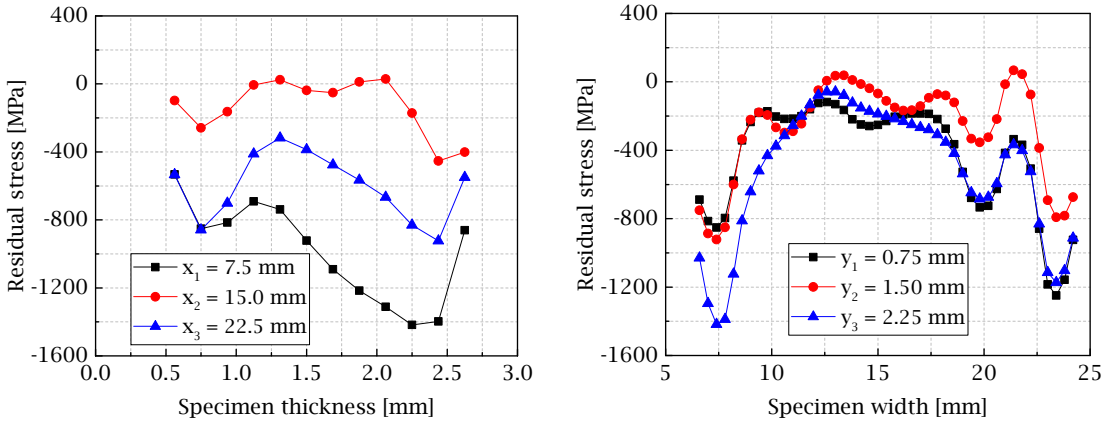


Figure 4.17: Residual stress profile of LSP (S-NS-2) along (a) thickness and (b) width.

Figures 4.16a and 4.17a show the residual stress profile through the thickness in the LSP treated regions ($x_1 = 7.5$ mm and $x_3 = 22.5$ mm) in the S-NS-1 and S-NS-2 specimens, respectively. These results show that the residual stress profile in LSP treated zones is compressive across the entire thickness, which suggests that the double side LSP application in thin sections can effectively create a fully compressive zone. The through-thickness residual stress profile in LSP non-affected region ($x_2 = 15.0$ mm) on S-NS-1 and S-NS-2 specimens fluctuates around zero or positive (tensile) values. The data points at the edges, exhibiting compressive values, should not be overestimated because they seem to be influenced by measurement errors.

Figures 4.16b and 4.17b present the residual stress profile through the width at different positions ($y_1 = 0.75$ mm, $y_2 = 1.50$ mm and $y_3 = 2.25$ mm) on the S-NS-1 and S-NS-2 specimens, respectively. As expected, the results indicate that throughout the specimen width, compressive residual stresses are present in the LSP affected zones. Besides, tensile stresses are present in the material core, particularly for $y_2 = 1.50$ mm, acting as balancing tensile stresses.

In the border areas, especially in LSP treated specimens (see Figures 4.13a and 4.13b), the residual stress obtained greatly exceeds the yield strength of the material ($\sigma_Y \approx 470$ MPa for BM and $\sigma_Y \approx 438$ MPa for LSP treated material). In this regard, it is important to emphasise that the estimated residual stresses located in the vicinity of the borders are presented but their reliability is known to suffer from measurement induced errors and should not, therefore, influence the overall judgement of the results. Several possible reasons for this problem can be identified. The CMM measurement may not be completely accurate because of the uncertainty of contact between CMM probe tip and the target surface near the borders. Such high stresses may also have resulted from local plastic deformation caused by inappropriate EDM cutting process. Figure 4.18 shows the resulting specimen surfaces after EDM cutting. The effect of the EDM on the target surface is evident, and it can be seen that excessive material removal has occurred on the edges with the most critical areas corresponding to the beginning and end of the cut. Therefore, it is possible to assume from Figure 4.18 that there was no constant material removal along the section, which suggests that results may be biased.

In face of the discussion above, in order to fully rely on the contour method, extreme care should be placed on the experimental setup. The ESPI hole drilling technique is both more expedite and overall reliable.

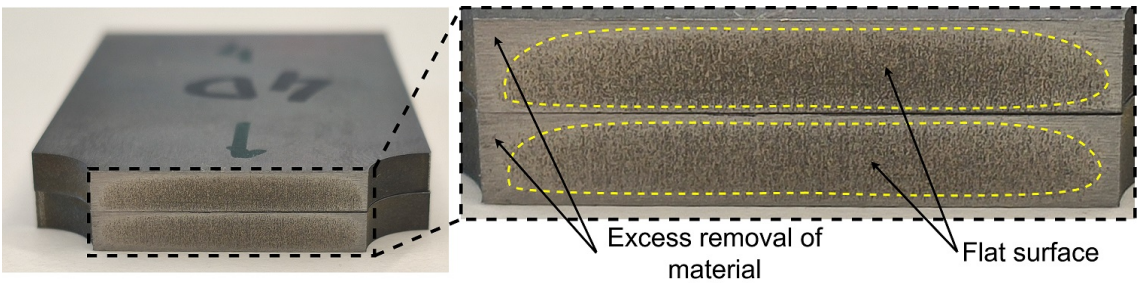


Figure 4.18: Resulting surface after wire-cutting EDM.

4.3 Surface roughness and topography

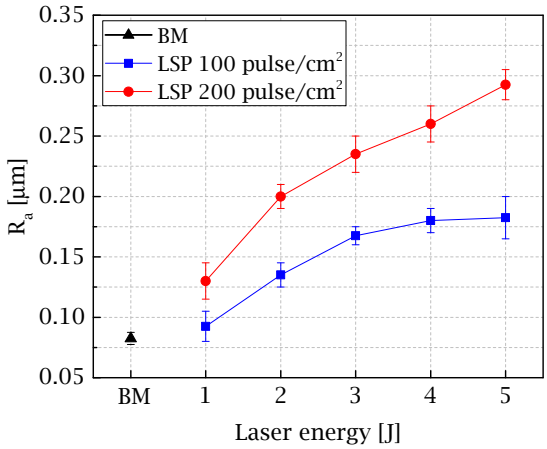
This section presents the effects of LSP treatment conditions on material roughness. The base material results are also included. In total, four individual measurements were performed for each LSP condition and BM. Each measurement was taken transversely (90º) to the laser scan direction and across a 12.5 mm evaluation length. All individual measurements are provided in Appendix D. Measurements of surface topography for base material and LSP treatment conditions are also presented.

Most surfaces are a combination of three surface texture elements which are rarely found in isolation but are commonly evaluated separately. Surface analysis, therefore, typically includes roughness (R), waviness (W) and form (P). An important consideration about surface texture is that there is no threshold between surface roughness and waviness, as these elements are dependent upon the nature of the application. In the context of cutting tools, the severity of the superficial texture modification after the application of LSP is excessive to be considered as roughness. For this reason, these elements have been evaluated separately. Thus, wavelengths were separated using a 0.25 mm cut off wavelength filter.

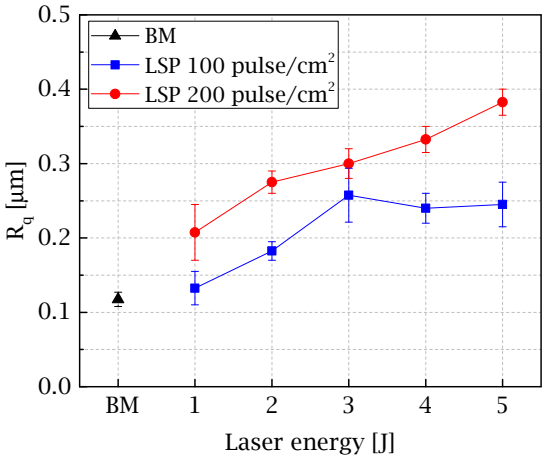
Figures 4.19a, 4.19b, 4.19c, 4.19d, 4.19e and 4.19f present the average surface roughness (R_a), root-mean-square roughness (R_q), maximum height profile (R_z), average waviness height (W_a), total waviness height (W_t) and profile height (P_t), respectively.

The average roughness of LSP treated material is significantly higher as compared to the average roughness of BM. According to Figure 4.19a, the average roughness increases with the increase of both laser energy and pulse density. For a pulse density of 100 pulses/cm^2, a slow-down of the increasing R_a above 3J is observed. Conversely, for 200 pulses/cm^2, R_a increases steadily with increasing laser energy. The LSP processing condition leading to the highest average roughness increase is 5J and 200 pulses/cm^2 with 0.293 ± 0.013 μm corresponding to a 254.5% increase over the BM (0.083 ± 0.005 μm). The R_a increase, in percentage, of the additional LSP treatment conditions as compared to the BM is summarised in Table 4.2.

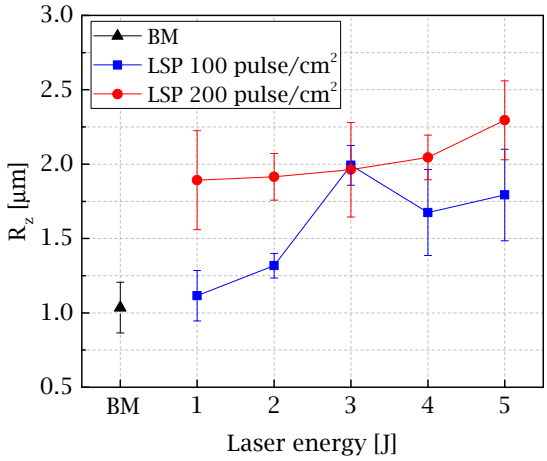
The root-mean-square roughness of LSP treated material is clearly higher as compared to the root-mean-square roughness of BM. According to Figure 4.19b, the R_q increases with the increase of both laser energy and pulse density. For a pulse density of 100 pulses/cm^2, a decrease of the R_q above 3J is observed. Conversely, for 200 pulses/cm^2, R_q increases steadily with increasing laser energy. The LSP processing condition leading to the highest root-mean-square roughness increase is 5J and 200 pulses/cm^2 with 0.383 ± 0.018 μm corresponding to a 225.5% increase over the BM (0.118 ± 0.010 μm). The R_q increase, in percentage, of the additional LSP treatment conditions as compared to the BM is summarised in Table 4.2.



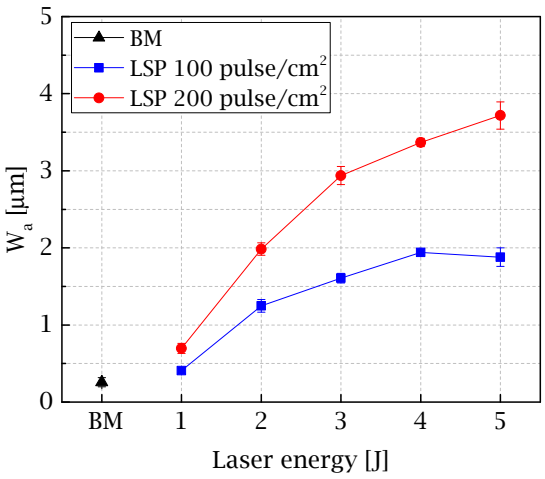
(a) Average surface roughness (R_a).



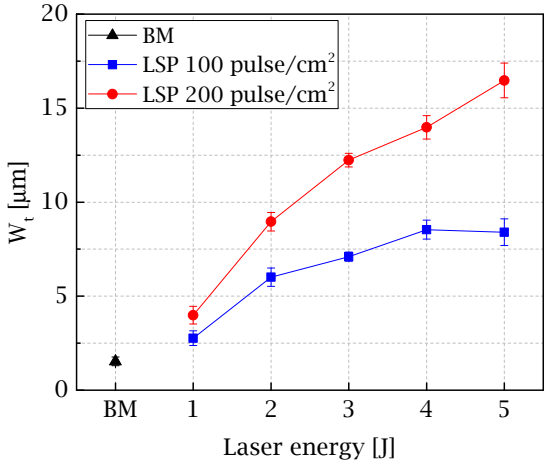
(b) Root-mean-square roughness (R_q).



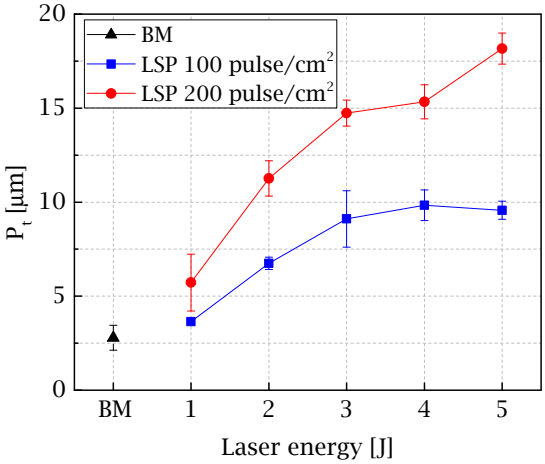
(c) Maximum height profile (R_z).



(d) Average waviness height (W_a).



(e) Total waviness height (W_t).



(f) Profile height (P_t).

Figure 4.19: Surface parameters of BM and LSP treated material at various laser energy levels and pulse densities. (a) Average surface roughness, (b) root-mean-square roughness, (c) maximum height profile, (d) average waviness height, (e) total waviness height and (f) profile height.

Table 4.2: Increase (in %) of the surface parameters after LSP (with varying processing conditions) as compared to BM.

Pulse density [pulses/cm^2]	Laser energy [J]	Surface parameters					
		R_a	R_q	R_z	W_a	W_t	P_t
100	1	12.1	12.8	7.7	58.3	80.4	30.8
	2	63.6	55.3	27.3	384.5	292.2	141.8
	3	103.0	119.1	92.5	524.3	363.3	226.5
	4	118.2	104.3	61.8	654.4	457.1	252.6
	5	121.2	108.5	73.2	630.1	448.3	242.9
200	1	57.6	76.6	82.9	169.9	160.2	105.1
	2	142.4	134.0	85.0	670.9	484.8	303.6
	3	184.8	155.3	89.6	1040.8	698.5	428.2
	4	215.2	183.0	97.6	1207.8	812.1	449.7
	5	254.5	225.5	121.7	1343.7	974.9	551.2

The maximum height roughness profile of LSP treated material is clearly higher as compared to the maximum height roughness profile of BM. According to Figure 4.19c, the R_z increases with the increase of both laser energy and pulse density. For pulse density of 100 pulses/cm^2, the increase of R_z up to 3J is observed, following a decrease for energy levels of 4 and 5J. Conversely, for 200 pulses/cm^2, a relatively small R_z variation is observed across all laser energy levels. However, the increasing trend of R_z occurs as energy increases. It should be noted, that contrarily to other surface parameter results, the standard deviation of the R_z values is high. The LSP processing condition leading to the highest maximum height roughness profile increase is 5J and 200 pulses/cm^2 with 2.295 $\pm$ 0.265 μm corresponding to a 121.7% increase over the BM (1.035 $\pm$ 0.171 μm). The R_z increase, in percentage, of the additional LSP treatment conditions as compared to the BM is summarised in Table 4.2.

The average waviness height of LSP treated material is significantly higher as compared to the average waviness height of BM. According to Figure 4.19d, the average waviness height increases with the increase of both laser energy and pulse density. For pulse density of 100 pulses/cm^2, W_a increases up to 4J, and then stabilizes at 5J. For 200 pulses/cm^2, however, a steady increase of W_a is observed as energy increases. The LSP processing condition leading to the highest average waviness height increase is 5J and 200 pulses/cm^2 with 3.718 $\pm$ 0.178 μm corresponding to a 1343.7% increase over the BM (0.258 $\pm$ 0.060 μm). The W_a increase, in percentage, of the additional LSP treatment conditions as compared to the BM is summarised in Table 4.2.

The total waviness height of LSP treated material is significantly higher as compared to the total waviness height of BM. According to Figure 4.19e, the total waviness height increases with the increase of both laser energy and pulse density. For pulse density of 100 pulses/cm^2, W_t increases up to 4J, and then stabilizes at 5J. For 200 pulses/cm^2, however, a steady increase of W_t is observed as energy increases. The LSP processing condition leading to the highest total waviness height increase is 5J and 200 pulses/cm^2 with 16.473 $\pm$ 0.923 μm corresponding to a 974.9% increase over the BM (1.532 $\pm$ 0.229 μm). The W_t increase, in percentage, of the

additional LSP treatment conditions as compared to the BM is summarised in Table 4.2.

The profile height of LSP treated material is significantly higher as compared to the profile height of BM. According to Figure 4.19f, the profile height increases with the increase of both laser energy and pulse density. For pulse density of 100 pulses/cm^2, P_t increases up to 4J, and then stabilizes at 5J. For 200 pulses/cm^2, however, a steady increase of P_t is observed as energy increases. The LSP processing condition leading to the highest profile height increase is 5J and 200 pulses/cm^2 with 18.168 $\pm$ 0.824 μm corresponding to a 551.2% increase over the BM (2.790 $\pm$ 0.660 μm). The W_t increase, in percentage, of the additional LSP treatment conditions as compared to the BM is summarised in Table 4.2.

It is remarkable the changes in the surface parameters of LSP treated material compared to BM. Figures 4.19a, 4.19b, 4.19c, 4.19d, 4.19e and 4.19f show a similar trend across the different LSP treatment conditions. For constant laser energy, an increase of the roughness values with an increase of the laser pulse density is observed. For constant laser pulse density, an increase in roughness values is observed with the increase in laser energy. Interestingly, a nearly linear increase of the roughness values can be observed along with the increase of energy to pulse density of 200 pulses/cm^2. In contrast, for a pulse density of 100 pulses/cm^2, the roughness values tend to stabilize for laser energy between 3 and 5J.

Typically, LSP treatment increases surface roughness due to surface ablation effect and severe plastic deformation caused by the interaction of laser radiation with the material (Siddaiah et al., 2018; Lu et al., 2012a). Surface roughness can be detrimental to the fatigue life of metal alloys, due to the introduction of stress concentrators (Peyre et al., 1996). Additionally, surface finishing operations can be applied as long as no excessive heat or excessive material removal occurs. However, the compressive residual stresses and surface hardened layer can reduce the adverse impact of the increased roughness caused by LSP. Besides the physical LSP process, more factors may contribute to the roughness increase. These include the surface ablation that may occur during the LSP process, despite being protected with an ablative layer, and irregularities in laser beam spatial profile (Dai et al., 2015). The irregularities may arise as a result of the laser radiation interaction with the confinement medium of the plasma: 1) The presence of water bubbles or impurities caused by the material ablation, which can cause non-uniformity of the pressure pulse (Trdan et al., 2012). 2) The confinement media layer thickness may cause a deflection or bending of the laser beam causing a self-focusing (Brodeur, 1999), which can produce non-uniformity of the laser intensity, and consequently non-uniformity of the pressure pulse. Surface roughness is observed to increase with LSP energy and pulse density. The surface roughness depends on the original surface condition of the base material, however, with LSP there is an irregular absorption of radiation in the ablative layer. Consequently, this attenuation results in a variation of intensity as the shock wave propagate between the ablative layer and the target material, resulting in a roughened surface.

The experimental findings reveal the surface roughness behaviour of BM and LSP treated AISI D2 tool steel. The average roughness increases sharply as laser energy increases. With the same laser pulse density, the higher laser energy can lead to a more severely deformed surface, thus causing a higher surface roughness. It is evident that due to the interaction of laser radiation with AISI D2 steel, plastic deformation has occurred which led to changes in surface topography as well as an increase in roughness. These changes can be attributed to surface ablation, spatial beam profile irregularities induced by the confinement media and absence of overlapping between laser shots.

The topography measurement location was selected to emphasize the superficial modifications caused by the LSP process according to Figure 4.20. Three different perspectives are presented to provide a better comparison between the LSP processing conditions and BM. The surface measurements are set on the same colour scale to enable a qualitative comparison. This highlights the effect of the LSP parameters on the material surface. Figures 4.21, 4.22, 4.23, 4.24 and 4.25 show the surface topography of LSP treated material at 1, 2, 3, 4 and 5J, respectively. Figure 4.26 shows the BM surface topography.

The sharp protrusions and microgrooves observed are the result of pre-processing applied to the specimens to create a brushed surface finish effect. That is evident in base material condition and in areas of untreated material of LSP processed specimens. The LSP treated surfaces exhibit a periodic surface waviness pattern which is more accentuated as laser energy and pulse density increase. This wavy surface pattern can be explained by the laser beam profile (see Figure 2.11a) and the absence of overlapping between laser shots.

As mentioned several times along this thesis, the application of LSP on the surface of the target material generates plastic deformation at surface and in depth. Naturally a noticeable change of surface roughness occurs. As opposed to SP, which generates high roughness and highly non-uniform surface modifications, LSP creates a well defined surface pattern resulting from the highly controlled and localised energy application.

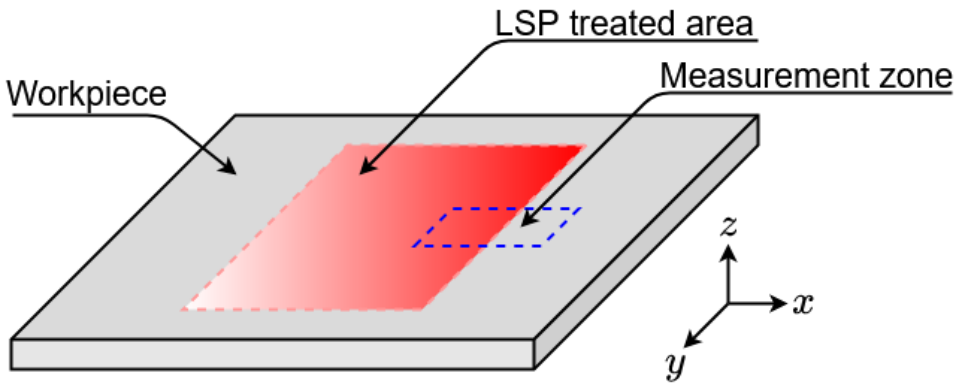
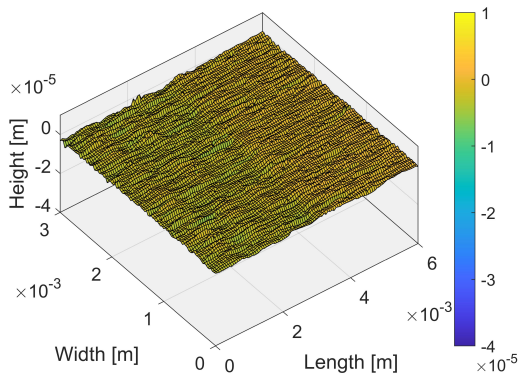
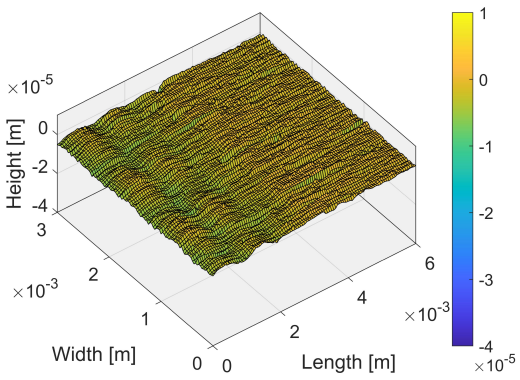


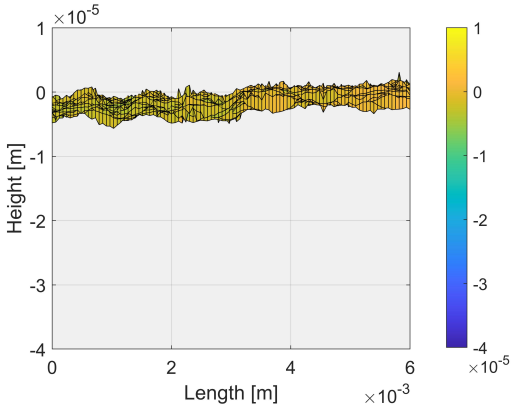
Figure 4.20: Schematic illustration of the non-contact surface topography measurement zone.



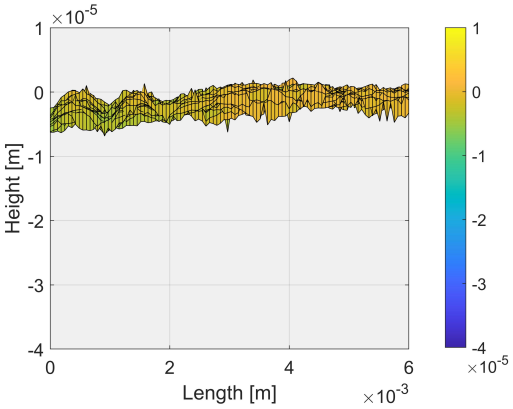
(a) Isometric view (100 pulses/cm^2)



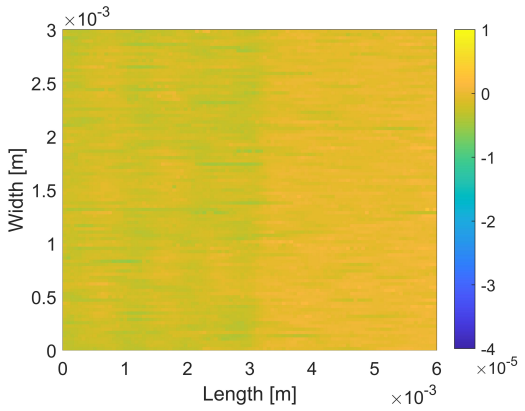
(b) Isometric view (200 pulses/cm^2)



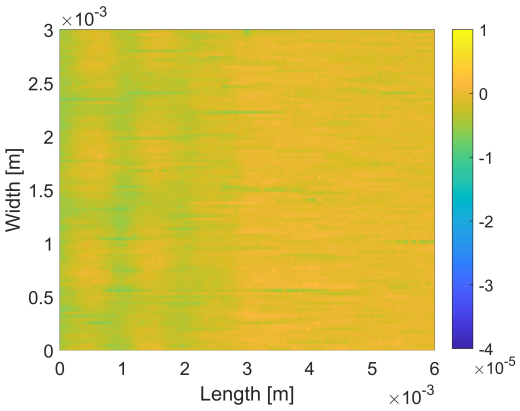
(c) Side view (100 pulses/cm^2)



(d) Side view (200 pulses/cm^2)

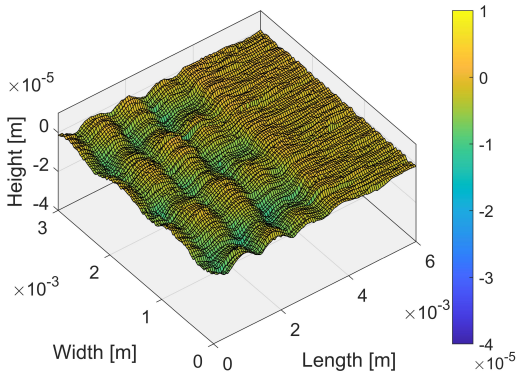


(e) Top view (100 pulses/cm^2)

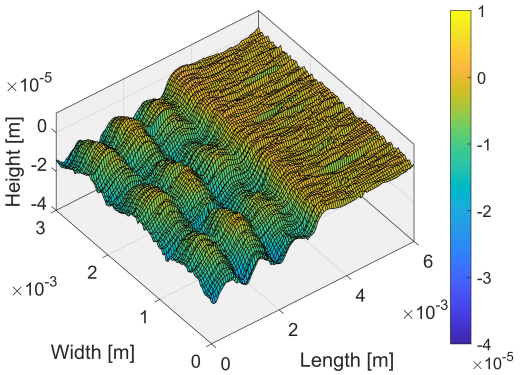


(f) Top view (200 pulses/cm^2)

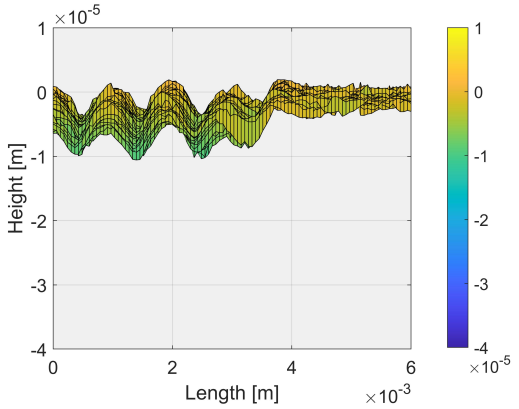
Figure 4.21: Surface topography of 1J LSP treated material at (a, c and e) 100 pulses/cm^2 and (b, d and f) 200 pulses/cm^2.



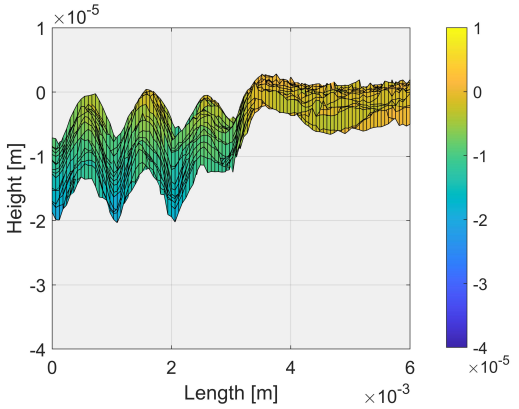
(a) Isometric view (100 pulses/cm^2)



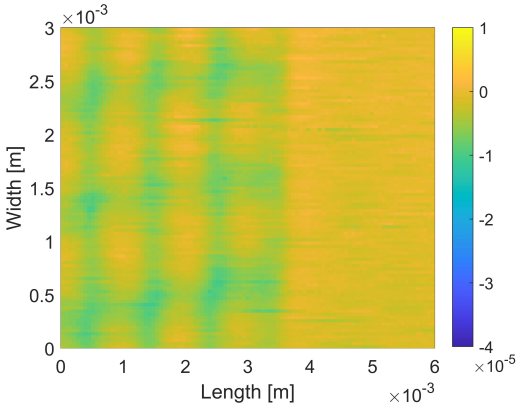
(b) Isometric view (200 pulses/cm^2)



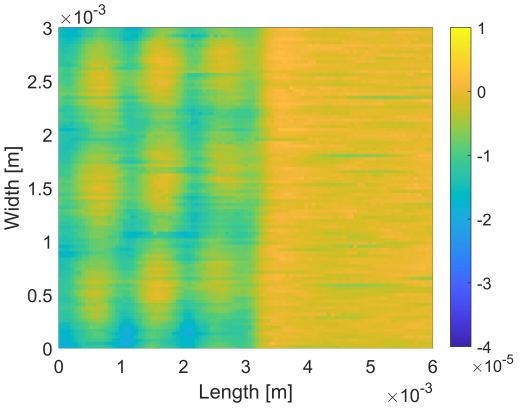
(c) Side view (100 pulses/cm^2)



(d) Side view (200 pulses/cm^2)

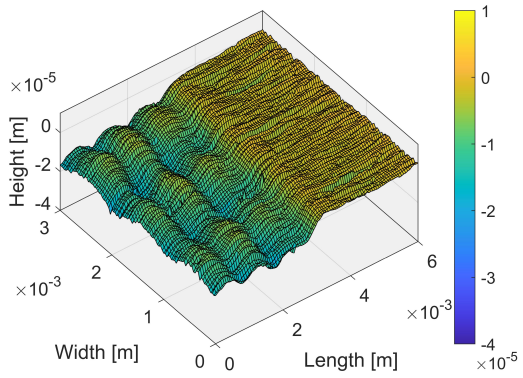


(e) Top view (100 pulses/cm^2)

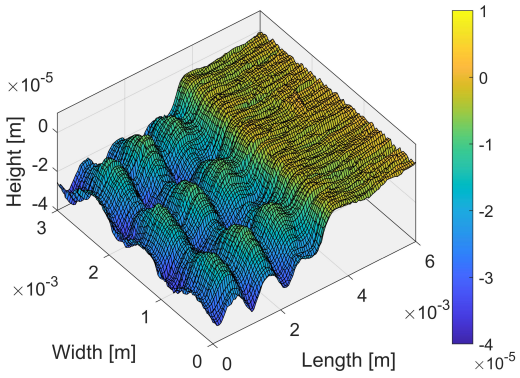


(f) Top view (200 pulses/cm^2)

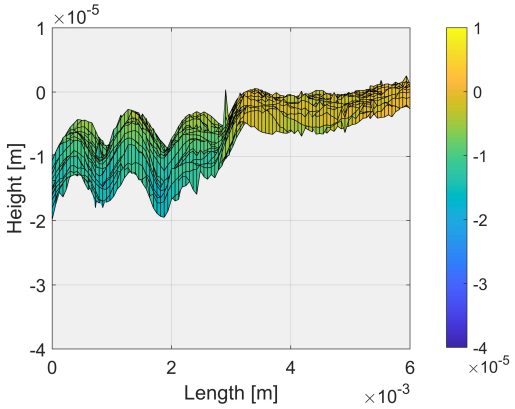
Figure 4.22: Surface topography of 2J LSP treated material at (a, c and e) 100 pulses/cm^2 and (b, d and f) 200 pulses/cm^2.



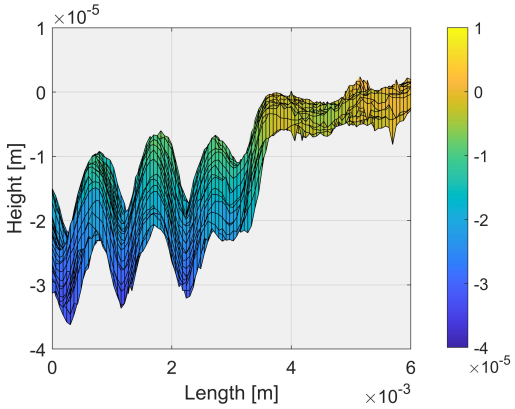
(a) Isometric view (100 pulses/cm^2)



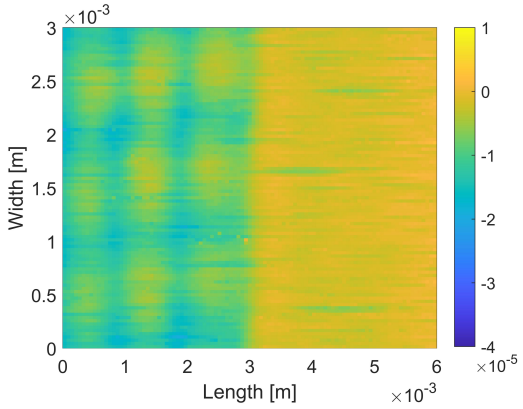
(b) Isometric view (200 pulses/cm^2)



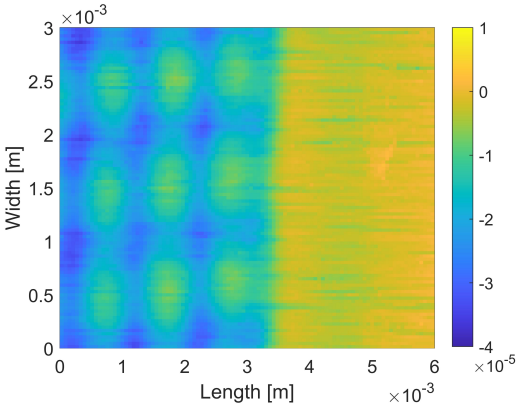
(c) Side view (100 pulses/cm^2)



(d) Side view (200 pulses/cm^2)

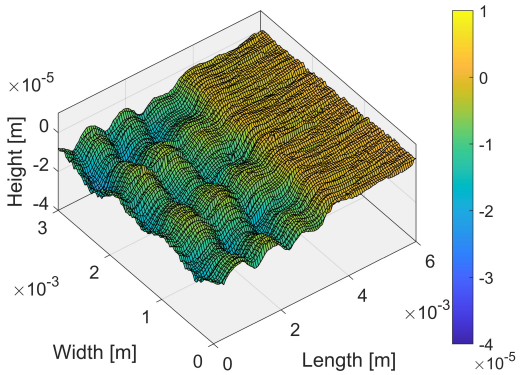


(e) Top view (100 pulses/cm^2)

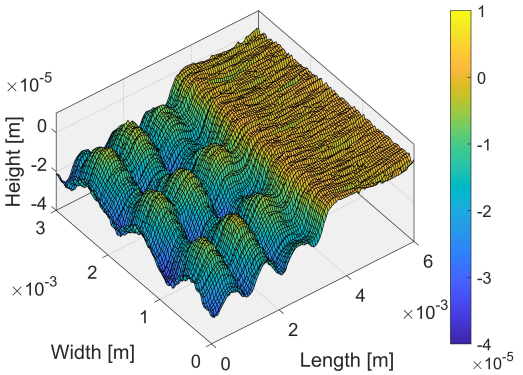


(f) Top view (200 pulses/cm^2)

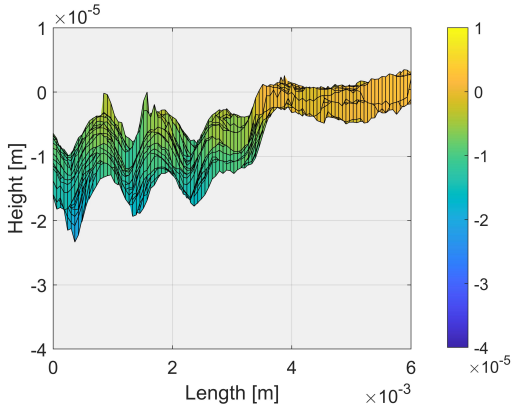
Figure 4.23: Surface topography of 3J LSP treated material at (a, c and e) 100 pulses/cm^2 and (b, d and f) 200 pulses/cm^2.



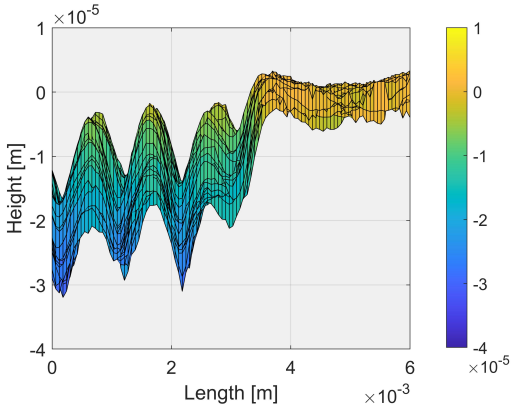
(a) Isometric view (100 pulses/cm^2)



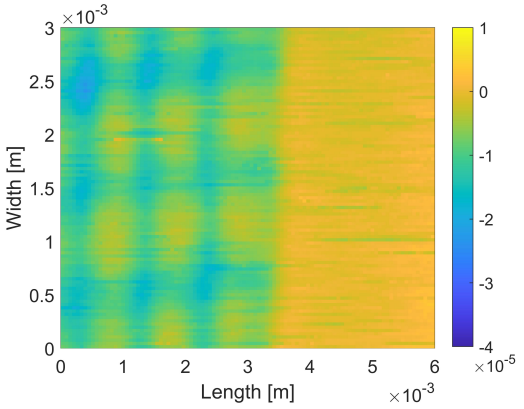
(b) Isometric view (200 pulses/cm^2)



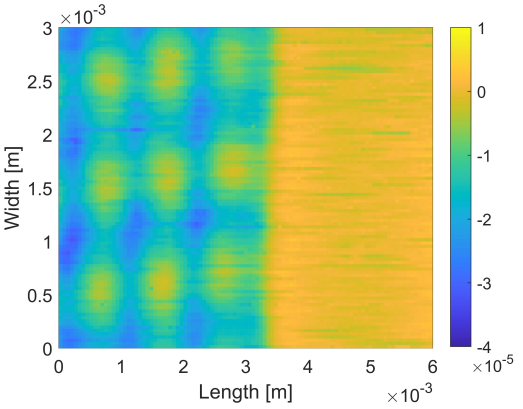
(c) Side view (100 pulses/cm^2)



(d) Side view (200 pulses/cm^2)

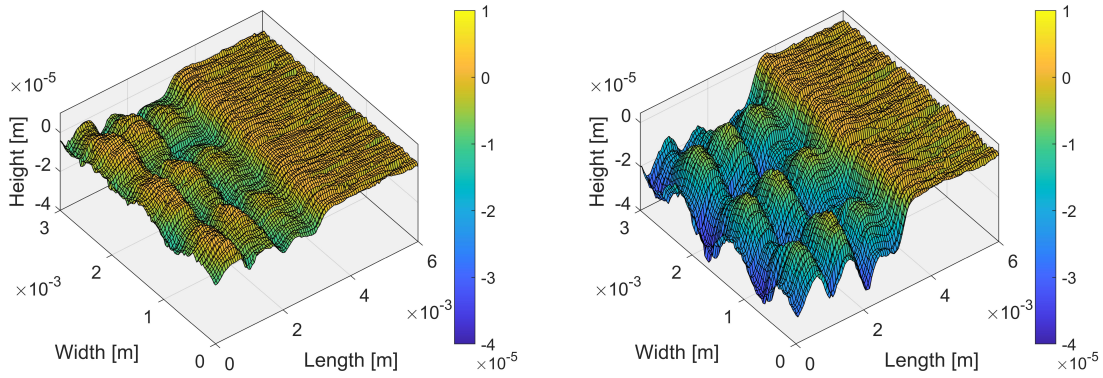


(e) Top view (100 pulses/cm^2)



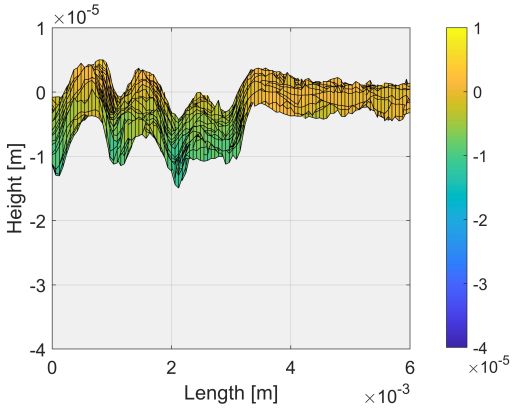
(f) Top view (200 pulses/cm^2)

Figure 4.24: Surface topography of 4J LSP treated material at (a, c and e) 100 pulses/cm^2 and (b, d and f) 200 pulses/cm^2.

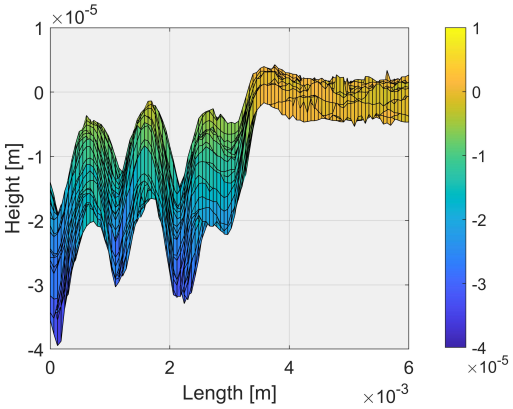


(a) Isometric view (100 pulses/cm^2)

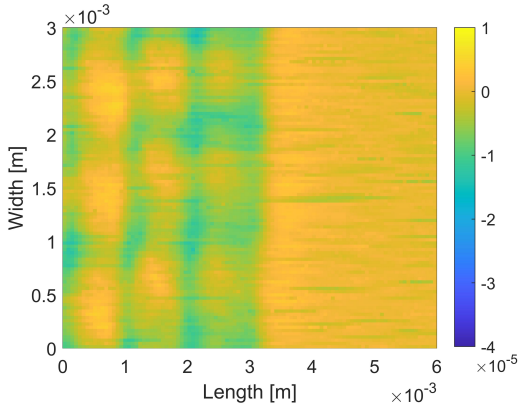
(b) Isometric view (200 pulses/cm^2)



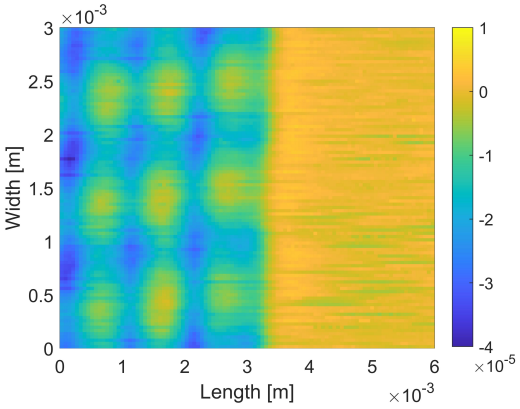
(c) Side view (100 pulses/cm^2)



(d) Side view (200 pulses/cm^2)

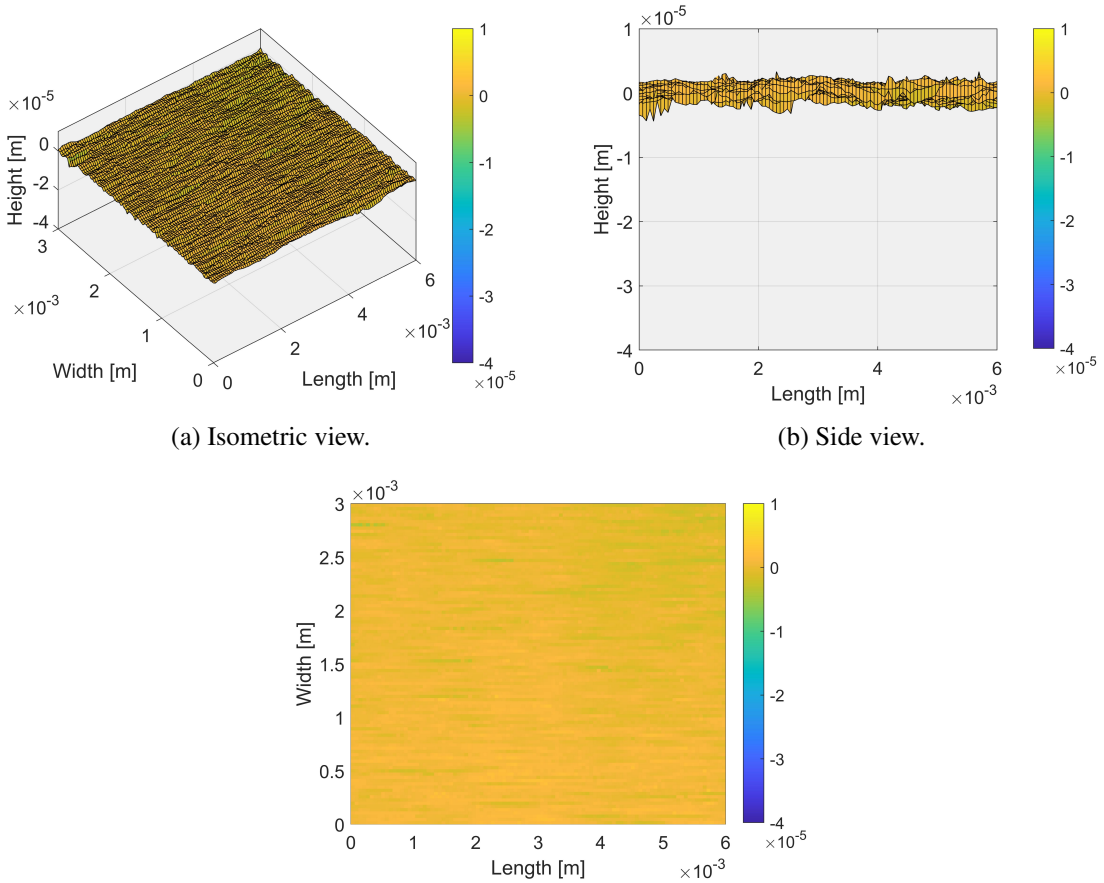


(e) Top view (100 pulses/cm^2)



(f) Top view (200 pulses/cm^2)

Figure 4.25: Surface topography of 5J LSP treated material at (a, c and e) 100 pulses/cm^2 and (b, d and f) 200 pulses/cm^2.



(a) Isometric view.

(b) Side view.

(c) Top view.

Figure 4.26: Surface topography of base material.

4.4 Micro hardness

In this section, the effect of different LSP treatment conditions on the micro hardness profile of AISI D2 tool steel is presented and discussed. A significant increase of micro hardness after LSP application on a variety of materials has been consistently reported in the scientific literature. Such effects are typically attributed to microstructural changes like grain refinement and strain hardening caused by the severe shock waves and high strain rates typical of LSP.

It is necessary to analyse these results carefully, in each specific application of the technique, and consider the overall trend of the micro hardness profile. The reason for this is that the material under study exhibits a strong presence of large carbides distributed in the ferritic matrix. These large carbides present a high hardness, which may result in a micro hardness profile with several peaks that are not truly representative of the effect intended to be observed in this study. Several smoothing methods are available depending on the nature of the results and the noise. Each method provides a specific performance to reveal significant aspects of the results. Given these highly

variable hardness values (noise), the mean can be biased by a small number of extremely high values, which can lead to incorrect interpretation of the results.

A signal processing technique designated as Percentile Filter was applied to remove noise resulting from extreme micro hardness values on the results. These results do not show a normally distributed noise, whereas the noise appears as localized peaks, so-called shot noise. For such noise, the percentile filtering method is appropriate as it allows to eliminate noise with abnormal amplitude. This method replaces the value of the signal at each data point with the median value of a group of surrounding data points. The percentile parameter determines the percentile used for filtering. This parameter was set to 50%, which corresponds to replacing the data point with the median value of the data points in the data window.

Results are divided according to the laser energy involved in the LSP process and plotted alongside the micro hardness profile of the BM for easy comparison. The micro hardness depth profiles for BM and LSP treated material are presented in Figures 4.27a, 4.27b, 4.27c, 4.27d and 4.27e corresponding to laser energy levels of 1, 2, 3, 4 and 5J, respectively. The raw measurement data is provided in Appendix E.

Table 4.3 presents the micro hardness results found in the vicinity of the target surface, since it is where higher micro hardness variations are expected to occur. Therefore, the results presented in Table 4.3 reflect the median of four measurements taken at 0.075 mm (distance in compliance with ASTM E92-17 (2017)) from the target surface of the material. Additionally, the variations (increase %) in micro hardness after LSP as compared to BM are also presented in Table 4.3.

From Figure 4.27, it can be observed that micro hardness progressively increases with both the increase in laser energy and pulse density when compared to the BM. The LSP treatment condition that generated higher surface micro hardness values was 5J (see Figure 4.27e).

Table 4.3: Surface micro hardness of BM and LSP treated material.

Material condition		Micro hardness [$HV_{0.1}$]	Increase over BM [%]
BM		203.8 ± 8.6	
Pulse density [pulses/cm^2]	Laser Energy [J]		
100	1	230.5 ± 59.4	13.1
	2	232.0 ± 2.3	13.8
	3	256.4 ± 25.3	25.8
	4	243.9 ± 5.0	19.7
	5	302.5 ± 53.4	48.4
200	1	239.6 ± 17.4	17.6
	2	263.8 ± 97.1	29.4
	3	281.7 ± 12.1	38.2
	4	272.7 ± 7.9	33.8
	5	264.6 ± 21.4	29.8

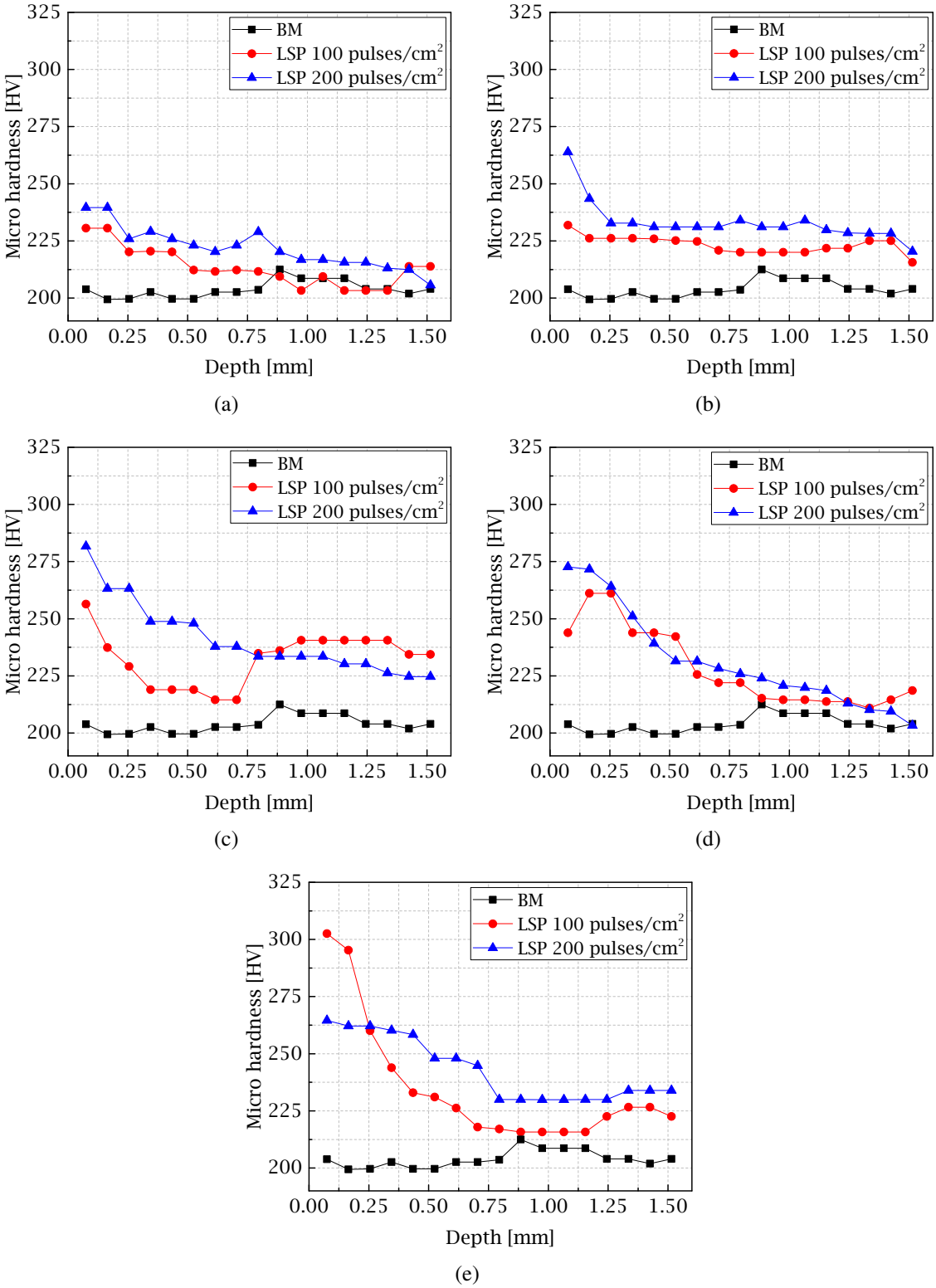


Figure 4.27: Micro hardness profile of BM and LSP treated material at different pulse densities and laser energy of (a) 1J, (b) 2J, (c) 3J, (d) 4J and (e) 5J.

Contrary to the expectations, the micro hardness profile for LSP treated specimen using laser energy of 5J exhibits substantially higher micro hardness values at the surface for a lower pulse density (see Figure 4.27e). This may suggest the influence of the high hardness of a carbide despite the smoothing operation applied.

Considering the LSP set of parameters (laser energy of 3J and pulse density of 200 pulses/cm^2, Figure 4.27c) regarded as the most appropriate (based on the residual stress profile in section 4.2), it was found to cause a surface micro hardness increase of 38.2% (see Table 4.3).

Rather than focusing solely on the micro hardness at the surface, it is important to consider the micro hardness depth profile to understand to what extent the LSP treatment impacts the material's micro hardness in depth. Different LSP treatment conditions, with varying energy levels and pulse density, exhibit a relatively similar trend, i.e. the peak micro hardness values are found near the surface and decrease in depth. This makes sense in the context of LSP since the effects of the treatment are experienced in the vicinity of the surface. It can also be observed that the micro hardness profile gradually decreases in depth until it reaches values close to those obtained for the base material around 1 mm in depth. This trend can be linked to the residual stress results as at 1 mm depth the material is still under the effect of LSP induced compressive stress.

After the LSP treatment, the residual stress state near the surface has changed from tensile to compressive, so hardness is expected to increase. This increasing trend in micro hardness reflects the definition of hardness, which is the capability of a metal to endure permanent deformation. When a material is under the influence of compressive residual stresses, the hardness is expected to be higher than that under the influence of tensile stresses, because the material in a compressive state requires a more severe loading to cause yielding or plastic deformation to deform the metal as in hardness measurements.

It is commonly reported that LSP generated compressive residual stresses and microstructural modifications may influence the hardness of metals. Several studies have established a correlation between these two quantities, and models were proposed to account for the contributions of residual stresses and plastic deformation (work hardening) in the hardness measurements. Huber and Heerens (2008) investigated the effect of residual stresses on the determination of hardness. Based on the results of the authors one can estimate the level of work hardening introduced through the LSP treatment.

It is possible to conclude that LSP can enhance the micro hardness of the surface layer of AISI D2 tool steel. It was observed that micro hardness in LSP treated specimens increased according to the laser energy and pulse density. The grain refinement and dislocation density are generally assumed as the mechanisms responsible for micro hardness increase (Rai et al., 2019).

4.5 Microstructural modification

The microstructure of BM and LSP treated AISI D2 cold work tool steel was investigated. The material was supplied after a soft-annealing process, i.e., the material was subjected to heating to 850°C followed by cooling in the furnace at a cooling rate of 10°C/h down to 650°C, then cooling freely in the air. As previously mentioned, AISI D2 tool steel exhibit carbon and carbide forming elements, particularly chromium, leading to the generation of large carbides undissolved into the ferritic matrix. A large amount of coarse carbides in AISI D2 tool steel often results in early cracking, which is primarily the reason for its poor toughness, tensile strength and fatigue resistance (Roberts et al., 1998). The morphology modification such as the refinement of coarse carbides at a high level of carbides volume fraction is responsible for enhancing wear resistance, toughness, and hardness properties (Das et al., 2009; Torkamani et al., 2011). Large eutectic chromium carbides (M_7C_3) are formed during the solidification due to the high content of carbon and chromium (Zelic et al., 2018). These large carbides are not desirable as they represent potential crack initiation sites during material post-processing, which harm fatigue resistance.

Figure 4.28 illustrates the calculated phase equilibrium for the range of temperatures between zero to 1600°C. As can be seen in Figure 4.28, austenite (γ-Fe) formation occurs from the liquid phase at approximately 1400°C and M_7C_3 carbides are formed at 1240°C. With temperature reduction, the austenite fraction drops, whereas the M_7C_3 carbide fraction increases. At approximately 800°C, a phase transition from austenite (γ-Fe) to ferrite (α-Fe) occurs and the amount of M_7C_3 carbides increases. This is followed by precipitation of $M_{23}C_6$. Below 400°C, MC carbides start to form, which is associated with the quick dissolution of M_7C_3 carbides and a mild increase in ferrite (α-Fe) content.

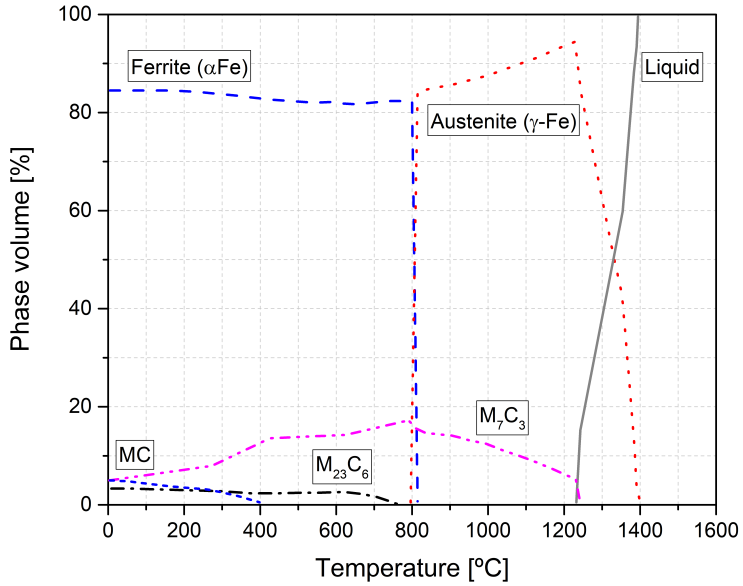


Figure 4.28: Phase equilibrium for AISI D2 tool steel base material. Depicted and adapted from (Bombač et al., 2013).

M_7C_3 carbides are observed in Fe-alloys with high chromium content and moderate amounts of other carbide forming elements. It is, therefore, a chromium-rich carbide with a hexagonal lattice structure and resistant to dissolution at higher temperatures as it dissolves very slowly in austenite (γ-Fe) during the hardening process. These carbides are typically present in annealed or highly tempered conditions. Similarly, $M_{23}C_6$ is a chromium-rich carbide with a face-centred cubic lattice structure. Also, MC carbides are present in AISI D2 tool steel and are a vanadium-rich carbide. The amount of carbides present in tool steels is generally higher in the annealed state than after austenitization and hardening, because the carbides provide the austenite (γ-Fe) with the carbon needed to attain higher hardness (Krauss, 2015; Voort, 2004).

4.5.1 Optical microscopy (OM)

Micrographs of base material (BM) and LSP treated material (3J and 200 pulses/cm^2) are presented. The micrographs show a cross-section relative to the direction of application of the LSP treatment. An optical microscope image of BM, exhibiting the ferrite matrix and the large carbide (yellow arrows), is illustrated in Figure 4.29. The elongated shape and lamellar orientation of primary carbides suggest the rolling direction of the material. Besides, secondary spheroidized carbides are finer and dispersed in the matrix of ferrite (α-Fe) grains due to the heat treatment of group D steels. Figure 4.30 shows the microstructure of AISI D2 tool steel after LSP treatment using laser energy of 3J and a pulse density of 200 pulses/cm^2.

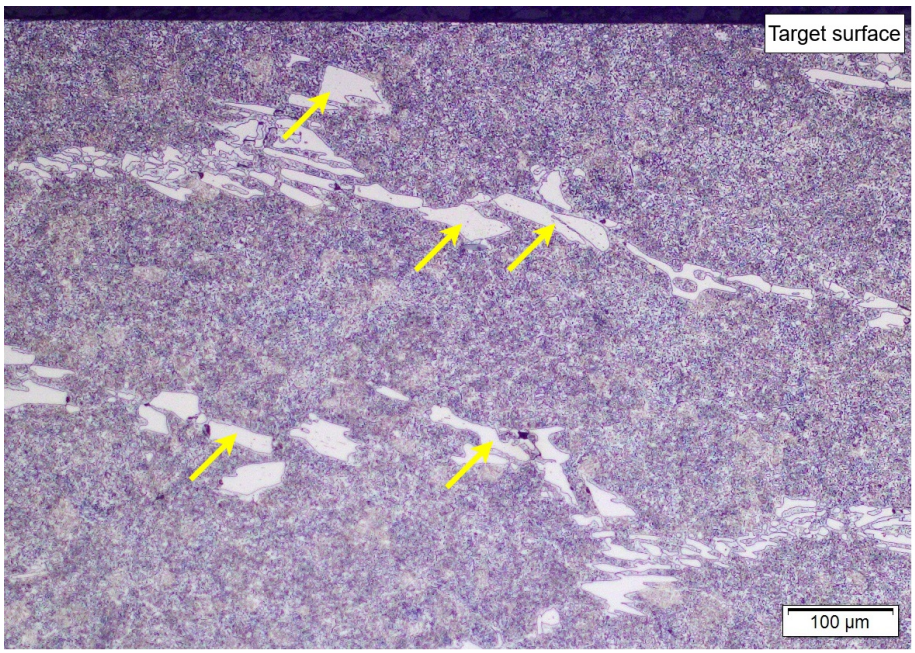


Figure 4.29: OM images of the etched base material AISI D2 tool steel microstructure with eutectic carbides network.

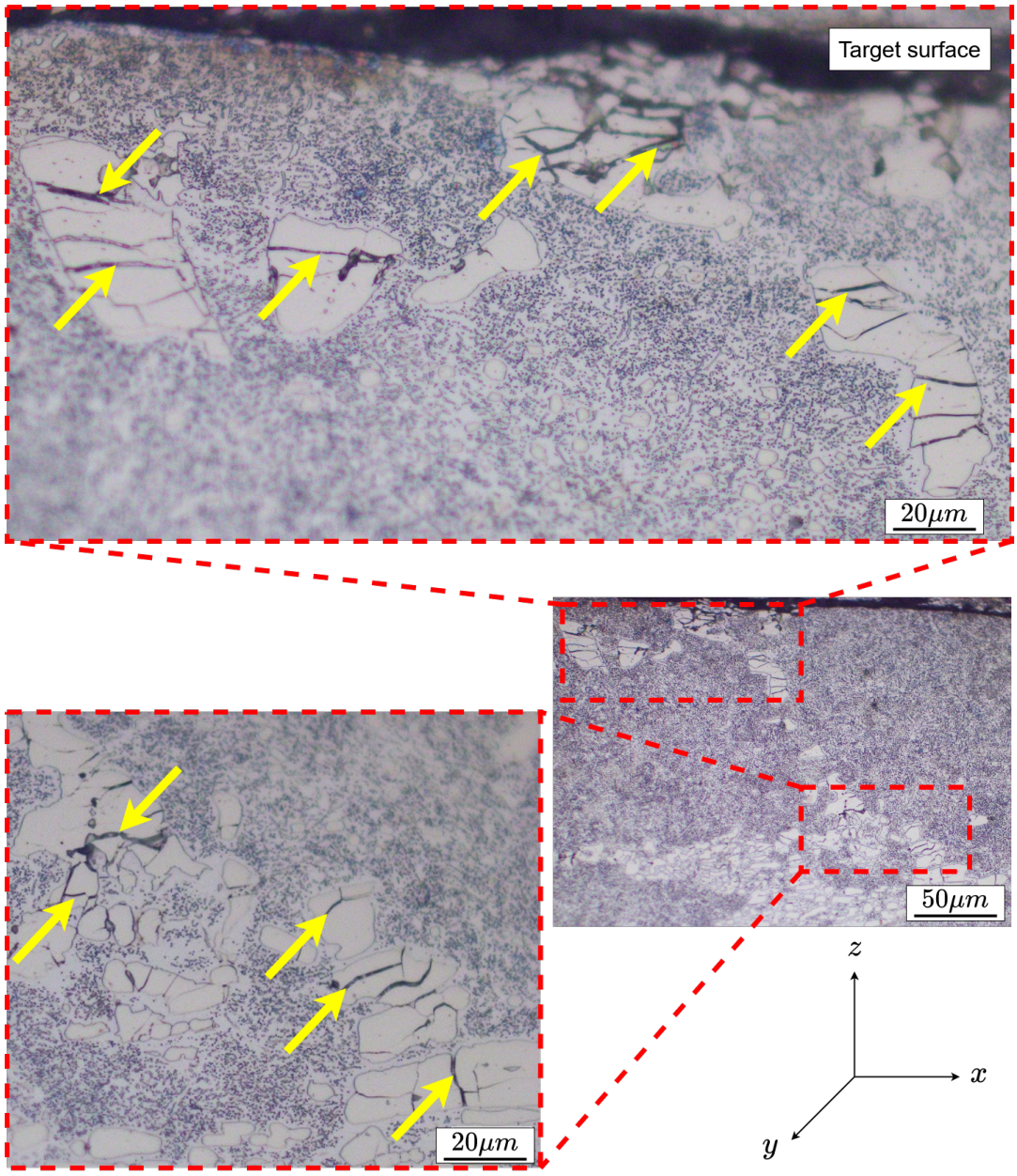


Figure 4.30: Micrograph of LSP treated material (3J and 200 pulses/cm^2).

The additional micrographs presenting the microstructure of LSP treated material at different energy levels and pulse densities are provided in Appendix F. A similar microstructure for the different LSP process conditions was found. The surface appears wavy due to plastic deformation and the microstructure of the LSP treated material consists of carbides distributed in a ferritic matrix. The carbides remained undissolved in the ferrite matrix due to the short time of laser radiation interaction.

According to the microstructural observations, no significant differences in the morphology of the eutectic carbides were observed between the base material condition and the different LSP processing conditions. All material conditions exhibit arrays of large coarse carbides with minor

carbides uniformly arranged in a ferrite (α-Fe) matrix. However, several cracks were found in larger carbides near the LSP treated surface (yellow arrows). These findings are significantly evident for LSP treated material using laser energy of 3J and pulse density of 200 pulses/cm^2, as can be seen in Figure 4.30. Such cracks can be detrimental to the material's strength and decrease its fatigue strength as they can act as cracking initiation sites near the surface or internal material defects. While the scientific literature is abundant on research focused on microstructural modifications caused by LSP in several materials, no research is available on the effect of LSP on AISI D2 tool steel. However, Lesyk et al. (2020) investigated the application of ultrasonic impact treatment (UIT), which is a surface processing technique with the same purpose as LSP. The analysis of XRD patterns for AISI D2 tool steel in the initial state and after UIT process revealed no phase transformations.

Phase transformations in AISI D2 tool steel occur at temperatures from approximately 800°C with the formation of austenite (γ-Fe) and the dissolution of $M_{23}C_6$ carbides (see Figure 4.28). The optical micrographs analysis does not show morphological changes of carbides nor dissolution of carbides. This suggests that temperature during LSP was not enough to cause phase transformation, carbide size reduction and carbide dissolution. This finding was anticipated, since an ablative layer of stainless steel was applied to protect the target surface against the possible thermal effects of the LSP process. However, several studies where LSP was applied with and without ablative layer showed phase transformation (form austenite to martensite, $\gamma \rightarrow \alpha'$) in austenitic stainless steels (Zhou et al., 2016; Karthik and Swaroop, 2016). An XRD analysis of the material before and after the application of LSP would be helpful to confirm if plastic-induced phase transformation at high strain rates has in fact occurred and, if so, the fraction of the resultant phases.

Carbide size reduction positively affect the fatigue resistance behaviour of metals. Hence, a contradiction seems to exist between these microstructural observations and fatigue results. These observations, combined with the cracking, suggest that fatigue performance will be adversely affected after LSP application. However, the fatigue test results presented in section 4.7 below reveal a significant increase in fatigue strength of AISI D2 tool steel after LSP treatment. Thus, it is possible to assume that fatigue strength improvement was not due to morphological changes in the carbides. Nevertheless, the material may have undergone microstructural changes which cannot be detected by OM.

The microstructural observation by means of OM is interesting as it allows the observation of carbide cracking and their distribution. However, it fails to detect the changes in terms of grain size, which is a very significant and relevant finding reported in the literature. As a result, Electron Backscatter Diffraction (EBSD) and Energy-Dispersive X-ray Spectroscopy (EDS) analysis was conducted on BM and LSP treated material.

4.5.2 Electron backscatter diffraction (EBSD)

EBSD was adopted to study the grain refinement, misorientation and grain shape before and after LSP with a detection area of 0.25 mm $\times$ 0.6 mm and a step size of 2 μm. Figure 4.31 presents the EBSD maps of BM and LSP treated material (3J and 200 pulses/cm^2). The reference direction

[001] was adopted for the inverse pole figure to code the colour scheme (red [001], green [101] and blue [111]), as indicated in Figure 3.17b and by the triangle in the bottom right corner of Figures 4.31c and 4.31d.

The qualitative analysis of the EBSD maps of the BM specimen microstructure, presented in Figure 4.31c, exhibits a relatively uniform distribution of coarse grains with some fine dispersed grains. In contrast, the microstructure resulting from the LSP treatment is significantly more

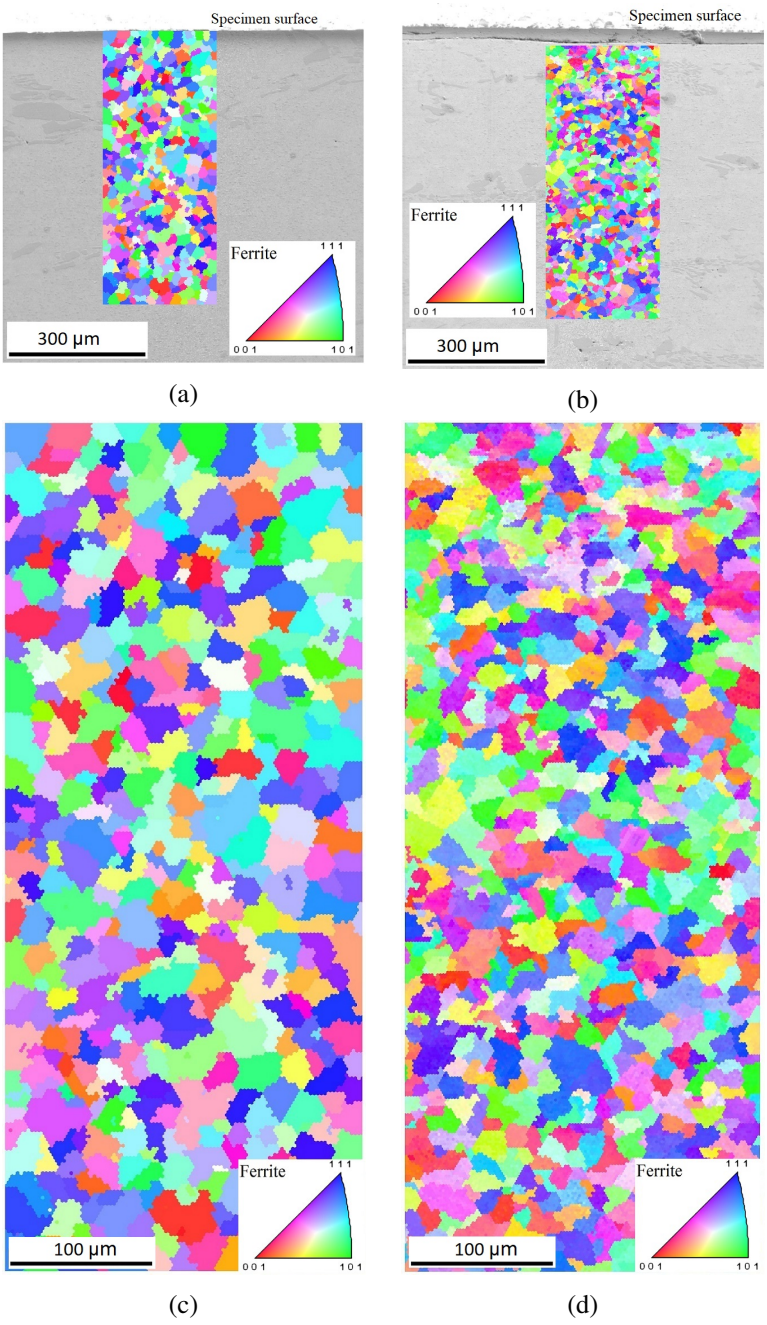


Figure 4.31: EBSD-SEM maps of the (a) BM and (b) LSP treated material (3J and 200 pulses/cm^2). EBSD maps of the (c) BM and (d) LSP treated material (3J and 200 pulses/cm^2).

refined, as shown in Figure 4.31d. A quantitative analysis is necessary, to adequately assess the effect of LSP on the microstructure of AISI D2 steel. Figure 4.32a shows the area fraction versus grain size for BM and LSP treated material. Figure 4.32b shows the number fraction versus the misorientation angle for BM and LSP treated material. Figure 4.32c shows the number fraction versus grain shape aspect ratio for BM and LSP treated material.

In Figures 4.31c and 4.31d there is clear evidence of changes in grain size. To confirm this, the calculation approach presented in subsection 3.4.3 was applied to determine the grain size diameter in BM and LSP treated material and the results are presented in Figure 4.32a. The increase in the area fraction of grains under 20 μm diameter and the significant decrease in the area fraction of grains over 20 μm diameter after LSP is shown in Figure 4.32a.

To simplify the grain size analysis, different grain size ranges were defined. All the grains within the EBSD map analysis range between 0 and 45 μm, thus intervals from 0 to 15 μm, 15 to 30 μm and 30 to 45 μm were set. Figure 4.32a shows the grain size distribution and the following findings can be highlighted as follows: (i) grains in the range size from 0 to 15 μm account for 11.80% and 34.56% of the total area for BM and LSP treated specimen, respectively. (ii) Grains within the range size from 15 to 30 μm account for 63.26% and 60.90% of the total area for BM and LSP treated specimen, respectively and (iii) grains within the range size from 30 to 45 μm account for 24.94% and 4.54% of the total area for BM and LSP treated specimen, respectively. The average grain size for BM and LSP treated material is summarized in the Table 4.4. In this regard, BM and LSP treated material show an average grain size diameter of 18.58 $\pm$ 7.05 μm and 13.48 $\pm$ 5.47 μm, respectively. As such, an average grain size diameter reduction of 27.4% was achieved after LSP treatment using laser energy of 3J and pulse density of 200 pulses/cm^2.

The formation of refined grains resulting from the ultra-high strain rate plastic deformation during LSP treatment is also reported in literature (Lu et al., 2010; Zhou et al., 2016). Whereas it is proven that LSP treatment can effectively achieve grain refinement, it is unclear the mechanism of grain refinement induced by plastic deformation during LSP on AISI D2 tool steel based on microstructural observations.

The misorientation angle provides useful information regarding the differences in the orientation of the grain boundary before and after LSP treatment. A significant difference was found between the misorientation angle exhibited before and after LSP treatment. It can be observed that 8.7% of the grain boundaries of BM exhibit low misorientation angle (< 15°). However, 91.2% of the grain boundaries of BM show high misorientation angles which range from 15° to 60°, as shown in Figure 4.32b. The BM grain boundary map and the misorientation angles are shown

Table 4.4: EBSD analysis average results.

Material condition	Grain size diameter [μm]	Misorientation angle [°]	Grain shape aspect ratio
BM	18.58 $\pm$ 7.05	38.83	0.51 $\pm$ 0.10
LSP	13.48 $\pm$ 5.47	25.84	0.49 $\pm$ 0.11

in Figure 4.33. In contrast, LSP treated material exhibits low misorientation angles at 42% of the grain boundaries and high misorientation angles at 58% of the grain boundaries (see Figure 4.32b). The grain boundary map of the LSP treated material and the misorientation angles are shown in Figure 4.34. A large number of low misorientation angles can be observed near the LSP treated surface (see Figure 4.34). Such difference, in low misorientations angles and particularly near the surface, can be attributed to laser-surface interaction, high magnitude shock waves and subsequent severe plastic strain. After LSP treatment, the coarse grains undergo a refinement by reducing their size. Figure 4.34 also suggests the sub-grain generation during LSP owing to the presence of low misorientation angles within the grain boundaries. The increasing fraction of low misorientation angle in LSP treated material demonstrates the effectiveness of LSP in the refinement of grains. Similar results were reported by Sun et al. (2018b), where grain refinement with higher percentage of low angle boundaries was achieved.

Potential variations in the grain shape, before and after the LSP application, were assessed.

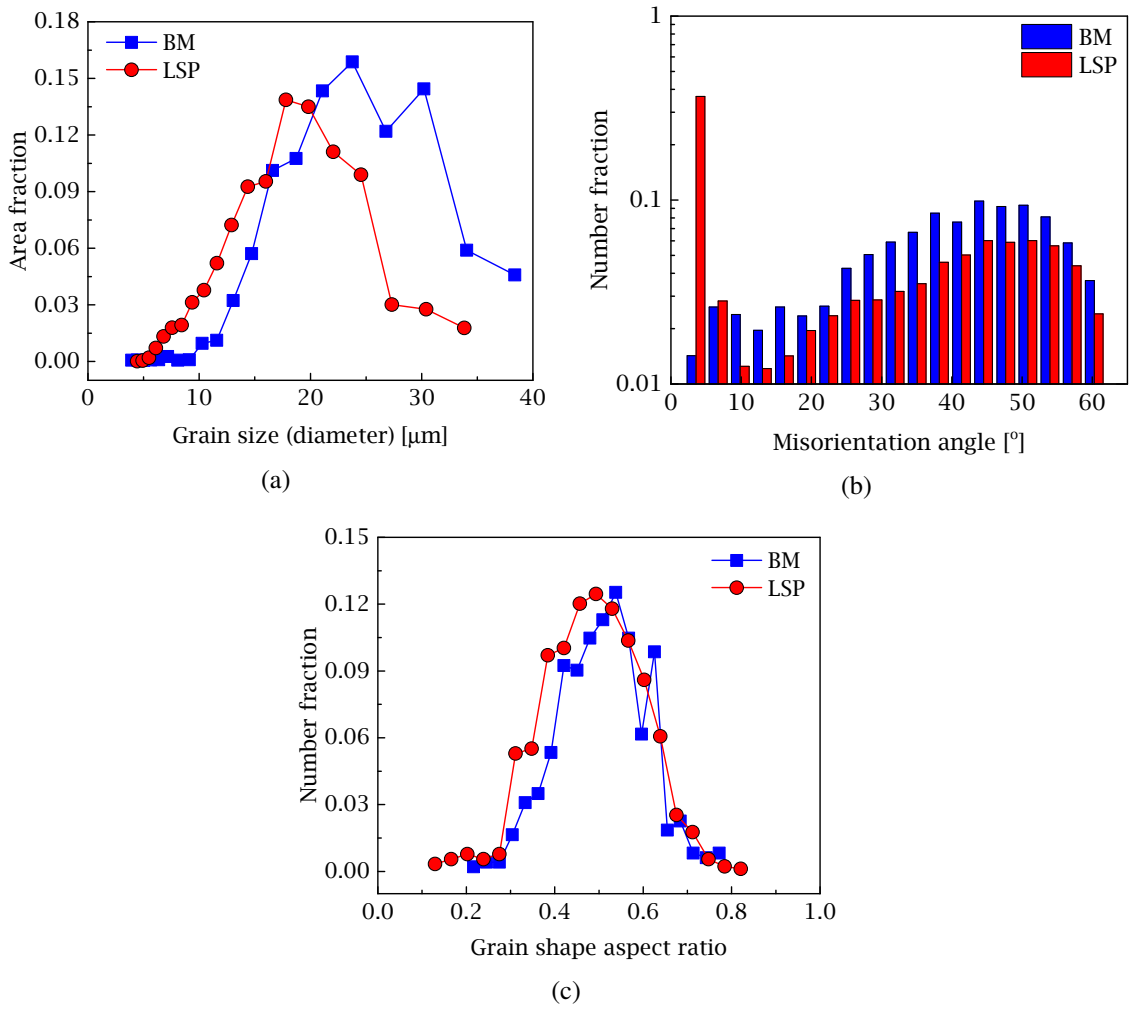


Figure 4.32: (a) Grain size, (b) misorientation angle, (c) grains shape aspect ratio of BM and LSP treated material (3J and 200 pulses/cm^2).

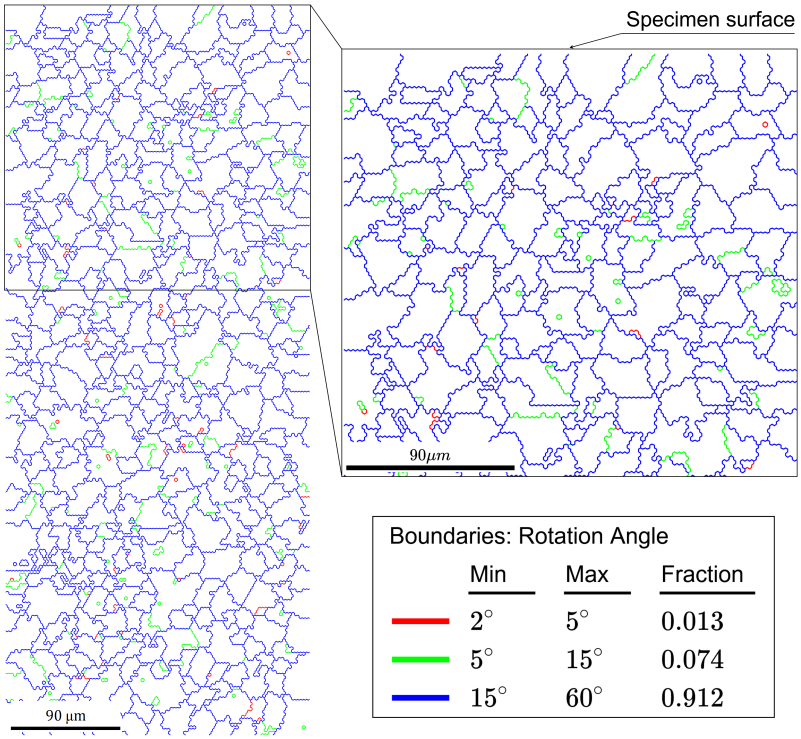


Figure 4.33: Grain boundary map of BM rotation angle.

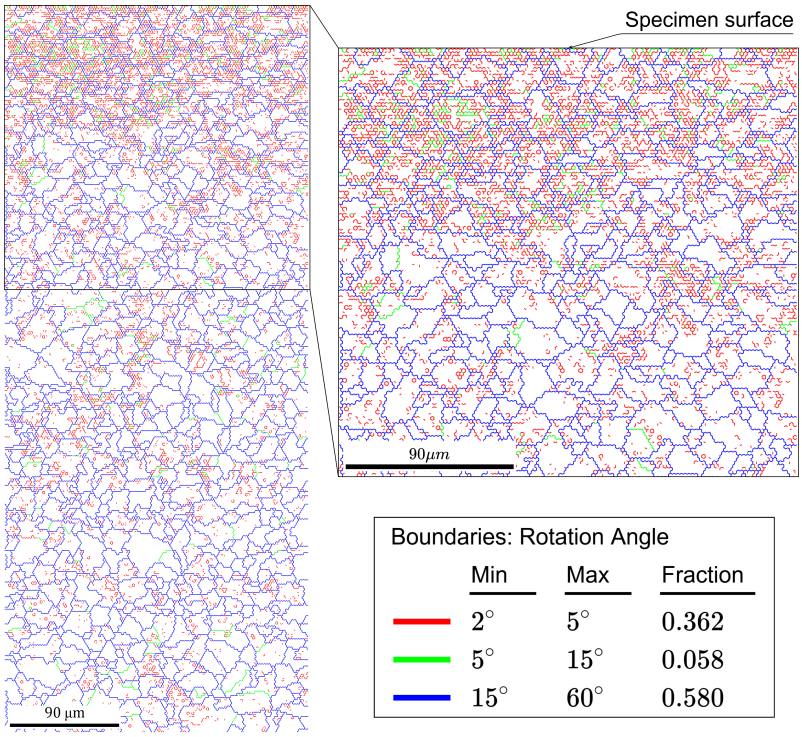


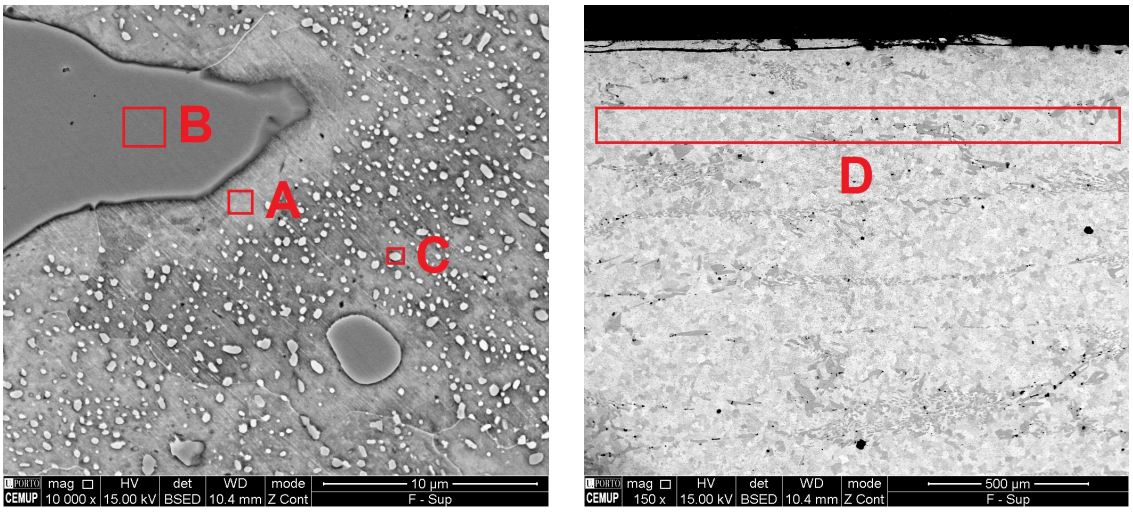
Figure 4.34: Grain boundary map of LSP treated material (3J and 200 pulses/cm^2) rotation angle.

Such changes were evaluated, according to the grain shape aspect ratio (see Figure 3.17a), as shown in Figure 4.32c. No significant grain size aspect ration changes were observed. However, the LSP treated material exhibits a slightly broader aspect ratio range, i.e. after LSP, the grains exhibit either a more elongated or a more circular shape. However, the difference in the number fraction is not significant. Furthermore, the average grain shape aspect ratio is very similar between BM and LSP treated material (see Table 4.4).

4.5.3 Energy-dispersive X-ray spectroscopy (EDS)

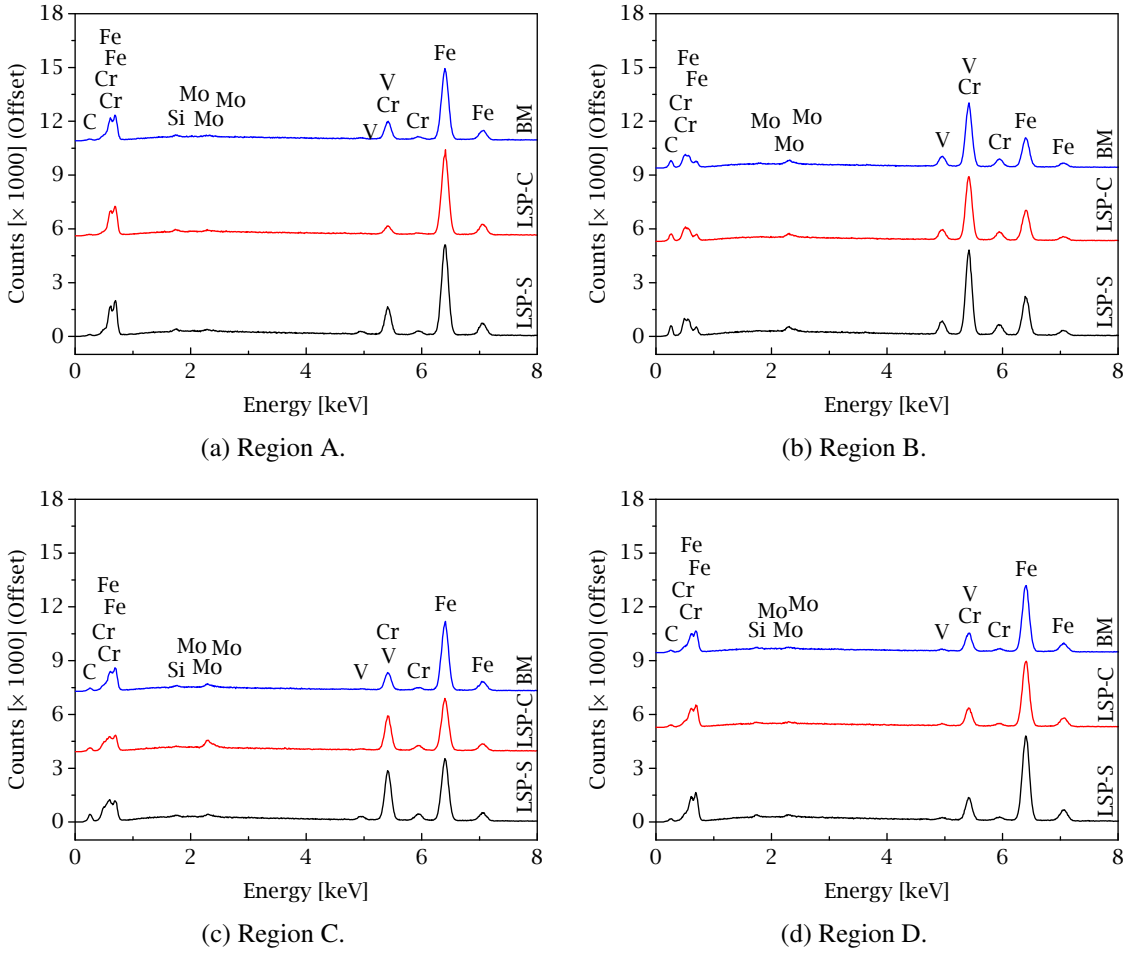
EDS analysis was performed on BM and LSP treated specimen (3J and 200 pulses/cm^2) to identify the chemical composition of microstructural features. LSP treated specimen was analyzed approximately 0.1 mm and 1 mm from the target surface, designated as LSP-S and LSP-C, respectively. The base material was analyzed, only at 1 mm from the surface, designated as BM. The typical cross-section SEM micrographs shown in Figures 4.35a and 4.35b represent the LSP-S analysis. However, these images are illustrative of the microstructural features and serve only as a reference for the identification of the regions in which EDS spectra were taken. SEM images for each material condition (BM, LSP-S and LSP-C) including the location of the EDS analysis regions and the corresponding EDS spectrum are provided in the Appendix F.2.

Three regions were selected (see Figure 4.35a), referred to as A, B and C corresponding to Fe-matrix, larger carbides and smaller spheroid carbides, respectively. Additionally, EDS was performed for a wide region identified as D, which comprises different microstructural features of material (see Figure 4.35b). Figures 4.36a, 4.36b, 4.36c and 4.36d show the EDS spectra of region A, B, C and D, respectively. The chemical composition in weight %, measured for individual EDS analysis regions within each material condition, are presented in Table 4.5.



(a) (b)

Figure 4.35: SEM/EDS images of LSP treated AISI D2 steel showing the selected region analysis (a) A, B and C, and (b) D.



(a) Region A.

(b) Region B.

(c) Region C.

(d) Region D.

Figure 4.36: EDS spectrum analysis of BM, LSP-S and LSP-C according to the selected regions (a) A, (b) B, (c) C and (d) D.

It should be mentioned that EDS analysis is not appropriate for the determination of general material chemical composition. However, EDS results, for region D (see Table 4.5), are consistent with chemical composition provided by the material supplier, as presented in Table 3.1. Also, EDS analysis shows limitations in the detection of elements with a low chemical composition, with a typical detection limit of 0.1 wt.%. Therefore, EDS is recommended for determining chemical compositions in local and homogeneous zones.

As presented in Table 4.5, the chemical composition is relatively similar for regions A and D, except for carbon content, which is higher for region D as a result of the presence of carbides within the analysed area.

A significant increase in carbon, vanadium, molybdenum and particularly chromium content is observed, in region B. Whereas the Fe content sharply decreased in comparison to the global material composition. The chromium content increase is visible in the EDS spectrum peaks presented in Figure 4.36b. Therefore, the large carbides exhibit a rich chromium and vanadium content (see Table 4.5). These findings are verified regardless of the material condition (BM, LSP-S, LSP-C).

The EDS analysis results for region C are not conclusive. The chemical composition of the

Table 4.5: Chemical composition (wt.%).

Surface Condition	Source Figure	Region	Element [wt.%]					
			C	Si	Mo	V	Cr	Fe
BM	4.36a	A	1.01	0.45	0.83	0.64	11.08	85.98
	4.36b	B	4.94	0	2.23	6.45	46.64	39.74
	4.36c	C	2.24	0.38	1.88	0.43	11.5	83.91
	4.36d	D	1.51	0.44	1.18	0.97	11.95	83.97
LSP-S	4.36a	A	0.76	0.4	0.79	1.19	12.94	83.93
	4.36b	B	4.94	0	2.07	6.36	47.31	39.33
	4.36c	C	4.34	0.28	1.3	1.72	28.05	64.31
	4.36d	D	1.72	0.41	1.07	1.07	11.48	84.25
LSP-C	4.36a	A	0.76	0.65	0.94	0	4.67	92.99
	4.36b	B	4.99	0	2.1	6.32	46.5	40.09
	4.36c	C	2.85	0	4.32	0.63	24.31	67.89
	4.36d	D	1.74	0.38	1.02	1.05	11.91	83.9

smaller carbides (analyzed in region C) shows a significant variance across the different material conditions, as shown in Table 4.5. In contrast, regions A, B and D exhibit a notably low result dispersion across the material conditions. High variance in the region C may result from a limitation of EDS, which is related to the dimension of the EDS analysis region, known as interaction volume. Therefore, the interaction volume may be larger than the selected region, which results in a non-uniform zone, containing information from the small carbide (region C) and surrounding microstructural features. Such inaccurate measurements are unlikely to affect the quantitative analysis of larger carbides (region B) or Fe matrix (region A), because, given their larger size, the interaction volume contains only information regarding these microstructural features.

According to the findings, no significant change in material chemical composition was caused by LSP.

4.6 Tensile properties

In order to observe the effect of LSP on tensile properties of the AISI D2 tool steel, uniaxial tensile testing has been carried out on BM and LSP treated specimens. Figure 4.37 shows the stress-strain curve for BM and LSP treated material.

Figure 4.37 shows the behaviour of materials containing LSP induced residual stresses compared to stress-free material. The stress-strain curves of BM show a well-defined elastic region with a 0.2% proof stress of 471 $\pm$ 19 MPa. On the other hand, no well-defined elastic region appears to exist on the stress-strain curves of LSP treated material, exhibiting a 0.2% proof stress of 438 $\pm$ 3 MPa. These findings indicate a 7% reduction in material yield stress after LSP application. Therefore, the plastic deformation gradient created by LSP results in a more extensive region of plastic behaviour. The material subject to LSP thus shows an increase in ductility when compared to the base material. A 3% enhancement of ultimate tensile strength (UTS) is verified

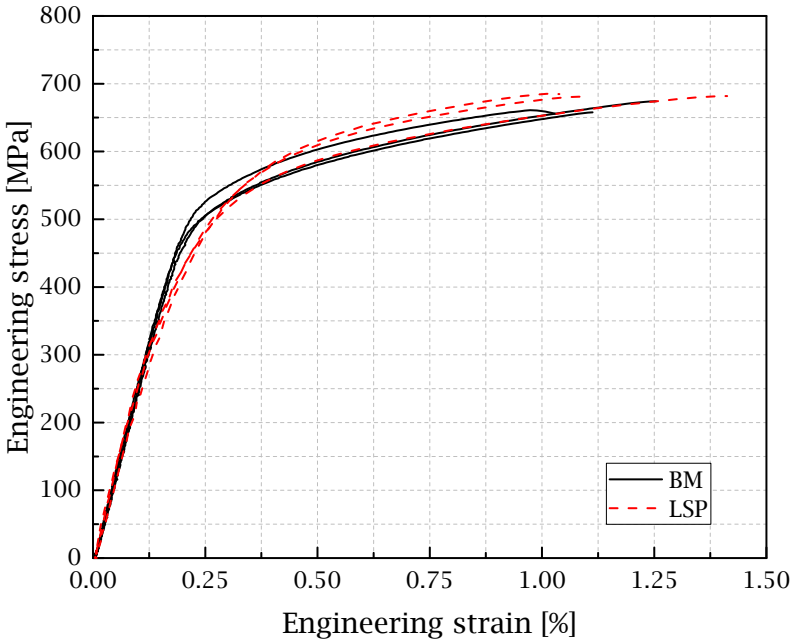


Figure 4.37: Tensile properties of BM and LSP treated AISI D2 tool steel.

for LSP treated material (682.2 ± 2 MPa) when compared to BM (662.5 ± 10 MPa). Table 4.6 presents the tensile results for each tested specimen.

Only a few studies are reported in the literature concerning the effect of LSP on tensile material properties. Out of the few studies available, the findings are not well-established yet, although an increase in the yield strength of the material has been reported (Sun et al., 2018b; Hatamleh, 2008). However, the results obtained in this work are not comparable with those reported in the literature, due to the different material choice, the different specimen geometry and LSP treatment conditions. Besides, a yield strength decrease of 7% after LSP treatment and an increase of 3% in UTS after LSP is no significant variation. A variability of less than 3% was found between values within each set of BM and LSP treated specimens.

Based on the residual stress results discussed in Section 4.2, the base material may be considered as a stress-free material since its residual stress profile remains approximately neutral. Conversely, the compressive residual stress has increased significantly in LSP treated material. Accordingly, the LSP treated material is strongly influenced by high compressive and tensile residual stresses. It should be noted that the balance of the overall stress state of the material is maintained

Table 4.6: Tensile properties of BM and LSP treated AISI D2 specimens.

Material properties	BM			Average ±SD	LSP			Average ±SD
0.2% Yield Strength [MPa]	463.4	492.2	456.6	470.7 ± 18.9	437.5	435	440.6	437.7 ± 2.8
Ultimate Tensile Strength [MPa]	657.8	655.7	674.2	662.6 ± 10.1	680.5	681.8	684.6	682.3 ± 2.1

by the tensile stress at the core of the material, balancing the compressive stresses induced by LSP on the surfaces. The magnitude of the equilibrium tensile stress reaches a peak at a level just below the depth of LSP induced compressive residual stresses, and the value of this stress increases as the thickness of the material decreases as most of the material available to balance the compressive stresses is reduced. As previously mentioned, the dogbone specimens (S-DB) feature a thickness of 3 mm and were treated with LSP on both sides. From the residual stress results discussed in Section 4.2, it is observed that for the treatment condition applied to dogbone specimens, the material is under compressive residual stress down to a depth of approximately 1 mm. As a result, the bulk material available to accommodate the equilibrium tensile residual stress decreases. Given the above information, it is reasonable to assume that a high tensile residual stress concentration is present in a thin section of the material core, which adversely affected the material's yield strength. Whereas the high degree of compressive residual stress induced by LSP may significantly enhance fatigue strength, it is important to avoid excessive compressive stress depth to such point that the equilibrium tensile stresses act as fatigue limiting agents. Therefore a maximum depth of compression effect needs to be established based on the material thickness. This may be problematic in the case of thin parts.

The residual stresses on homogeneous materials, arise from the non-uniform plastic deformation distribution. Thereby, the treated specimen developed a non-uniform distribution of cold-work in its transverse section resulting from the application of LSP. The influence of the non-linearity in the performance of the specimen, under uniaxial loading, starts once any portion of the cross-section begins to flow plastically. The non-uniformity of the LSP treated material may have decreased during tensile testing given that the tensile test introduces a uniform plastic deformation. In other words, the initial non-uniformity of the LSP treated material was likely partially mitigated by the increasing accumulation of plastic deformation resulting from the tensile testing.

4.7 Fatigue behaviour

LSP introduces plastic deformation into the superficial layer of the material and may be used to prevent fatigue problems or to delay the effects of fatigue which are already occurring in a structure or component. After LSP treatment, compressive residual stresses are left in a surface layer that can exceed 1 mm in thickness, as presented in section 4.2. These residual stresses do not affect the cyclic shear stresses, and cyclic sliding can still be observed. Additionally, it can lead to micro-cracks (Schijve, 2009). However, the compressive residual stresses can reduce or prevent micro-crack initiation. As a consequence, the stress concentration at the crack tip is lower and the crack growth can be delayed or possibly inhibited. Thus, the surface layer under the influence of compressive residual stress can act as a barrier to micro-crack initiation and growth.

The number of fatigue cycles depends on the material condition and stress amplitude applied during the tests. The threshold between high and low-cycle fatigue is not strictly defined by a given cycle count. However, it is often referred to as low-cycle fatigue if the number of cycles is in the range up to 10^4 cycles, which is associated with high-stress amplitudes. If the number

of fatigue cycles exceeds 10^5 cycles, high-cycle fatigue is commonly assumed. This regime is usually associated with stress amplitudes well below the material yield strength (σ_Y). Figure 4.38 shows the S-N results of fatigue tests for BM and LSP treated specimens.

The LSP treated specimens exhibit higher fatigue strength when compared to BM specimens. However, the difference is not significant for stress amplitudes near to and above the yield strength (σ_Y) of AISI D2 tool steel. This is caused by the non-uniform stress distribution and rapidly accumulating plastic deformation on the double edge notch, which is the fatigue critical location under cyclic loading, caused by high-stress amplitudes on both material conditions. Therefore, the major distinction between both fatigue regimes is that low-cycle fatigue is associated with macro plastic deformation occurring in every cycle. Conversely, high-cycle fatigue is mostly associated with a macro scale material elastic response. The beneficial effect of LSP induced compressive residual stress is not observed, at high stress amplitude fatigue testing, due to the stress relaxation from rapid accumulation of plastic deformation during cyclic loading.

The difference in the fatigue cycles to failure between BM and LSP treated specimens gets noticeable at high-cycle fatigue regime. For a total of 10^7 cycles (run-out), BM and LSP treated specimens exhibited a fatigue resistance of 250 MPa and 300 MPa, respectively. Results indicate a 20% improvement of fatigue resistance in LSP treated specimen. A significant improvement in fatigue cycles to failure was found for a stress amplitude of 325 MPa. This stress amplitude (325 MPa) was selected to compare the number of fatigue cycles because it exhibits the largest difference in the number of cycles between both material conditions. The number of fatigue cycles to failure for BM was 99397 cycles and for LSP treated material was 714584 cycles, achieving an impressive increase of 7.2 times in the number of fatigue cycles to failure for LSP treated material

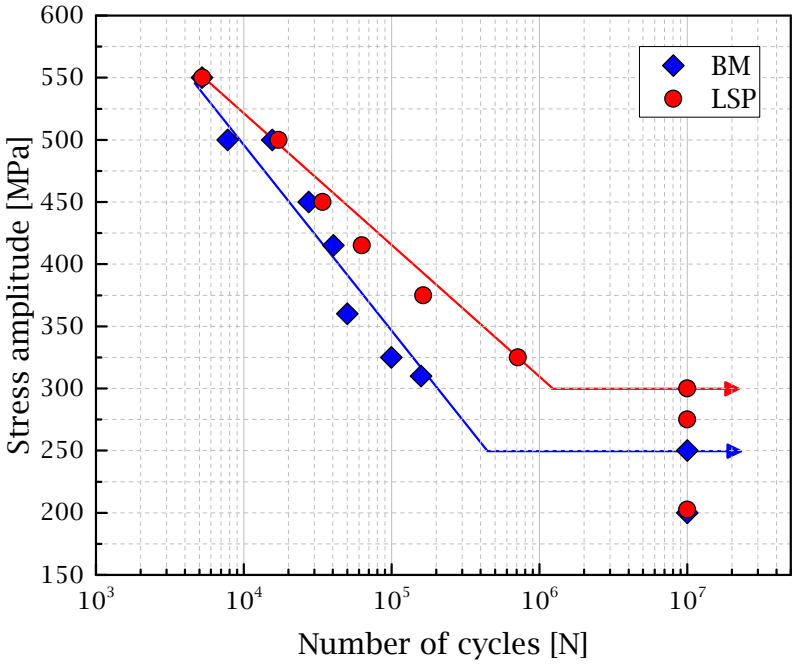


Figure 4.38: Fatigue testing results for BM and LSP treated AISI D2 specimens.

working at approximately 31% below the yield strength threshold.

The microstructural analysis performed using OM has been inconclusive regarding the material modifications that can support fatigue testing results. Furthermore, the microstructure of AISI D2 steel, particularly the strong presence of largely dispersed carbides in the ferritic matrix undermines fatigue resistance, since these large carbides can act as internal flaws, crack initiation zones and stress concentration sites. After LSP treatment, cracking of large carbides near the surface was observed, suggesting the presence of internal flaws and a consequent reduction in fatigue strength. However, Figure 4.38 demonstrates that LSP can effectively improve fatigue resistance. The analysis of the EBSD maps provided more evidence regarding microstructural modifications after LSP treatment. Grain refinement (27.4% of average gran size reduction) was observed after LSP along with increasing low misorientation angle near the surface, suggesting sub-grain formation. Therefore, grain refinement in combination with the beneficial effect of compressive residual stresses and work hardening layer can be considered as the strengthening mechanism responsible for fatigue resistance improvement (Lu et al., 2011; Ye et al., 2011; Wang et al., 2016; Yella et al., 2019).

It is well established that residual stresses generally affect the fatigue strength of materials, depending on the sign of the residual stresses in the direction of the fatigue loading, and on the onset of a fatigue crack. Thus, tensile residual stresses decrease fatigue strength, whereas compressive residual stresses can improve fatigue strength. However, it is difficult to accurately assess the role of residual stresses in fatigue strength since LSP typically modifies the material properties, and the material fatigue strength depends on these properties. Also, the magnitude of residual stresses may change during fatigue testing as a result of the mechanisms of fatigue crack initiation and propagation. Although LSP effectively induces compressive residual stresses, it also increases the material hardness near the surface. Hence, as the fatigue strength of most materials increases with their strength and hardness, it is difficult to determine to which extent the improvement in fatigue strength is attributed to compressive residual stress, and which part is attributed to increased surface strength. In addition, the materials may suffer mechanical relaxation during fatigue testing, which reduces the surface strength of the material as well as the magnitude of the residual stress.

According to the findings regarding the tensile properties of BM and LSP treated material (Figure 4.37), LSP treatment caused a 7% decrease in the yield strength of the material, which suggests that the fatigue strength increase may be attributed to compressive residual stress. These findings demonstrate that LSP treatment with the parameters adopted can substantially enhance the fatigue resistance of AISI D2 tool steel. These results are consistent with several studies showing that improved fatigue life after LSP is more effective at high cycle regime (HCR) than for a low cycle regime (LCR) (Yella et al., 2019; Ye et al., 2011; Correa et al., 2015a). Despite the fact that the quantitative contribution of the residual stresses cannot be accurately assessed, compressive stresses are generally considered to improve strength. As a result, surface modification techniques such as LSP find application in improving the fatigue strength of metals.

4.7.1 Fractography observations

A microfractographic analysis was performed to understand the microstructural features of fatigue fractured specimens with high residual stresses induced by LSP treatment as well as BM specimens. The microfractographic SEM examination of the respective specimens was carried out at three positions: left side edge region, core region and right side edge region (see Figure 4.39).

The fracture surfaces in the LSP treated specimens were observed close to the surface, i.e. top left and top right edge regions. The magnifications specified were 27× for macro representations, 500× for overviews and 5000× and 3000× for detail representations. Table 4.7 presents the list of examined specimens.

Each image set provides the fracture surface corresponding to the edge region of the left side, core region and the edge region of right side for BM and LSP treated specimens. Figures 4.40, 4.41 and 4.42 show the overview of BM and LSP fractured surfaces (σ_{max} = 500 MPa) at magnifications of 27×, 500× and 5000×, respectively. Figures 4.43, 4.44 and 4.45 show the overview of BM and LSP fractured surfaces (σ_{max} = 325 MPa) at magnifications of 27×, 500× and 5000×, respectively.

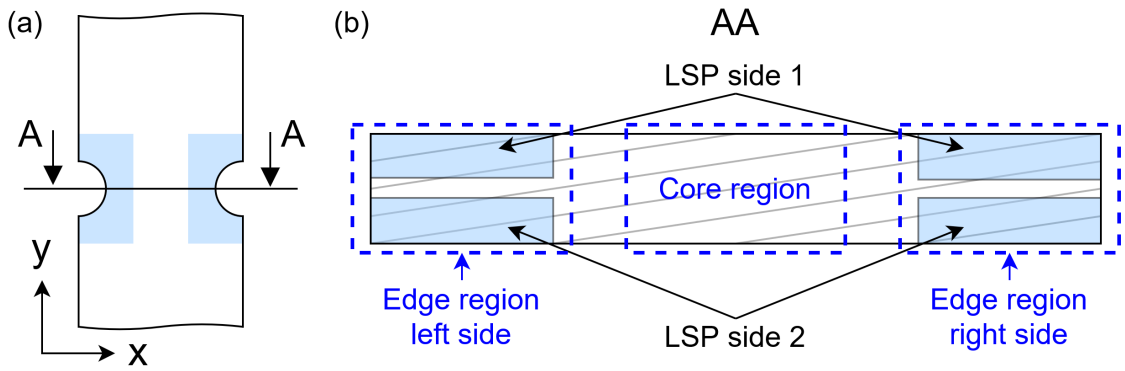


Figure 4.39: Schematic representation of (a) fatigue fracture location on dogbone specimens (S-DB) and (b) distinct SEM observed regions within the fracture surface. The edge regions on the left and right sides correspond to LSP application zones.

Table 4.7: List of examined fractured fatigue specimens.

Specimen ID	Stress amplitude [MPa]	Cycles to failure [N]	Material condition
S-DB-17	500	7760	BM
S-DB-1	500	17158	LSP
S-DB-22	325	99397	BM
S-DB-6	325	714584	LSP

In Figure 4.40(a), the distance from the left edge to the end of the fatigue fracture surface is about 0.5 mm and the remaining fracture surface exhibits a linear structure. Figure 4.40(b) exhibits a flat fracture surface that merges into the linear residual fracture surface. In contrast to BM specimen (S-DB-17), the proportion of the fatigue fracture surface appears higher (2 mm). Figures 4.40(c) and 4.40(d) show the core region of BM (S-DB-17) and LSP treated specimen (S-DB-1), respectively. Figures 4.40(e) and 4.40(f) show the edge region on right side of BM (S-DB-17) and LSP treated specimen (S-DB-1), respectively.

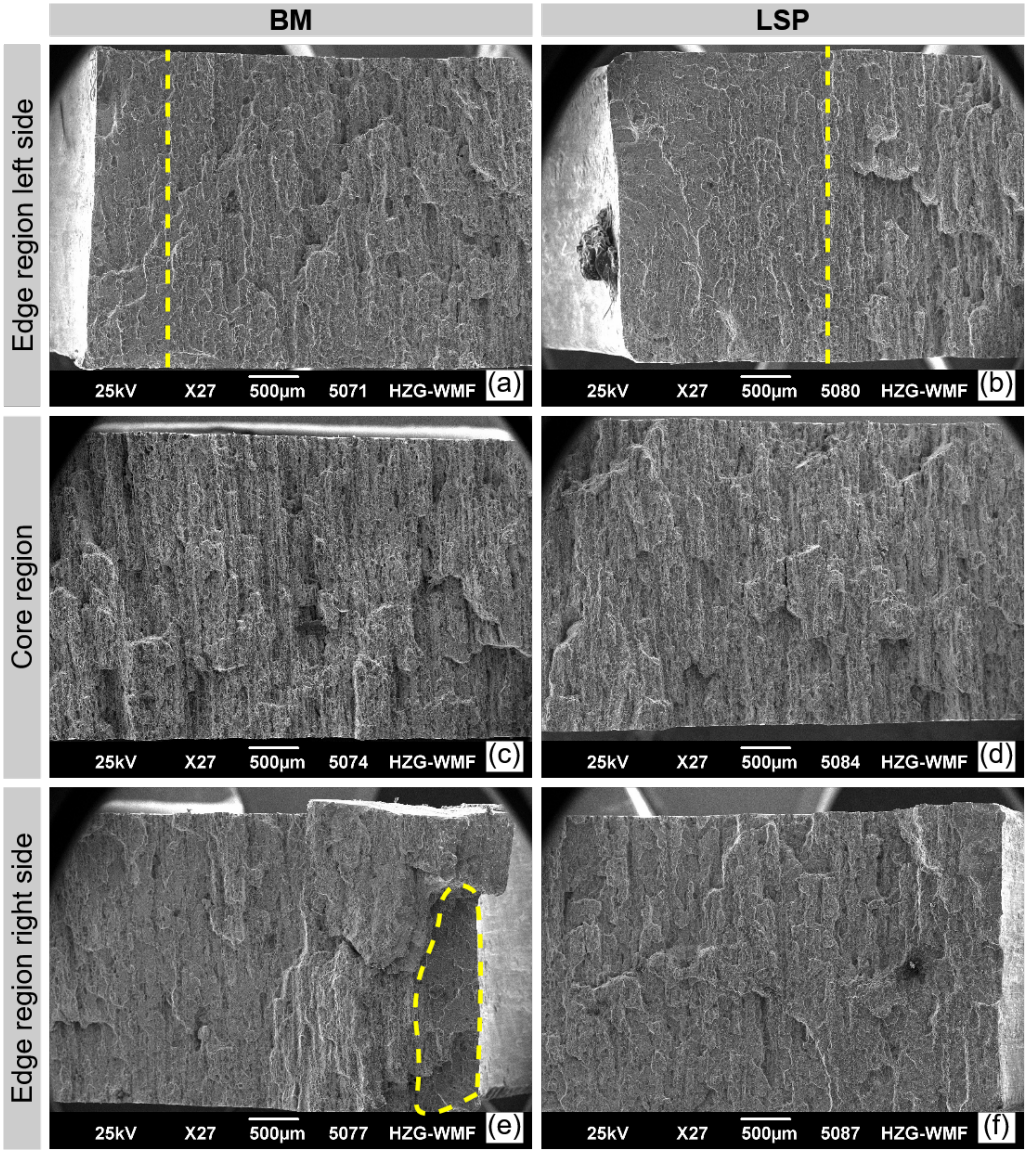


Figure 4.40: Macro representations of the fractured surfaces at 27× magnification. (a, c and e) for the BM specimen (S-DB-17); and (b, d and f) for the LSP treated specimen (S-DB-1).

Figures 4.41(a) and 4.41(b) exhibit chromium carbides (arrows) embedded in a fine crystalline ferritic matrix. Chromium carbides are smooth suggesting brittle fracture. Figures 4.41(c) and 4.41(d) show the core region of BM (S-DB-17) and LSP treated specimen (S-DB-1), respectively. The surface fracture in the core region exhibits tear ridges on both material conditions, indicating ductile fracture. The dimples diameter and depth are small and transcrystalline brittle fracture in the chromium carbides (arrows) is observed. Figure 4.41(e) exhibits chromium carbides (arrows) embedded in a fine crystalline ferritic matrix and 4.41(f) shows the position top right in LSP influenced area where transcrystalline oscillation break area (circled) is observed.

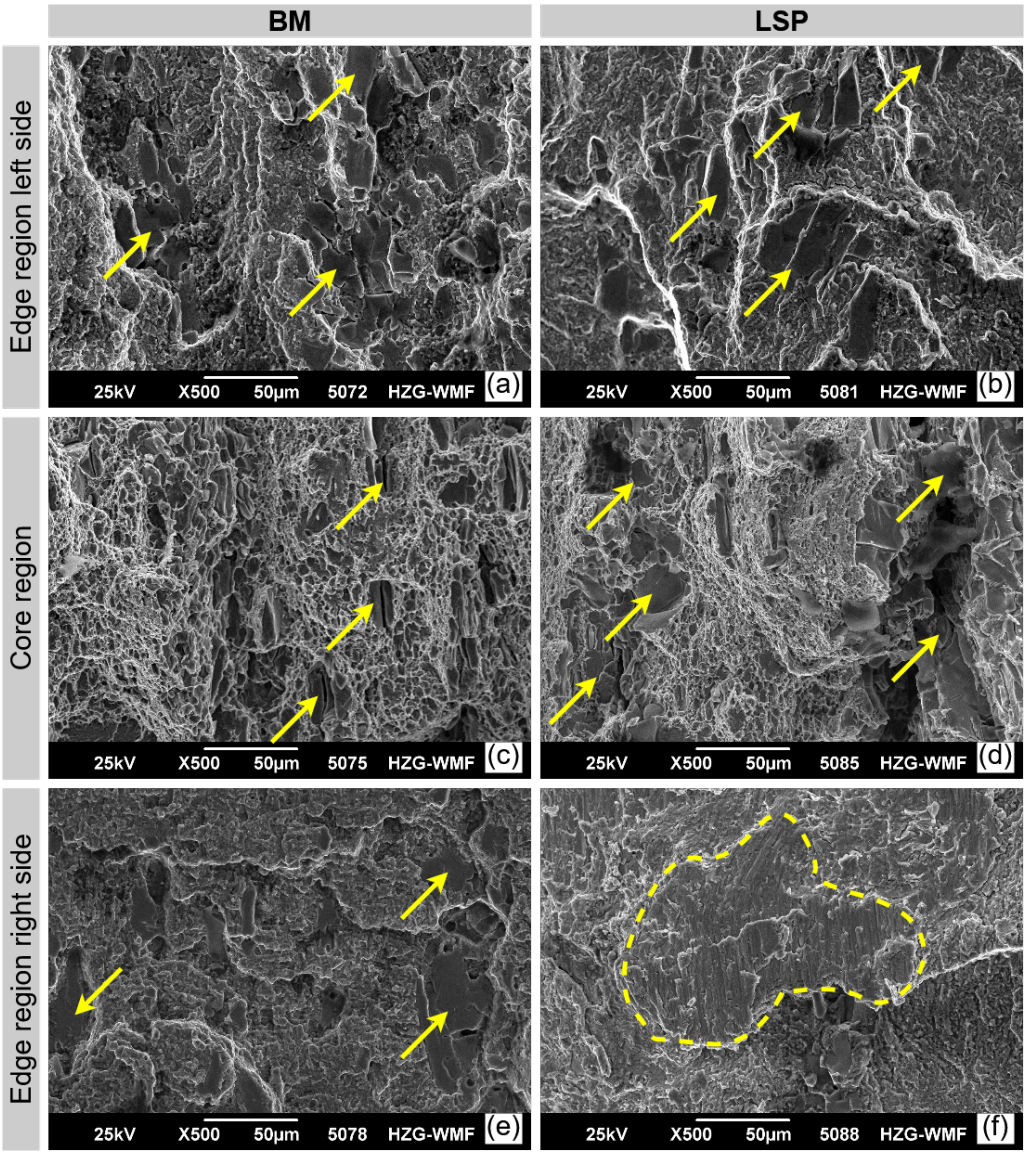


Figure 4.41: Overview of the fractured surfaces at 500× magnification. (a, c and e) for the BM specimen (S-DB-17); and (b, d and f) for the LSP treated specimen (S-DB-1).

Figure 4.42(a) exhibits smooth facets indicating an intercrystalline fracture, an embedded transcrystalline fractured area with weakly pronounced oscillating stripes (circled), and transcrystalline brittle fracture in chromium carbide (arrow). Figure 4.42(b) shows transcrystalline oscillation fracture and transcrystalline brittle fracture in chromium carbide (arrow). Figure 4.42(c) exhibits transcrystalline ductile fracture with carbide inclusions, smooth honeycomb walls (tear ridges), and transcrystalline brittle fracture in chromium carbide with secondary cracks (arrow). Figure 4.42(d) shows transcrystalline ductile fracture with carbide inclusions and transcrystalline brittle fracture in chromium carbide (arrow). In Figure 4.42(e), the smooth appearing fracture surface at the right edge of (S-DB-17) shows a transcrystalline fatigue fracture with intercrystalline fracture (arrows). Figure 4.42(f) exhibits transcrystalline oscillation fracture adjacent to intercrystalline oscillation fracture.

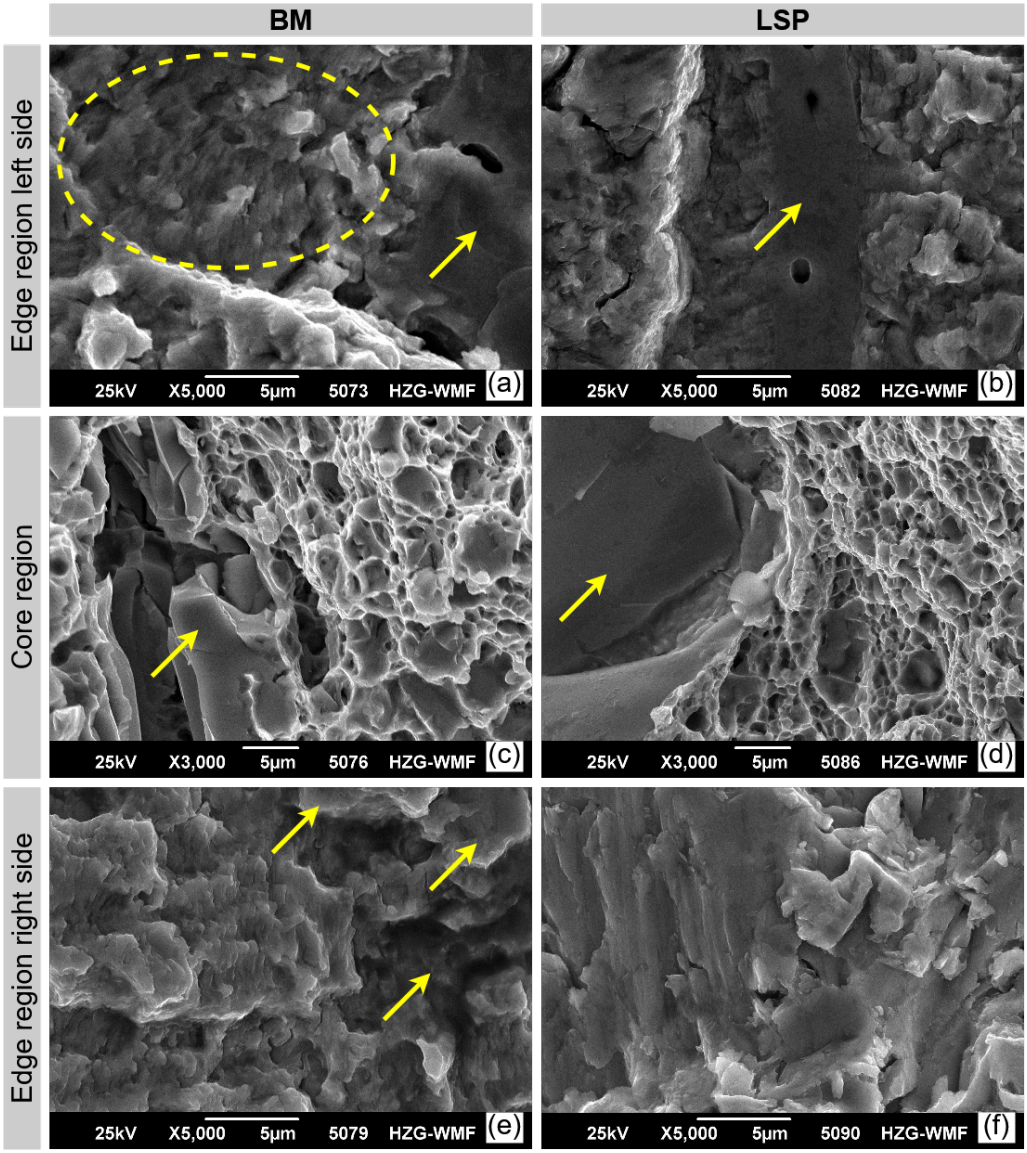


Figure 4.42: Detail representations of the fractured surfaces at 5000× magnification. (a, c and e) for the BM specimen (S-DB-17); and (b, d and f) for the LSP treated specimen (S-DB-1).

Figures 4.43(a) and 4.43(b) show the fatigue fracture surface (left side) of BM (S-DB-22) and LSP treated specimen (S-DB-6), respectively. The proportion of fatigue fracture in LSP treated specimen (S-DB-6) area appears larger at approximately 3 mm (yellow line), as compared to BM specimen (S-DB-22). Figures 4.43(c) and 4.43(d) show the core region (remaining line break area) of BM (S-DB-22) and LSP treated specimen (S-DB-6), respectively. Figure 4.43(e) shows the linear fracture surface on the edge region (right side) of BM specimen (S-DB-22). Figure 4.43(f) exhibits the remaining fracture surface on the edge region (right side) of LSP treated specimen (S-DB-6).

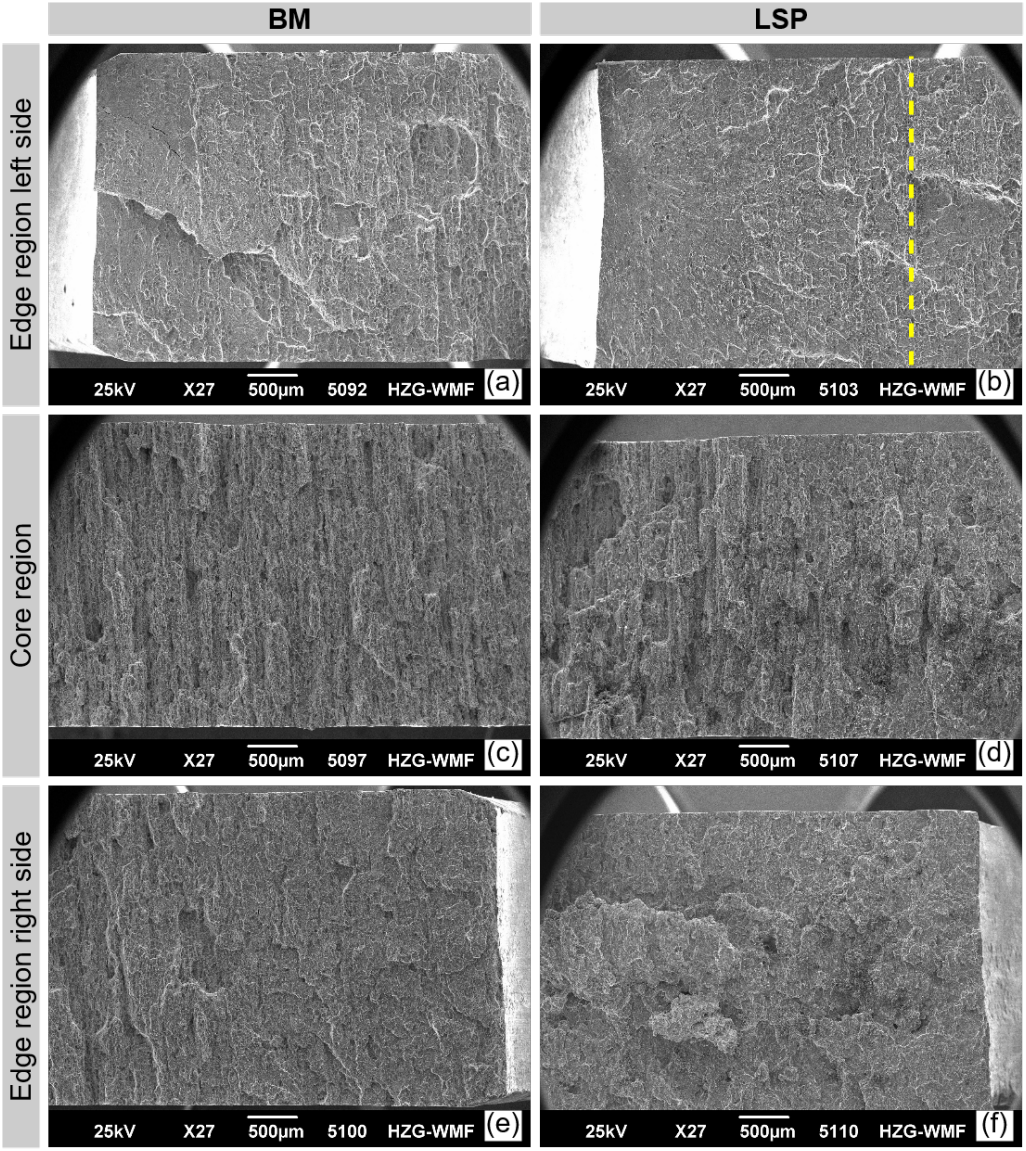


Figure 4.43: Macro representations of the fractured surfaces at 27× magnification. (a, c and e) for the BM specimen (S-DB-22); and (b, d and f) for the LSP treated specimen (S-DB-6).

Figure 4.44(a) exhibits chromium carbides (arrows) embedded in a fine crystalline ferritic matrix and the fracture surface of the chromium carbides are rough. Figure 4.44(b) shows the top left region in the LSP influenced area where a fine crystalline ferritic matrix can be observed as well as isolated chromium carbides. Figures 4.44(c) and 4.44(d) show a honeycomb (tear ridges and dimples) ductile fracture where the dimples diameter and depth are small. Also, transcrystalline brittle fractures can be observed in the chromium carbides (arrows). Figure 4.44(e) exhibits accumulation of chromium carbides and transcrystalline brittle fractures in the chromium carbides. Figure 4.44(f) shows the top right region in the LSP influenced area exhibiting intercrystalline oscillation fracture.

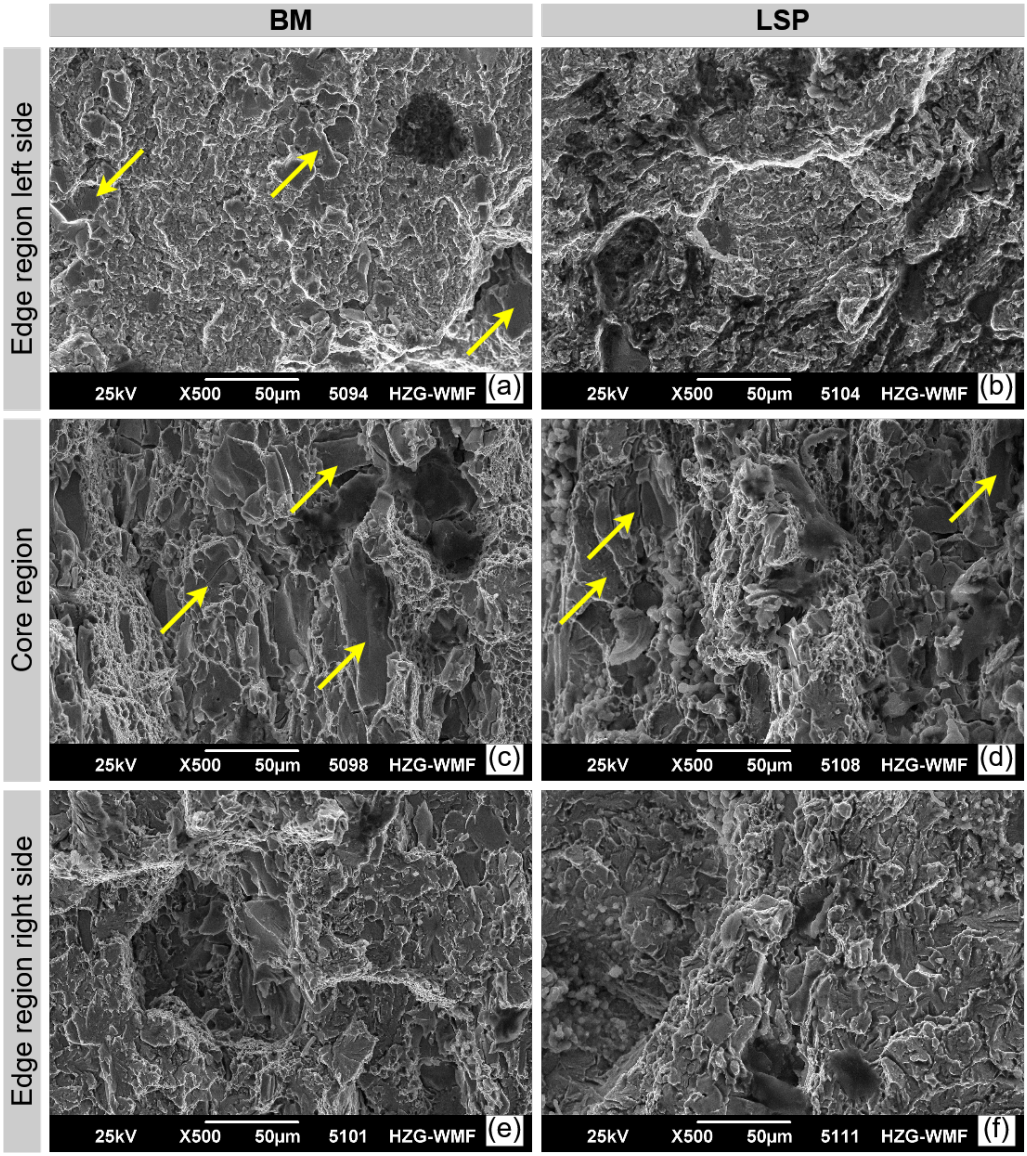


Figure 4.44: Overview of the fractured surfaces at 500× magnification. (a, c and e) for the BM specimen (S-DB-22); and (b, d and f) for the LSP treated specimen (S-DB-6).

Figure 4.45(a) exhibits transcrystalline oscillation fracture in the ferritic matrix and rough fracture structure in the chromium carbides (arrows) can be observed. Figure 4.45(b) shows the top left region in the LSP influenced area. Transcrystalline oscillation fracture can be observed. Figures 4.45(c), 4.45(d) and 4.45(e) exhibit transcrystalline ductile fracture with carbide inclusions, smooth honeycomb (tear ridges and dimples) walls and transcrystalline brittle fracture in chromium carbides with secondary cracks (arrow). Figure 4.45(f) shows the top right region in LSP influenced area where intercrystalline oscillation fracture can be observed.

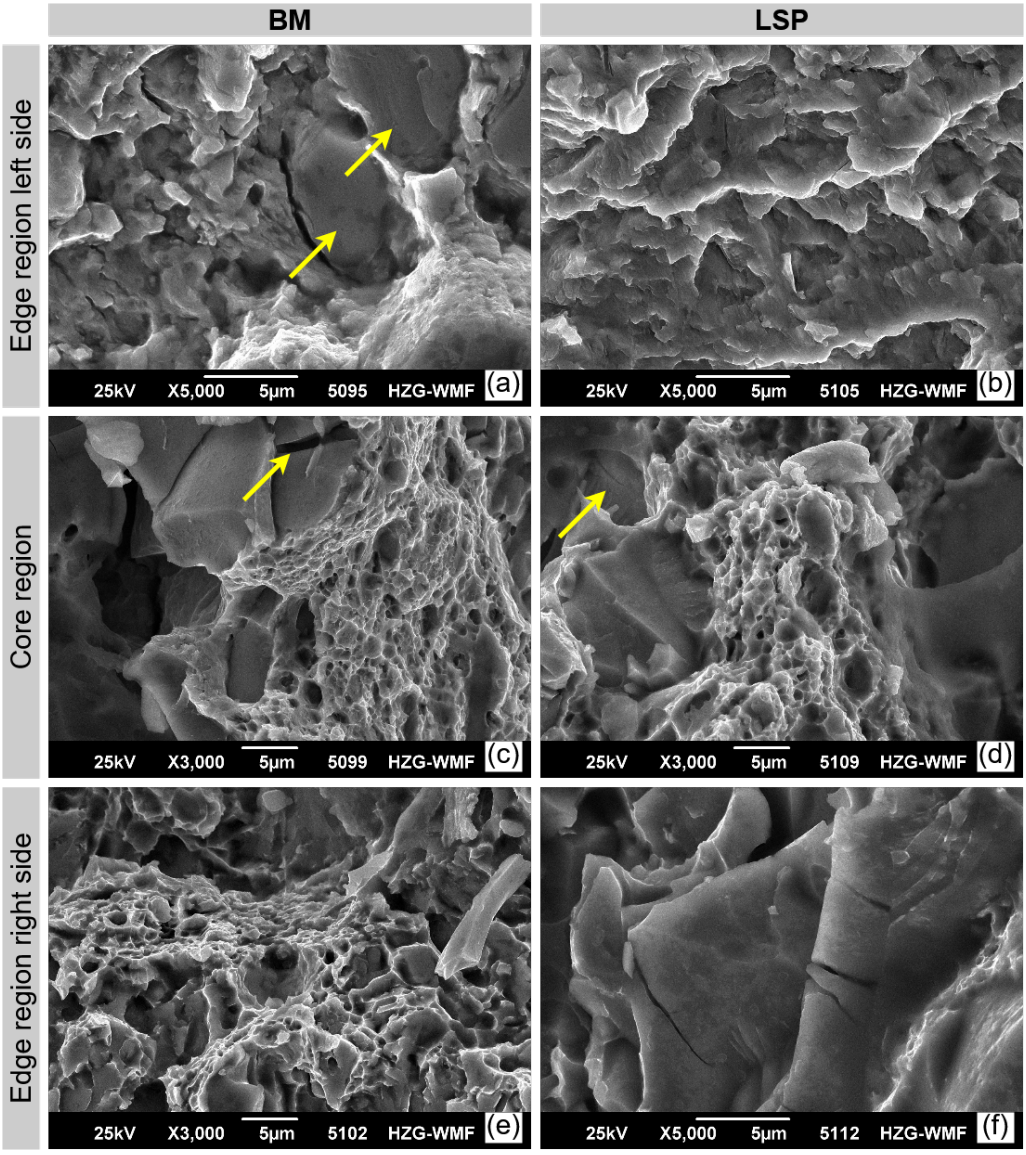


Figure 4.45: Detail representations of the fractured surfaces at 5000× magnification. (a, c and e) for the BM specimen (S-DB-22); and (b, d and f) for the LSP treated specimen (S-DB-6).

From the microfractographic analysis of BM and LSP treated specimens, several features can be observed, which are highlighted below:

- BM specimen (S-DB-17)
  - **Edge region of the left side** (see Figures 4.40(a), 4.41(a) and 4.42(a)): Intercrystalline oscillation fracture with transcrystalline fracture components and transcrystalline brittle fracture in the enclosed chromium carbides. The oscillation stripes and oscillation lines typical for a fatigue fracture are not pronounced in the fracture surface section considered.
  - **Core region** (see Figures 4.40(c), 4.41(c) and 4.42(c)): Characteristic for the residual fracture surface is a transcrystalline-ductile fracture at low deformation and transcrystalline brittle fracture in the chromium carbides.
  - **Edge region of the right side** (see Figures 4.40(e), 4.41(e) and 4.42(e)): Transcrystalline oscillation fracture with intercrystalline fracture fraction. The oscillation stripes and oscillation lines typical for a fatigue fracture are not pronounced in the fracture surface section considered.
- LSP specimen (S-DB-1)
  - **Edge region of the left side** (see Figures 4.40(b), 4.41(b) and 4.42(b)): Fracture surface shows a transcrystalline oscillation fracture. Compared to S-DB-17, the morphological character of the fatigue fracture is more pronounced and the proportion of the fatigue fracture surface is higher.
  - **Core region** (see Figures 4.40(d), 4.41(d) and 4.42(d)): Transcrystalline ductile fracture at low deformation and transcrystalline brittle fracture in the chromium carbides.
  - **Edge region of the right side** (see Figures 4.40(f), 4.41(f) and 4.42(f)): Transcrystalline and intercrystalline fatigue fracture in the LSP influenced area.
- BM specimen (S-DB-22)
  - **Edge region of the left side** (see Figures 4.43(a), 4.44(a) and 4.45(a)): Transcrystalline oscillation fracture, chromium carbides exhibit a rough transcrystalline fracture structure.
  - **Core region** (see Figures 4.43(c), 4.44(c) and 4.45(c)): Characteristic for the residual fracture surface is a transcrystalline-ductile fracture at low deformation and transcrystalline brittle fracture in the chromium carbides.
  - **Edge region of the right side** (see Figures 4.43(e), 4.44(e) and 4.45(e)): In the area to the right of S-DB-22 the brittle fracture character predominates due to accumulation of chromium carbides.
- LSP specimen (S-DB-6)

- **Edge region of the left side** (see Figures 4.43(b), 4.44(b) and 4.45(b)): Fracture surface shows a transcrystalline oscillation fracture. Compared to S-DB-22, the morphological character of the fatigue fracture is more pronounced and the proportion of the fatigue fracture surface is higher.
- **Core region** (see Figures 4.43(d), 4.44(d) and 4.45(d)): Characteristic for the residual fracture surface is a transcrystalline-ductile fracture at low deformation and transcrystalline brittle fracture in the chromium carbides.
- **Edge region of the right side** (see Figures 4.43(f), 4.44(f) and 4.45(f)): Intercrystalline oscillation fracture in the LSP influenced area.

In summary, the LSP influence is evident in the increase in the proportion of the fatigue fracture area relative to the total fracture area, i.e. the mean crack length was greater. Transcrystalline and partly intercrystalline fatigue fractures can be found in the microstructure matrix. The chromium carbides show a transcrystalline brittle fracture, and their brittle fracture surfaces are generally smooth. At higher magnifications, a honeycomb structure, consisting of tear ridges and dimples, is visible. Diameter and depth of the dimples are small, which indicates a low deformation. Carbides inclusions were found in the honeycomb structure. The chromium carbides also showed a transcrystalline brittle fracture in the remaining fracture surface. The fatigue fracture started from the edges of the respective specimens. However, the crack propagation was not symmetrical. The distribution of the chromium carbides on the respective fracture surfaces of specimens S-DB-1, S-DB-6, S-DB-17 and S-DB-22 was uneven.

4.8 Fatigue crack propagation

The effect of laser shock peening on fatigue crack propagation was studied in M(T) specimens of AISI D2 tool steel. The specimens were subjected to LSP and cyclic loading for fatigue crack propagation. The high levels of compressive residual stresses found on the specimen surface are predictive of considerable retardation of cracking as it reaches the treatment site. However, compressive residual stress fields are always associated with balancing tensile stress fields, which may eliminate any improvement caused by compression. This tensile core of the material, which emerges as a by-product of LSP, is essential for the equilibrium of the internal forces in the unloaded part.

When dealing with LSP treated specimens, the superimposition of applied stresses and residual stresses may result in inaccurate predictions. Therefore, a three-dimensional analysis incorporating the residual stress values obtained may be necessary to increase accuracy (Chahardehi et al., 2010). Accordingly, the implementation of the residual stress intensity factor K_{res} to models for fatigue crack growth has allowed accurate estimation of the fatigue crack growth rates and service life associated to the presence of residual stresses (Keller et al., 2019a). A commonly used approach for accounting the effect of residual stress on crack growth involves using the effective

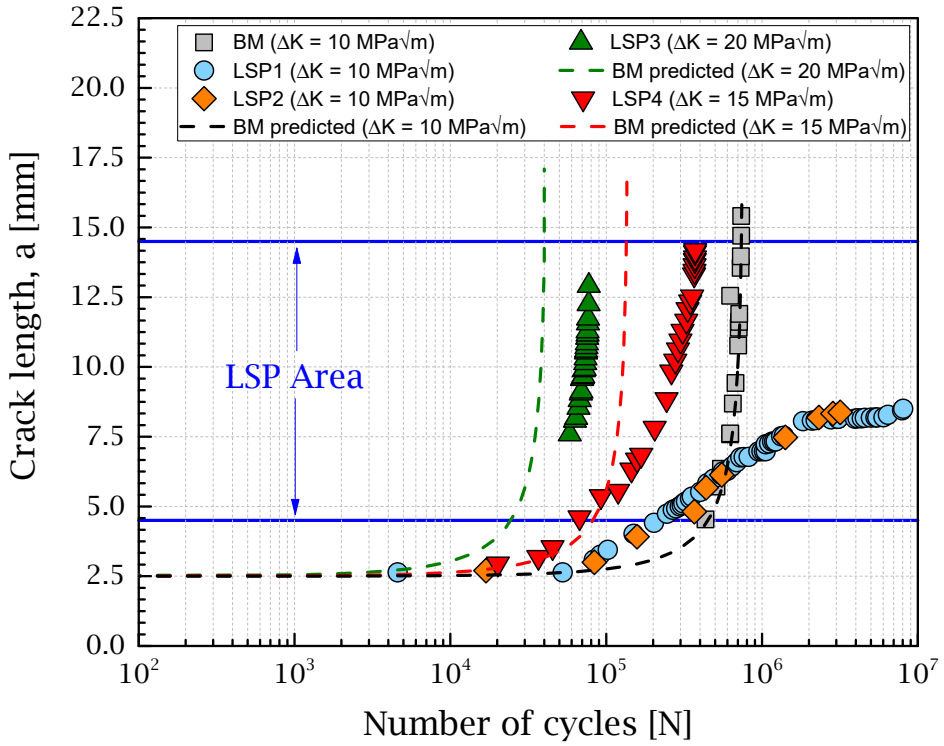
stress intensity factor, K_{eff}, which results from the initial residual stress intensity factor, K_{res}, and the applied stress intensity factor, K_{app}, i.e, $K_{eff} = K_{res} + K_{app}$.

Figures 4.46a and 4.46b show the relationship between the fatigue crack length, a, and the number of load cycles, N in AISI D2 M(T) BM specimens and LSP treated specimens. The final crack length and corresponding number of cycles for BM and LSP treated specimens according to initial crack length and SIF range are presented in Table 4.8. During the FCP testing, the crack length was monitored by an optical microscope and a crack opening displacement (COD) gauge device.

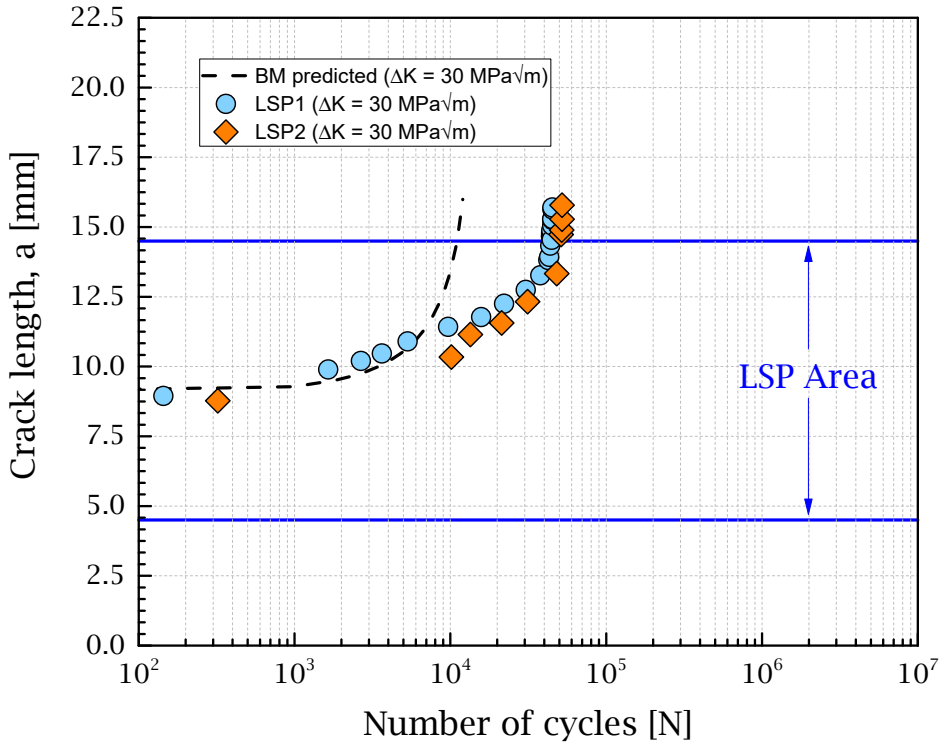
At the early testing stage ($a_0 = 2.5$ mm) a $\Delta K = 10\ MPa\sqrt{m}$ was applied on BM and LSP treated specimens. It was observed that crack length in the LSP treated specimens (LSP1 and LSP2) grow slightly faster than in the BM specimen before the crack reaching the LSP treated area. This can be due to balancing tensile residual stress from the LSP treatment. After entering the LSP treated zone, the crack length in the LSP treated specimens shows a linear growth until it stabilizes, and little variation in crack length was verified with increasing the number of cycles after 2×10^6. In contrast, the exponential growth of the crack in the BM specimen was verified. From 2×10^6 to 1×10^7 cycles, the crack length, a, for LSP1 and LSP2 specimens has remained almost constant. The final crack length of the BM specimen was 15.41 mm for a total number of 7.36×10^5 cycles, while LSP treated specimens (LSP1 and LSP2) exhibit crack lengths of 8.50 mm and 8.38 mm for 8.06158×10^6 and 3.17439×10^6 cycles, respectively. The crack growth for the BM specimen with $\Delta K = 10\ MPa\sqrt{m}$ and an initial crack length $a = 2.5$ mm was also analytically predicted according to the standard ASTM E647-08 (2008) showing good agreement with experimental results, as can be seen in the Figure 4.46a. Therefore, the effect of LSP on crack retardation is clearly visible.

Due to the stabilized crack growth for LSP treated specimens (LSP1 and LSP2), the testing has been stopped and restarted after increasing $\Delta K = 30\ MPa\sqrt{m}$ for a crack length of $a_0 = 9.0$ mm (see Figure 4.46b). Additionally, the crack length, a as a function of the number of cycles, N was predicted for BM specimen ($a_0 = 9.0$ mm and $\Delta K = 30\ MPa\sqrt{m}$). After restarting the test for LSP1 and LSP2 specimens, a final crack length of 15.7 mm and 15.78 mm was observed for a total of 45182 and 52112 cycles, respectively. A very similar trend can be observed between these specimens. Besides, a considerable increase can be observed over the estimated BM ($\Delta K = 30\ MPa\sqrt{m}$, $a_0 = 9.0$ mm) which exhibited a final estimated crack length of 16.00 mm for 12000 cycles. A comparison of the crack length of LSP treated specimens and the predicted crack length for BM specimen presented in Figure 4.46b shows an approximate increase of 2.8 - 3.3 times in the number of cycles for LSP treated material, which confirmed the potential benefit of LSP in retarding fatigue crack propagation.

One LSP treated specimen, designated LSP3, was tested for initial $\Delta K = 20\ MPa\sqrt{m}$ and $a_0 = 2.5$ mm (see Figure 4.46a). Under the same condition, the a vs N curve for BM was calculated. The LSP treated specimen (LSP3) exhibits a final crack length of 12.91 mm for 77364 fatigue cycles and the estimated BM exhibits a final crack length of 17.10 mm for 40004 fatigue cycles. This represents an increase in the number of cycles of 93.4%. Additionally, the LSP treated specimen, LSP4, was tested for initial $\Delta K = 15\ MPa\sqrt{m}$ and $a_0 = 2.5$ mm (see Figure 4.46a). Under the



(a) Initial crack length a_0 = 2.5 mm.



(b) Initial crack length a_0 = 9.0 mm.

Figure 4.46: Fatigue crack growth, *a* vs *N* for the BM and LSP treated specimens at initial crack length (a) a_0 = 2.5 mm and (b) a_0 = 9.0 mm.

same condition, the a vs N curve for the base material was calculated. The LSP treated specimen (LSP4) exhibits a final crack length of 14.18 mm for 372578 fatigue cycles and the estimated BM exhibits a final crack length of 17.16 mm for 136001 fatigue cycles. This represents an increase in the number of cycles of 174%.

The crack growth rate, da/dN, of M(T) specimens is plotted as a function of ΔK in Figure 4.47. The total FCP rate curve can be divided into crack initiation period (Stage I), crack growth period or power growth (Stage II) and final failure or instability (Stage III). This study focused on the performance of AISI D2 FCP in M(T) specimens during the region of stable crack expansion (Stage II). The growth of fatigue cracks at Stage II is no longer affected by the surface conditions of the material, but rather a phenomenon involving bulk material (Schijve, 2009). The M(T) test specimens used in this analysis are symmetrical and uni-axially loaded, leading to macroscopically perpendicular crack growth in the loading direction, as can be seen in Figure 3.28.

LSP treated specimens show a significant retardation in the FCP rate when compared to BM specimens. The decline in da/dN is evident when the crack propagates through the LSP treated area with high compressive residual stresses through the thickness. However, when ΔK increases to high values towards the end of the FCP, all specimens show a similar FCP rate. This suggests that the improvement in LSP induced FCP resistance is mainly reflected by a large increase in the early stage of FCP testing. During FCP testing, the LSP induced compressive residual stresses may cause crack closure and lower the crack driving stress intensity factor, which benefits the reduction of FCP rate (Pant et al., 2016; Kashaev et al., 2017; Sun et al., 2018a; Keller et al., 2019a). Hence, the fatigue crack retardation and the crack closure effect can be attributed to the introduction of a

Table 4.8: FCP results. Final crack length and corresponding number of cycles for BM and LSP treated specimens according to initial crack length and SIF range.

a_0 [mm]	Specimen	SIF range, ΔK [MPa$\sqrt{m}$]			
		10	15	20	30
2.5	BM	15.41 mm N = 7.36×10^5	17.16 mm N = 1.36×10^5	17.10 mm N = 4.00×10^4	
	LSP1	8.50 mm N = 8.06×10^6			
	LSP2	8.38 mm N = 3.17×10^6			
	LSP3			12.91 mm N = 7.74×10^4	
	LSP4		14.18 mm N = 3.73×10^5		
9.0	BM				16.00 mm N = 1.20×10^4
	LSP1				15.70 mm N = 4.52×10^4
	LSP2				15.78 mm N = 5.21×10^4

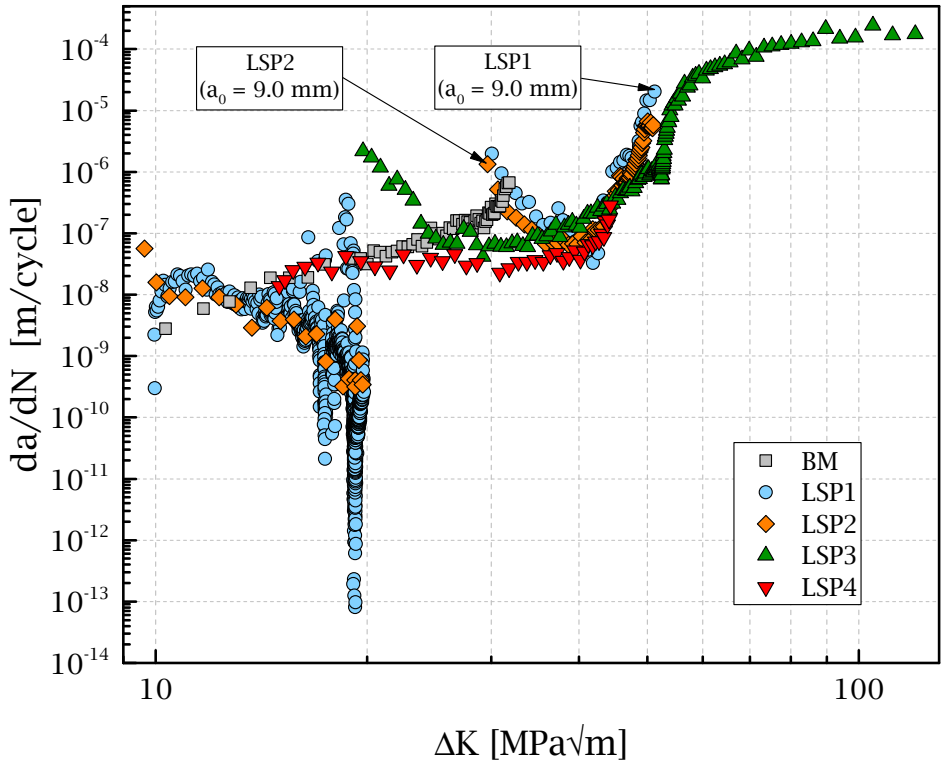


Figure 4.47: Fatigue crack growth rate, da/dN vs ΔK for the BM and LSP treated specimens.

sufficiently high compressive residual stress in a region in front of the crack tip. The effect of LSP induced compressive residual stresses can be explained according to Figure 4.48, which shows the crack closure behaviour when external loading is applied.

The LSP induced compressive stresses act towards moving the effective load ratio, R_{eff}, from positive to negative values, thereby reducing the effective stress intensity factor range, ΔK_{eff}, and increasing crack closure (Figure 4.48a). The tensile residual stresses act in the opposite direction, increasing the effective stress intensity factor range, ΔK_{eff}, as shown in Figure 4.48b. Consequently, the crack growth rates will increase and the overall fatigue life will drop (Dorman et al., 2012). The major concern regarding this approach occurs when the average compressive residual stress exceeds the externally applied load, which results in a $K_{eff} \leq 0$ MPa$\sqrt{m}$. This suggests that the model cannot predict crack growth neither can Paris law coefficients be used to predict the test result under such circumstances.

Under the assumption that the residual state of the LSP treated M(T) specimen is similar to the residual stress profile verified for the same treatment condition (3J and 200 pulses/cm^2) in Figure 4.3b, the crack propagation is not expected to occur within the treated region since the average compressive residual stress is higher than the applied load ($K_{eff} \leq 0$ MPa$\sqrt{m}$). For LSP1 and LSP2 specimens tested with $\Delta K = 10$ MPa$\sqrt{m}$, it was found that the crack has stopped growing and propagating with an increasing number of cycles shortly after entering the LSP treated area. In other words, the compressive residual stress was able to prevent the crack growth in LSP1 and LSP2 specimens, also clearly shown in Figure 4.47 when the growth rate da/dN decreases to near

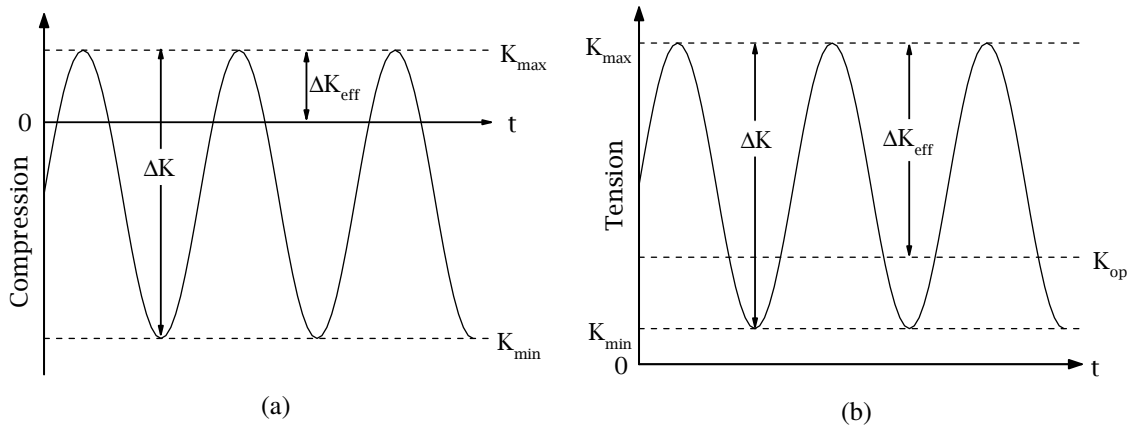


Figure 4.48: Crack closure behaviour.

zero in LSP1 and LSP2.

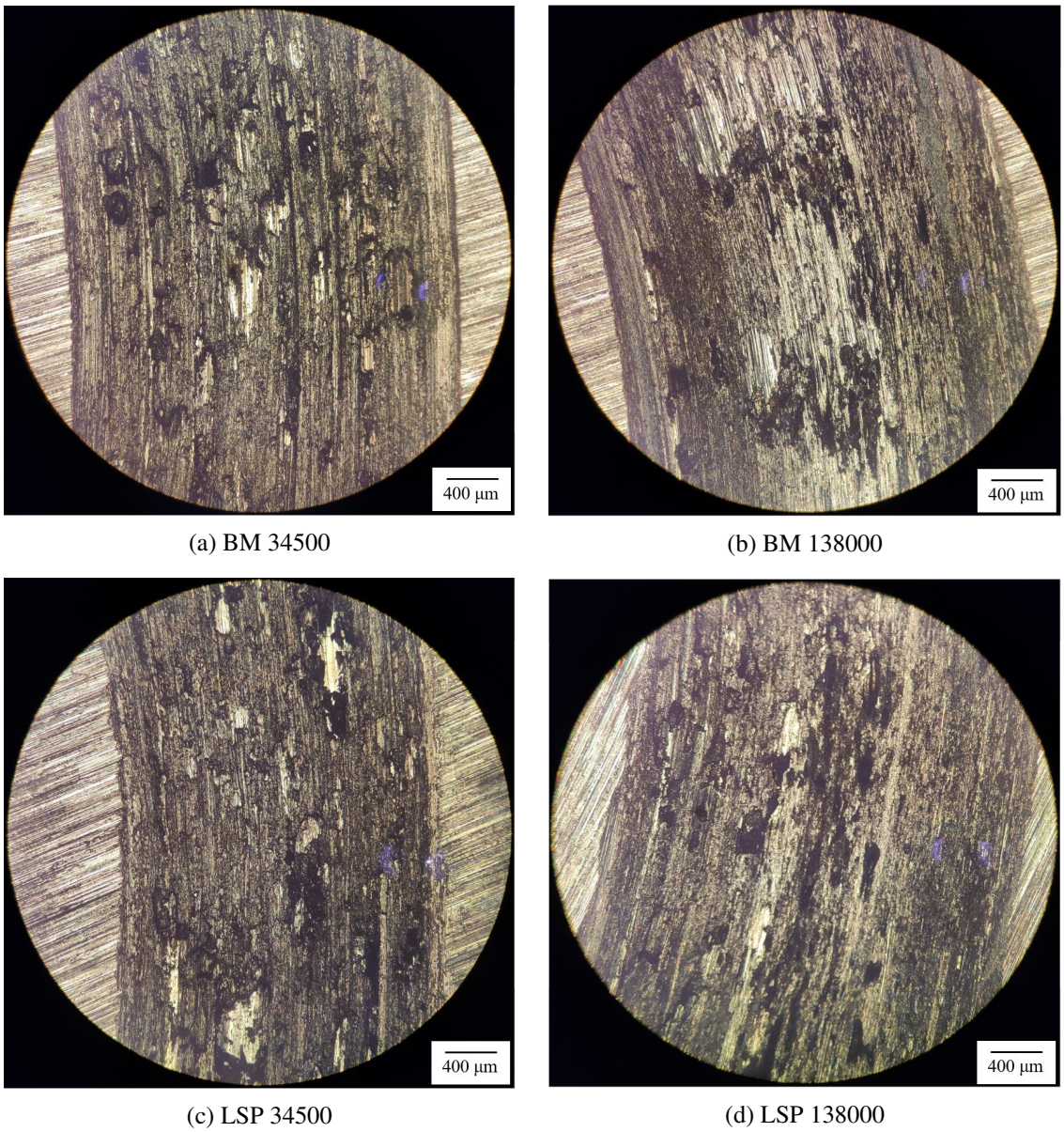
Despite the fact the average compressive residual stress was higher than external loading, crack propagation was observed for LSP3 (ΔK = 20 MPa$\sqrt{m}$) and LSP4 (ΔK = 15 MPa$\sqrt{m}$) specimens. The crack growth is an indicator that the $K_{eff} \geq 0$ MPa$\sqrt{m}$. These results suggest that the equilibrium tensile stress was acting towards the increase of the stress intensity factor range. Additionally, the obtained compressive residual stress for the present LSP treatment condition (3J and 200 pulses/cm^2) may indeed have been overestimated. The compressive residual stresses may influence the crack initiation behaviour as well, however, the mechanisms are not well understood.

Based on the above results, and even considering the most severe loading condition (ΔK = 30 MPa$\sqrt{m}$ and a_0 = 9 mm), it can be observed that LSP treatment, using laser energy of 3J and laser pulse density of 200 pulses/cm^2, can significantly extend the fatigue life of AISI D2 tool steel.

4.9 Wear behavior

Dry sliding wear tests were performed for BM and LSP treated AISI D2 specimens on a pin-on-disk test. A constant load of 10N was applied at a test speed of 575RPM. Microscopic figures of the wear track morphology produced on BM after 34500 and 138000 wear cycles are shown in Figures 4.49a and 4.49b, respectively. Figures 4.49c and 4.49d show the microscopic figures of the worn surface of LSP treated material after 34500 and 138000 wear cycles, respectively.

Figure 4.49 is particularly useful to analyse the morphology of worn surfaces and identify the wear mechanisms involved. The selection criteria for the areas presented in Figure 4.49 was the amount of features found in order to assist the identification of wear mechanisms. The LSP treated specimen (see Figure 4.49c) exhibits a track width, at 34500 cycles, considerably smaller than the track width of the BM specimen (see Figure 4.49a). No significant difference is observed in the track width of BM and LSP treated specimen at 138000 cycles, as presented in Figures 4.49b and 4.49d, respectively. Moreover, there are generally no differences in terms of surface features. It can be observed that both BM and LSP treated specimens show a considerable roughness, and large grooves and deep craters along the sliding direction can be observed. These features are dispersed



(a) BM 34500 (b) BM 138000

(c) LSP 34500 (d) LSP 138000

Figure 4.49: Microscopic images of the wear track.

along the worn surfaces. In addition, debris was found on the wear track. No clear evidence of the presence of plastic deformation or build-up of plastic deformation around the borders of the wear track was found. Some randomly distributed smooth areas along the wear track suggest adhesion. Observation of the worn surfaces of BM and LSP treated specimens indicates that the wear mechanisms involved are abrasive and adhesive wear.

Figures 4.50a, 4.50b, 4.50c, 4.50d, 4.51a, 4.51b, 4.51c, 4.51d show the 2D profile of the wear tracks for BM and LSP treated specimens at 1800, 3600, 34500, 69000, 103500, 138000, 172500 and 207000 cycles, respectively. The 2D wear track plots of BM and LSP treated specimens are arranged together and divided according to the number of wear cycles to aid comparison and analysis of the effect of LSP treatment on wear performance of AISI D2 tool steel. The average

cross-sectional area was measured from the 2D profiles of the wear track for the different material conditions. The wear volume loss was calculated by multiplying the cross-sectional area by the circumferential length of the wear track. The non-contact 3D measurements of surface topography after wear testing for BM and LSP treated specimens are provided in Appendix C.

According to Figures 4.50 and 4.51 the evolution of wear in BM and LSP treated specimens can be observed. The wear profiles examined are the average of three equidistant measurements of the wear track. The evolution of the wear tracks is similar for BM and LSP treated specimens. Not surprisingly, a progressive increase of the wear track can be observed both in width and depth with the increase in wear cycles. Interestingly, at an early stage of wear testing the wear profiles are quite rough, whereas by the end of the test the wear profiles are smoother.

Figures 4.52a and 4.52b present the average wear volume loss and wear track depth for BM and LSP treated material, respectively. Figures 4.52c and 4.52d show the wear rate and specific wear rate for BM and LSP treated material, respectively.

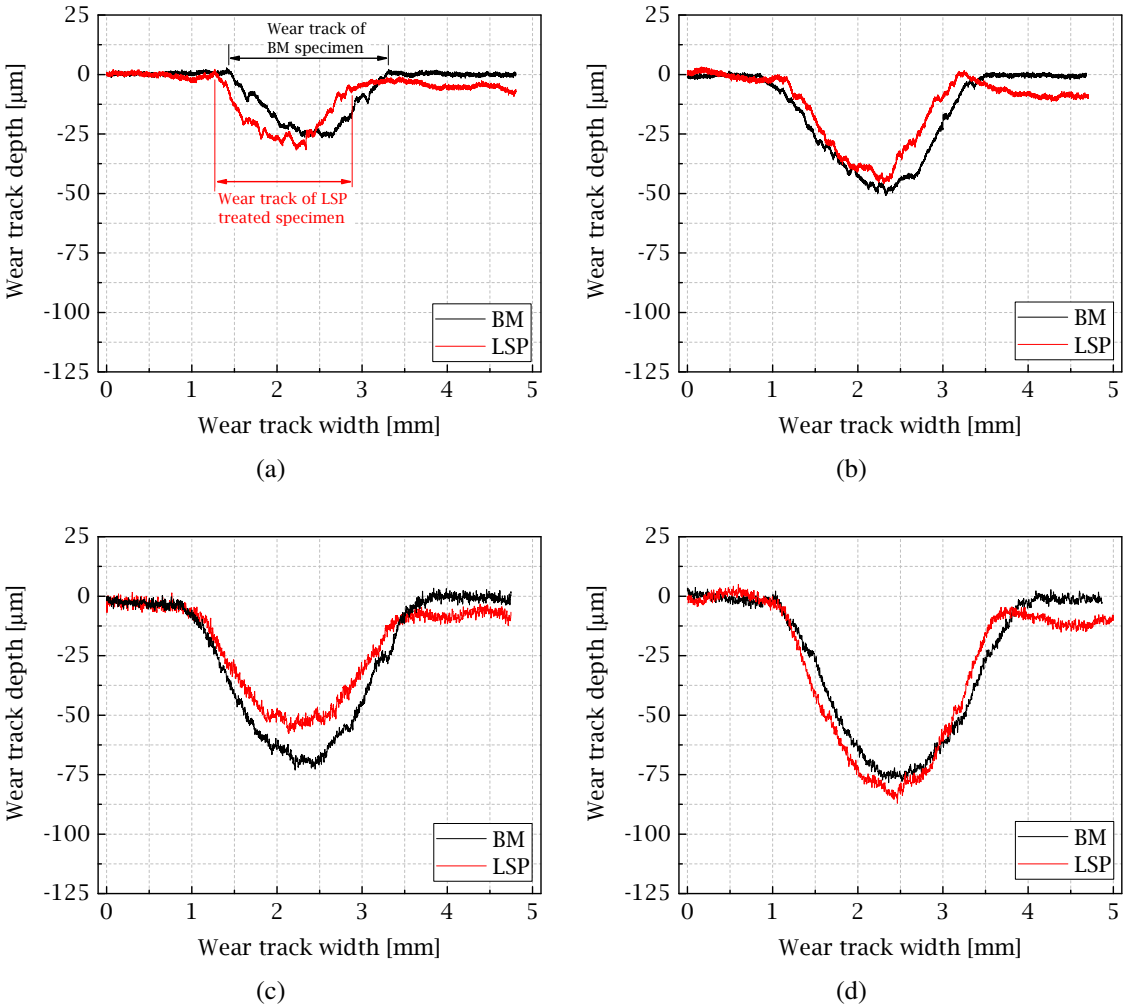


Figure 4.50: 2D wear track profile of BM and LSP treated specimen at (a) 1800, (b) 3600, (c) 34500 and (d) 69000 cycles.

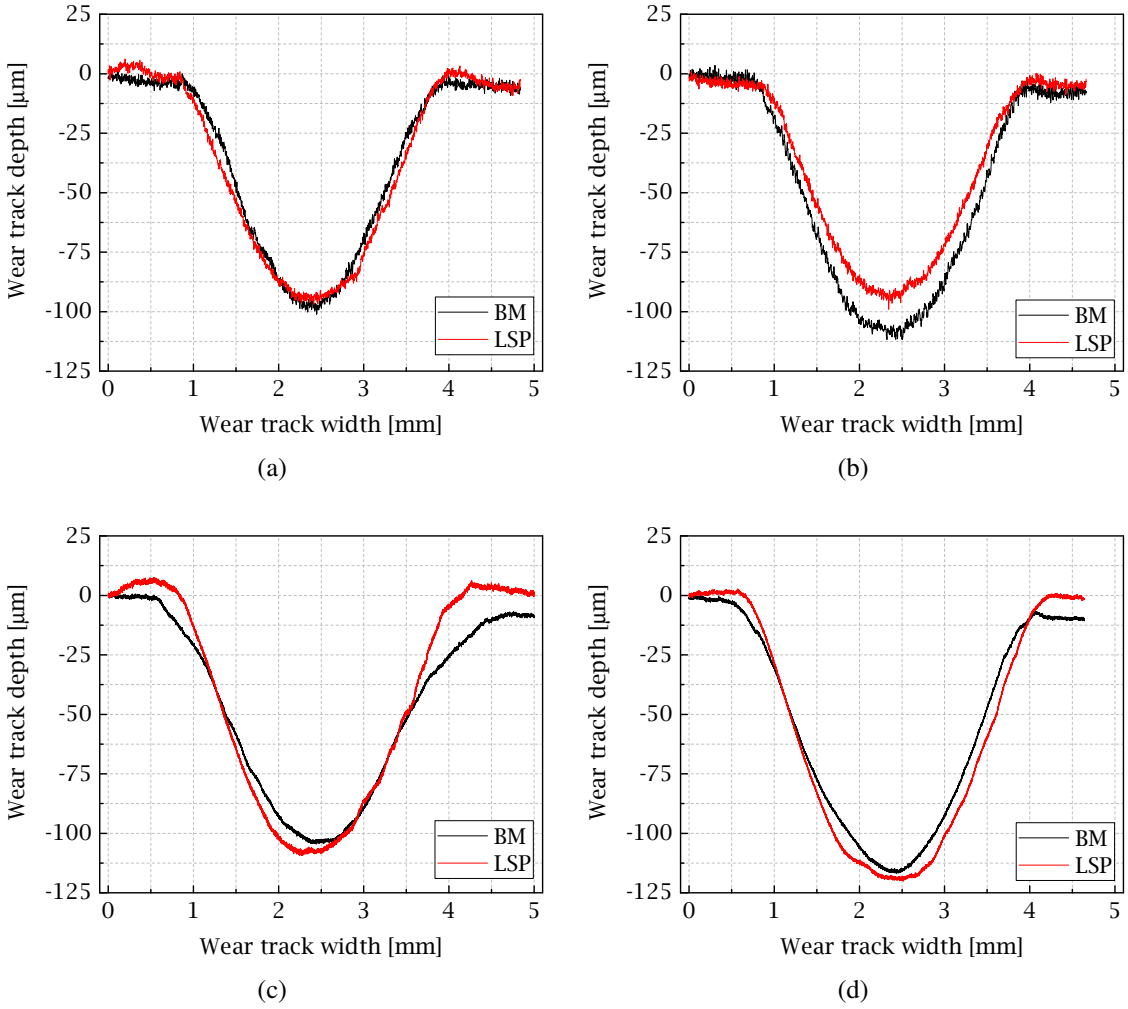


Figure 4.51: 2D wear track profile of BM and LSP treated specimen at (a) 103500, (b) 138000, (c) 172500 and (d) 207000 cycles.

The average wear volume losses for the LSP treated specimen are substantially lower than those found on the BM for N $\leq$ 34500. As the wear testing progresses, the average volume losses in LSP treated specimen remain lower than BM, although the results tend to get similar in both material conditions. This demonstrates that LSP can effectively improve wear resistance in AISI D2 tool steel. The average wear volume loss for BM is 3.634, 8.335, 15.117, 16.308, 20.190 and 24.198 mm^3. In comparison, the LSP treated material exhibits average wear volume values of 2.972, 4.717, 8.684, 14.299, 19.503, 19.754 mm^3, representing a reduction in wear volume loss of 18.2, 43.4, 42.6, 12.3, 3.4 and 18.4%, respectively. With the progress of the wear test, an approximation of the average wear volume trends for both material conditions can be observed. However, for N $\geq$ 172500 the LSP treated specimen shows a higher average wear volume loss compared to BM. The average wear volume values for BM (N $\geq$ 172500) are 24.975 and 26.613 mm^3, while the LSP treated specimen shows average values of 25.399 and 29.795 mm^3. This represents an increase of 1.7% and 12% in the average wear volume loss, suggesting a decrease

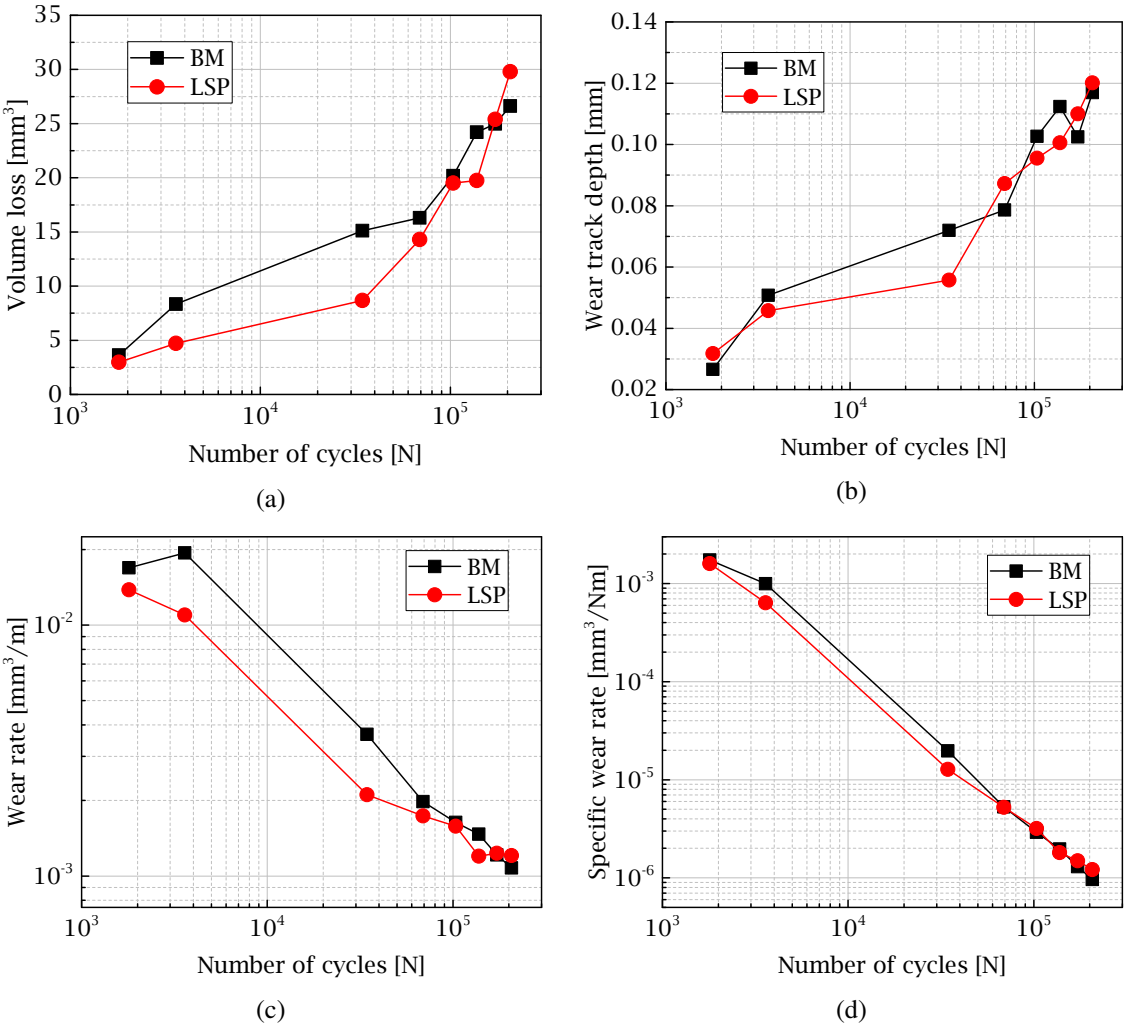


Figure 4.52: (a) Average wear volume loss, (b) wear track depth, (c) wear rate and (d) specific wear rate of BM and LSP treated material.

in the wear resistance of LSP treated material for high wear cycles. This is confirmed by the increased wear rate and specific wear rate of LSP treated material compared to BM for this range of cycles, as it can be seen in Figures 4.52c and 4.52d, respectively.

The surface roughness generated by the LSP process can improve the tribological behaviour under dry contact conditions. According to Trdan et al. (2018) the increased number of contact points between surfaces leads to a decrease in contact pressure, thereby reducing the friction between surfaces. Additionally, the surface peaks and valleys induced by LSP can facilitate the collection of wear debris, which can reduce the friction energy. Therefore, the increased wear resistance observed for LSP treated material within the given range of wear cycles can be attributed to the combined effect of work hardening and compressive residual stresses.

To further understand these results, cross-section samples of the wear track were obtained from the disk specimens after complete wear testing. The micro hardness profiles were measured below the deeper portion of the wear track for BM and LSP treated material. This analysis provides

an insight into the evolution of the material hardness condition before and after undergoing wear testing. Figure 4.53 shows the micro hardness profile for BM and LSP treated material both before and after wear testing.

The micro hardness of unworn BM specimen is substantially inferior compared to the micro hardness of LSP treated specimen, which may account for the difference in the wear volume loss and wear rate. As the wear cycles progress, material changes are expected to occur due to the severe loading conditions, such as contact pressure and shear stress. These changes potentially result in degradation of the beneficial effects of LSP induced compressive residual stresses. The surface micro hardness of worn BM specimen increased from 206 $HV_{0.1}$ to 246 $HV_{0.1}$, and a slight decrease of the worn LSP treated material, from 255 $HV_{0.1}$ to 253 $HV_{0.1}$, was observed (see Figure 4.53). Therefore, is not surprising that the tribological performance is similar for both material conditions at the end of the wear tests.

Comparing LSP treatment to base material condition, LSP offers better wear performance at low and intermediate wear cycles and similar performance at higher wear cycles for the specific conditions used in this work. The wear resistance found at $N \geq 172500$ should not be overvalued within the framework of a tool for cold-working applications. When considering, for instance, a forming die, the wear loss observed at $N \geq 172500$ does not seem to be acceptable, i.e. under such conditions, the tool would probably have reached its replacement stage because the dimensional requirements are compromised. Therefore, it might be more appropriate to evaluate the wear volume at an early and intermediate stage of the wear testing. Furthermore, it should be noted that this type of wear conditions may not represent the real wear of tools because of the different loads and speed conditions. Overall, LSP can effectively be employed as a viable technique to improve wear performance on AISI D2 tool steel.

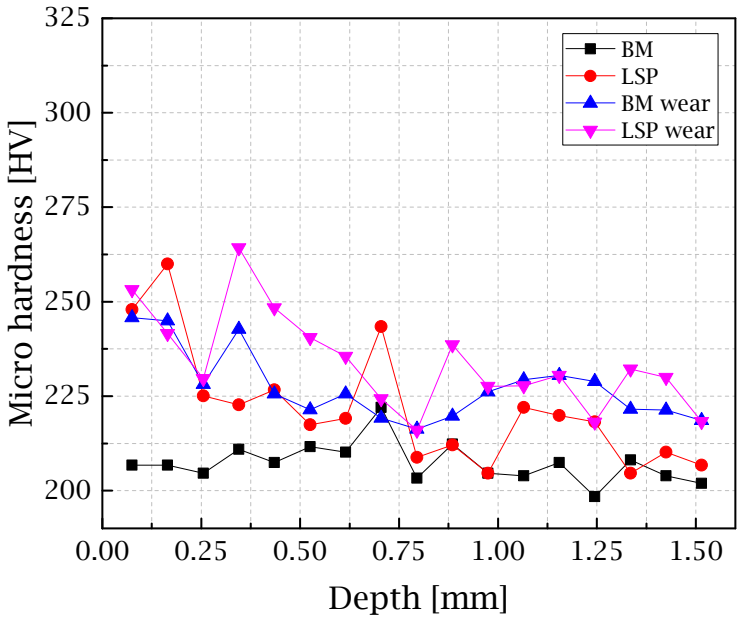


Figure 4.53: Micro hardness profile of BM and LSP treated specimen at 207000 cycles.

Chapter 5

Concluding remarks & future work

This chapter aims to outline the main conclusions drawn from this work. The most relevant aspects are highlighted in this chapter. After summarizing the main conclusions, a brief overview of future developments is provided.

5.1 Conclusions

The investigation and review of state-of-the-art related to the subject under study has revealed a significant lack of information on the applicability, parameters and effects of the LSP in tool steels for cold working applications.

A comprehensive assessment of the effect of LSP in the adopted material was performed, constantly comparing the results to the original material condition, providing a robust baseline for their interpretation. A variety of testing procedures were conducted to demonstrate the applicability and feasibility of LSP as a superior metal surface processing technique. The main conclusions can be summarized as follows:

1. LSP generates a high magnitude compressive residual stress field, which varies with depth. The peak compressive residual stress was reached at a certain depth and, as the layer depth increased, the compressive residual stress decreased towards the tensile regime. The increase in laser energy and or pulse density causes an increase of the peak compressive residual stress value as well as the affected depth ($\geq$ 1 mm). Hence, a progressive increase of peak compressive residual stress was observed by increasing the energy up to 4J, followed by a decline with 5J. The findings indicate a power drop at energy levels exceeding 4J. Such a phenomenon is commonly referred to in the literature as the breakdown plasma. It is recommended to be careful when selecting the laser energy level because excessive energy can generate a detrimental effect on the material as a result of equilibrium tensile stresses. The criteria for selecting the optimum LSP condition, for AISI D2 tool steel, was based on compressive residual stress magnitude, profile uniformity and affected depth. Accordingly, within the framework of this research, the LSP treatment condition featuring 3J of energy and pulse density of 200 pulses/cm^2 provided the best outcome.

2. The surface roughness is a consequence of the typical severe impacts that occur during the LSP process. It is, therefore an unintended but inevitable secondary outcome. However, the LSP effects on the surface roughness can be attenuated. The surface roughness parameters increase sharply with increasing laser energy and pulse density. The interaction of the laser radiation with the AISI D2 steel causes plastic deformation leading to changes in the surface topography and increased roughness. Besides, the roughness increase can also be attributed to partial surface ablation, irregularities in the spatial beam profile and the absence of laser shots overlapping.

3. LSP application increases the surface micro hardness of the target material. All LSP treatment conditions were found to increase the micro hardness when compared to the base material. The micro hardness profile, which is strongly influenced by the large carbides dispersed in the ferritic matrix of AISI D2 tool steel, exhibits peak values located near the surface and progressively decreases in depth. This is reasonable in the framework of LSP, as the effects of the treatment are experienced in the vicinity of the surface. The fact can be related to the residual stress results since the material at a depth of 1 mm is under the effect of the compressive stress, which have to be balanced with tensile stress at a certain depth.

4. Microstructural observations have revealed no significant variations in the morphology of the eutectic carbides between the base material and different LSP processing conditions. This would suggest that temperature during LSP was insufficient to cause phase transformation and dissolution of the carbides. However, cracks were observed in large carbides near the treated surface. All material conditions exhibit large coarse carbides with smaller carbides evenly arranged in a ferrite matrix (α-Fe). In addition, grain refinement was observed after LSP with a 27.4% reduction in average grain size. After LSP application, the material exhibits an increase of low misorientation angle near the target surface suggesting the formation of both smaller grains and sub grains.

5. LSP treated AISI D2 exhibited a slight decrease in material yield strength coupled with a slight increase in ultimate tensile strength. The decrease in yield strength may be caused by the high concentration of balancing tensile residual stress present in a thin section of the material core, which adversely affected the yield strength of the material. Hence, it is important to avoid excessively compressive stress depth to the point where equilibrium stresses act as fatigue limiting agents. However, the observed variations of yield strength and ultimate tensile strength in BM and LSP treated specimens are not significant.

6. Compressive residual stresses effectively inhibit the formation and propagation of cracks under cyclic loading and thereby increase fatigue strength of AISI D2 tool steel. A fatigue resistance improvement of 20% was verified in LSP treated specimens when compared to the base material. The beneficial effect of LSP induced compressive residual stress is not observed, at high stress amplitude fatigue testing, due to the stress relaxation from rapid accumulation of plastic deformation during cyclic loading. Compressive residual stresses

have a more pronounced influence on high and medium fatigue cycle than in low fatigue cycle.

7. Fatigue crack propagation specimens were successfully tested. A strong influence of the compressive residual stress on crack growth retardation and crack closure was observed. LSP treated specimens exhibit a significant decline in FCP compared to BM specimens. The declining FCP is visible when the crack penetrates the LSP treated area. Hence, the crack retardation and the crack closure effect can be attributed to the introduction of a sufficiently high compressive residual stress in a region in front of the crack tip.

8. The wear testing performed under dry contact conditions highlighted the improvements in the wear resistance of LSP treated AISI D2 tool steel. A 42.6% reduction in the average wear volume of LSP treated material was observed after 34500 cycles as compared to BM. The reduction of the wear rates and wear volume loss can be attributed to the combined effect of the strain hardening and the compressive residual stresses. The wear mechanism found on both the BM and LSP treated specimens is adhesive and abrasive wear. LSP can effectively create a hardened layer on the material surface, which is effective for improving the wear resistance of AISI D2 steel during low-wear cycles under the present conditions.

As a final remark, the LSP is a surface processing technique whose success largely depends upon controlling the parameters involved. It is essential to achieve a sufficiently high and deep compressive residual stress field to positively affect the material properties. However, one should be aware that residual stress is always in self-balance, which implies that both compressive stress and tensile stress are present. Such consideration is of the utmost importance when applying LSP to thin-walled structures. Therefore, the process parameters must be selected to ensure the beneficial effects of compressive residual stresses, whereas equilibrium tensile stress does no act as a limiting factor.

This thesis allowed to explore the benefits, limitations and the applicability of LSP in AISI D2 tool steel for cold work applications. The developed know-how can positively contribute to the evolution of this company/industry, whether in the improvement of existing tools or the development of innovative high-performance products offering enhanced properties.

5.2 Future work

This thesis includes a topic of high relevance for the tool-making industry, and naturally, can be further investigated. A solid basis is provided for an in-depth analysis of the effects of LSP in AISI D2 tool steel and similar alloys. While promising results were achieved using the adopted parameters, further optimisation can be accomplished with additional testing.

The development of robust numerical models for the prediction and optimization of residual stress fields will allow a better combination of compressive residual stress, affected depth and balancing tensile residual stress. Relevant research topics for further investigation include the analysis of the control of process parameters such as the overlap between adjacent laser shots and the laser scanning pattern. It would potentially reduce or eliminate non-equibiaxial stress profile problems observed at high energy levels, leading to a better understanding of the LSP process. Topics of interest certainly include a comprehensive study of wear under different load scenarios and test conditions.

The incremental hole-drilling technique is extensively used for residual stress analysis. Typically the clamping devices involve manual force control of the specimen tightening. Therefore, results may differ significantly depending on the user because, in case of excessive force, the clamping device can act as an external load on the specimen, leading to changes in the stress state of the material. Hence, the development of clamping devices, for residual stress analysis using the ESPI hole-drilling technique, that eliminates any external influence and ensures reliable data acquisition, is of great interest.

Future work certainly includes the LSP treatment of several tools and further implementation in a production line, which will allow evaluating the real performance of the tools subject to LSP.

From the knowledge acquired during the course of this thesis, whether in terms of process parameters or material effects, it will be possible to implement an LSP application cell at Quantal S.A. by integrating several components. This LSP cell will be developed and adapted to the current needs of Quantal S.A. and cover a range of relevant materials. This technology, in combination with the extensive range of manufacturing processes available at Quantal S.A., enables the manufacturing of tools or components to fulfil both internal and customer demands. Besides, a new business field will be created at Quantal based on LSP know-how for on-site surface processing of additively manufactured parts using powder bed fusing and direct energy deposition.

In conclusion, the research conducted has contributed to a substantial knowledge gain, offering a feasible solution to a productive challenge at Quantal S.A., simultaneously creating interesting opportunities in the development of high-performance and high-value products and services which contribute to sustain the company's competitive edge. Therefore, this work contributes to providing Quantal with the knowledge and skills enabling the company to strategically position itself in the manufacture of high-performance products.

Appendix A

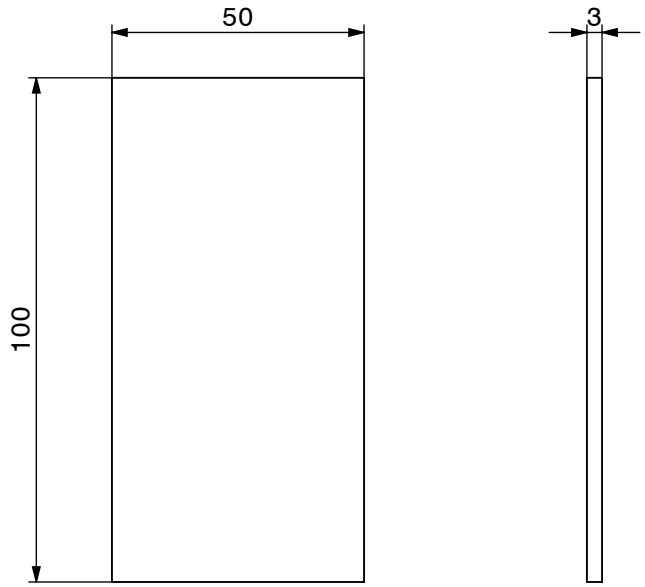
Technical drawings of the specimens

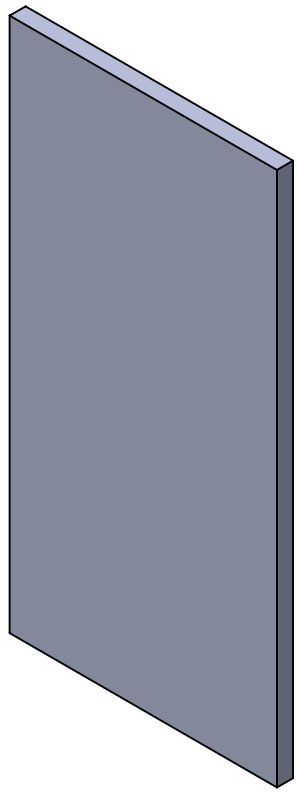
A.1 Plate specimen

SEQ.	OPERAÇÕES	FERRAMENTA/OBS.
1	CORTE FIO	-
2	MAQUINAÇÃO	-

CORTE FIO:
A PARTIR DO BLOCO 105x55x105mm, CORTAR 15 PARTES COM 3mm DE ESPESSURA.

MAQUINAÇÃO





A	27-5-19	EMISSÃO DOCUMENTO	MARIANA
INDEX	DATA	DESCRIÇÃO	DESENHOU

Desenhou:		Verificou:		Cliente: Designação:	Referência:
MARIANA	27-5-19	MARIANA	27-5-19		

Cliente:	Material	Acabamento	Referência QTL
QTL	1.2379	-	0707 K84A 0 FAA A

Ref.Montagem:	Escala:	Designação:
FAA	S/ESC	RESIDUAL STRESS HOLE DRILLING-LSP

TOLERANCIAS DIMENCIONAIS GERAIS PARA COTAS SEM TOLERANCIAMENTO BASEADA NA ISO 2768-1									
MAIOR DE ATÉ	0,5 . . . 3	3 . . . 6	6 . . . 30	30 . . . 120	120 . . . 400	400 . . . 1000	1000 . . . 2000	2000 . . . 4000	4000 . . . 8000
Classe média	±0.1	±0.1	±0.2	±0.3	±0.5	±0.8	±1	±2	±3
PARA COTAS ANGULARES CONSIDERA-SE UMA TOLERÂNCIA DE ±1º									

LEGENDA	
-	COTA A GARANTIR
F	COTA FUNCIONAL

A4	MASSA: 0.02kg	Quantal SA	Pag. 1/1

O conteudo deste desenho, é propriedade de QUANTAL SA. Nos termos da lei, é proibido a sua reprodução sem autorização expressa.

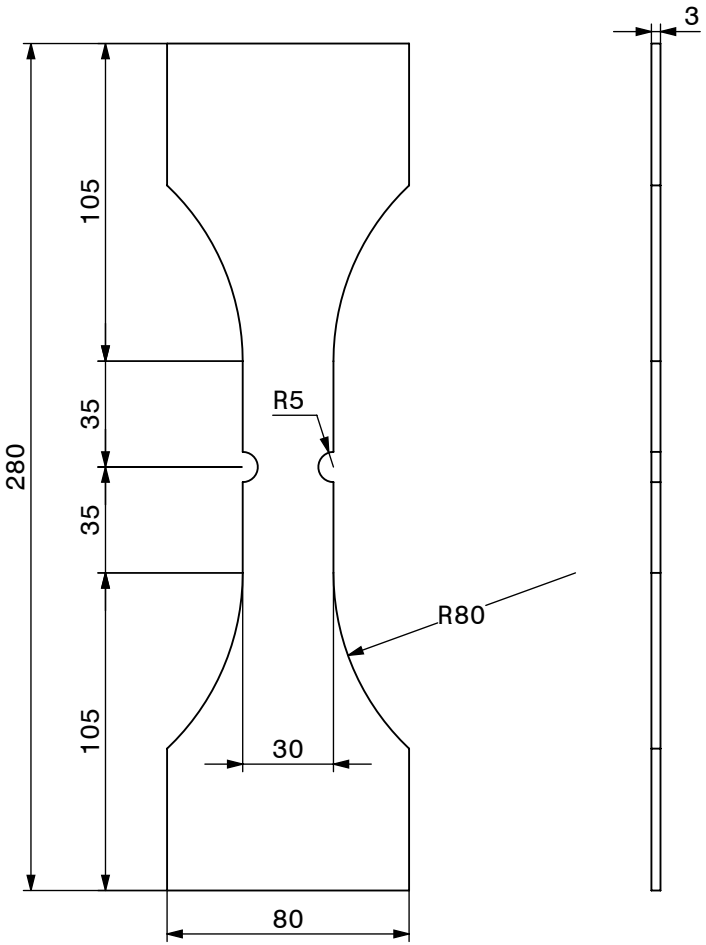
IMP024-7

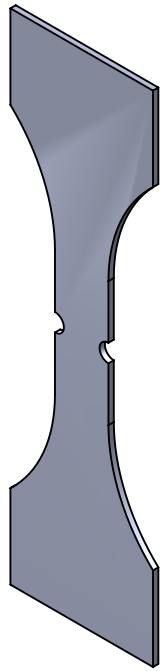
A.2 Dogbone specimen

SEQ.	OPERAÇÕES	FERRAMENTA/OBS.
1	CORTE FIO	-
2	MAQUINAÇÃO	-

CORTE FIO:
A PARTIR DO BLOCO 285x86x150mm, CORTAR 30 PARTES COM 3mm DE ESPESSURA.

MAQUINAÇÃO:





INDEX	DATA	DESCRIÇÃO	DESENHOU
A	27-5-19	EMISSÃO DOCUMENTO	MARIANA

Desenhou:		Verificou:		Cliente: Designação:	Referência:
MARIANA	27-5-19	MARIANA	27-5-19		

Cliente:	Material	Acabamento	Referência QTL
QTL	1.2379	-	0707 K84A 0 BAA A

Ref.Montagem:	Escala:	Designação:
BAA	S/ESC	DOGBONE-LSP TRESTED

TOLERANCIAS DIMENCIONAIS GERAIS PARA COTAS SEM TOLERANCIAMENTO BASEADA NA ISO 2768-1									
MAIOR DE ATÉ	0,5 . . . 3	3 . . . 6	6 . . . 30	30 . . . 120	120 . . . 400	400 . . . 1000	1000 . . . 2000	2000 . . . 4000	4000 . . . 8000
Classe média	±0.1	±0.1	±0.2	±0.3	±0.5	±0.8	±1	±2	±3
PARA COTAS ANGULARES CONSIDERA-SE UMA TOLERÂNCIA DE ±1º									

LEGENDA	
-	COTA A GARANTIR
F	COTA FUNCIONAL

A4

MASSA: 0.04kg

Quantal SA

O conteudo deste desenho, é propriedade de QUANTAL SA. Nos termos da lei, é proibido a sua reprodução sem autorização expressa.

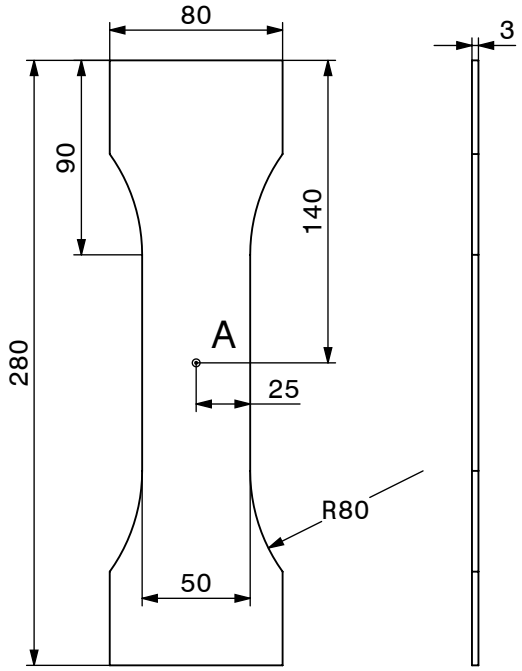
IMP024-7

A.3 M(T) specimen

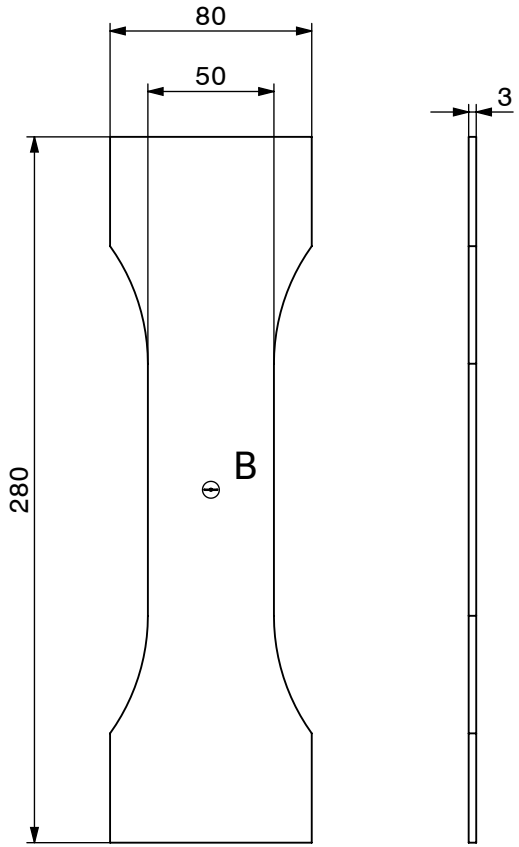
1º CORTE FIO:
A PARTIR DO BLOCO 285x86x85mm,
CORTAR 8 PARTES COM 3mm
DE ESPESSURA.

SEQ.	OPERAÇÕES	FERRAMENTA/OBS.
1	CORTE FIO	-
2	MAQUINAÇÃO	-
3	CORTE FIO	-

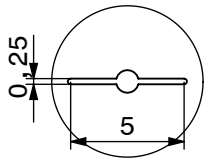
MAQUINAÇÃO:

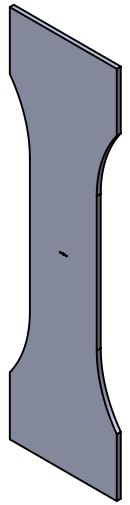


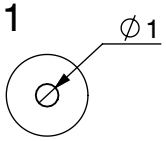
A
3 : 1



B
3 : 1







INDEX	DATA	DESCRIÇÃO	DESENHOU
A	27-5-19	EMISSÃO DOCUMENTO	MARIANA

Desenhou:		Verificou:		Cliente: Designação:	Referência:
MARIANA	27-5-19	MARIANA	27-5-19		

Cliente:	Material	Acabamento	Referência QTL
QTL	1.2379	-	0707 K84A 0 CAA A

Ref.Montagem:	Escala:	Designação:
CAA	S/ESC	MT SPECIMEN-LSP

TOLERANCIAS DIMENCIONAIS GERAIS PARA COTAS SEM TOLERANCIAMENTO BASEADA NA ISO 2768-1									
MAIOR DE ATÉ	0,5 . . . 3	3 . . . 6	6 . . . 30	30 . . . 120	120 . . . 400	400 . . . 1000	1000 . . . 2000	2000 . . . 4000	4000 . . . 8000
Classe média	±0.1	±0.1	±0.2	±0.3	±0.5	±0.8	±1	±2	±3
PARA COTAS ANGULARES CONSIDERA-SE UMA TOLERÂNCIA DE ±1º									

LEGENDA
- COTA A GARANTIR
F COTA FUNCIONAL

A4

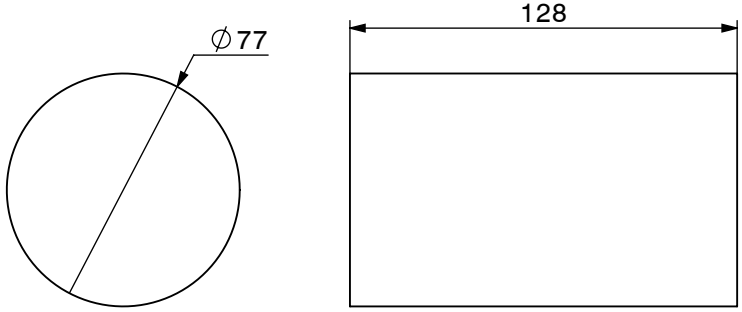
MASSA: 0.05kg

Quantal SA
O conteudo deste desenho, é propriedade de QUANTAL SA. Nos termos da lei, é proibido a sua reprodução sem autorização expressa.
IMP024-7

A.4 Disk specimen

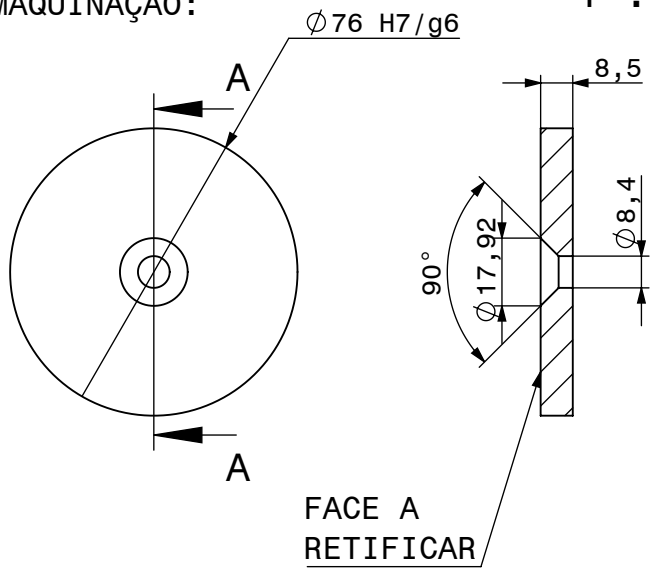
SEQ.	OPERAÇÕES	FERRAMENTA/OBS.
1	TORNEAR	-
2	CORTE FIO	-
3	MAQUINAÇÃO	-
4	RETIFICAR	-

TORNEAR:

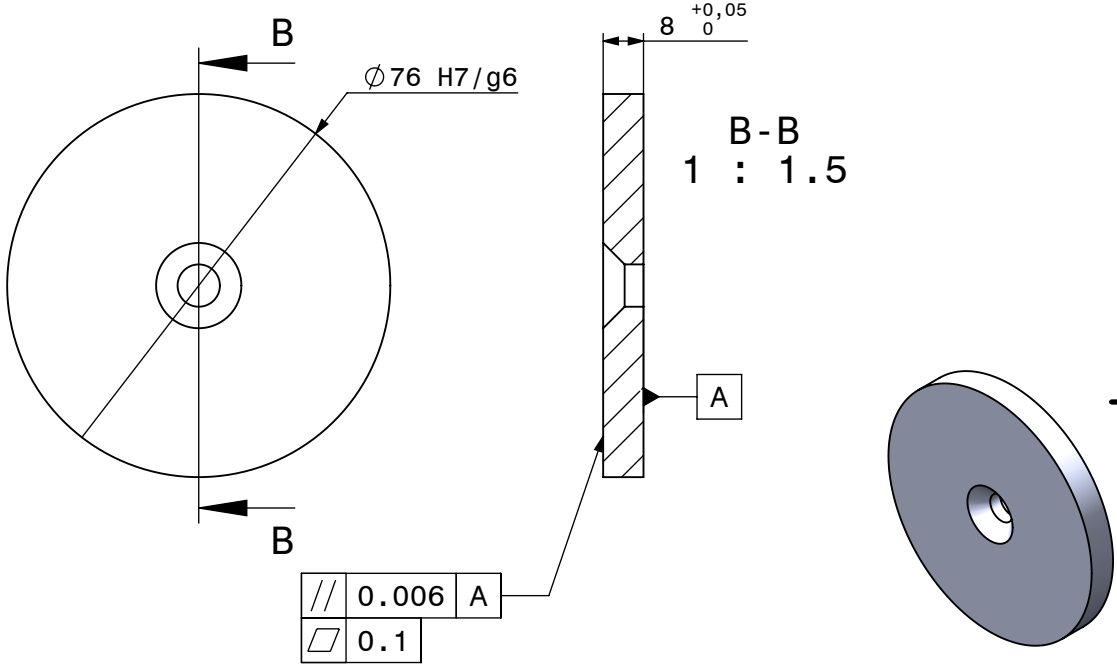


CORTE FIO:
CORTAR 8 DISCOS COM 8,5 mm
DE ESPESSURA.

MAQUINAÇÃO:



DESENHO APÓS RETIFICAR:



A	27-5-19	EMISSÃO DOCUMENTO	MARIANA
INDEX	DATA	DESCRIÇÃO	DESENHOU

Desenhou:		Verificou:		Cliente: Designação:	Referência:
MARIANA	27-5-19	MARIANA	27-5-19		

Cliente:	Material	Acabamento	Referência QTL
QTL	1.2379		0707 K84A 0 AAA A

Ref.Montagem:	Escala:	Designação:
K84A	S/ESC	DISC SPECIMEN FOR PIN-ON-DISC MACHINE

TOLERANCIAS DIMENCIONAIS GERAIS PARA COTAS SEM TOLERANCIAMENTO BASEADA NA ISO 2768-1									
MAIOR DE ATÉ	0,5 . . . 3	3 . . . 6	6 . . . 30	30 . . . 120	120 . . . 400	400 . . . 1000	1000 . . . 2000	2000 . . . 4000	4000 . . . 8000
Classe média	±0.1	±0.1	±0.2	±0.3	±0.5	±0.8	±1	±2	±3
PARA COTAS ANGULARES CONSIDERA-SE UMA TOLERÂNCIA DE ±1º									

LEGENDA	
-	COTA A GARANTIR
F	COTA FUNCIONAL

A4

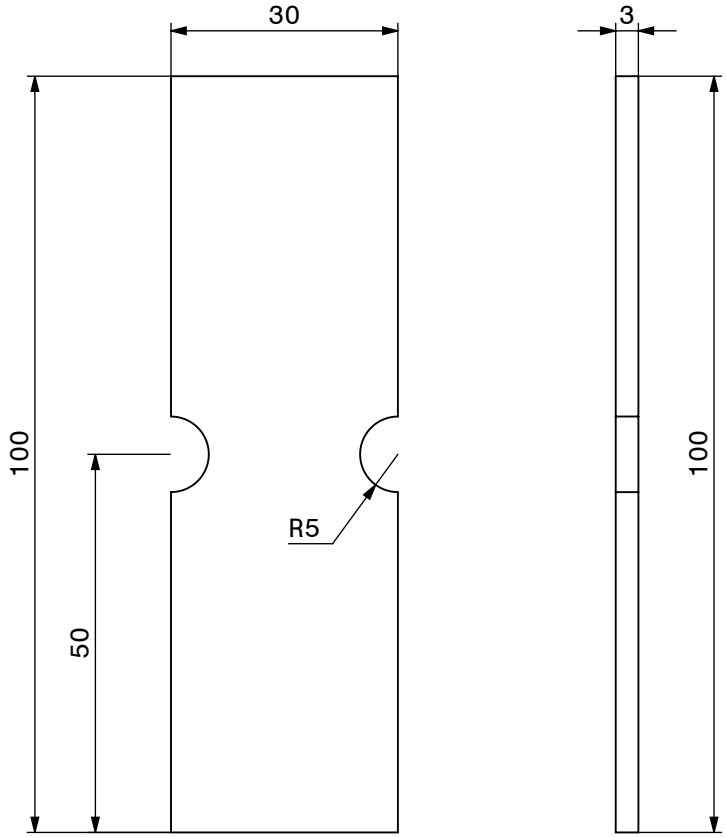
MASSA: 0.04kg

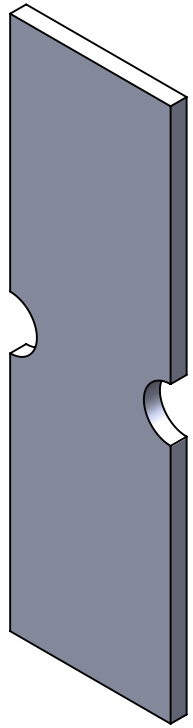
Quantal SA
O conteudo deste desenho, é propriedade de QUANTAL SA. Nos termos da lei, é proibido a sua reprodução sem autorização expressa.
IMP024-7

A.5 Notched specimen

SEQ.	OPERAÇÕES	FERRAMENTA/OBS.
1	CORTE FIO	-
2	MAQUINAÇÃO	-

CORTE FIO:
A PARTIR DO BLOCO 105x35x75mm, CORTAR 4 PARTES COM 3mm DE ESPESSURA.





A	27-5-19	EMISSÃO DOCUMENTO		MARIANA
INDEX	DATA	DESCRIÇÃO		DESENHOU

Desenhou:		Verificou:		Cliente: Designação:	Referência:
MARIANA	27-5-19	MARIANA	27-5-19		

Cliente:	Material	Acabamento	Referência QTL
QTL	1.2379	-	0707 K84A 0 EAA A

Ref.Montagem:	Escala:	Designação:
EAA	S/ESC	RESIDUAL STRESS CONTOUR II - LSP

TOLERANCIAS DIMENCIONAIS GERAIS PARA COTAS SEM TOLERANCIAMENTO BASEADA NA ISO 2768-1									
MAIOR DE ATÉ	0,5 . . . 3	3 . . . 6	6 . . . 30	30 . . . 120	120 . . . 400	400 . . . 1000	1000 . . . 2000	2000 . . . 4000	4000 . . . 8000
Classe média	±0.1	±0.1	±0.2	±0.3	±0.5	±0.8	±1	±2	±3
PARA COTAS ANGULARES CONSIDERA-SE UMA TOLERÂNCIA DE ±1º									

LEGENDA	
-	COTA A GARANTIR
F	COTA FUNCIONAL

A4	MASSA: 0.01kg

Quantal SA
O conteudo deste desenho, é propriedade de QUANTAL SA. Nos termos da lei, é proibido a sua reprodução sem autorização expressa.
IMP024-7

Appendix B

Residual stresses

This Appendix provides the individual residual stress measurements according to the different LSP treatment conditions as well as the base material.

B.1 ESPI Hole-Drilling method

Figures B.1, B.2, B.3, B.4, B.5 and B.6 present the individual residual stress measurements of BM and LSP treated material, using laser energy of 1, 2, 3, 4 and 5J, respectively.

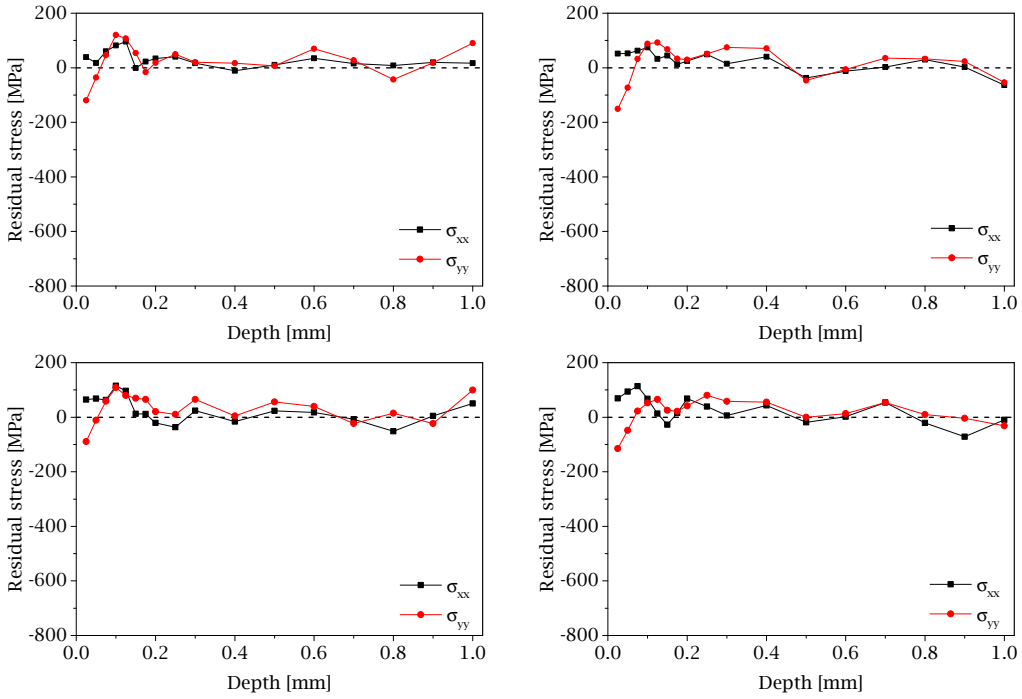
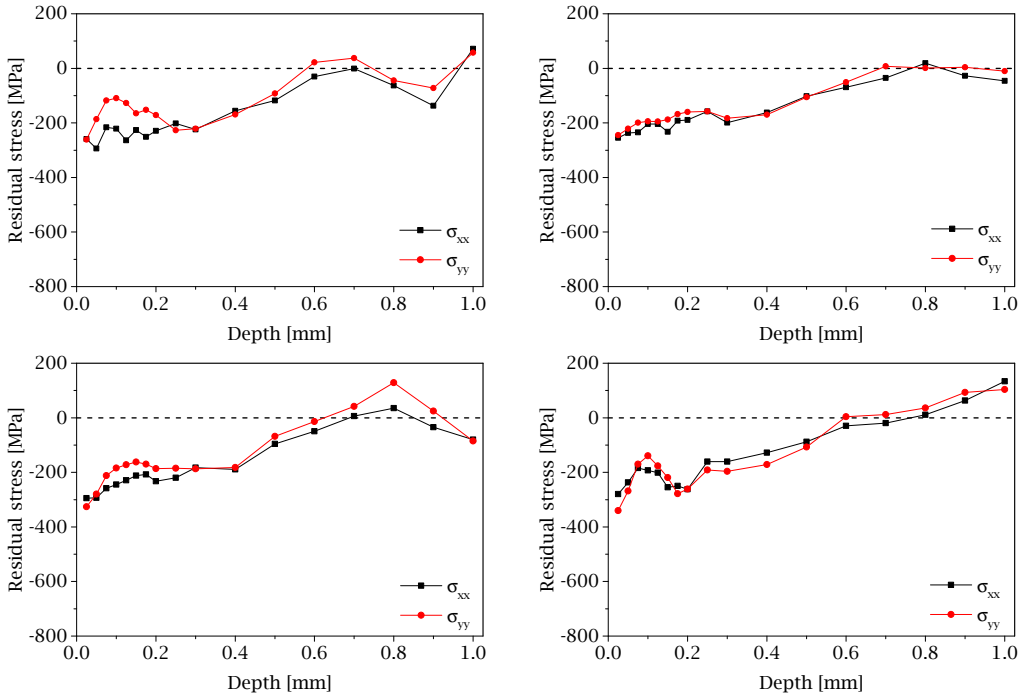
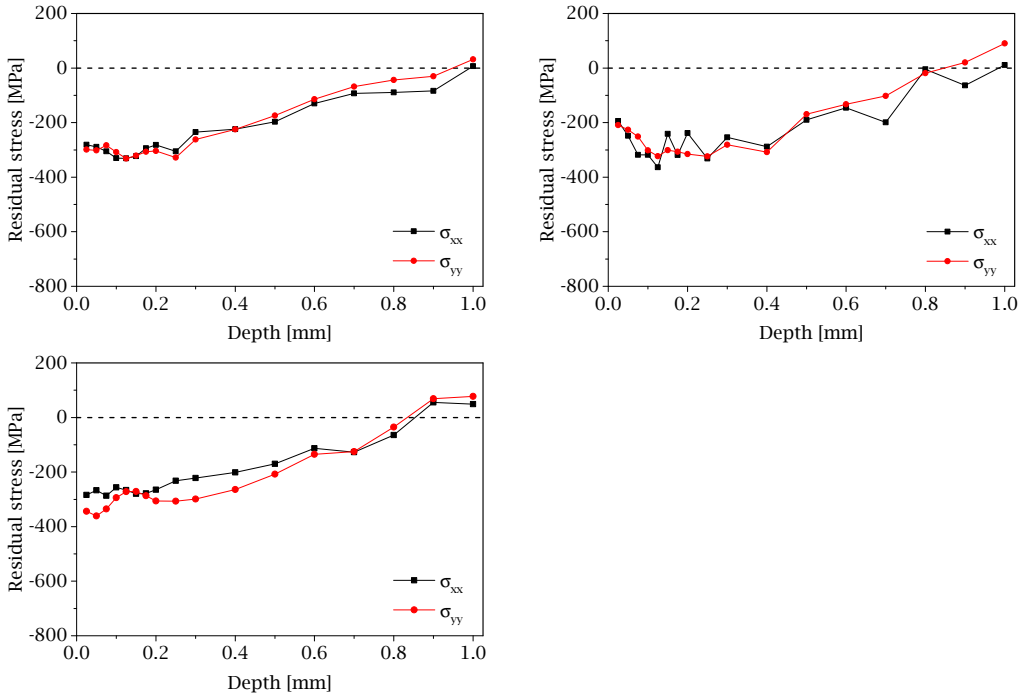


Figure B.1: Residual stress profile of BM.

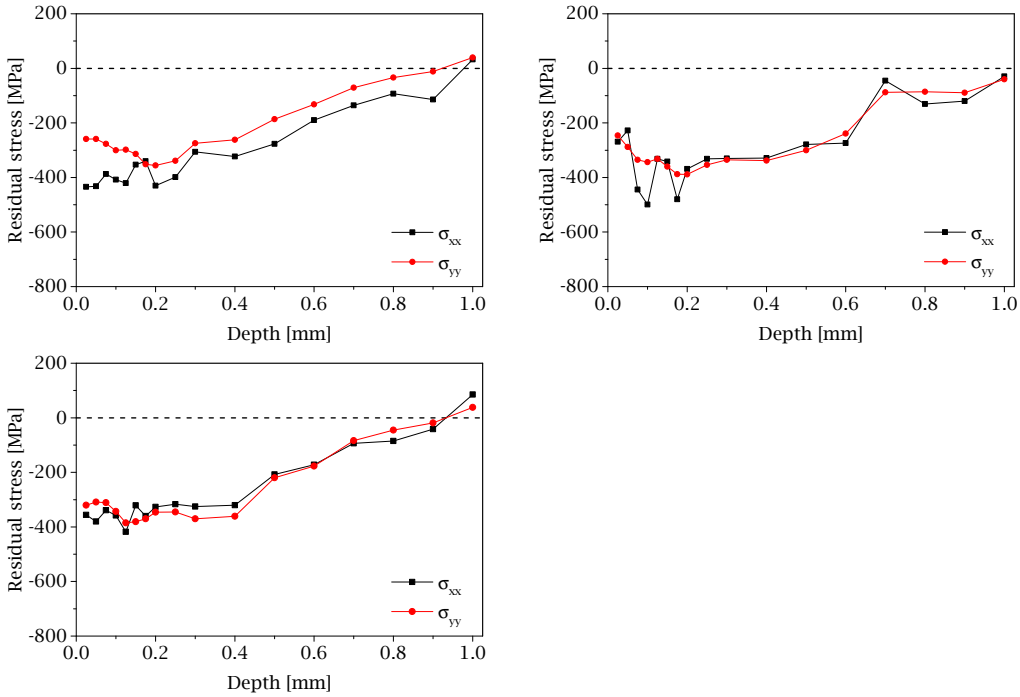


(a) Laser pulse density of 100 pulses/cm^2.

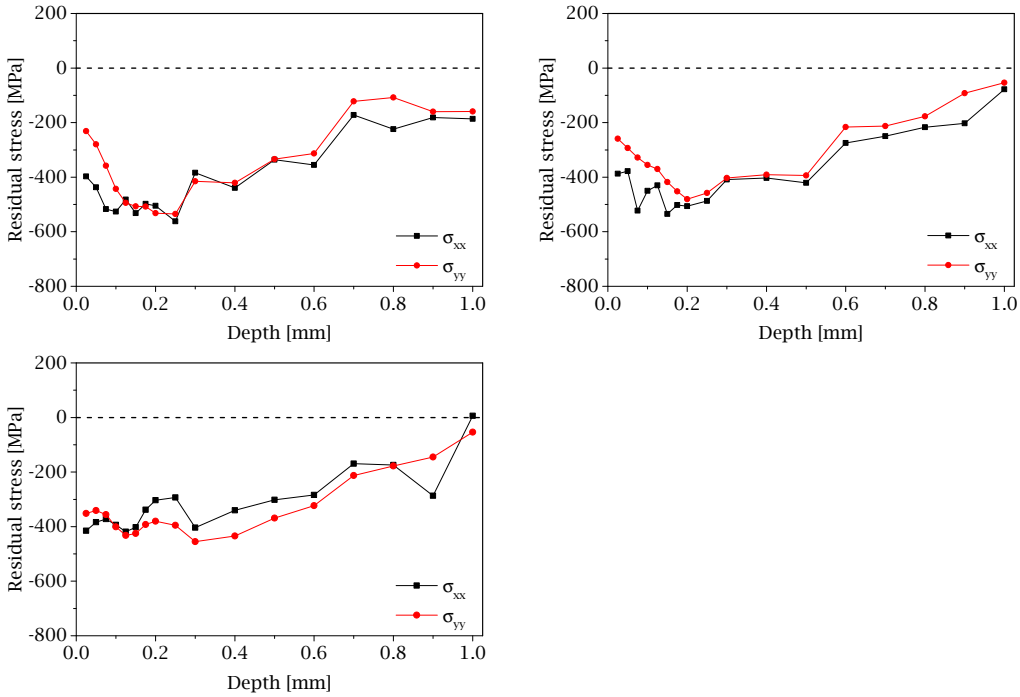


(b) Laser pulse density of 200 pulse/cm^2.

Figure B.2: Residual stress profile of LSP treated material using laser energy of 1J and laser pulse density of (a) 100 and (b) 200 pulses/cm^2.

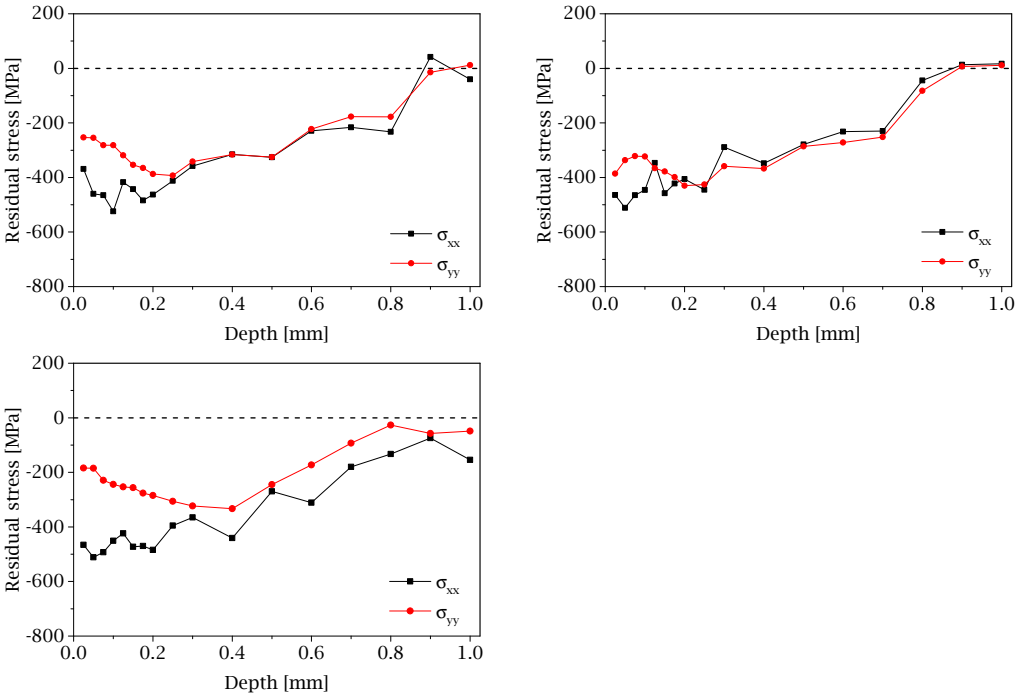


(a) Laser pulse density of 100 pulses/cm^2.

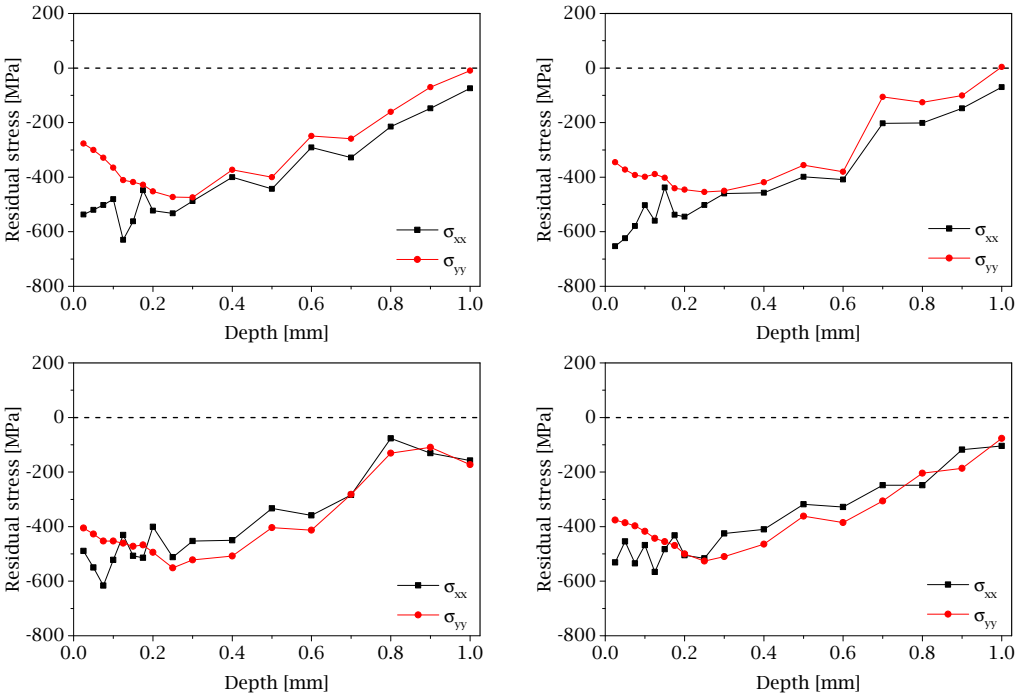


(b) Laser pulse density of 200 pulses/cm^2.

Figure B.3: Residual stress profile of LSP treated material using laser energy of 2J and laser pulse density of (a) 100 and (b) 200 pulses/cm^2.

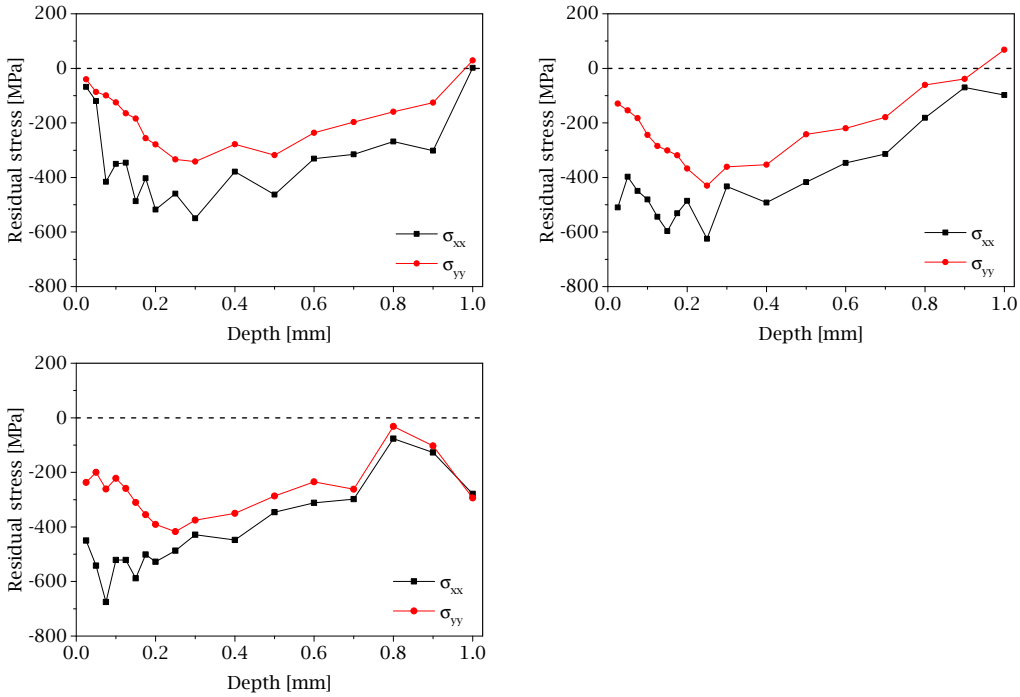


(a) Laser pulse density of 100 pulses/cm^2.

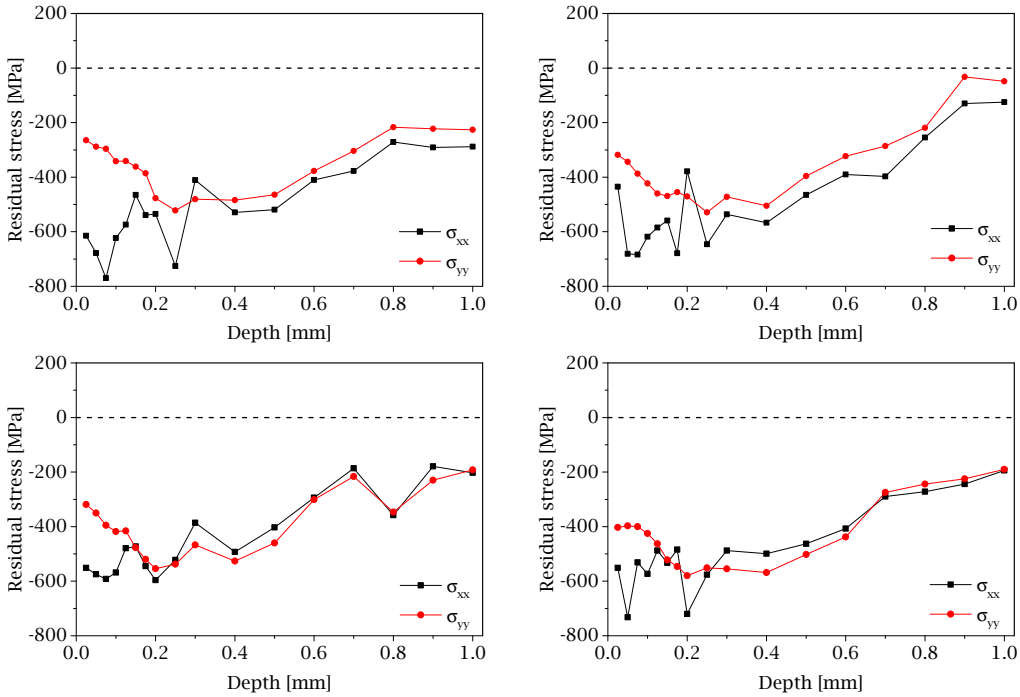


(b) Laser pulse density of 200 pulses/cm^2.

Figure B.4: Residual stress profile of LSP treated material using laser energy of 3J and laser pulse density of (a) 100 and (b) 200 pulses/cm^2.

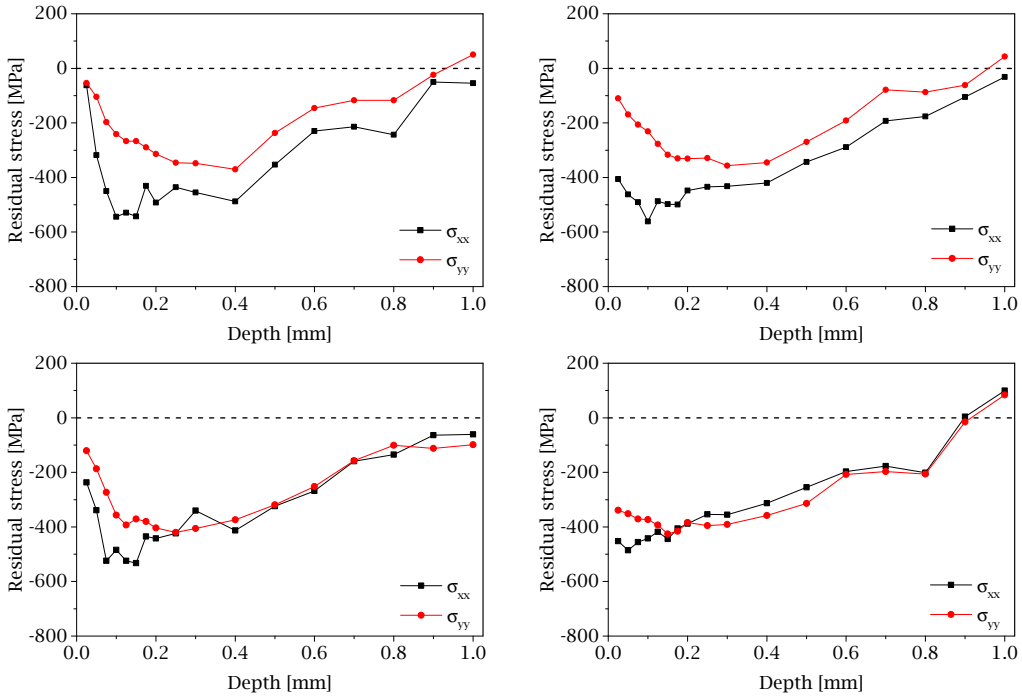


(a) Laser pulse density of 100 pulses/cm^2.

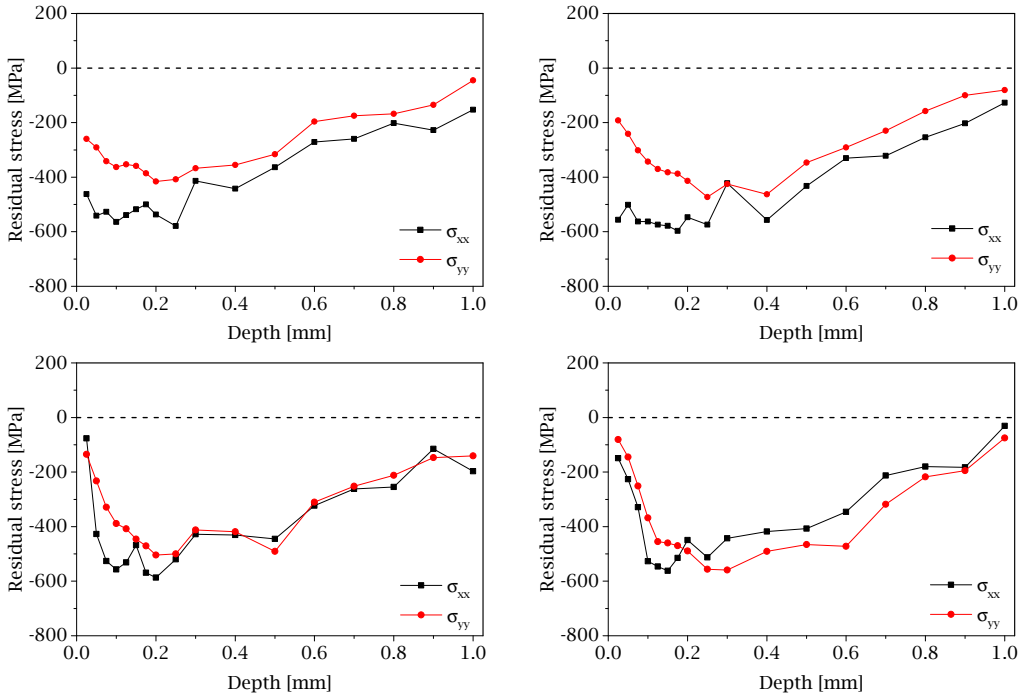


(b) Laser pulse density of 200 pulses/cm^2.

Figure B.5: Residual stress profile of LSP treated material using laser energy of 4J and laser pulse density of (a) 100 and (b) 200 pulses/cm^2.



(a) Laser pulse density of 100 pulses/cm^2.



(b) Laser pulse density of 200 pulses/cm^2.

Figure B.6: Residual stress profile of LSP treated material using laser energy of 5J and laser pulse density of (a) 100 and (b) 200 pulses/cm^2.

B.2 Compressive stress area

Figures B.7, B.8, B.9, B.10, B.11 and B.12 present the compressive stress area of base material (BM) and LSP treated material using laser energy of 1, 2, 3, 4 and 5J, respectively.

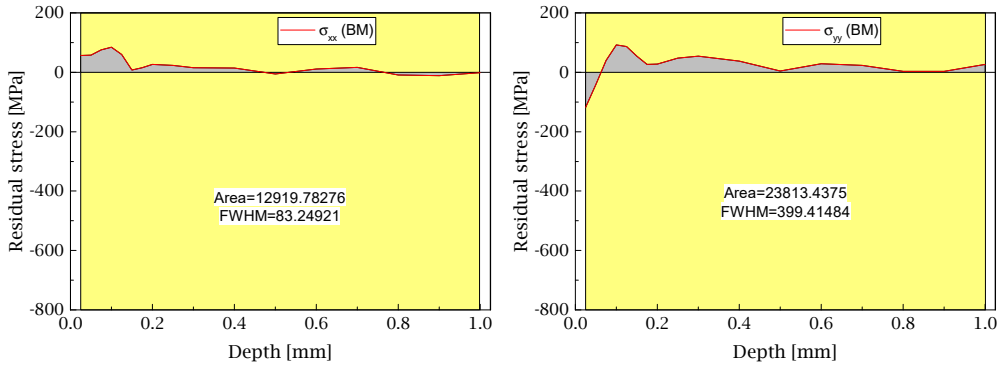


Figure B.7: Compressive stress area of BM.

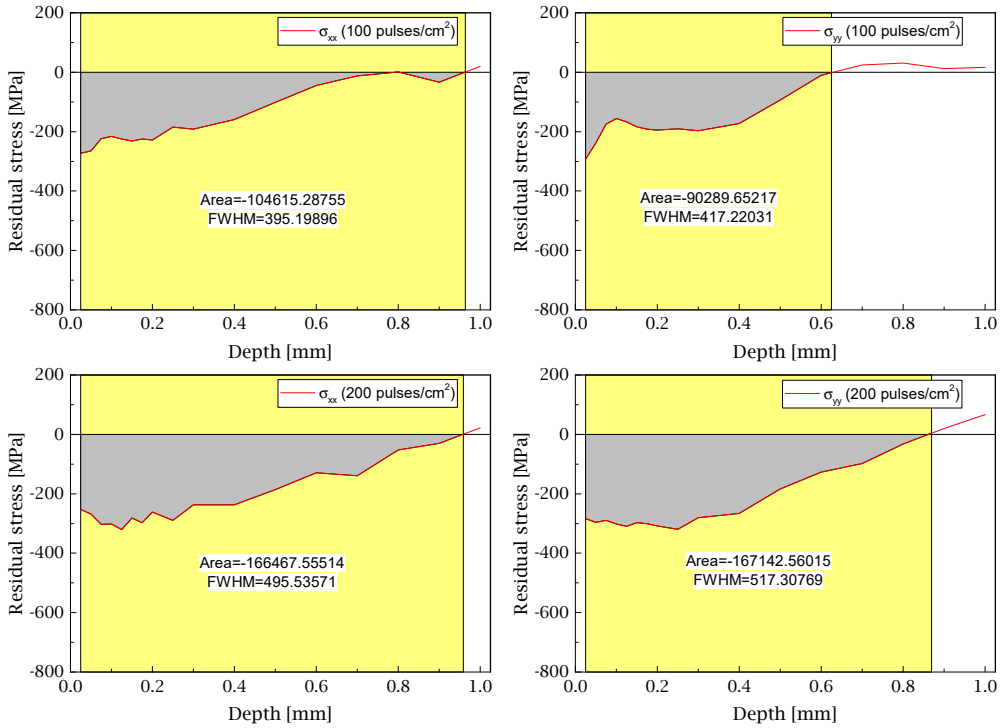


Figure B.8: Compressive stress area of LSP treated material using laser energy of 1J and laser pulse density of 100 and 200 pulses/cm^2.

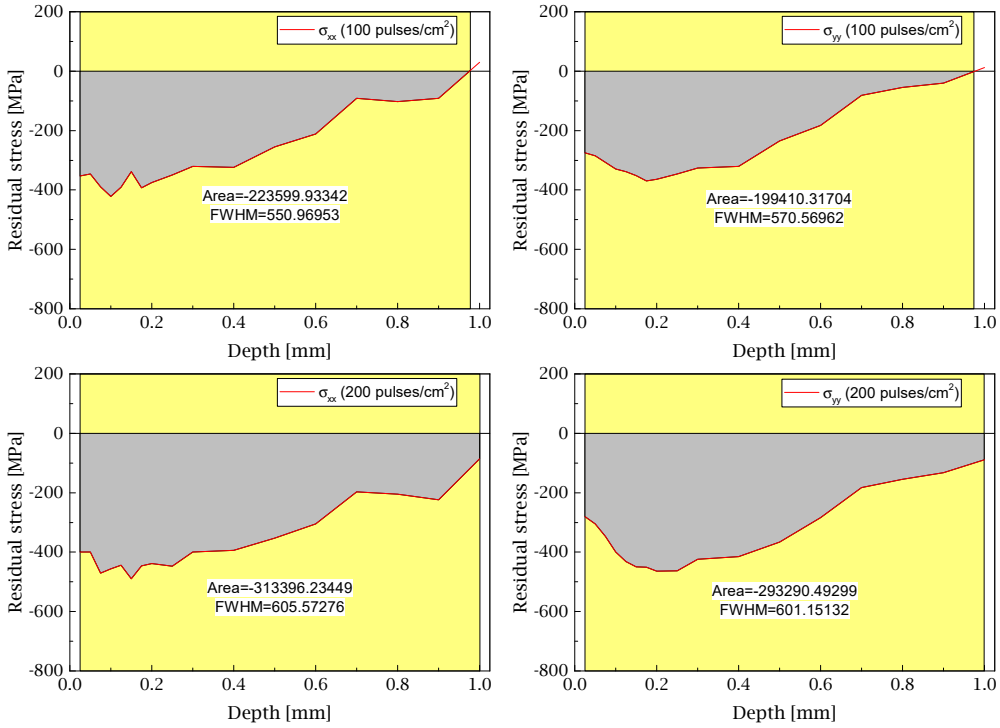


Figure B.9: Compressive stress area of LSP treated material using laser energy of 2J and laser pulse density of 100 and 200 pulses/cm^2.

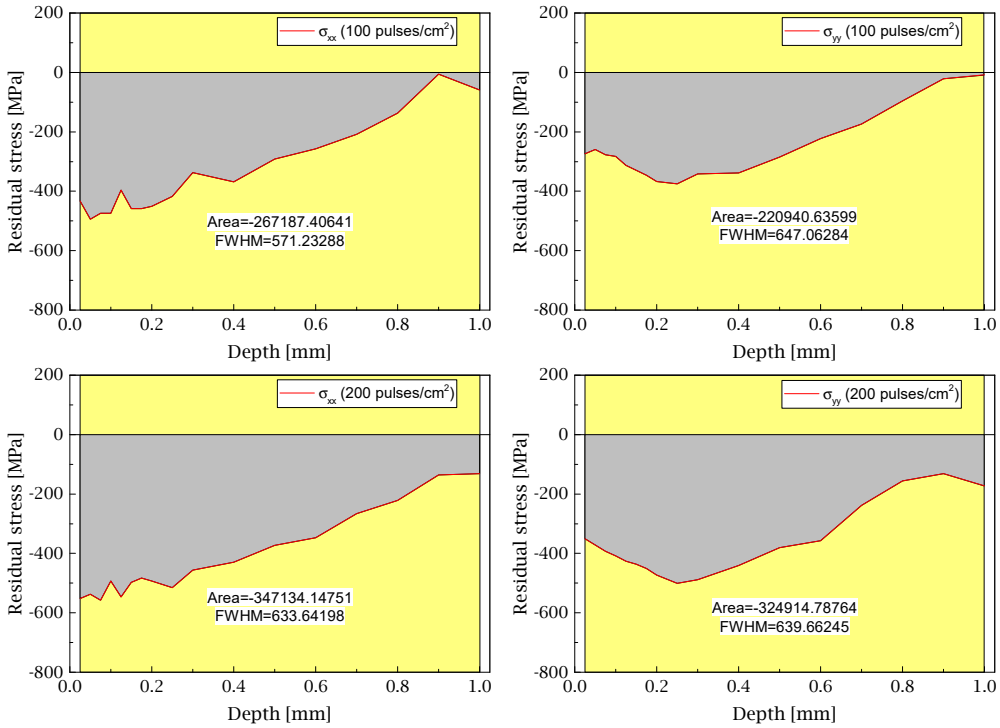


Figure B.10: Compressive stress area of LSP treated material using laser energy of 3J and laser pulse density of 100 and 200 pulses/cm^2.

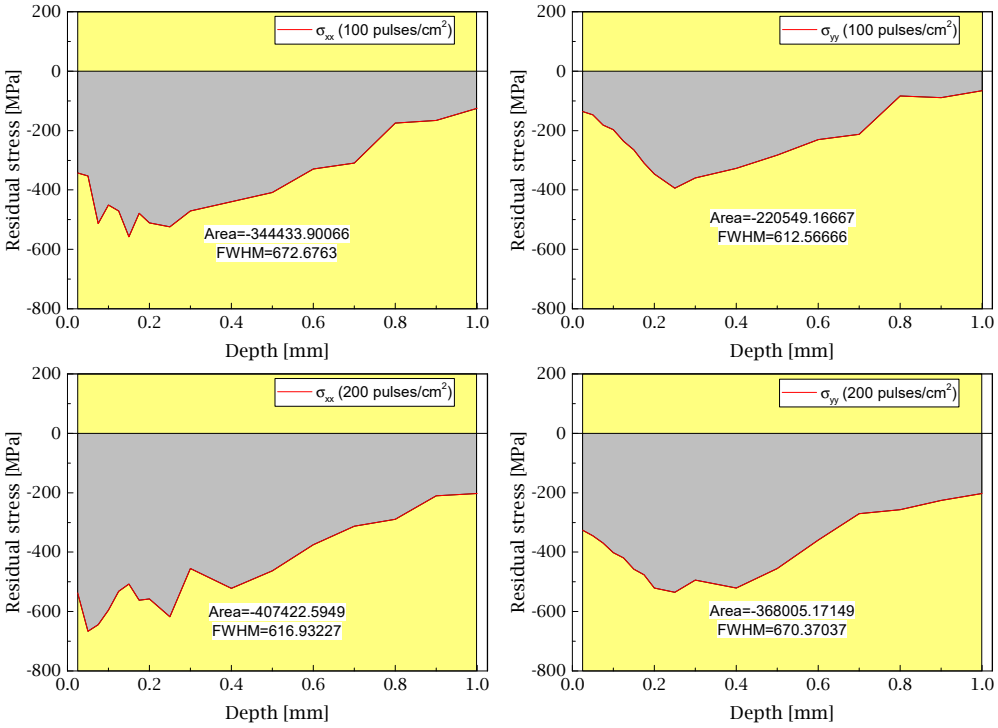


Figure B.11: Compressive stress area of LSP treated material using laser energy of 4J and laser pulse density of 100 and 200 pulses/cm^2.

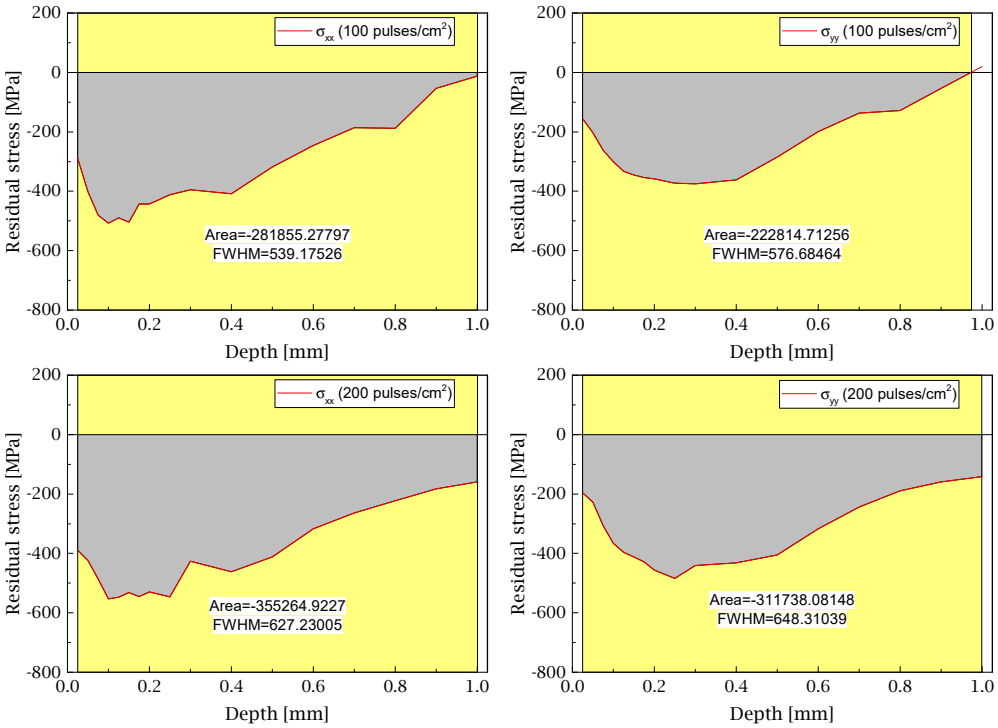


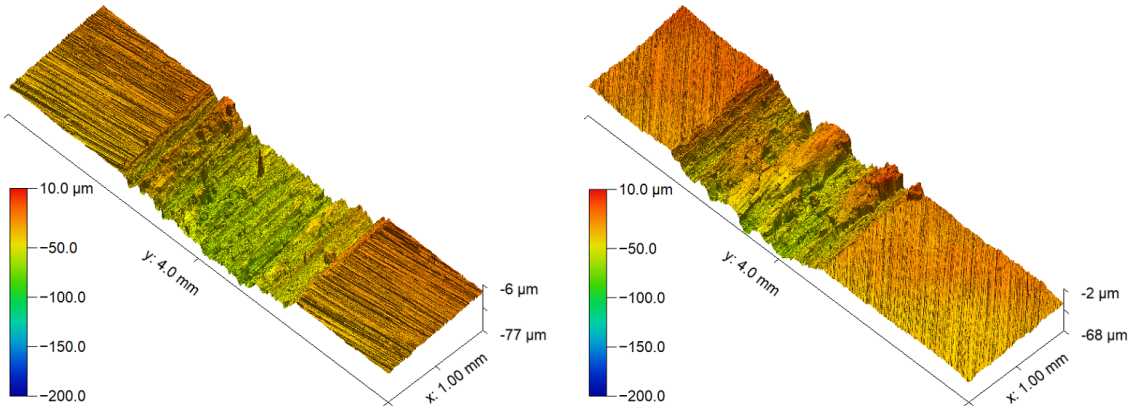
Figure B.12: Compressive stress area of LSP treated material using laser energy of 5J and laser pulse density of 100 and 200 pulses/cm^2.

Appendix C

3D wear track profile

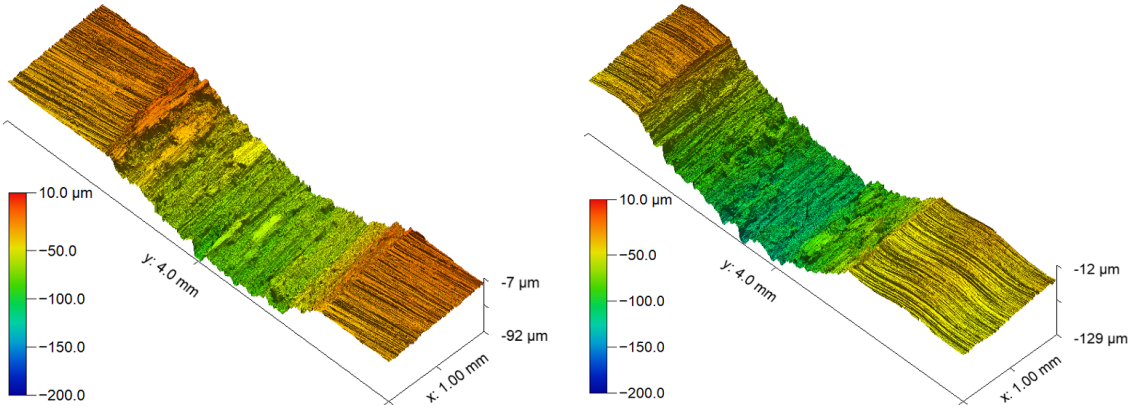
This Appendix provides the non-contact 3D measurements of surface topography after wear testing for BM and LSP treated specimens.

Figures C.1a and C.1b illustrate the 3D profile of the wear tracks, at 1800 cycles, of the BM and LSP treated material. Figures C.2a and C.2b illustrate the 3D profile of the wear tracks, at 3600 cycles, of the BM and LSP treated material. Figures C.3a and C.3b illustrate the 3D profile of the wear tracks, at 34500 cycles, of the BM and LSP treated material. Figures C.4a and C.4b illustrate the 3D profile of the wear tracks, at 69000 cycles, of the BM and LSP treated material. Figures C.5a and C.5b illustrate the 3D profile of the wear tracks, at 103500 cycles, of the BM and LSP treated material. Figures C.6a and C.6b illustrate the 3D profile of the wear tracks, at 138000 cycles, of the BM and LSP treated material. Figures C.7a and C.7b illustrate the 3D profile of the wear tracks, at 172500 cycles, of the BM and LSP treated material. Figures C.8a and C.8b illustrate the 3D profile of the wear tracks, at 207000 cycles, of the BM and LSP treated material.



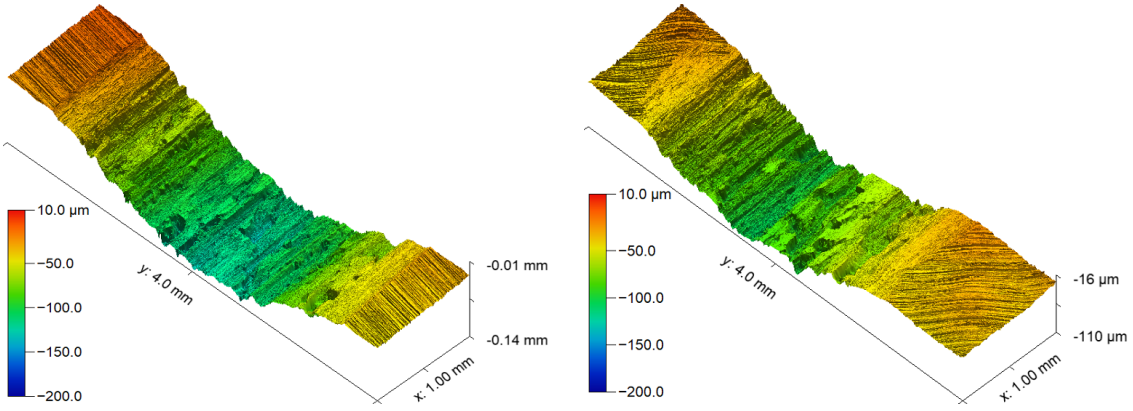
(a) (b)

Figure C.1: 3D Wear track profile after 1800 cycles for (a) BM and (b) LSP treated material.



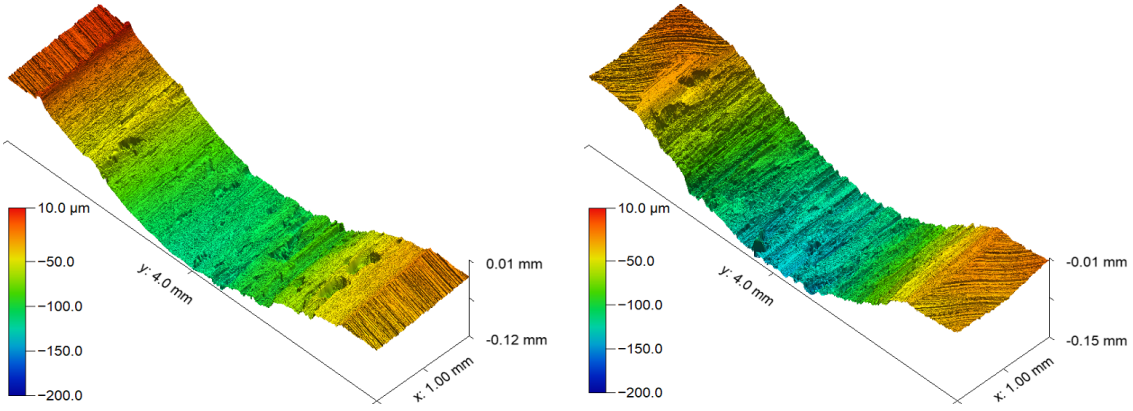
(a) (b)

Figure C.2: 3D Wear track profile after 3600 cycles for (a) BM and (b) LSP treated material.



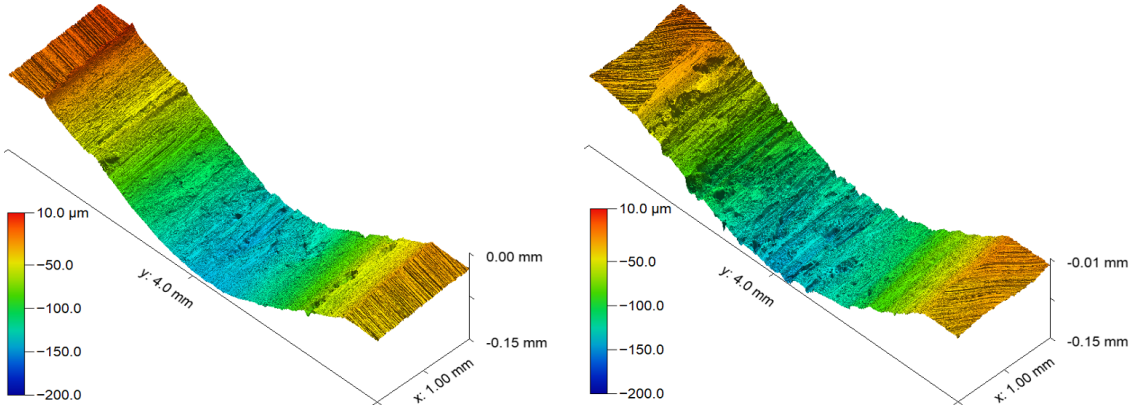
(a) (b)

Figure C.3: 3D Wear track profile after 34500 cycles for (a) BM and (b) LSP treated material.



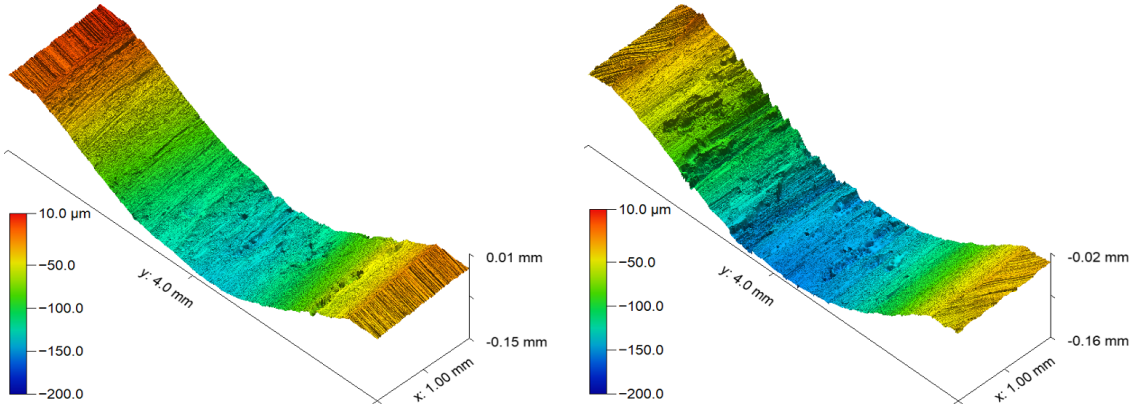
(a) (b)

Figure C.4: 3D Wear track profile after 69000 cycles for (a) BM and (b) LSP treated material.



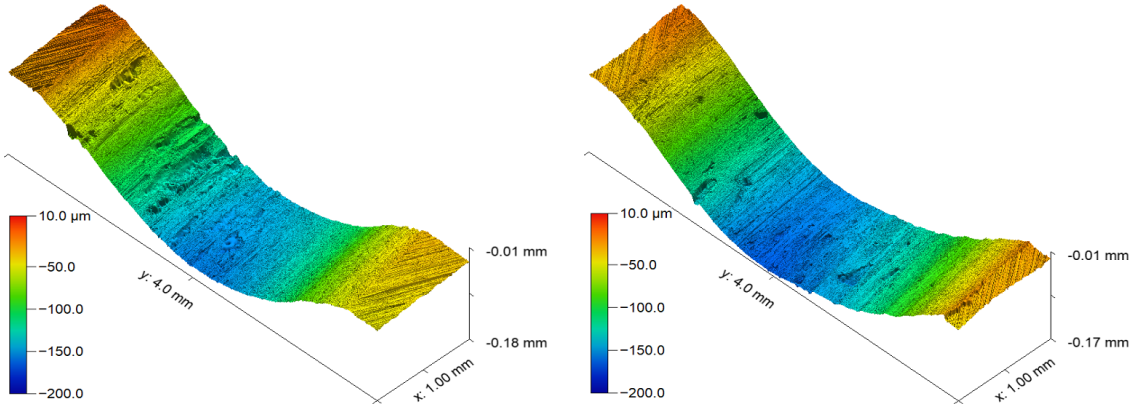
(a) (b)

Figure C.5: 3D Wear track profile after 103500 cycles for (a) BM and (b) LSP treated material.



(a) (b)

Figure C.6: 3D Wear track profile after 138000 cycles for (a) BM and (b) LSP treated material.



(a) (b)

Figure C.7: 3D Wear track profile after 172500 cycles for (a) BM and (b) LSP treated material.

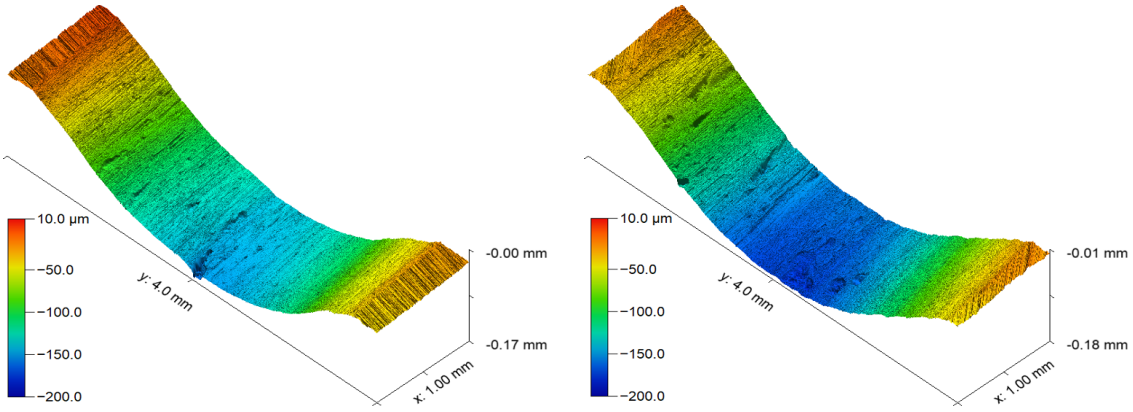


Figure C.8: 3D Wear track profile after 207000 cycles for (a) BM and (b) LSP treated material.

Appendix D

Surface roughness parameters

This Appendix provides the individual results for each surface parameter measurement according to the different LSP treatment conditions as well as the base material. Four different positions were measured for each specimen. The average roughness (R_a), maximum height of the profile (R_z), the root-mean-square roughness (R_q), average waviness (W_a), total waviness (W_t) and total height of profile (P_t) were measured for each condition applying a roughness filter cut off wavelength (0.25 mm) in accordance with standards DIN 4768, ISO 4287 and 4288.

D.1 Surface parameters

Table D.1 presents the results of the surface parameters for the base material. Table D.2, D.3, D.4, D.5, and D.6 present the single measurement results of the surface parameters for LSP treated material using pulse density of 100 pulses/cm^2 and laser energy of 1, 2, 3, 4 and 5J, respectively. Table D.7, D.8, D.9, D.10, and D.11 present the single measurement results of the surface parameters for LSP treated material using a pulse density of 200 pulses/cm^2 and laser energy of 1, 2, 3, 4 and 5J, respectively.

Table D.1: Surface parameters of BM.

Measurement	R_a [μm]	R_z [μm]	R_q [μm]	P_t [μm]	W_t [μm]	W_a [μm]
1	0.08	0.97	0.12	2.25	1.75	0.29
2	0.09	1.24	0.13	3.09	1.64	0.30
3	0.08	0.84	0.11	3.58	1.52	0.27
4	0.08	1.09	0.11	2.24	1.22	0.17

Table D.2: Surface parameters of LSP treated material using laser energy of 1J and laser pulse density of 100 pulses/cm^2.

Measurement	R_a [μm]	R_z [μm]	R_q [μm]	P_t [μm]	W_t [μm]	W_a [μm]
1	0.08	1.06	0.11	3.53	1.98	0.34
2	0.08	0.83	0.11	3.85	2.93	0.42
3	0.11	1.24	0.16	3.75	3.17	0.44
4	0.10	1.33	0.15	3.47	2.98	0.43

Table D.3: Surface parameters of LSP treated material using laser energy of 2J and laser pulse density of 100 pulses/cm^2.

Measurement	R_a [μm]	R_z [μm]	R_q [μm]	P_t [μm]	W_t [μm]	W_a [μm]
1	0.12	1.30	0.17	6.41	5.19	1.10
2	0.14	1.32	0.19	6.81	6.28	1.33
3	0.13	1.17	0.17	6.43	5.86	1.23
4	0.15	1.48	0.20	7.33	6.71	1.33

Table D.4: Surface parameters of LSP treated material using laser energy of 3J and laser pulse density of 100 pulses/cm^2.

Measurement	R_a [μm]	R_z [μm]	R_q [μm]	P_t [μm]	W_t [μm]	W_a [μm]
1	0.18	2.26	0.33	9.81	7.48	1.57
2	0.16	1.94	0.25	8.10	6.82	1.52
3	0.17	1.98	0.23	8.32	7.21	1.68
4	0.16	1.79	0.22	7.91	6.89	1.66

Table D.5: Surface parameters of LSP treated material using laser energy of 4J and laser pulse density of 100 pulses/cm^2.

Measurement	R_a [μm]	R_z [μm]	R_q [μm]	P_t [μm]	W_t [μm]	W_a [μm]
1	0.19	1.79	0.25	10.49	9.48	1.92
2	0.19	2.14	0.27	9.52	8.42	1.97
3	0.17	1.44	0.22	8.53	7.65	1.98
4	0.17	1.33	0.22	10.81	8.60	1.90

Table D.6: Surface parameters of LSP treated material using laser energy of 5J and laser pulse density of 100 pulses/cm^2.

Measurement	R_a [μm]	R_z [μm]	R_q [μm]	P_t [μm]	W_t [μm]	W_a [μm]
1	0.20	2.20	0.28	9.02	7.71	1.77
2	0.20	1.72	0.27	10.43	9.49	1.95
3	0.18	2.00	0.24	9.67	8.73	2.05
4	0.15	1.25	0.19	9.15	7.68	1.75

Table D.7: Surface parameters of LSP treated material using laser energy of 1J and laser pulse density of 200 pulses/cm^2.

Measurement	R_a [μm]	R_z [μm]	R_q [μm]	P_t [μm]	W_t [μm]	W_a [μm]
1	0.15	1.99	0.23	5.67	3.90	0.65
2	0.14	2.46	0.26	8.74	4.93	0.79
3	0.12	1.52	0.17	4.00	3.32	0.73
4	0.11	1.60	0.17	4.48	3.80	0.61

Table D.8: Surface parameters of LSP treated material using laser energy of 2J and laser pulse density of 200 pulses/cm^2.

Measurement	R_a [μm]	R_z [μm]	R_q [μm]	P_t [μm]	W_t [μm]	W_a [μm]
1	0.20	1.89	0.27	11.68	9.14	2.08
2	0.21	1.84	0.28	10.08	8.98	2.05
3	0.21	2.23	0.30	12.72	9.75	1.98
4	0.18	1.70	0.25	10.56	7.98	1.83

Table D.9: Surface parameters of LSP treated material using laser energy of 3J and laser pulse density of 200 pulses/cm^2.

Measurement	R_a [μm]	R_z [μm]	R_q [μm]	P_t [μm]	W_t [μm]	W_a [μm]
1	0.22	1.58	0.28	14.21	12.96	3.02
2	0.22	1.71	0.28	14.46	11.84	2.81
3	0.26	2.43	0.34	16.12	12.24	3.09
4	0.24	2.13	0.30	14.16	11.91	2.83

Table D.10: Surface parameters of LSP treated material using laser energy of 4J and laser pulse density of 200 pulses/cm^2.

Measurement	R_a [μm]	R_z [μm]	R_q [μm]	P_t [μm]	W_t [μm]	W_a [μm]
1	0.28	2.19	0.36	14.14	13.14	3.42
2	0.25	2.20	0.33	15.26	13.97	3.37
3	0.24	1.78	0.30	17.14	15.22	3.26
4	0.27	2.01	0.34	14.81	13.58	3.42

Table D.11: Surface parameters of LSP treated material using laser energy of 5J and laser pulse density of 200 pulses/cm^2.

Measurement	R_a [μm]	R_z [μm]	R_q [μm]	P_t [μm]	W_t [μm]	W_a [μm]
1	0.31	2.52	0.40	19.38	17.87	3.53
2	0.30	2.60	0.40	18.32	16.92	3.89
3	0.28	2.06	0.36	16.52	14.79	3.55
4	0.28	2.00	0.37	18.45	16.31	3.90

D.2 Roughness profile

Figure D.1 presents the roughness profile of base material. Figures D.2a and D.2b present the roughness profile of LSP treated material using laser energy of 1J and pulse density of 100 and 200 pulses/cm^2, respectively. Figures D.3a and D.3b present the roughness profile of LSP treated material using laser energy of 2J and pulse density of 100 and 200 pulses/cm^2, respectively. Figures D.4a and D.4b present the roughness profile of LSP treated material using laser energy of 3J and pulse density of 100 and 200 pulses/cm^2, respectively. Figures D.5a and D.5b present the roughness profile of LSP treated material using laser energy of 4J and pulse density of 100 and 200 pulses/cm^2, respectively. Figures D.6a and D.6b present the roughness profile of LSP treated material using laser energy of 5J and pulse density of 100 and 200 pulses/cm^2, respectively.

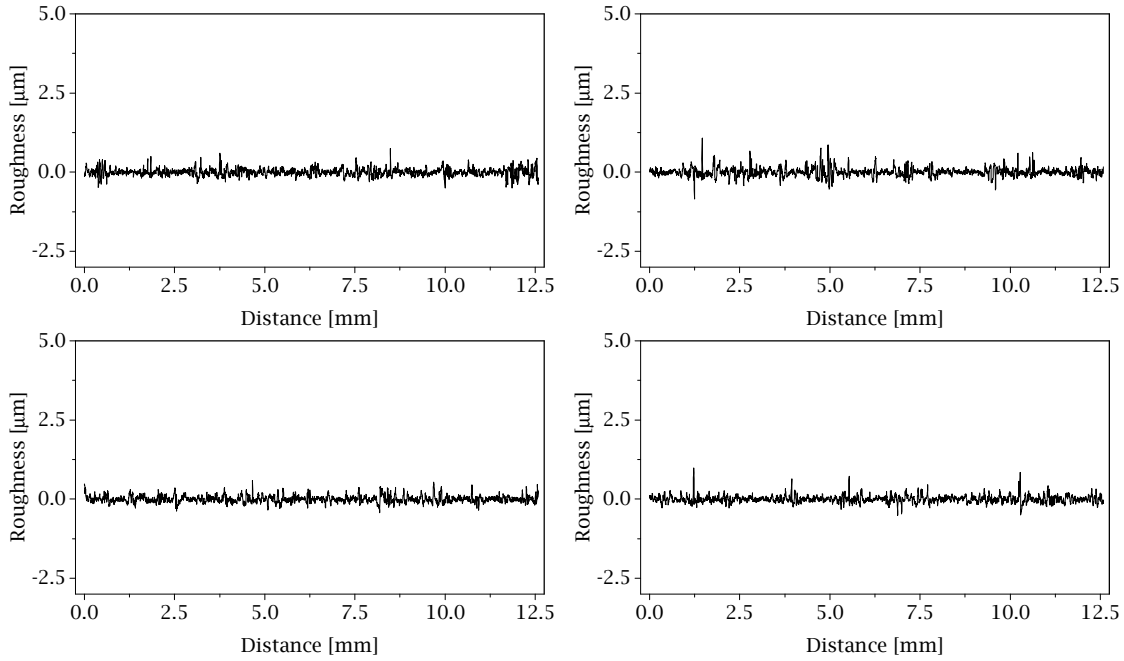
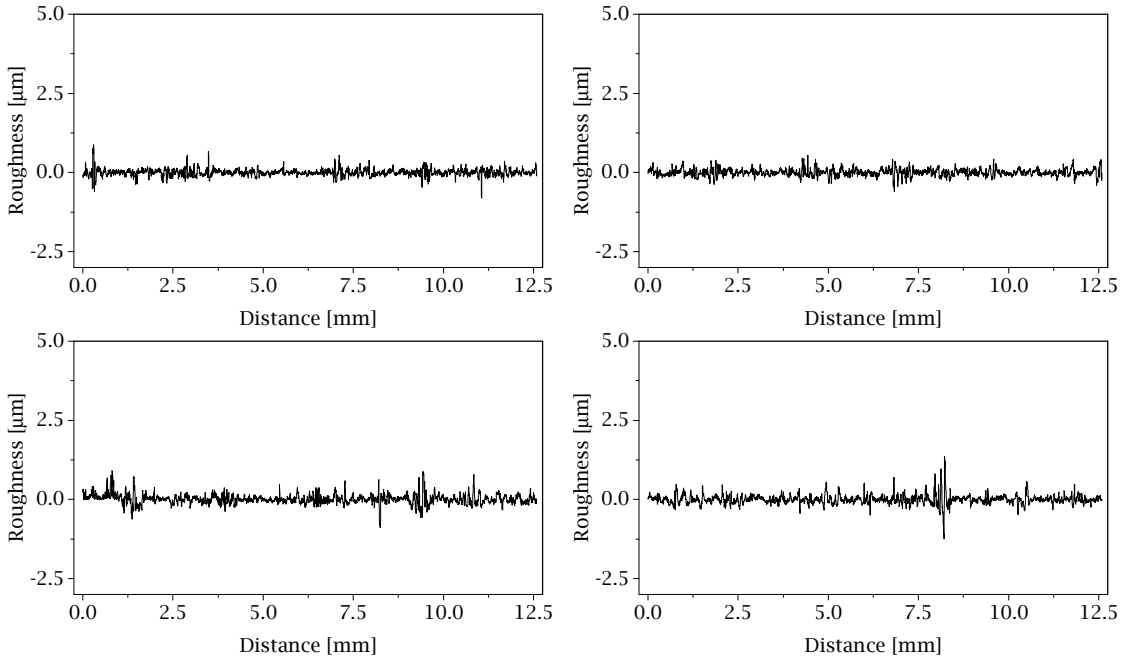
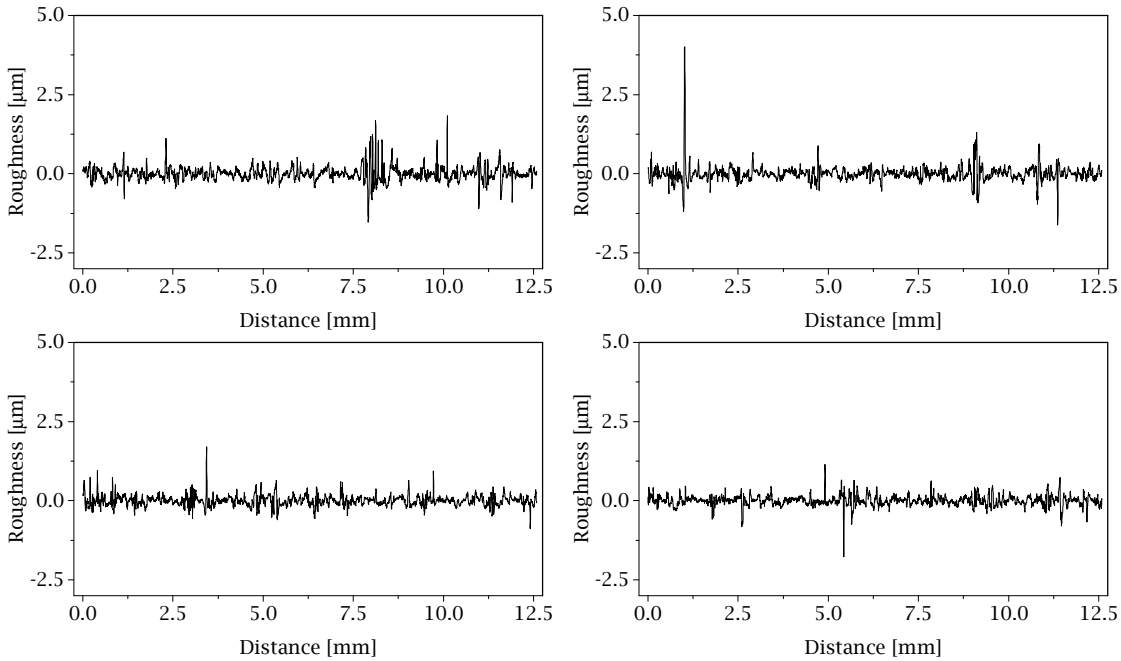


Figure D.1: Roughness profile of BM.

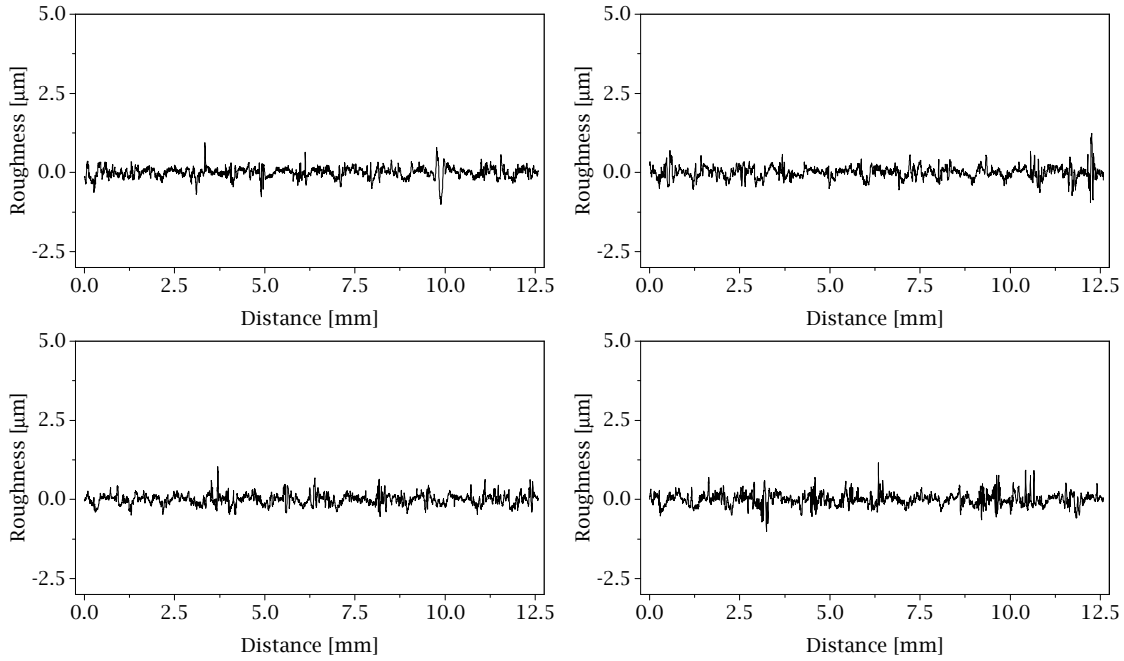


(a) Laser pulse density of 100 pulses/cm^2.

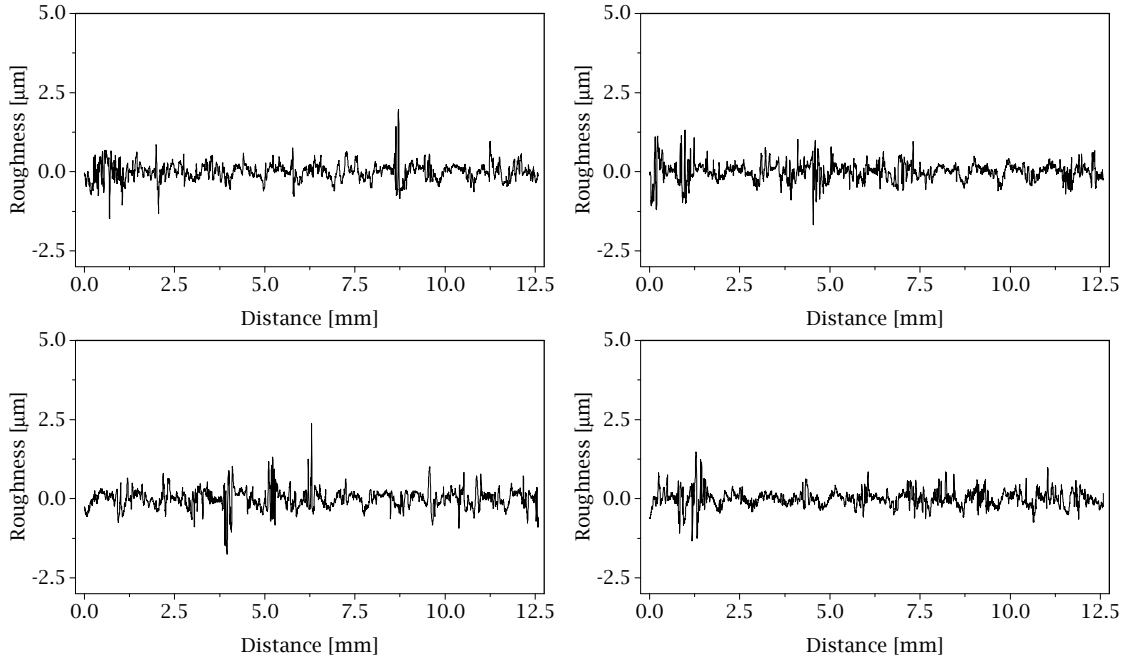


(b) Laser pulse density of 200 pulses/cm^2.

Figure D.2: Roughness profile of LSP treated material using laser energy of 1J and pulse density of (a) 100 and (b) 200 pulses/cm^2.

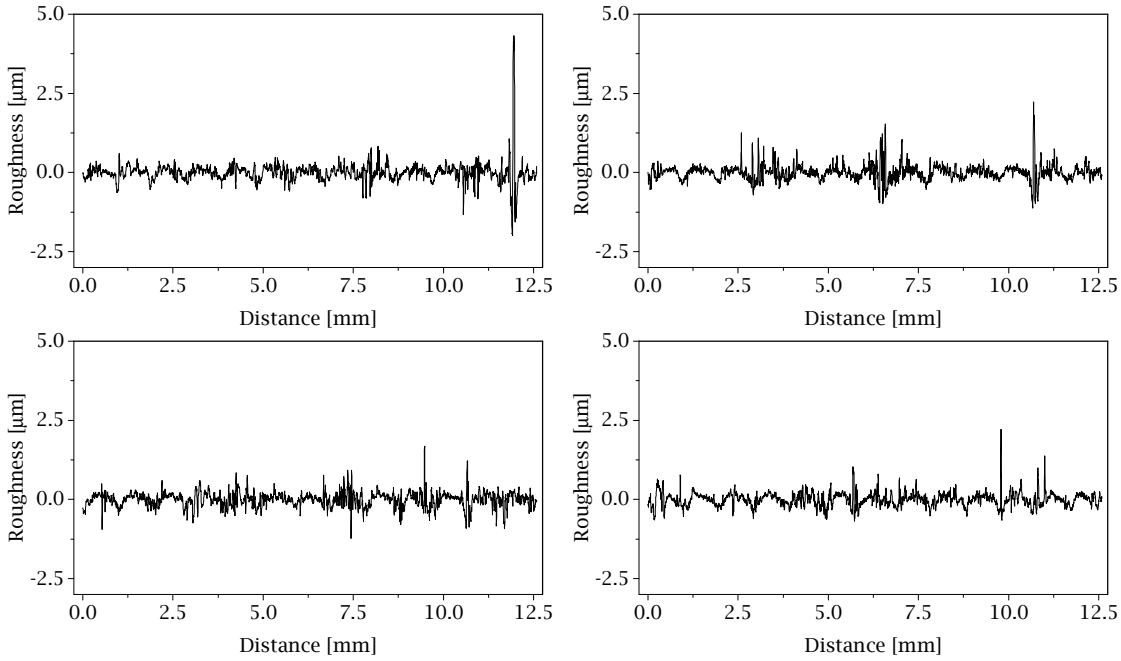


(a) Laser pulse density of 100 pulses/cm^2.

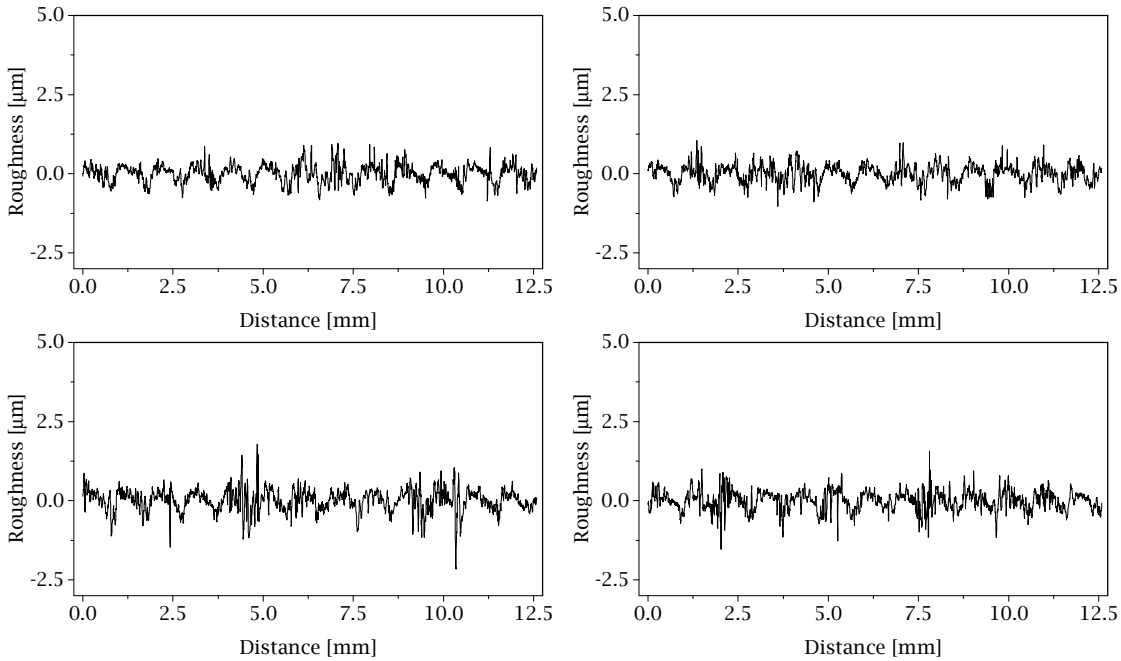


(b) Laser pulse density of 200 pulses/cm^2.

Figure D.3: Roughness profile of LSP treated material using laser energy of 2J and pulse density of (a) 100 and (b) 200 pulses/cm^2.

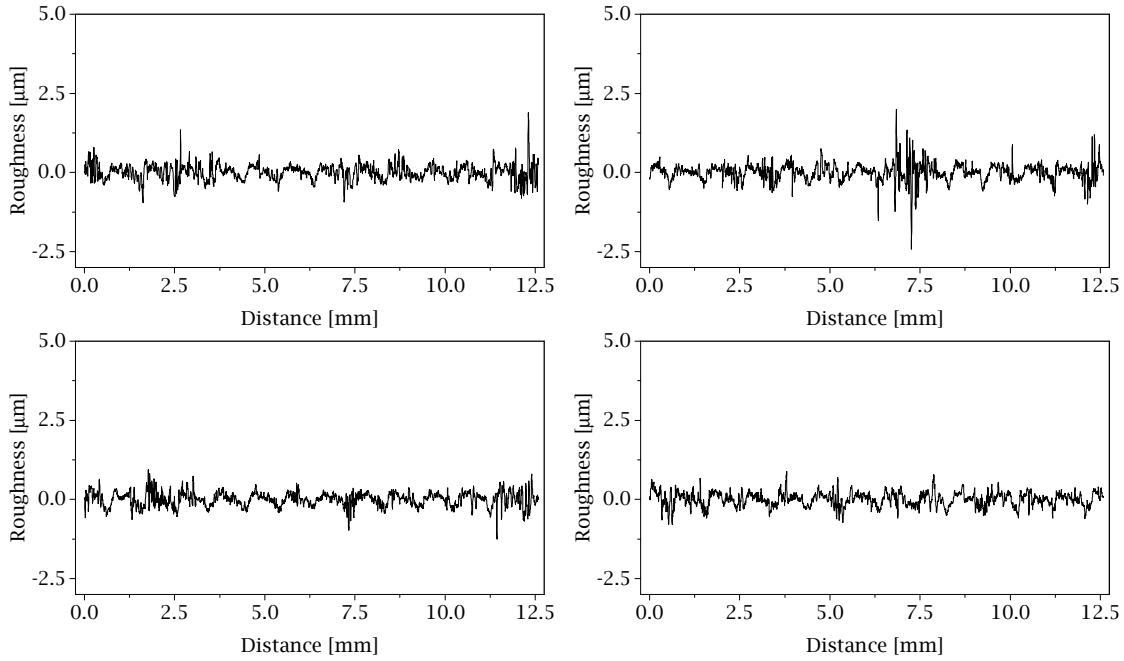


(a) Laser pulse density of 100 pulses/cm^2.

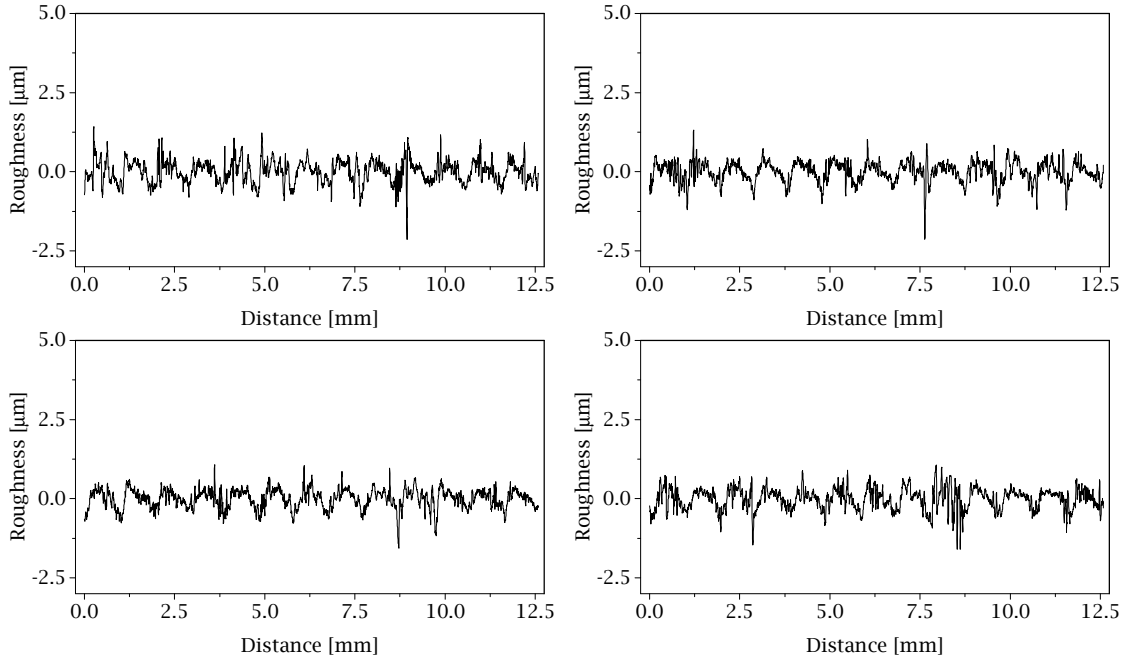


(b) Laser pulse density of 200 pulses/cm^2.

Figure D.4: Roughness profile of LSP treated material using laser energy of 3J and pulse density of (a) 100 and (b) 200 pulses/cm^2.

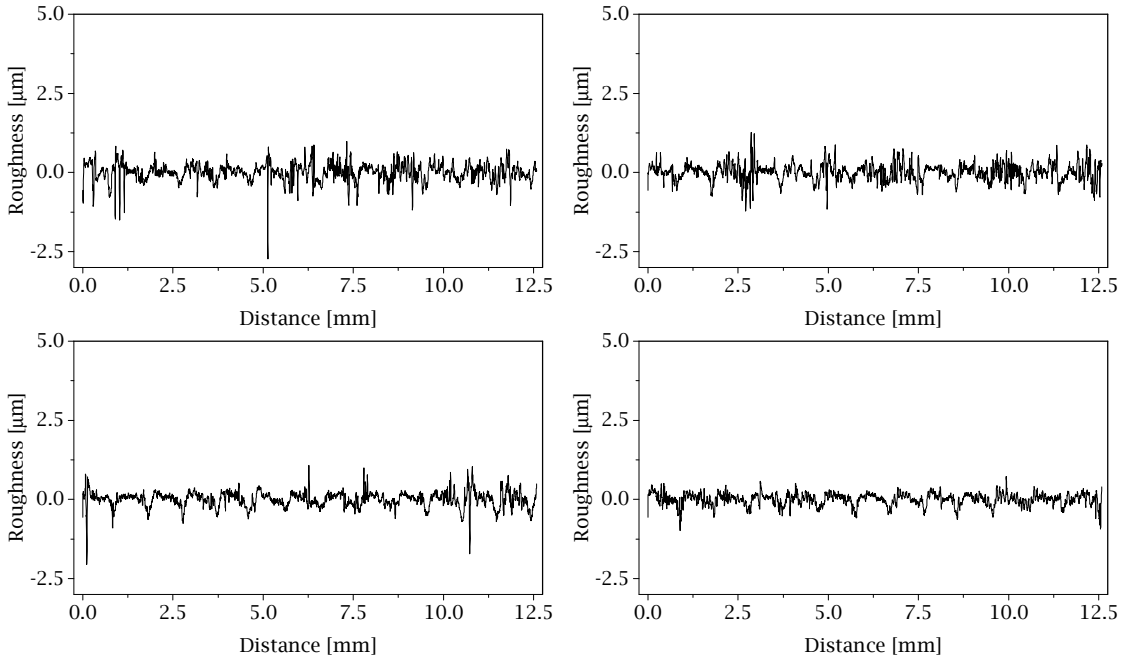


(a) Laser pulse density of 100 pulses/cm^2.

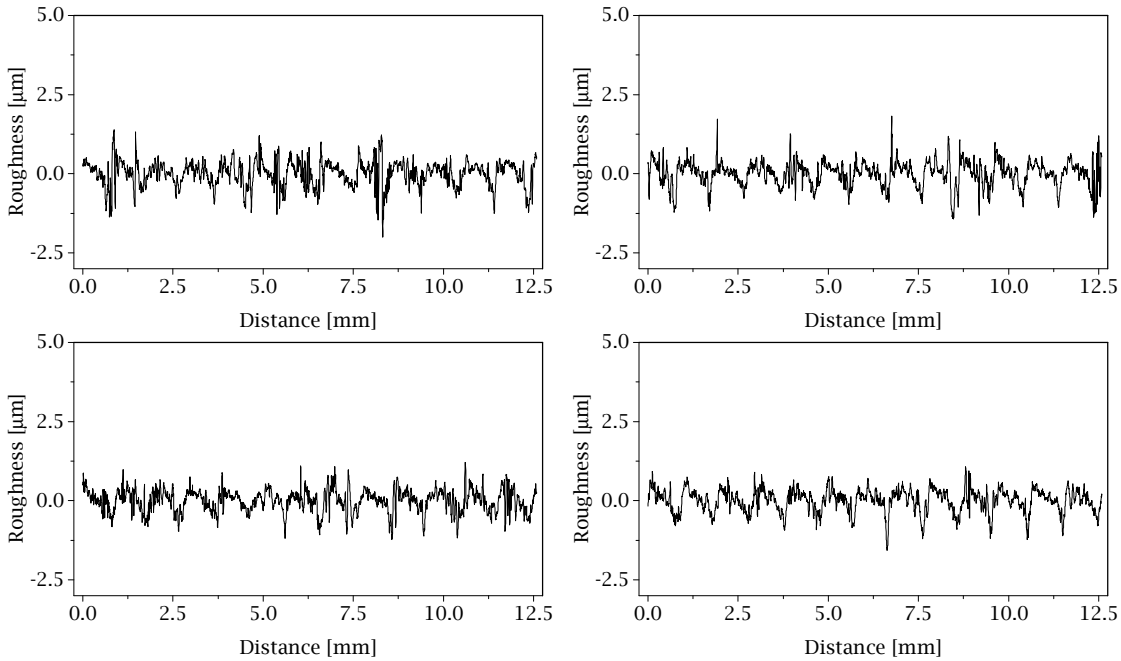


(b) Laser pulse density of 200 pulses/cm^2.

Figure D.5: Roughness profile of LSP treated material using laser energy of 4J and pulse density of (a) 100 and (b) 200 pulses/cm^2.



(a) Laser pulse density of 100 pulses/cm^2.



(b) Laser pulse density of 200 pulses/cm^2.

Figure D.6: Roughness profile of LSP treated material using laser energy of 5J and pulse density of (a) 100 and (b) 200 pulses/cm^2.

Appendix E

Micro hardness

This Appendix provides micro hardness measurements according to the different LSP treatment conditions as well as the base material. Figure E.1 presents the micro hardness profile for base material. Figures E.2a and E.2b present the micro hardness profile of LSP treated material using laser energy of 1J and pulse density of 100 and 200 pulses/cm^2, respectively. Figures E.3a and E.3b present the micro hardness profile of LSP treated material using laser energy of 2J and pulse density of 100 and 200 pulses/cm^2, respectively. Figures E.4a and E.4b present the micro hardness profile of LSP treated material using laser energy of 3J and pulse density of 100 and 200 pulses/cm^2, respectively. Figures E.5a and E.5b present the micro hardness profile of LSP treated material using laser energy of 4J and pulse density of 100 and 200 pulses/cm^2, respectively. Figures E.6a and E.6b present the micro hardness profile of LSP treated material using laser energy of 5J and pulse density of 100 and 200 pulses/cm^2, respectively.

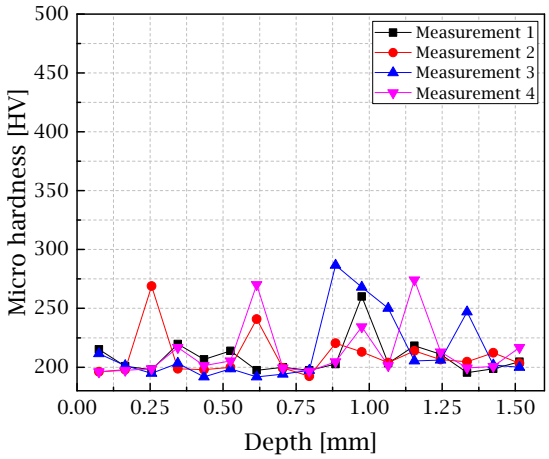
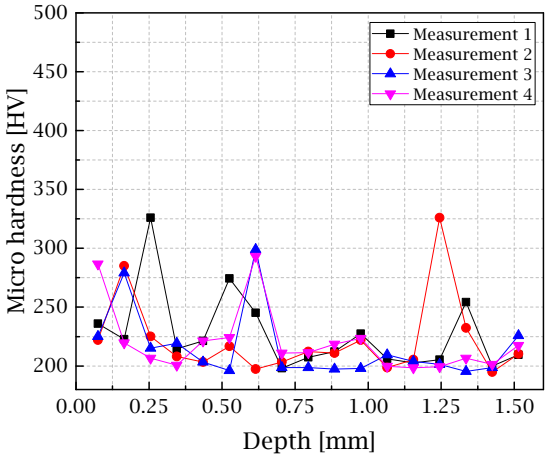
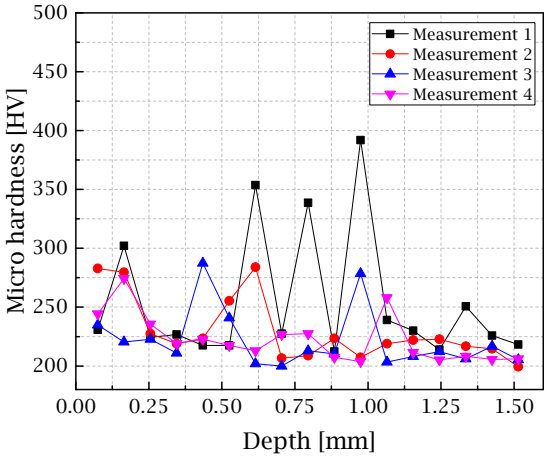


Figure E.1: Vickers micro hardness test results of BM.

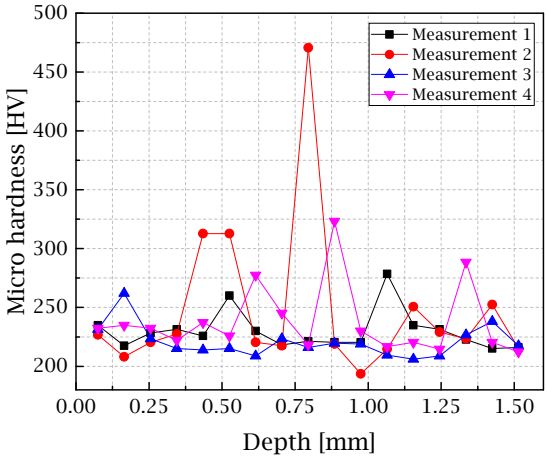


(a) Laser pulse density of 100 pulses/cm^2.

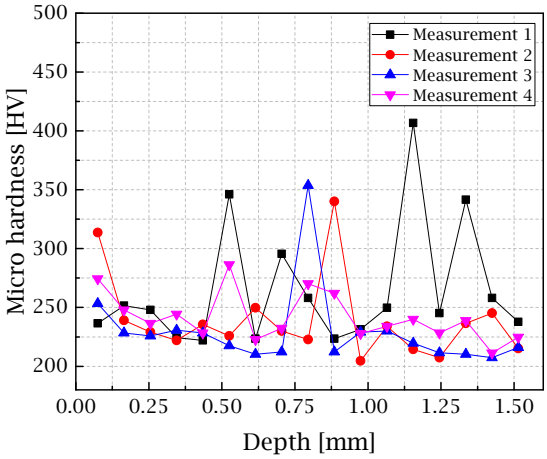


(b) Laser pulse density of 200 pulses/cm^2.

Figure E.2: Vickers micro hardness test results of LSP treated material using laser energy of 1J and laser pulse density of (a) 100 and (b) 200 pulses/cm^2.

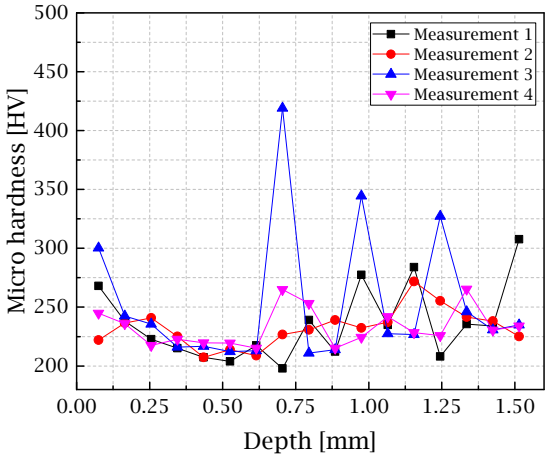


(a) Laser pulse density of 100 pulses/cm^2.

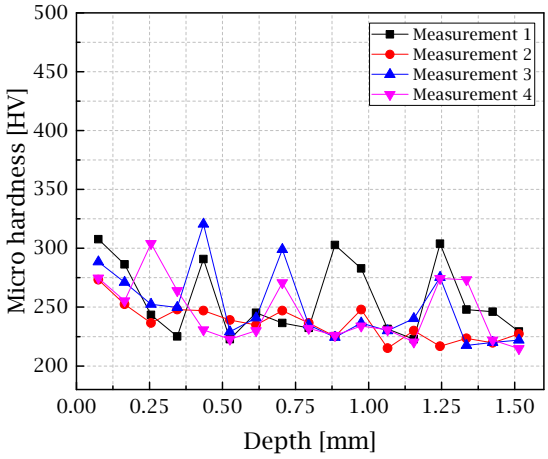


(b) Laser pulse density of 200 pulses/cm^2.

Figure E.3: Vickers micro hardness test results of LSP treated material using laser energy of 2J and laser pulse density of (a) 100 and (b) 200 pulses/cm^2.

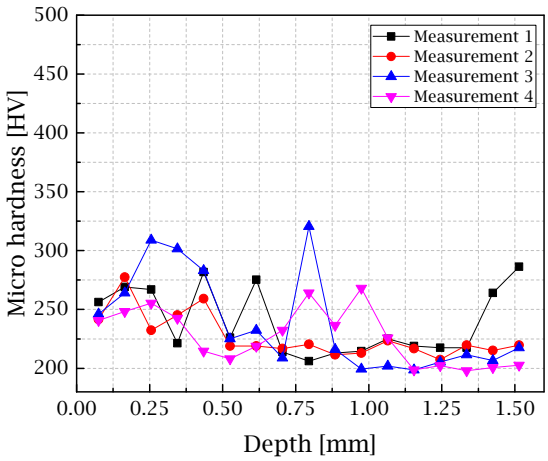


(a) Laser pulse density of 100 pulses/cm^2.

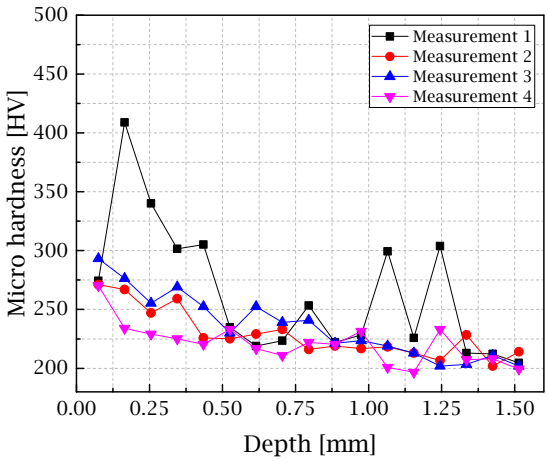


(b) Laser pulse density of 200 pulses/cm^2.

Figure E.4: Vickers micro hardness test results of LSP treated material using laser energy of 3J and laser pulse density of (a) 100 and (b) 200 pulses/cm^2.

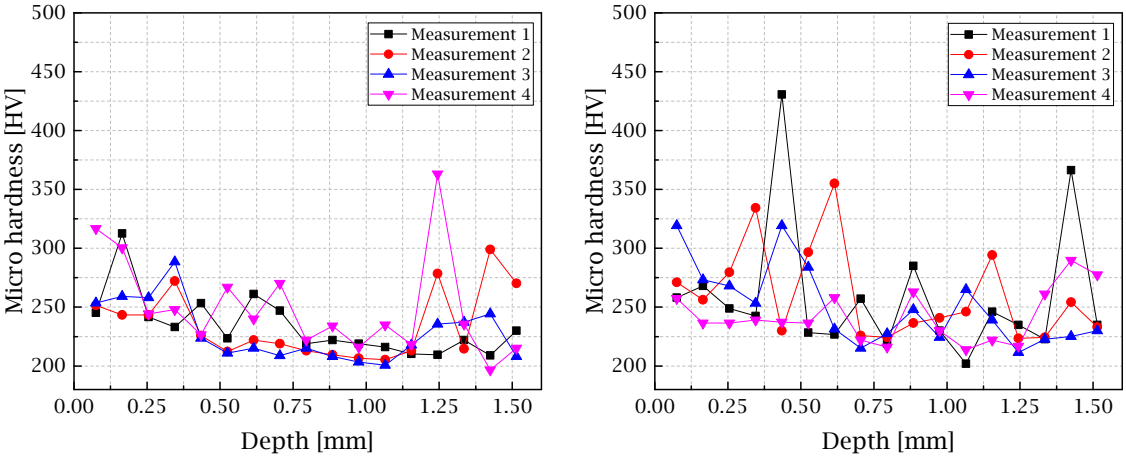


(a) Laser pulse density of 100 pulses/cm^2.



(b) Laser pulse density of 200 pulses/cm^2.

Figure E.5: Vickers micro hardness test results of LSP treated material using laser energy of 4J and laser pulse density of (a) 100 and (b) 200 pulses/cm^2.



(a) Laser pulse density of 100 pulses/cm^2.

(b) Laser pulse density of 200 pulses/cm^2.

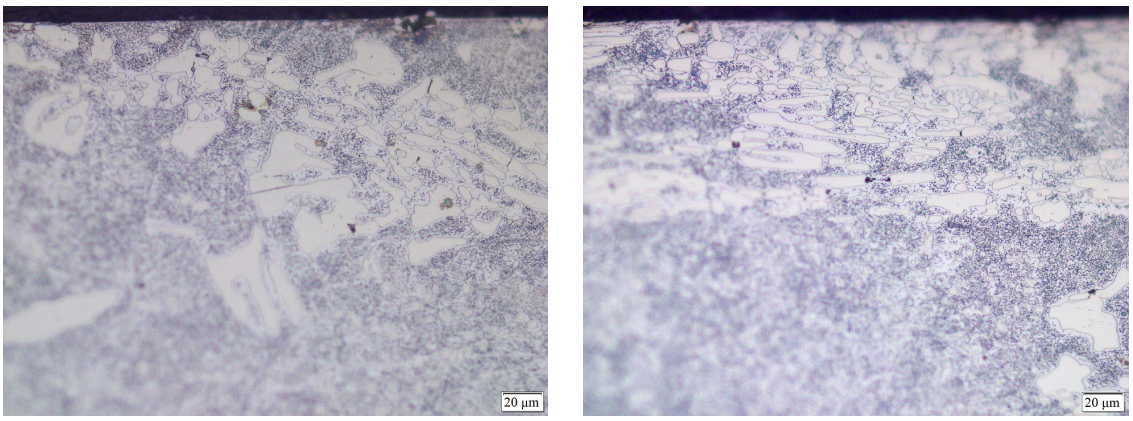
Figure E.6: Vickers micro hardness test results of LSP treated material using laser energy of 5J and laser pulse density of (a) 100 and (b) 200 pulses/cm^2.

Appendix F

Microstructure

F.1 Optical microscopy

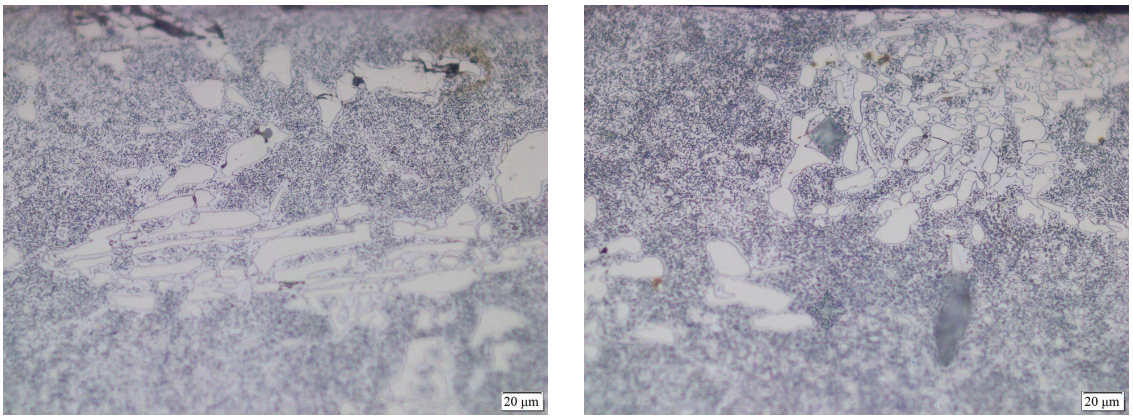
Figures F.1a and F.1b show the micrographs of LSP treated material using laser energy of 1J and laser pulse density of 100 and 200 pulses/cm^2, respectively.



(a) Laser pulse density of 100 pulses/cm^2. (b) Laser pulse density of 200 pulses/cm^2.

Figure F.1: Micrographs of LSP treated material using laser energy of 1J and laser pulse density of (a) 100 and (b) 200 pulses/cm^2.

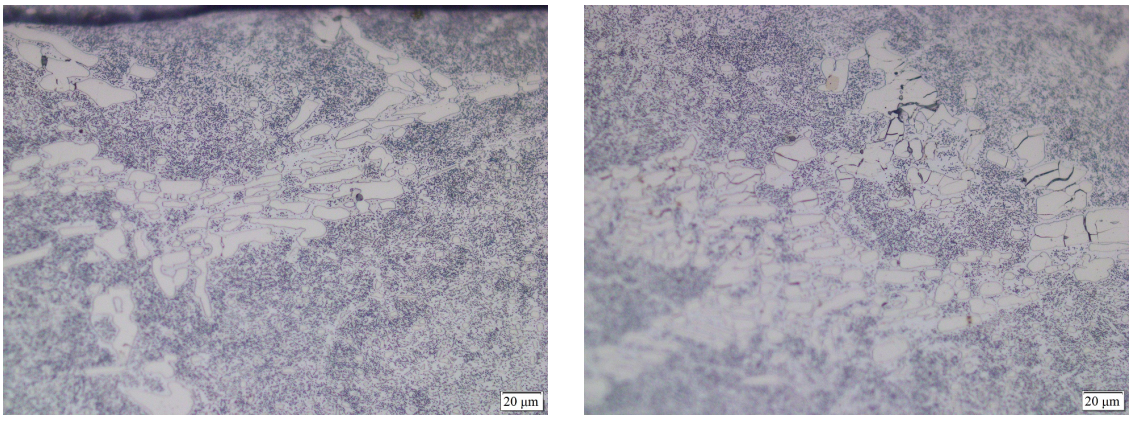
Figures F.2a and F.2b show the micrographs of LSP treated material using laser energy of 2J and laser pulse density of 100 and 200 pulses/cm^2, respectively.



(a) Laser pulse density of 100 pulses/cm^2. (b) Laser pulse density of 200 pulses/cm^2.

Figure F.2: Micrographs of LSP treated material using laser energy of 2J and laser pulse density of (a) 100 and (b) 200 pulses/cm^2.

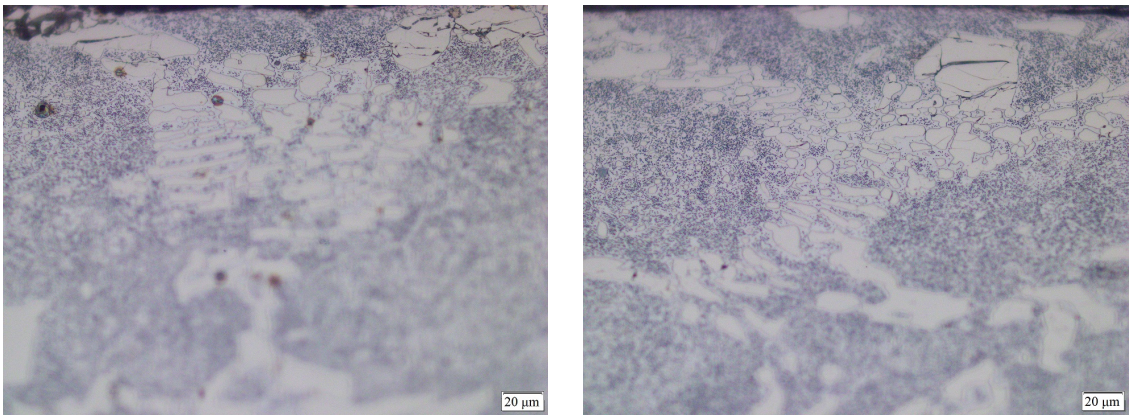
Figures F.3a and F.3b shows the micrographs of LSP treated material using laser energy of 3J and laser pulse density of 100 and 200 pulses/cm^2, respectively.



(a) Laser pulse density of 100 pulses/cm^2. (b) Laser pulse density of 200 pulses/cm^2.

Figure F.3: Micrographs of LSP treated material using laser energy of 3J and laser pulse density of (a) 100 and (b) 200 pulses/cm^2.

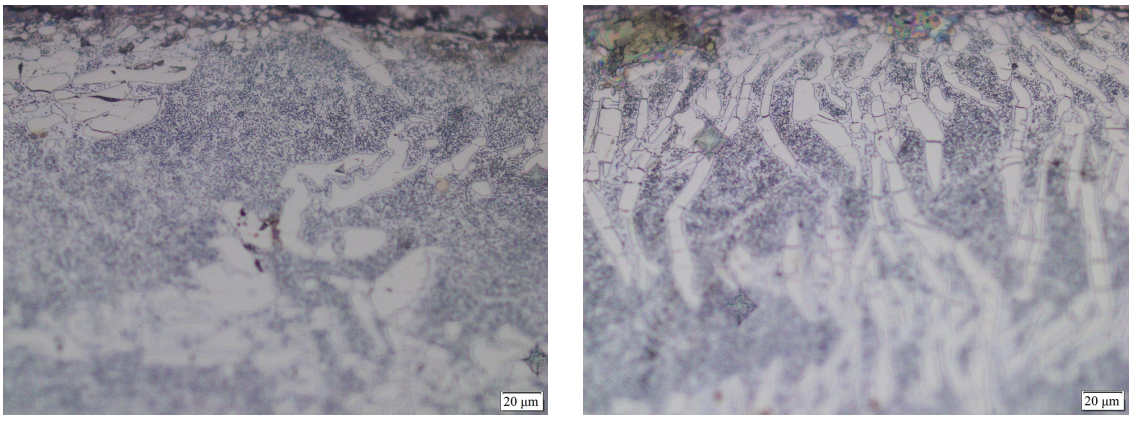
Figures F.4a and F.4b show the micrographs of LSP treated material using laser energy of 4J and laser pulse density of 100 and 200 pulses/cm^2, respectively.



(a) Laser pulse density of 100 pulses/cm^2. (b) Laser pulse density of 200 pulses/cm^2.

Figure F.4: Micrographs of LSP treated material using laser energy of 4J and laser pulse density of (a) 100 and (b) 200 pulses/cm^2.

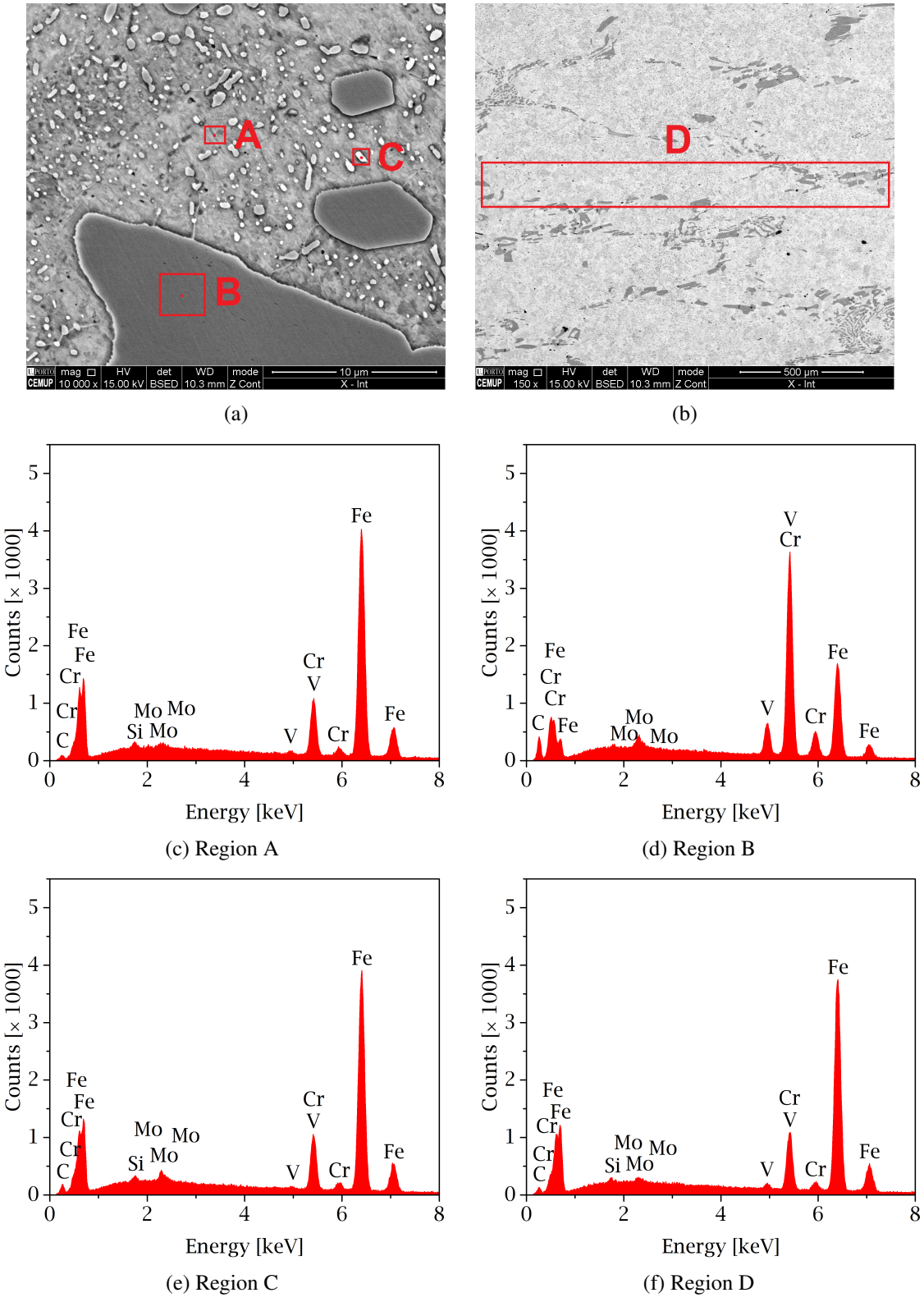
Figures F.5a and F.5b show the micrographs of LSP treated material using laser energy of 5J and laser pulse density of 100 and 200 pulses/cm^2, respectively.



(a) Laser pulse density of 100 pulses/cm^2. (b) Laser pulse density of 200 pulses/cm^2.

Figure F.5: Micrographs of LSP treated material using laser energy of 5J and laser pulse density of (a) 100 and (b) 200 pulses/cm^2.

F.2 EDS

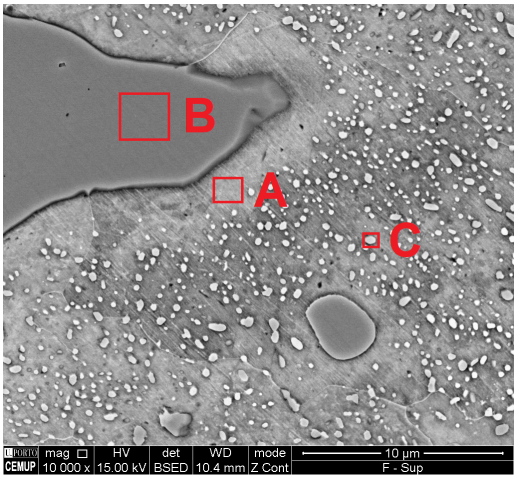


(a) (b)

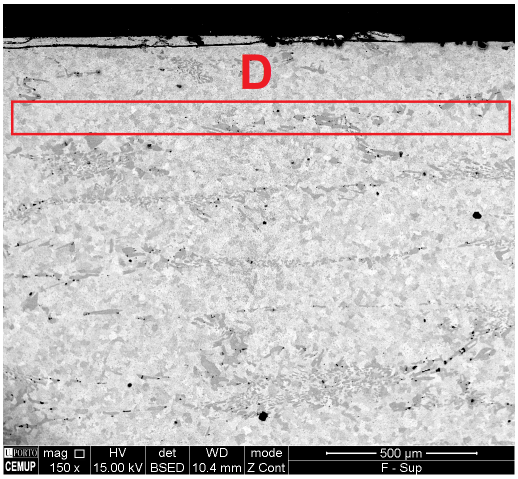
(c) Region A (d) Region B

(e) Region C (f) Region D

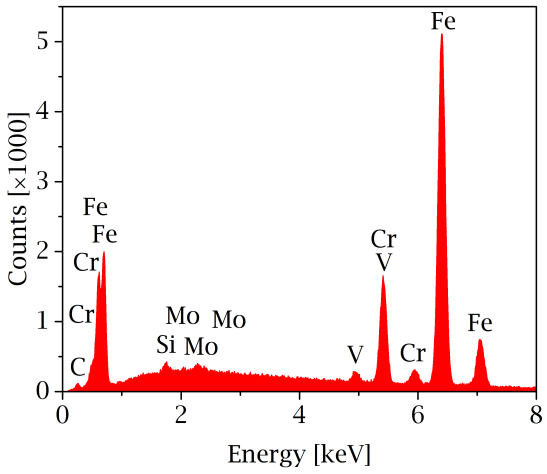
Figure F.6: (a and b) SEM figures of BM with marked regions and EDS spectra for region (c) A, (d) B, (e) C and (f) D.



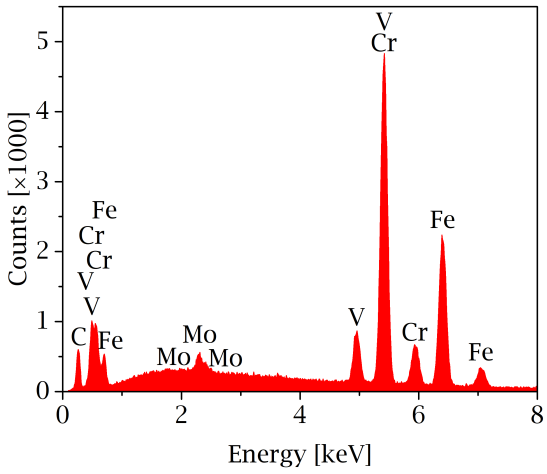
(a)



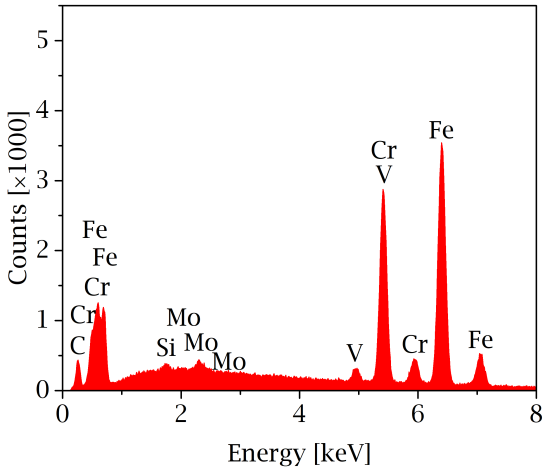
(b)



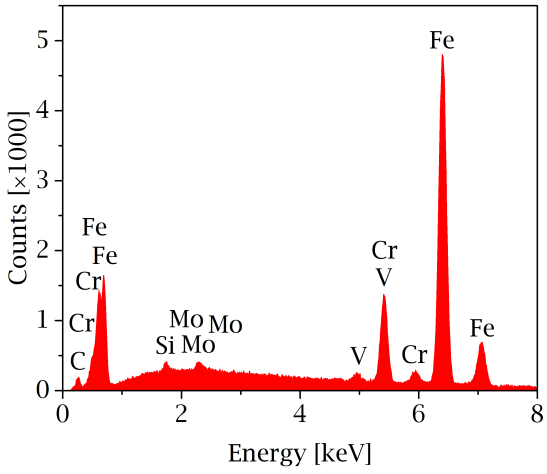
(c) Region A



(d) Region B

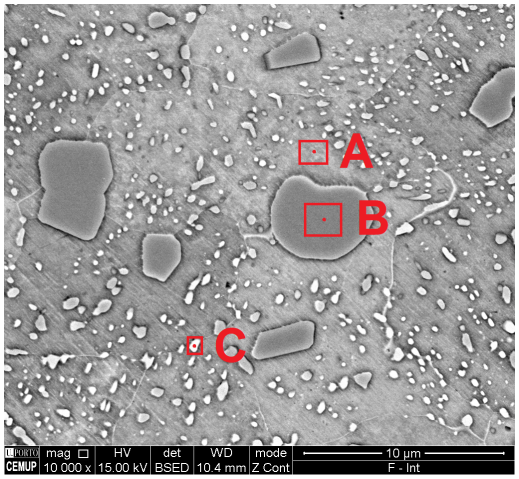


(e) Region C

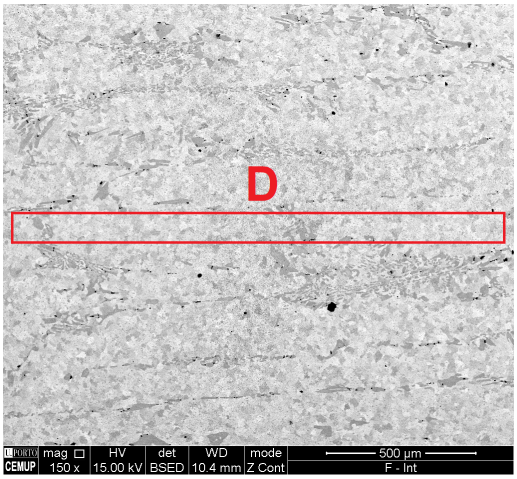


(f) Region D

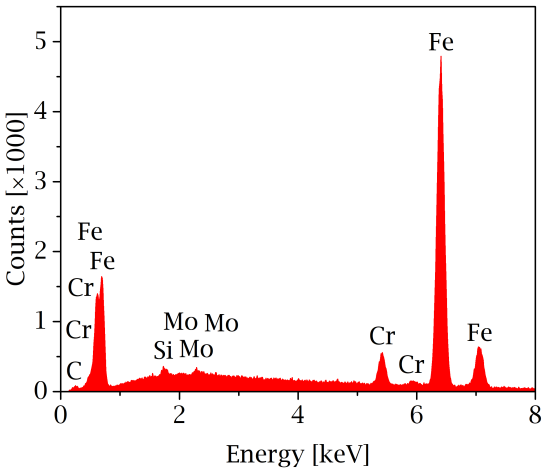
Figure F.7: (a and b) SEM figures of LSP-C with marked regions and EDS spectra for region (c) A, (d) B, (e) C and (f) D.



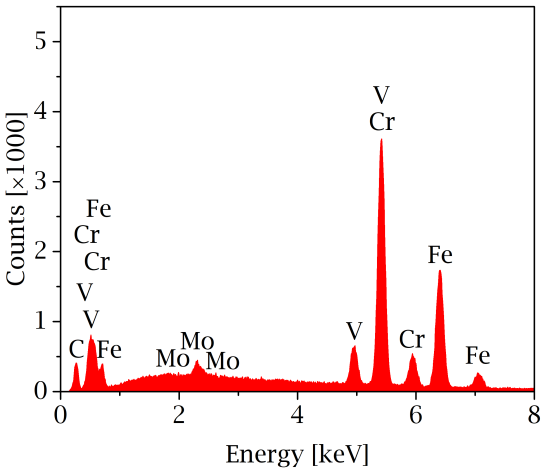
(a)



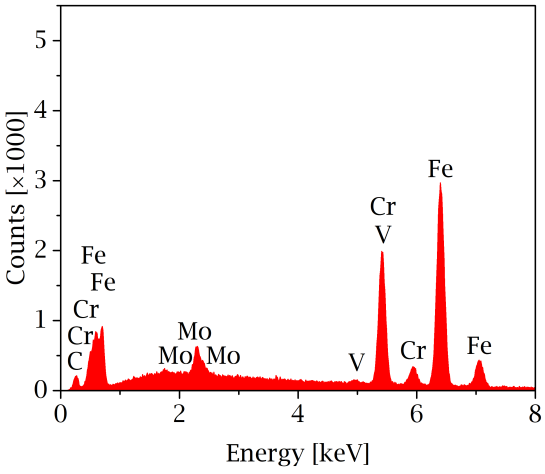
(b)



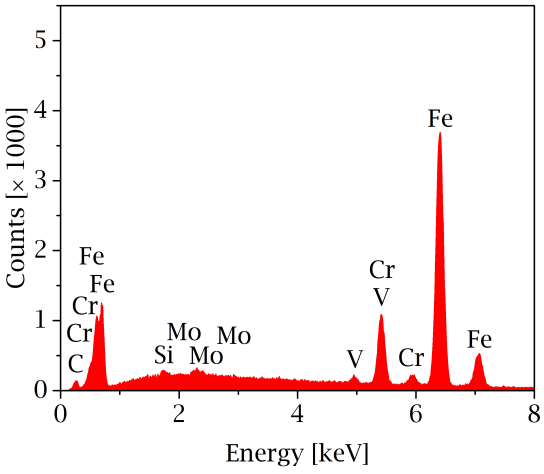
(c) Region A



(d) Region B

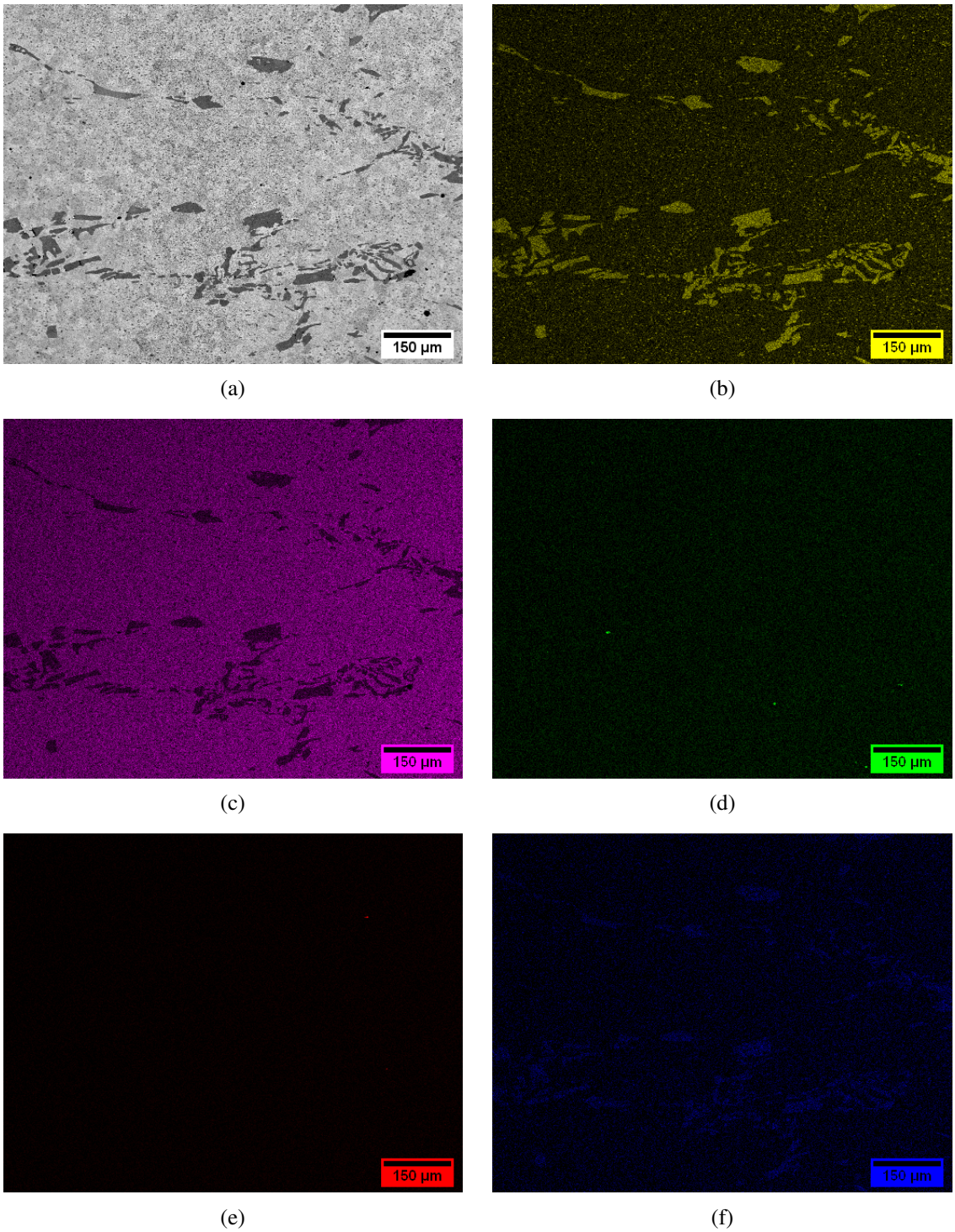


(e) Region C



(f) Region D

Figure F.8: (a and b) SEM figures of LSP-S with marked regions and EDS spectra for region (c) A, (d) B, (e) C and (f) D.

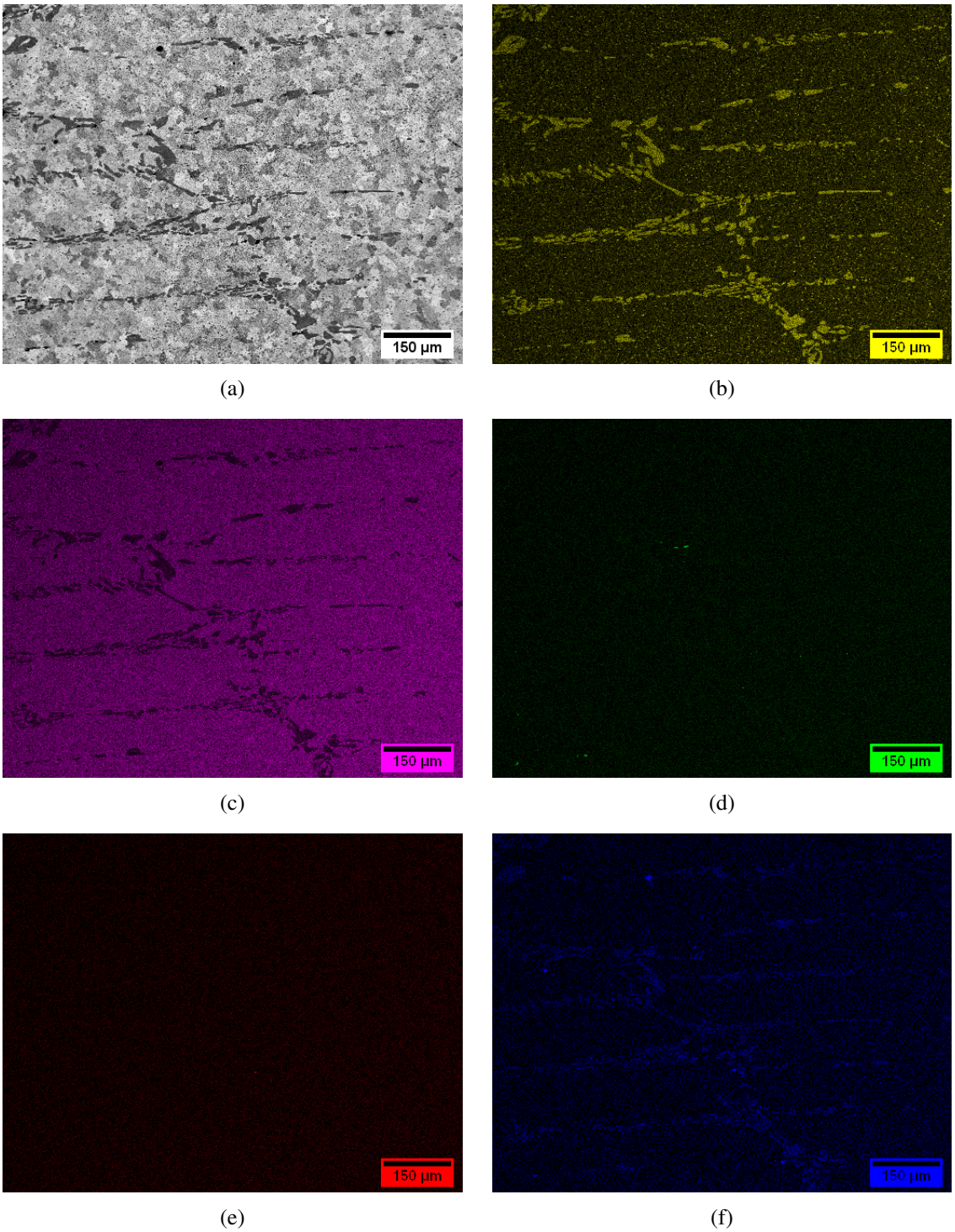


(a) (b)

(c) (d)

(e) (f)

Figure F.9: (a) SEM figure and EDS maps: (b) Cr, (c) Fe, (d) Mo (e) Si and (f) V for BM specimen.



(a) (b)

(c) (d)

(e) (f)

Figure F.10: (a) SEM figure and EDS maps: (b) Cr, (c) Fe, (d) Mo (e) Si and (f) V for LSP treated specimen.

References

N. C. Anderholm. Laser-generated stress waves. *Applied Physics Letters*, 16(3):113–115, 1970.

R. A. Antunes and M. C. L. Oliveira. 9 - Effect of surface treatments on the fatigue life of magnesium and its alloys for biomedical applications. In T. Narayanan, I.-S. Park, and M.-H. Lee, editors, *Surface Modification of Magnesium and its Alloys for Biomedical Applications*, pages 283 – 310. Woodhead Publishing, Oxford, 2015. ISBN 978-1-78242-078-1.

J. F. Archard. Contact and rubbing of flat surfaces. *Journal of Applied Physics*, 24(8):981–988, 1953.

A. F. Arif. Numerical prediction of plastic deformation and residual stresses induced by laser shock processing. *Journal of Materials Processing Technology*, 136(1):120 – 138, 2003.

D. R. Askeland and W. J. Wright. *The Science and Engineering of Materials*. Cengage Learning, SI edition, 2015. ISBN 1305077105.

ASTM E466-15. Standard Practice for Conducting Force Controlled Constant Amplitude Axial Fatigue Tests of Metallic Materials. Standard, ASTM International, West Conshohocken, PA, 2015.

ASTM E647-08. Standard Test Method for Measurement of Fatigue Crack Growth Rates. Standard, ASTM International, West Conshohocken, PA, 2008.

ASTM E837-13a. Standard Test Method for Determining Residual Stresses by the Hole-Drilling Strain-Gage Method. Standard, ASTM International, West Conshohocken, PA, 2013.

ASTM E8M. Standard Test Methods for Tension Testing of Metallic Materials. Standard, ASTM International, West Conshohocken, PA, 2016.

ASTM E92-17. Standard Test Methods for Vickers Hardness and Knoop Hardness of Metallic Materials. Standard, ASTM International, West Conshohocken, PA, 2017.

ASTM G99-17. Standard Test Method for Wear Testing with a Pin-on-Disk Apparatus. Standard, ASTM International, West Conshohocken, PA, 2017.

P. Ballard, J. Fournier, R. Fabbro, and J. Frelat. Residual stresses induced by laser-shocks. *Journal de Physique IV Colloque*, 01(C3):487–494, 1991.

S. Banerjee, P. J. Phillips, J. Nygaard, P.D. Mason, K. Ertel, M. De Vido, T. Butcher, S. Tomlinson, J. Smith, R. Allott, C. Edwards, and J. Collier. Acoustic signature of laser shock peening for a qualitative evaluation of residual stresses. *Applied Physics A*, 125(8):571, Jul 2019.

C. Barile, K. Casavola, G. Pappalettera, and C. Pappalettere. Analysis of the effects of process parameters in residual stress measurements on titanium plates by HDM/ESPI. *Measurement*, 48:220–227, 02 2014a.

C. Barile, K. Casavola, G. Pappalettera, and C. Pappalettere. Remarks on residual stress measurement by hole-drilling and electronic speckle pattern interferometry. *The Scientific World Journal*, 2014:487149, 07 2014b.

L. Berthe, R. Fabbro, P. Peyre, L. Tollier, and E. Bartnicki. Shock waves from a water-confined laser-generated plasma. *Journal of Applied Physics*, 82(6):2826–2832, 1997.

L. Berthe, R. Fabbro, P. Peyre, and E. Bartnicki. Experimental study of the transmission of breakdown plasma generated during laser shock processing. *European Physical Journal Applied Physics*, 3(2):215–218, 1998.

L. Berthe, R. Fabbro, P. Peyre, and E. Bartnicki. Wavelength dependent of laser shock-wave generation in the water-confinement regime. *Journal of Applied Physics*, 85(11):7552–7555, 1999.

D. Bombač, M. Fazarinc, A. Podder, and G. Kugler. Study of Carbide Evolution During Thermo-Mechanical Processing of AISI D2 Tool Steel. *Journal of Materials Engineering and Performance*, 22:742–747, 03 2013.

G. E. P. Box and N. R. Draper. *Empirical Model-Building and Response Surfaces*. John Wiley & Sons, 1987. ISBN 978-0471810339.

C. Le Bras, A. Rondepierre, R. Seddik, M. Scius-Bertrand, Y. Rouchausse, L. Videau, B. Fayolle, M. Gervais, L. Morin, S. Valadon, R. Ecault, D. Furfari, and L. Berthe. Laser shock peening: Toward the use of pliable solid polymers for confinement. *Metals*, 9:793, 07 2019.

R. Brockman, W. Braisted, S. Olson, R. Tenaglia, A. Clauer, K. Langer, and M. J. Shepard. Prediction and characterization of residual stresses from laser shock peening. *International Journal of Fatigue*, 36(1):96 – 108, 2012.

A. Brodeur. Ultrafast white-light continuum generation and self-focusing in transparent condensed media. *Journal of the Optical Society of America B*, 16:637, 04 1999.

W. E. Bryson. *Heat Treatment, Selection and Application of Tool Steels*. Hanser Publications, 2nd edition, 2009. ISBN 978-3-446-43670-1.

A. A. Bugayev, M. C. Gupta, and R. Payne. Laser processing of Inconel 600 and surface structure. *Optics and Lasers in Engineering*, 44(2):102 – 111, 2006.

P. N. Butcher and D. Cotter. *The Elements of Nonlinear Optics*. Cambridge Studies in Modern Optics. Cambridge University Press, 1990. ISBN 9781139167994.

Y. Cao, Y. C. Shin, and B. Wu. Parametric Study on Single Shot and Overlapping Laser Shock Peening on Various Metals via Modeling and Experiments. *Journal of Manufacturing Science and Engineering*, 132:1 – 10, 2010.

Z. Cao, H. Xu, S. Zou, and Z. Che. Investigation of surface integrity on TC17 titanium alloy treated by square-spot laser shock peening. *Chinese Journal of Aeronautics*, 25(4):650 – 656, 2012.

V. K. Caralapatti and S. Narayanswamy. Analyzing the effect of high repetition laser shock peening on dynamic corrosion rate of magnesium. *Optics & Laser Technology*, 93:165 – 174, 2017a.

V. K. Caralapatti and S. Narayanswamy. Effect of high repetition laser shock peening on biocompatibility and corrosion resistance of magnesium. *Optics & Laser Technology*, 88:75 – 84, 2017b.

A. Chahardehi, F.P. Brennan, and A. Steuwer. The effect of residual stresses arising from laser shock peening on fatigue crack growth. *Engineering Fracture Mechanics*, 77(11):2033 – 2039, 2010.

L. Chen, X. Ren, W. Zhou, Z. Tong, S. Adu-Gyamfi, Y. Ye, and Y. Ren. Evolution of microstructure and grain refinement mechanism of pure nickel induced by laser shock peening. *Materials Science and Engineering: A*, 728:20 – 29, 2018.

X. Chen, J. Wang, Y. Fang, B. Madigan, G. Xu, and J. Zhou. Investigation of microstructures and residual stresses in laser peened Incoloy 800H weldments. *Optics & Laser Technology*, 57:159 – 164, 2014.

S. Chupakhin, N. Kashaev, and N. Huber. Effect of elasto-plastic material behaviour on determination of residual stress profiles using the hole drilling method. *The Journal of Strain Analysis for Engineering Design*, 51:572–581, 08 2016.

S. Chupakhin, N. Kashaev, B. Klusemann, and N. Huber. Artificial neural network for correction of effects of plasticity in equibiaxial residual stress profiles measured by hole drilling. *The Journal of Strain Analysis for Engineering Design*, 52:137–151, 2017.

A. Clauer. Laser Shock Peening, the Path to Production. *Metals*, 9:626, 05 2019.

A. Clauer, B. P. Fairand, and B. A. Wilcox. Laser shock hardening of weld zones in aluminum alloys. *Metallurgical Transactions A*, 8(12):1871–1876, 1977.

C. Correa, L. Ruiz de Lara, M. Díaz, A. Gil-Santos, J. A. Porro, and J. L. Ocaña. Effect of advancing direction on fatigue life of 316L stainless steel specimens treated by double-sided laser shock peening. *International Journal of Fatigue*, 79:1 – 9, 2015a.

C. Correa, D. Peral, J. A. Porro, M. Díaz, L. Ruiz de Lara, A. García-Beltrán, and J. L. Ocaña. Random-type scanning patterns in laser shock peening without absorbing coating in 2024-T351 Al alloy: A solution to reduce residual stress anisotropy. *Optics & Laser Technology*, 73:179 – 187, 2015b.

F. Dai, J. Zhou, J. Lu, and X. Luo. A technique to decrease surface roughness in overlapping laser shock peening. *Applied Surface Science*, 370:501 – 507, 2016.

F. Z. Dai, J. Z. Lu, Y. K. Zhang, D. P. Wen, X. D. Ren, and J. Z. Zhou. Effect of laser spot size on the residual stress field of pure Al treated by laser shock processing: Simulations. *Applied Surface Science*, 316:477 – 483, 2014.

F. Z. Dai, Y. K. Zhang, J. Z. Lu, D. P. Wen, X. J. Hua, X. D. Ren, and J. Zhou. A method to decrease surface roughness in laser shock processing. *Surface and Coatings Technology*, 261: 35–40, 01 2015.

D. Das, A. Dutta, and K. K. Ray. On the refinement of carbide precipitates by cryotreatment in AISI D2 steel. *Philosophical Magazine*, 89:55–76, 01 2009.

D. Devaux, R. Fabbro, L. Tollier, and E. Bartnicki. Generation of Shock Waves by Laser-Induced Plasma in Confined Geometry. *Journal of Applied Physics*, 74:2268 – 2273, 09 1993.

B. Dhakal and S. Swaroop. Review: Laser shock peening as post welding treatment technique. *Journal of Manufacturing Processes*, 32:721 – 733, 2018.

K. Ding and L. Ye. *Laser shock peening. Performance and process simulation*. Woodhead Publishing, 2006. ISBN 9781845691097.

M. Dorman, M. B. Toparli, N. Smyth, A. Cini, M. E. Fitzpatrick, and P. E. Irving. Effect of laser shock peening on residual stress and fatigue life of clad 2024 aluminium sheet containing scribe defects. *Materials Science and Engineering: A*, 548:142 – 151, 2012.

R. Fabbro, J. Fournier, P. Ballard, D. Devaux, and J. Virmont. Physical study of laser-produced plasma in confined geometry. *Journal of Applied Physics*, 68(2):775–784, 1990.

R. Fabbro, P. Peyre, L. Berthe, and X. Scherpereel. Physics and applications of laser-shock processing. *Journal of Laser Applications*, 10(6):265 – 279, 1998.

Y. Fang, Y. Li, W. He, and P. Li. Effects of laser shock processing with different parameters and ways on residual stresses fields of a TC4 alloy blade. *Materials Science and Engineering: A*, 559:683 – 692, 2013a.

Y. Fang, Y. Li, W. He, Y. Lu, and P. Li. Numerical simulation of residual stresses fields of DD6 blade during laser shock processing. *Materials & Design*, 43:170 – 176, 2013b.

G. H. Farrahi, J. L. Lebrijn, and D. Couratin. Effect of shot peening on residual stress and fatigue life of a spring steel. *Fatigue & Fracture of Engineering Materials & Structures*, 18(2):211–220, 1995.

Y. Gao. Improvement of fatigue property in 7050–T7451 aluminum alloy by laser peening and shot peening. *Materials Science and Engineering: A*, 528(10):3823 – 3828, 2011.

M. Ge and J. Xiang. Effect of laser shock peening on microstructure and fatigue crack growth rate of AZ31B magnesium alloy. *Journal of Alloys and Compounds*, 680:544 – 552, 2016.

M. Ge, J. Xiang, Z. Fan, Y. Lu, and W. Lei. Effect of laser energy on microstructure of Mg-3Al-1Zn alloy treated by LSP. *Journal of Alloys and Compounds*, 734:266 – 274, 2018a.

M. Ge, J. Xiang, Y. Tang, X. Ye, Z. Fan, Y. Lu, and X. Zhang. Wear behavior of Mg-3Al-1Zn alloy subjected to laser shock peening. *Surface and Coatings Technology*, 337:501 – 509, 2018b.

A. Gill, A. Telang, and V. K. Vasudevan. Characteristics of surface layers formed on Inconel 718 by laser shock peening with and without a protective coating. *Journal of Materials Processing Technology*, 225:463 – 472, 2015.

G. Gomez-Rosas, C. Rubio-Gonzalez, J. L Ocaña, C. Molpeceres, J. A. Porro, W. Chi-Moreno, and M. Morales. High level compressive residual stresses produced in aluminum alloys by laser shock processing. *Applied Surface Science*, 252(4):883 – 887, 2005.

G. Gomez-Rosas, C. Rubio-Gonzalez, J. L. Ocaña, C. Molpeceres, J. A. Porro, M. Morales, and F.J. Casillas. Laser shock processing of 6061-T6 Al alloy with 1064 nm and 532 nm wavelengths. *Applied Surface Science*, 256(20):5828 – 5831, 2010.

V. Granados-Alejo, C. Rubio-González, C. A. Vázquez-Jiménez, J. A. Banderas, and G. Gómez-Rosas. Influence of specimen thickness on the fatigue behavior of notched steel plates subjected to laser shock peening. *Optics & Laser Technology*, 101:531 – 544, 2018.

Y. Guo, M. P. Sealy, and C. Guo. Significant improvement of corrosion resistance of biodegradable metallic implants processed by laser shock peening. *CIRP Annals*, 61(1):583 – 586, 2012.

Y. Guo, S. Wang, W. Liu, T. Xiao, G. Zhu, and Z. Sun. The Effect of Laser Shock Peening on the Corrosion Behavior of Biocompatible Magnesium Alloy ZK60. *Metals*, 9:1237, 2019.

G. Hammersley, L. A. Hackel, and F. Harris. Surface prestressing to improve fatigue strength of components by laser shot peening. *Optics and Lasers in Engineering*, 34(4):327 – 337, 2000.

O. Hatamleh. Effects of peening on mechanical properties in friction stir welded 2195 aluminum alloy joints. *Materials Science and Engineering: A*, 492(1):168 – 176, 2008.

O. Hatamleh, J. Lyons, and R. Forman. Laser and shot peening effects on fatigue crack growth in friction stir welded 7075-T7351 aluminum alloy joints. *International Journal of Fatigue*, 29 (3):421 – 434, 2007.

J. Hecht. *The laser guidebook*. McGraw-Hill Professional, 2nd edition, 1999. ISBN 0071359672.

X. Hong, S. Wang, D. Guo, H. Wu, J. Wang, Y. Dai, X. Xia, and Y. Xie. Confining medium and absorptive overlay: Their effects on a laser-induced shock wave. *Optics and Lasers in Engineering*, 29(6):447 – 455, 1998.

Y. Hu and Z. Yao. FEM simulation of residual stresses induced by laser shock with overlapping laser spots. *Acta Metallurgica Sinica (English Letters)*, 21(2):125 – 132, 2008.

Y. Hu, C. Gong, Z. Yao, and J. Hu. Investigation on the non-homogeneity of residual stress field induced by laser shock peening. *Surface and Coatings Technology*, 203(23):3503 – 3508, 2009.

Y. Hu, R. Yang, D. Wang, and Z. Yao. Geometry distortion and residual stress of alternate double-sided laser peening of thin section component. *Journal of Materials Processing Technology*, 251:197 – 204, 2018.

S. Huang, J. Zhou, J. Sheng, J. Lu, G. Sun, X. Meng, L. Zuo, H. Ruan, and H. Chen. Effects of laser energy on fatigue crack growth properties of 6061-T6 aluminum alloy subjected to multiple laser peening. *Engineering Fracture Mechanics*, 99:87 – 100, 2013a.

S. Huang, Y. Zhu, W. Guo, P. Peng, and X. Diao. Impact toughness and microstructural response of Ti-17 titanium alloy subjected to laser shock peening. *Surface and Coatings Technology*, 327:32 – 41, 2017.

X. Huang, Z. Liu, and H. Xie. Recent progress in residual stress measurement techniques. *Acta Mechanica Solida Sinica*, 26(6):570 – 583, 2013b.

N. Huber and J. Heerens. On the effect of a general residual stress state on indentation and hardness testing. *Acta Materialia*, 56:6205–6213, 2008.

I. Hutchings, M. Gee, and E. Santner. Friction and wear. In H. Czichos, T. Saito, and L. Smith, editors, *Springer Handbook of Materials Measurement Methods*, page 685–710. Springer, 2007. ISBN 978-3-540-30300-8.

J. C. Ion. *Laser Processing of Engineering Materials*. Butterworth-Heinemann, Oxford, 2005. ISBN 978-0-7506-6079-2.

S. Irizalp, N. Saklakoglu, E. Akman, and A. Demir. Pulsed Nd:YAG laser shock processing effects on mechanical properties of 6061-T6 alloy. *Optics & Laser Technology*, 56:273 – 277, 2014.

ISO 4287. Geometrical Product Specifications (GPS)-Surface texture: Profile method-Terms, definitions and surface texture parameters. Standard, International Organization for Standardization, Geneve, Switzerland, 1997.

ISO 4288. Geometrical Product Specifications (GPS)-Surface texture: Profile method-Rules and procedures for the assessment of surface texture. Standard, International Organization for Standardization, Geneve, Switzerland, 1998.

S. Kalainathan, S. Sathyajith, and S. Swaroop. Effect of laser shot peening without coating on the surface properties and corrosion behavior of 316L steel. *Optics and Lasers in Engineering*, 50 (12):1740 – 1745, 2012.

Z. Kallien, S. Keller, V. Ventzke, N. Kashaev, and B. Klusemann. Effect of Laser Peening Process Parameters and Sequences on Residual Stress Profiles. *Metals*, 9:655, 06 2019.

F. Kandil, D. Lord, and A. Fry. A review of residual stress measurement methods - A guide to technique selection. *NPL Report*, MATC(A)O4, 2001.

E. Kannatey-Asibu. *Principles of Laser Materials Processing*. John Wiley & Sons, 2009. ISBN 9780470459300.

D. Karthik and S. Swaroop. Laser peening without coating induced phase transformation and thermal relaxation of residual stresses in AISI 321 steel. *Surface and Coatings Technology*, 291:161 – 171, 2016.

N. Kashaev, V. Ventzke, M. Horstmann, Se. Chupakhin, S. Riekehr, R. Falck, E. Maawad, P. Staron, N. Schell, and N. Huber. Effects of laser shock peening on the microstructure and fatigue crack propagation behaviour of thin AA2024 specimens. *International Journal of Fatigue*, 98:223 – 233, 2017.

M. Kattoura, S. Mannava, D. Qian, and V.K. Vasudevan. Effect of laser shock peening on residual stress, microstructure and fatigue behavior of ATI 718 Plus alloy. *International Journal of Fatigue*, 102:121 – 134, 2017.

S. Keller, S. Chupakhin, P. Staron, E. Maawad, N. Kashaev, and B. Klusemann. Experimental and numerical investigation of residual stresses in laser shock peened AA2198. *Journal of Materials Processing Technology*, 255:294 – 307, 2018.

S. Keller, M. Horstmann, N. Kashaev, and B. Klusemann. Crack closure mechanisms in residual stress fields generated by laser shock peening: A combined experimental-numerical approach. *Engineering Fracture Mechanics*, 221:106630, 2019a.

S. Keller, M. Horstmann, N. Kashaev, and B. Klusemann. Experimentally validated multi-step simulation strategy to predict the fatigue crack propagation rate in residual stress fields after laser shock peening. *International Journal of Fatigue*, 124:265 – 276, 2019b.

G. Krauss. *Steels: Processing, Structure, and Performance*. ASM International, 2nd edition, 2015. ISBN 978-1-62708-083-5.

Y. Kudryavtsev. Residual stresses management: Measurements, Fatigue Analysis and Beneficial Redistribution. In Tom Proulx, editor, *Engineering Applications of Residual Stress, Volume 8: Proceedings of the 2011 Annual Conference on Experimental and Applied Mechanics*, volume 8 of *Conference Proceedings of the Society for Experimental Mechanics Series volume 999*, pages 119–129. Springer-Verlag New York, 2011.

D. Kumar, S. N. Akhtar, A. K. Patel, J. Ramkumar, and K. Balani. Tribological performance of laser peened Ti–6Al–4V. *Wear*, 322-323:203 – 217, 2015.

S. R. Lampman, editor. *ASM handbook: Fatigue and Fracture*, volume 19. ASM International, 1996. ISBN 978-0-87170-385-9.

K. Leitz, B. Redlingshöfer, Y. Reg, A. Otto, and M. Schmidt. Metal ablation with short and ultrashort laser pulses. *Physics Procedia*, 12:230 – 238, 2011. Lasers in Manufacturing 2011 - Proceedings of the Sixth International WLT Conference on Lasers in Manufacturing.

D. Lesyk, S. Martinez, B. Mordyuk, V. Dzhemelinskyi, and O. Danyleiko. Effects of the Combined Laser-Ultrasonic Surface Hardening Induced Microstructure and Phase State on Mechanical Properties of AISI D2 Tool Steel. In V. Ivanov, J. Trojanowska, J. Machado, O. Liaposhchenko, J. Zajac, I. Pavlenko, M. Edl, and D. Perakovic, editors, *Advances in Design, Simulation and Manufacturing II*, pages 188–198. Springer International Publishing, 2020. ISBN 978-3-030-22365-6.

K. Li, Y. Hu, and Z. Yao. Experimental study of micro dimple fabrication based on laser shock processing. *Optics & Laser Technology*, 48:216 – 225, 2013.

H. Lim, P. Kim, H. Jeong, and S. Jeong. Enhancement of abrasion and corrosion resistance of duplex stainless steel by laser shock peening. *Journal of Materials Processing Technology*, 212 (6):1347 – 1354, 2012.

X. Ling, W. Peng, and G. Ma. Influence of Laser Peening Parameters on Residual Stress Field of 304 Stainless Steel. *Journal of Pressure Vessel Technology*, 130:21201–1, 2008.

L. Liu, J. Wang, and J. Zhou. Effects of laser shock peening on mechanical behaviors and microstructural evolution of brass. *Vacuum*, 148:178 – 183, 2018a.

P. Liu, S. Sun, S. Xu, Y. Li, and G. Ren. Microstructure and properties in the weld surface of friction stir welded 7050-T7451 aluminium alloys by laser shock peening. *Vacuum*, 152:25 – 29, 2018b.

G. Lu, J. Liu, H. Qiao, Y. Zhou, T. Jin, J. Zhao, X. Sun, and Z. Hu. Surface nano-hardness and microstructure of a single crystal nickel base superalloy after laser shock peening. *Optics & Laser Technology*, 91:116 – 119, 2017a.

J. Z. Lu, K. Luo, Y. Zhang, G. Sun, Y. Gu, J. Zhou, X. D. Ren, X. Zhang, L. F. Zhang, K. M. Chen, C. Cui, and Y. Jiang. Grain refinement mechanism of multiple laser shock processing impacts on ANSI 304 stainless steel. *Acta Materialia*, 58:5354–5362, 2010.

J. Z. Lu, J. W. Zhong, K. Y. Luo, L. Zhang, F. Z. Dai, K. M. Chen, Q. W. Wang, J. S. Zhong, and Y. K. Zhang. Micro-structural strengthening mechanism of multiple laser shock processing impacts on AISI 8620 steel. *Materials Science and Engineering: A*, 528(19):6128 – 6133, 2011.

J. Z. Lu, K. Y. Luo, F. Z. Dai, J. W. Zhong, L. Z. Xu, C. J. Yang, L. Zhang, Q. W. Wang, J. S. Zhong, D. K. Yang, and Y. K. Zhang. Effects of multiple laser shock processing (LSP) impacts on mechanical properties and wear behaviors of AISI 8620 steel. *Materials Science and Engineering: A*, 536:57 – 63, 2012a.

J. Z. Lu, K. Y. Luo, D. K. Yang, X. N. Cheng, J. L. Hu, F. Z. Dai, H. Qi, L. Zhang, J. S. Zhong, Q. W. Wang, and Y. K. Zhang. Effects of laser peening on stress corrosion cracking (SCC) of ANSI 304 austenitic stainless steel. *Corrosion Science*, 60:145 – 152, 2012b.

J. Z. Lu, H. Qi, K. Y. Luo, M. Luo, and X. N. Cheng. Corrosion behaviour of AISI 304 stainless steel subjected to massive laser shock peening impacts with different pulse energies. *Corrosion Science*, 80:53 – 59, 2014.

J. Z. Lu, W. W. Deng, K. Y. Luo, L. J. Wu, and H. F. Lu. Surface EBSD analysis and strengthening mechanism of AISI304 stainless steel subjected to massive LSP treatment with different pulse energies. *Materials Characterization*, 125:99 – 107, 2017b.

J. Z. Lu, B. Han, C. Y. Cui, C. J. Li, and K. Y. Luo. Electrochemical and pitting corrosion resistance of AISI 4145 steel subjected to massive laser shock peening treatment with different coverage layers. *Optics & Laser Technology*, 88:250 – 262, 2017c.

J. Z. Lu, L. J. Wu, G. F. Sun, K. Y. Luo, Y. K. Zhang, J. Cai, C. Y. Cui, and X. M. Luo. Microstructural response and grain refinement mechanism of commercially pure titanium subjected to multiple laser shock peening impacts. *Acta Materialia*, 127:252 – 266, 2017d.

Q. Lu, S. Mao, X. Mao, and R. Russo. Delayed phase explosion during high-power nanosecond laser ablation of silicon. *Applied Physics Letters*, 80(17):3072–3074, 2002.

K. Y. Luo, J. Z. Lu, Y. K. Zhang, J. Z. Zhou, L. F. Zhang, F. Z. Dai, L. Zhang, J. W. Zhong, and C. Y. Cui. Effects of laser shock processing on mechanical properties and micro-structure of ANSI 304 austenitic stainless steel. *Materials Science and Engineering: A*, 528(13):4783 – 4788, 2011.

K. Y. Luo, J. Z. Lu, Q. W. Wang, M. Luo, H. Qi, and J. Z. Zhou. Residual stress distribution of Ti-6Al-4V alloy under different ns-LSP processing parameters. *Applied Surface Science*, 285: 607 – 615, 2013.

K. Y. Luo, T. Lin, F. Z. Dai, X. M. Luo, and J. Z. Lu. Effects of overlapping rate on the uniformities of surface profile of LY2 Al alloy during massive laser shock peening impacts. *Surface and Coatings Technology*, 266:49 – 56, 2015.

S. Luo, W. He, K. Chen, X. Nie, L. Zhou, and Y. Li. Regain the fatigue strength of laser additive manufactured Ti alloy via laser shock peening. *Journal of Alloys and Compounds*, 750:626 – 635, 2018.

H. Luong and M. R. Hill. The effects of laser peening and shot peening on high cycle fatigue in 7050-T7451 aluminum alloy. *Materials Science and Engineering: A*, 527(3):699 – 707, 2010.

P. T. Mannion, J. Magee, E. Coyne, G. M. O'Connor, and T. J. Glynn. The effect of damage accumulation behaviour on ablation thresholds and damage morphology in ultrafast laser micromachining of common metals in air. *Applied Surface Science*, 233(1):275 – 287, 2004.

B. Mao, Y. Liao, and B. Li. Gradient twinning microstructure generated by laser shock peening in an AZ31B magnesium alloy. *Applied Surface Science*, 457:342 – 351, 2018a.

B. Mao, A. Siddaiah, P. L. Menezes, and Y. Liao. Surface texturing by indirect laser shock surface patterning for manipulated friction coefficient. *Journal of Materials Processing Technology*, 257:227 – 233, 2018b.

J. E. Masse and G. Barreau. Laser generation of stress waves in metal. *Surface and Coatings Technology*, 70(2):231 – 234, 1995.

J. Mathar. Determination of initial stresses by measuring the deformation around drilled holes. *Transactions ASME*, 56:249 – 254, 1934.

X. Meng, J. Zhou, C. Su, S. Huang, K. Luo, J. Sheng, and W. Tan. Residual stress relaxation and its effects on the fatigue properties of Ti6Al4V alloy strengthened by warm laser peening. *Materials Science and Engineering: A*, 680:297 – 304, 2017.

A. Miotello and R. Kelly. Laser-induced phase explosion: new physical problems when a condensed phase approaches the thermodynamic critical temperature. *Applied Physics A*, 69(1): S67–S73, 1999.

C. S. Montross, V. Florea, and M. V. Swain. The influence of coatings on subsurface mechanical properties of laser peened 2011-T3 aluminum. *Journal of Materials Science*, 36(7):1801–1807, 2001.

C. S. Montross, T. Wei, L. Ye, G. Clark, and Y. W. Mai. Laser shock processing and its effects on microstructure and properties of metal alloys: a review. *International Journal of Fatigue*, 24 (10):1021 – 1036, 2002.

N. Mukai, N. Aoki, M. Obata, A. Ito, Y. Sano, and C. Konagai. Laser processing for underwater maintenance in nuclear plants. In *Proceedings of the 3rd JSME/ASME Joint International Conference on Nuclear Engineering*, volume 3, Japan, 1995.

T. Mura. *Micromechanics of Defects in Solids*, volume 3 of *Mechanics of Elastic and Inelastic Solids*. Springer Netherlands, 2 edition, 1987. ISBN 978-94-009-3489-4.

T. Nguyen, R. Tanabe, and Y. Ito. Comparative study of the expansion dynamics of laser-driven plasma and shock wave in in-air and underwater ablation regimes. *Optics & Laser Technology*, 100:21 – 26, 2018.

X. Nie, W. He, S. Zang, X. Wang, and J. Zhao. Effect study and application to improve high cycle fatigue resistance of TC11 titanium alloy by laser shock peening with multiple impacts. *Surface and Coatings Technology*, 253:68 – 75, 2014.

I. Nikitin and I. Altenberger. Comparison of the fatigue behavior and residual stress stability of laser-shock peened and deep rolled austenitic stainless steel AISI 304 in the temperature range 25–600°C. *Materials Science and Engineering: A*, 465(1):176 – 182, 2007.

F. Di Niso, C. Gaudiuso, T. Sibillano, F. P. Mezzapesa, A. Ancona, and P. M. Lugarà. Influence of the Repetition Rate and Pulse Duration on the Incubation Effect in Multiple-Shots Ultrafast Laser Ablation of Steel. *Physics Procedia*, 41:698 – 707, 2013.

J. A. Oliveira. Contour method for mapping residual stress, 2018. URL https://www.stressmap.co.uk/contour-method/.

C. Oros. Investigations involving shock waves generation and shock pressure measurement in direct ablation regime and confined ablation regime. *Shock Waves*, 11(5):393–397, 2002.

B. K. Pant, R. Sundar, H. Kumar, R. Kaul, A. H. Pavan, K. Ranganathan, K. S. Bindra, S. M. Oak, L. M. Kukreja, R. V. Prakash, and M. Kamaraj. Studies towards development of laser peening technology for martensitic stainless steel and titanium alloys for steam turbine applications. *Materials Science and Engineering: A*, 587:352 – 358, 2013.

B. K. Pant, A. H. Pavan, R. V. Prakash, and M. Kamaraj. Effect of laser peening and shot peening on fatigue striations during FCGR study of Ti6Al4V. *International Journal of Fatigue*, 93:38 – 50, 2016.

P. Paris and F. Erdogan. A Critical Analysis of Crack Propagation Laws. *Journal of Basic Engineering*, 85(4):528–533, 1963.

J. Park, I. Yeo, I. Jang, and S. Jeong. Improvement of friction characteristics of cast aluminum-silicon alloy by laser shock peening. *Journal of Materials Processing Technology*, 266:283 – 291, 2019.

M. Pavan, D. Furfari, B. Ahmad, M. A. Gharghouri, and M. E. Fitzpatrick. Fatigue crack growth in a laser shock peened residual stress field. *International Journal of Fatigue*, 123:157 – 167, 2019.

C. Peng, Y. Xiao, Y. Wang, and W. Guo. Effect of laser shock peening on bending fatigue performance of AISI 9310 steel spur gear. *Optics & Laser Technology*, 94:15 – 24, 2017.

N. Perez. *Fracture Mechanics*. Mathematics and Its Applications. Kluwer Academic Publishers, 1 edition, 2004. ISBN 9781402078613.

L. Petan, J. L. Ocaña, and J. Grum. Influence of laser shock peening pulse density and spot size on the surface integrity of X2NiCoMo18-9-5 maraging steel. *Surface and Coatings Technology*, 307:262 – 270, 2016.

S. Petronić, K. Čolić, B. Đorđević, D. Milovanović, M. Burzić, and F. Vučetić. Effect of laser shock peening with and without protective coating on the microstructure and mechanical properties of Ti-alloy. *Optics and Lasers in Engineering*, 129:106052, 2020.

P. Peyre, R. Fabbro, P. Merrien, and H. P. Lieurade. Laser shock processing of aluminium alloys. Application to high cycle fatigue behaviour. *Materials Science and Engineering: A*, 210(1):102 – 113, 1996.

P. Peyre, X. Scherpereel, L. Berthe, and R. Fabbro. Current trends in laser shock processing. *Surface Engineering*, 14(5):377–380, 1998.

P. Peyre, A. Sollier, I. Chaieb, L. Berthe, E. Bartnicki, C. Braham, and R. Fabbro. Fem simulation of residual stresses induced by laser peening. *The European Physical Journal Applied Physics*, 23(2):83–88, 2003.

P. Peyre, C. Carboni, P. Forget, G. Beranger, C. Lemaitre, and D. Stuart. Influence of thermal and mechanical surface modifications induced by laser shock processing on the initiation of corrosion pits in 316L stainless steel. *Journal of Materials Science*, 42(16):6866–6877, 2007a.

P. Peyre, I. Chaieb, and C. Braham. FEM calculation of residual stresses induced by laser shock processing in stainless steels. *Modelling and Simulation in Materials Science and Engineering*, 15(03):205, 2007b.

P. Peyre, L. Berthe, V. Vignal, I. Popa, and T. Baudin. Analysis of laser shock waves and resulting surface deformations in an Al–Cu–Li aluminum alloy. *Journal of Physics D Applied Physics*, 45(33), 2012.

S. Prabhakaran, A. Kulkarni, G. Vasanth, S. Kalainathan, P. Shukla, and V. K. Vasudevan. Laser shock peening without coating induced residual stress distribution, wettability characteristics and enhanced pitting corrosion resistance of austenitic stainless steel. *Applied Surface Science*, 428:17 – 30, 2018.

M. B. Prime. Cross-sectional mapping of residual stresses by measuring the surface contour after a cut. *Journal of Engineering Materials and Technology*, 123:162–168, 2001.

F. E. Purkert. Prevention of decarburization in annealing of high carbon steel. *Journal of Heat Treating*, 2(3):225–231, 1982.

H. Qiao, J. Zhao, and H. Yang. Study and development of high peak power short pulse Nd:YAG laser for peening applications. *Science China Technological Sciences*, 58(7):1154–1161, 2015a.

H. Qiao, J. Zhao, G. Zhang, and Y. Gao. Effects of laser shock peening on microstructure and residual stress evolution in Ti–45Al–2Cr–2Nb–0.2B alloy. *Surface and Coatings Technology*, 276:145 – 151, 2015b.

A. K. Rai, R. Biswal, R. Gupta, R. Singh, S. Rai, K. Ranganathan, P. Ganesh, R. Kaul, and K. Bindra. Study on the effect of multiple laser shock peening on residual stress and microstructural changes in modified 9Cr-1Mo (P91) steel. *Surface and Coatings Technology*, 358: 125–135, 2019.

K. D. Ramkumar, S. Singh, J. C. George, S. Anirudh, G. Brahadees, S. Goyal, S. K. Gupta, C. Vishnu, N. R. Sharan, and S. Kalainathan. Effect of pulse density and the number of shots on hardness and tensile strength of laser shock peened, activated flux TIG welds of AISI 347. *Journal of Manufacturing Processes*, 28(1):295 – 308, 2017.

T. Rickert. Residual Stress Measurement by ESPI Hole-Drilling. *Procedia CIRP*, 45:203 – 206, 2016. 3rd CIRP Conference on Surface Integrity.

G. Roberts, G. Krauss, and R. Kennedy. *High-Carbon, High-Chromium, Cold-Work Tool Steels*, pages 203–217. ASM International, 5th edition, 1998. ISBN 978-0-87170-599-0.

N. Saklakoglu, S. G. Irizalp, E. Akman, and A. Demir. Near surface modification of aluminum alloy induced by laser shock processing. *Optics & Laser Technology*, 64:235 – 241, 2014.

T. Sano, T. Eimura, R. Kashiwabara, T. Matsuda, Y. Isshiki, A. Hirose, S. Tsutsumi, K. Arakawa, T. Hashimoto, K. Masaki, and Y. Sano. Femtosecond laser peening of 2024 aluminum alloy without a sacrificial overlay under atmospheric conditions. *Journal of Laser Applications*, 29 (1):012005, 2017.

Y. Sano, N. Mukai, K. Okazaki, and M. Obata. Residual stress improvement in metal surface by underwater laser irradiation. *Nuclear Instruments and Methods in Physics Research Section B: Beam Interactions with Materials and Atoms*, 121(1):432 – 436, 1997.

Y. Sano, K. Akita, K. Masaki, Y. Ochi, I. Altenberger, and B. Scholtes. Laser Peening without Coating as a Surface Enhancement Technology. *Journal of Laser Micro/Nanoengineering*, 1 (3):161–166, 2006a.

Y. Sano, M. Obata, T. Kubo, N. Mukai, M. Yoda, K. Masaki, and Y. Ochi. Retardation of crack initiation and growth in austenitic stainless steels by laser peening without protective coating. *Materials Science and Engineering: A*, 417(1):334 – 340, 2006b.

G. Schajer. Hole-Drilling Residual Stress Profiling With Automated Smoothing. *Journal of Engineering Materials and Technology*, 129(3):440–445, 2007.

G. Schajer. Advances in Hole-Drilling Residual Stress Measurements. *Experimental Mechanics*, 50(2):159–168, 2010.

G. Schajer and P. Whitehead. *Practical Residual Stress Measurement Methods: Hole Drilling and Ring Coring*, pages 29–64. John Wiley & Sons, Ltd, 2013. ISBN 9781118402832.

J. Schijve. *Fatigue of structures and materials*. Springer, 2nd edition, 2009. ISBN 0195153766.

B. Scholtes and O. Voehringer. Mechanical Surface Treatment. In K. H. Jürgen Buschow, R. W. Cahn, M. C. Flemings, B. Ilschner, E. J. Kramer, S. Mahajan, and P. Veyssière, editors, *Encyclopedia of Materials: Science and Technology*, pages 5253 – 5261. Elsevier, Oxford, 2001. ISBN 978-0-08-043152-9.

X. Shen, P. Shukla, S. Nath, and J. Lawrence. Improvement in mechanical properties of titanium alloy (Ti-6Al-7Nb) subject to multiple laser shock peening. *Surface and Coatings Technology*, 327:101 – 109, 2017.

J. Sheng, S. Huang, J. Z. Zhou, J. Z. Lu, S. Q. Xu, and H. F. Zhang. Effect of laser peening with different energies on fatigue fracture evolution of 6061-T6 aluminum alloy. *Optics & Laser Technology*, 77:169 – 176, 2016.

A. Siddaiah, B. Mao, Y. Liao, and P. L. Menezes. Surface characterization and tribological performance of laser shock peened steel surfaces. *Surface and Coatings Technology*, 351:188 – 197, 2018.

M. Singh, D. Sood, R. Gupta, R. Kumar, P. Gautam, B. Sewak, A. Sharma, and T. Mathew. Dynamic Yield Strength of Mild Steel under Impact Loading. *Defence Science Journal*, 58(2): 275–284, 2008.

L. Spadaro, G. Gomez-Rosas, C. Rubio-González, R. Bolmaro, A. Chavez-Chavez, and S. Hereñú. Fatigue behavior of superferritic stainless steel laser shock treated without protective coating. *Optics & Laser Technology*, 93:208 – 215, 2017.

M. Steinzig and E. Ponslet. Residual stress measurement using the hole drilling method and laser speckle interferometry: part 1. *Experimental Techniques*, 27(3):43–46, 2003.

M. Sticchi, D. Schnubel, N. Kashaev, and N. Huber. Review of Residual Stress Modification Techniques for Extending the Fatigue Life of Metallic Aircraft Components. *Applied Mechanics Reviews*, 67(1), 2014.

M. Sticchi, P. Staron, Y. Sano, M. Meixer, M. Klaus, J.R. Kornmeier, N. Huber, and N. Kashaev. A parametric study of laser spot size and coverage on the laser shock peening induced residual stress in thin aluminium samples. *The Journal of Engineering*, 2015(13):97–105, 2015.

G. Straffelini. *Friction and Wear - Methodologies for Design and Control*. Springer International Publishing, 1st edition, 2015. ISBN 978-3-319-05894-8.

R. Sun, Y. Zhu, L. Li, W. Guo, and P. Peng. High Strain Rate Response of 7055 Aluminum Alloy Subject to Square-spot Laser Shock Peening. *IOP Conference Series: Materials Science and Engineering*, 275(1):012041, 2017.

R. Sun, L. Li, W. Guo, P. Peng, T. Zhai, Z. Che, B. Li, C. Guo, and Y. Zhu. Laser shock peening induced fatigue crack retardation in Ti-17 titanium alloy. *Materials Science and Engineering: A*, 737:94 – 104, 2018a.

R. Sun, L. Li, Y. Zhu, W. Guo, P. Peng, B. Cong, J. Sun, Z. Che, B. Li, C. Guo, and L. Liu. Microstructure, residual stress and tensile properties control of wire-arc additive manufactured 2319 aluminum alloy with laser shock peening. *Journal of Alloys and Compounds*, 747:255 – 265, 2018b.

U. Sánchez-Santana, C. Rubio-González, G. Gomez-Rosas, J. L. Ocaña, C. Molpeceres, J. Porro, and M. Morales. Wear and friction of 6061-T6 aluminum alloy treated by laser shock processing. *Wear*, 260(7):847 – 854, 2006.

D. Tan, J. Mo, W. He, J. Luo, Q. Zhang, M. Zhu, and Z. Zhou. Suitability of laser shock peening to impact-sliding wear in different system stiffnesses. *Surface and Coatings Technology*, 358: 22 – 35, 2019.

LSP Technologies. Laser peening equipment and services, Feb 2020. URL https://www.lsptechnologies.com/.

A. N. Tikhonov, A. V. Goncharsky, V. V. Stepanov, and A. G. Yagola. *Numerical Methods for the Solution of Ill-Posed Problems*. Mathematics and Its Applications. Springer Netherlands, 1st edition, 1995. ISBN 978-94-015-8480-7.

Tech Note TN-503. Measurement of Residual Stresses by the Hole-Drilling Strain Gage Method. Technical report, Vishay Precision Group, 2010.

Z. Tong, X. Ren, Y. Ren, F. Z. Dai, Y. Ye, W. Zhou, L. Chen, and Z. Ye. Effect of laser shock peening on microstructure and hot corrosion of TC11 alloy. *Surface and Coatings Technology*, 335:32 – 40, 2018.

Z. Tong, X. Ren, W. Zhou, S. Adu-Gyamfi, L. Chen, Y. Ye, Y. Ren, F. Z. Dai, J. Yang, and L. Li. Effect of laser shock peening on wear behaviors of TC11 alloy at elevated temperature. *Optics & Laser Technology*, 109:139 – 148, 2019.

H. Torkamani, S. Raygan, and J. Rassizadehghani. Evaluation of Microstructure and Toughness of AISI D2 Steel by Bright Hardening in Comparison with Oil Quenching. *AIP Conference Proceedings*, 1400(1):438–442, 2011.

G. Totten, M. Howes, and T. Inoue, editors. *Handbook of Residual Stress and Deformation of Steel*, chapter Effect of Materials and Processing, pages 12–26. ASM International, 2002. ISBN 978-0-87170-729-1.

U. Trdan and J. Grum. SEM/EDS characterization of laser shock peening effect on localized corrosion of Al alloy in a near natural chloride environment. *Corrosion Science*, 82:328 – 338, 2014.

U. Trdan, S. Žagar, J. Grum, and J.L. Ocanã. Surface modification of laser and shot peened 6082 aluminium alloy: Laser peening effect to pitting corrosion. *International Journal of Structural Integrity*, 2(1):9 – 21, 2011.

U. Trdan, J. Porro, J. L. Ocaña, and J. Grum. Laser shock peening without absorbent coating (LSPwC) effect on 3D surface topography and mechanical properties of 6082-T651 Al alloy. *Surface and Coatings Technology*, 208:109–116, 2012.

U. Trdan, M. Skarba, J. A. Porro, J. L. Ocaña, and J. Grum. Application of massive laser shock processing for improvement of mechanical and tribological properties. *Surface and Coatings Technology*, 342:1 – 11, 2018.

S.-T. Tu and X.-C. Zhang. Fatigue crack initiation mechanisms. In *Reference Module in Materials Science and Materials Engineering*. Elsevier, 2016. ISBN 978-0-12-803581-8.

A. Umapathi and S. Swaroop. Wavelength dependent deformation in a laser peened Ti-2.5Cu alloy. *Materials Science and Engineering: A*, 684:344 – 352, 2017.

A. Umapathi and S. Swaroop. Deformation of single and multiple laser peened TC6 titanium alloy. *Optics & Laser Technology*, 100:309 – 316, 2018.

G. Voort. *Metallography and Microstructures*. ASM International, 9th edition, 2004. ISBN 978-0-87170-706-2.

C. Wang, X.J. Shen, Z.B. An, L.C. Zhou, and Y. Chai. Effects of laser shock processing on microstructure and mechanical properties of K403 nickel-alloy. *Materials & Design*, 89:582 – 588, 2016.

J. Wang, Y. Lu, D. Zhou, L. Sun, L. Xie, and J. Wang. Mechanical properties and microstructural response of 2A14 aluminum alloy subjected to multiple laser shock peening impacts. *Vacuum*, 165:193 – 198, 2019.

X. Wang, W. Xia, X. Wu, Y. Wei, and C. Huang. Microstructure and mechanical properties of an austenite NiTi shape memory alloy treated with laser induced shock. *Materials Science and Engineering: A*, 578:1 – 5, 2013.

I. Watanabe, M. McBride, P. Newton, and K. S. Kurtz. Laser surface treatment to improve mechanical properties of cast titanium. *Dental Materials*, 25(5):629 – 633, 2009.

X. Wei and X. Ling. Numerical modeling of residual stress induced by laser shock processing. *Applied Surface Science*, 301:557 – 563, 2014.

P. J. Withers and H. Bhadeshia. Residual stress. Part 1 – Measurement techniques. *Materials Science and Technology*, 17(4):355–365, 2001.

L. J. Wu, K. Y. Luo, Y. Liu, C. Y. Cui, W. Xue, and J. Z. Lu. Effects of laser shock peening on the micro-hardness, tensile properties, and fracture morphologies of CP-Ti alloy at different temperatures. *Applied Surface Science*, 431:122 – 134, 2018. 5th Asian Conference on Heat Treatment and Surface Engineering.

X. Wu, C. Huang, X. Wang, and H. Song. A new effective method to estimate the effect of laser shock peening. *International Journal of Impact Engineering*, 38(5):322 – 329, 2011.

Y. Xiong, Q. Hu, R. Song, and X. Hu. LSP/MAO composite bio-coating on AZ80 magnesium alloy for biomedical application. *Materials Science and Engineering: C*, 75:1299 – 1304, 2017.

I. Yakimets, C. Richard, G. Béranger, and P. Peyre. Laser peening processing effect on mechanical and tribological properties of rolling steel 100Cr6. *Wear*, 256(3):311 – 320, 2004.

J.-M. Yang, Y. Her, N. Han, and A. Clauer. Laser shock peening on fatigue behavior of 2024-T3 Al alloy with fastener holes and stopholes. *Materials Science and Engineering: A*, 298(1):296 – 299, 2001.

C. Ye, S. Suslov, B.-J. Kim, E. Stach, and G. Cheng. Fatigue performance improvement in AISI 4140 steel by dynamic strain aging and dynamic precipitation during warm laser shock peening. *Acta Materialia*, 59(3):1014–1025, 2011.

P. Yella, P. Venkateswarlu, R. K. Buddu, D. V. Vidyasagar, K. Rao, P. Kiran, and K. V. Rajulapati. Laser shock peening studies on SS 316LN plate with various sacrificial layers. *Applied Surface Science*, 435:271 – 280, 2018.

P. Yella, K. V. Rajulapati, G. V. Reddy, R. Sandhya, P. Kiran, R. K. Buddu, and K. Rao. Effect of laser shock peening on high cycle fatigue characteristics of 316LN stainless steel. *International Journal of Pressure Vessels and Piping*, 176:103972, 2019.

C. J. Yocom, X. Zhang, and Y. Liao. Research and development status of laser peen forming: A review. *Optics & Laser Technology*, 108:32 – 45, 2018.

K. Zelic, J. Burja, P. J. McGuiness, and M. Godec. Effect of Rare Earth Elements on the Morphology of Eutectic Carbides in AISI D2 Tool Steels: Experimental and Modelling Approaches. *Scientific reports*, 8, 2018.

L. Zhang, Y. K. Zhang, J. Z. Lu, F. Z. Dai, A. X. Feng, K. Y. Luo, J. S. Zhong, Q. W. Wang, M. Luo, and H. Qi. Effects of laser shock processing on electrochemical corrosion resistance of ANSI 304 stainless steel weldments after cavitation erosion. *Corrosion Science*, 66:5 – 13, 2013.

R. Zhang, X. Zhou, H. Gao, S. Mankoci, Y. Liu, X. Sang, H. Qin, X. Hou, Z. Ren, G. L. Doll, A. Martini, Y. Dong, N. Sahai, and C. Ye. The effects of laser shock peening on the mechanical properties and biomedical behavior of AZ31B magnesium alloy. *Surface and Coatings Technology*, 339:48 – 56, 2018.

X. C. Zhang, Y. K. Zhang, J. Z. Lu, F. Z. Xuan, Z. D. Wang, and S. T. Tu. Improvement of fatigue life of Ti–6Al–4V alloy by laser shock peening. *Materials Science and Engineering: A*, 527 (15):3411 – 3415, 2010a.

Y. Zhang, X. Ren, J. Z. Zhou, J. Z. Lu, and L. C. Zhou. Investigation of the stress intensity factor changing on the hole crack subject to laser shock processing. *Materials & Design*, 30(7):2769 – 2773, 2009.

Y. Zhang, J. You, J. Lu, C. Cui, Y. Jiang, and X. Ren. Effects of laser shock processing on stress corrosion cracking susceptibility of AZ31B magnesium alloy. *Surface and Coatings Technology*, 204(24):3947 – 3953, 2010b.

Y. Zhang, Q. Lian, and X. Wang. Enhancement of rolling contact fatigue performance of ferrite–pearlite steel with laser shock peening. *Advances in Mechanical Engineering*, 11(5), 2019.

L. Zheng, C. Zhang, C. Zhang, and F. Dai. Performance of micro-dent array fabricated by laser shock peening on the surface of A304 stainless steel. *Vacuum*, 138:93 – 100, 2017.

J. Z. Zhou, J. C. Yang, Y. K. Zhang, and M. Zhou. A study on super-speed forming of metal sheet by laser shock waves. *Journal of Materials Processing Technology*, 129(1):241 – 244, 2002. The 10th International Manufacturing Conference in China (IMCC 2002).

J. Z. Zhou, S. Huang, L. D. Zuo, X. K. Meng, J. Sheng, Q. Tian, Y. H. Han, and W. L. Zhu. Effects of laser peening on residual stresses and fatigue crack growth properties of Ti–6Al–4V titanium alloy. *Optics and Lasers in Engineering*, 52:189 – 194, 2014.

L. Zhou, W. He, S. Luo, C. Long, C. Wang, X. Nie, G. He, X. Shen, and Y. Li. Laser shock peening induced surface nanocrystallization and martensite transformation in austenitic stainless steel. *Journal of Alloys and Compounds*, 655:66 – 70, 2016.

L. Zhou, C. Long, W. He, L. Tian, and W. Jia. Improvement of high-temperature fatigue performance in the nickel-based alloy by LSP-induced surface nanocrystallization. *Journal of Alloys and Compounds*, 744:156 – 164, 2018.

Z. Zhou, A. S. Gill, D. Qian, S. R. Mannava, K. Langer, Y. Wen, and V. K. Vasudevan. A finite element study of thermal relaxation of residual stress in laser shock peened IN718 superalloy. *International Journal of Impact Engineering*, 38(7):590 – 596, 2011.

S. Zou, S. Gong, and E. Guo. Surface profile and microstructure of laser peened Ti-6Al-4V. *Rare Metals*, 31(5):430–433, 2012.